

Transactions of the ASME

FLUIDS ENGINEERING DIVISION

Technical Editor
FRANK M. WHITE (1984)
Executive Secretary
L. T. NELSON (1984)
Calendar Editor
M. F. ACKERSON

Associate Editors

Fluid Machinery
AWATEF A. HAMED (1985)
WILLIAM E. THOMPSON (1984)
Fluid Measurements
THEODORE R. HEIDRICK (1984)
Fluid Mechanics
SHLOMO CARMİ (1984)
CHARLES DALTON (1983)
KIRTI N. GHIA (1984)
THOMAS J. MUELLER (1985)
Fluid Transients
M. HANIF CHAUDHRY (1983)
Multiphase Flow
JOHN T. JUREWICZ (1985)
OKITSUGU FURUYA (1984)
Review Articles
RICHARD A. BAJURA (1985)

FOREIGN CORRESPONDENTS

Europe and Russia
JACQUES CHAUVIN
Europe and Russia
JOHN H. HORLOCK
India and Middle East
ARUN PRASAD
Japan and China
YASUTOSHI SENOO

BOARD ON COMMUNICATIONS

Chairman and Vice President
MICHAEL J. RABINS

Members-at-Large

W. BEGELL, J. CALLAHAN,
D. KOENIG, M. KUTZ, F. LANDIS,
J. W. LOCKE, J. ORTLOFF, C. PHILLIPS,
H. C. REEDER, K. REID

President, SERGE GRATCH

Executive Director
PAUL ALLMENDINGER
Treasurer,
ROBERT A. BENNETT

PUBLISHING STAFF

Mng. Dir. Publ., **J. J. FREY**
Dep. Mng. Dir. Publ.,
JOS. SANSONE

Managing Editor, **CORNELIA MONAHAN**
Editorial Production Assistant,
BETH DARCHI

The Journal of FLUIDS ENGINEERING

(USPS 278-480) is edited
and published quarterly at the offices of
The American Society of
Mechanical Engineers,
United Engineering Center,
345 E. 47th St., New York,
N. Y. 10017. Cable Address, "Mechaneer," New York.

Second-class postage paid at New York.

CHANGES OF ADDRESS must be received at
Society headquarters seven weeks before
they are to be effective. Please send
old label and new address.

PRICES: To members, \$36.00, annually;
to nonmembers, \$72.00. Single copies, \$24.00
each. Add \$6.00 for postage to countries
outside the United States and Canada.

STATEMENT from By-Laws.

The Society shall not be responsible
for statements or opinions
advanced in papers or . . . printed in its
publications (B7.1, Par. 3).

COPYRIGHT © 1983 by The American Society
of Mechanical Engineers. Reprints from this
publication may be made on condition that full
credit be given the TRANSACTIONS OF THE ASME,
JOURNAL OF FLUIDS ENGINEERING
and the author, and date of
publication be stated.

INDEXED by the Engineering Index, Inc.

Journal of Fluids Engineering

Published Quarterly by The American Society of Mechanical Engineers

VOLUME 105 • NUMBER 1 • MARCH 1983

- 2 Fluids Engineering Calendar
- 5 Fluid Mechanics in Crystal Growth—The 1982 Freeman Scholar Lecture
Simon Ostrach
- 21 Radial Vaneless Diffusers: A Re-Examination of the Theories of Dean and Senoo and of
Johnston and Dean
M. Inoue
- 28 A Stall Margin Design Method for Planar and Axisymmetric Diffusers (82-WA/FE-8)
R. C. Strawn and S. J. Kline
- 34 Reynolds Number Effects on the Nearfield Mean Characteristics of a Laboratory Model
Thermal Plume (81-FE-7)
J. M. Kuhlman and L.-C. Chu
- 42 Regular Structures in a Plane Triple Jet
G. Schweiger
- 47 Supersonic Diffusers With Reverse Flow Injection (82-WA/FE-7)
D. W. Kuntz, J. C. Dutton, S. H. White, and A. L. Addy
- 53 Aerodynamic Loads on a Darrieus Rotor Blade
R. E. Wilson, P. B. S. Lissaman, M. James, and W. R. McKie
- 59 Development of Stratification in a Rectangular Tank by Horizontal Inflow
W. D. Baines, W. W. Martin, and D. M. Smith
- 65 Computer Prediction of Local Destratification Near Low-Level Release Structures of
Reservoirs (81-FE-11)
A. A. Busnaina and D. G. Lilley
- 71 Development of Magnetohydrodynamic Flow in a Parallel-Plate Channel in an Inclined Field
(82-WA/FE-6)
S. Rajaram and C. P. Yu
- 76 A Multigrid Scheme for Three-Dimensional Body-Fitted Coordinates in Turbomachine Ap-
plications
R. Camarero and M. Reggio
- 83 Transient Droplet Heating at High Peclet Number
H. A. Dwyer, R. J. Kee, P. K. Barr, and B. R. Sanders
- 89 Simple and Explicit Formulas for the Friction Factor in Turbulent Pipe Flow
S. E. Haaland
- 91 Prediction of the Trajectory of Triple Jets in a Uniform Crossflow
T. Makihata and Y. Miyai
- 98 Flow Around a Normal Plate of Finite Width Immersed in a Turbulent Boundary Layer
H. Sakamoto and M. Arie
- 105 Squish and Swirl-Squish Interaction in Motored Model Engines
C. Arcoumanis, A. F. Bicen, and J. H. Whitelaw
- 113 Air Release During Column Separation
Muin Baasiri and J. Paul Tullis

Technical Brief

- 119 Effects of Surface Solidification on the Stability of Multi-Layered Liquid Films
S. P. Lin

- 122 Discussion on Previously Published Papers

Announcements and Special Notices

- 1 ASME Prior Publication Policy
- 1 Submission of Papers
- 1 Statement of Experimental Uncertainty
- 52 Transactions Change of Address Form
- 82 Mandatory Excess-Page Charge for Transactions

Simon Ostrach

Wilbert J. Austin Distinguished Professor
of Engineering,
Department of Mechanical and Aerospace
Engineering,
Case Western Reserve University,
Cleveland, OH 44106
Fellow ASME

Fluid Mechanics in Crystal Growth—The 1982 Freeman Scholar Lecture

Introduction

Single crystals are solids with the most uniform structure (on an atomic scale) that can be attained and this is the basis for their technological applications. One of the most important features of the uniformity is that it permits the transmission without scattering of both acoustic and electromagnetic waves and charged particles. This transparency, which can be selectively modified by the controlled addition of impurities (dopants), is the foundation of the modern electronics industry and has made possible transistors, lasers, quartz piezo-electric filters, microwave devices, infrared detectors, magnetic bubble memory devices, and many other electromechanical and magneto- and electro-optical components. In short, crystals are vital elements in some of the most sophisticated, advanced, and rapidly-developing industries. That the methods now used for the growth of single crystals have been developed empirically attests to the ingenuity of the pioneers in these fields. However, to bring about the next major development of this technology and to improve the economics so that new products can be made feasible it is necessary to understand the complex physical and chemical transport phenomena that prevail during the processing of materials.

Single crystals result from carefully controlled phase changes that involve latent heats of transformation. Most crystals are formed by solidification of a melt, growth from a super-saturated solution (which can be aqueous, a metallic solution or a molten flux), condensation of a vapor, or by chemical reaction of gases.

The removal of the latent heat is an important part of the process. Because the composition of the growing crystal is different from that of the nutrient phase, mass transfer must also be considered. The rate of crystal growth is often limited by the mass transfer because it is the slowest process. In almost all of the commonly used techniques the parent phase is a fluid, i.e., a liquid or a gas. As in most nonequilibrium processes involving a fluid, convection (macroscopic fluid motion) plays a dominant role in that it affects the fluid-phase composition and temperature at the phase interface. The fluid

motion, in turn, is determined by the interplay of externally imposed motion (forced convection) and locally generated motion. The latter flows are due either to the effects of temperature and/or concentration density gradients in a body-force field (natural convection) or to the effects of surface-tension gradients on free surfaces. Thus, in general, the growth of crystals in a coupled process of heat and mass transfer, fluid flow, and phase transformations and chemical reactions. (Solidification processes also involve many of the same aspects.) Although the technology of crystal growth is well grounded in physical chemistry, the treatment of the transport phenomena has been relatively rudimentary and empirical.

It has been realized in the last decade or so that the transport processes in the fluid phase during the growth of crystals have a profound influence on the structure and quality of the solid phase. Thus, with the need for ever more perfect crystals, attention began to be focused on the role of convection in crystal growth. For the most part the earlier work in this regard consists essentially of qualitative descriptions or explanations of specific growth aspects that are observed in current processing methods. Much of that work was also based on the premise that convection is deleterious. Thus, with the advent of spaceflight it was thought that crystal quality would be enhanced by the low-gravity environment that would eliminate or greatly reduce natural convection. However, crystal growth experiments aboard Skylab did not produce such definitive results. In order to evaluate the Skylab results and to plan for future space processing programs a few fluid dynamicists were exposed to the problems. One of the real benefits of the materials processing in space program is that it brought about interaction among materials scientists and fluid dynamicists. However, this did not bring about an immediate improvement even in the understanding of the phenomena because many of the relevant transport problems are beyond the frontiers of the current knowledge in the related fields. This interaction of disciplines has, however, indicated gaps in fluid dynamics topics that require serious attention.

In recent years a more intensive and basic research effort has been underway to address some of these problems. The

Contributed by the Fluids Engineering Division for publication in the JOURNAL OF FLUIDS ENGINEERING. Manuscript received by the Fluids Engineering Division, November 19, 1982.

various interactions of physical and chemical phenomena lead to interesting flow and stability problems. The knowledge derived from such research investigations should not only indicate new techniques for improving crystal quality and cost, but also is relevant to many other physicochemical fluid mechanics processes.

It is the aim of this lecture to help bridge the gap between the art of crystal growth and the science of fluid mechanics. Within the time and space limitations, representative crystal growth processes will be described and the important fluid dynamic problems will be identified. Then research results obtained to date will be presented. In this way it is hoped that the crystal growers will become more aware of the design options and configurational changes that can be utilized to deal with the undesirable flow aspects and, at the same time, fluid dynamicists will become aware of the numerous and challenging flow problems associated with this field.

The major effort to date has been directed to describe the nature and extent of the bulk transport under realistic conditions in the more important methods of growing crystals. It is important that these be well characterized because the bulk flows determine the heat and solute transport which strongly influence the temperature and concentration fields in the vicinity of the growth interface. Proper treatment of the "near-field" problem (i.e., the interface) cannot be given until the "far-field" (or global flow) is properly described. The present lecture will, therefore, deal only with the global flows. Critical evaluations of work done on the convective effects in crystals grown by two methods are presented by Solan and Ostrach [1] and Pimputkar and Ostrach [2]. A recent review of convection and fluid flow in crystal growth is given in a volume edited by Hurlle and Jakeman [3]. Some aspects of the "near-field" problem are treated by Coriell and Sekerka [4].

Crystals are required in various forms for research and commercial use, viz.:

- (i) Large single crystals (for example, to make laser rods).
- (ii) Epitaxial layers of thicknesses from submicrons to hundreds of microns (for example, in making integrated circuits).
- (iii) Many small crystals of controlled size and shape (for example, salt or sugar).

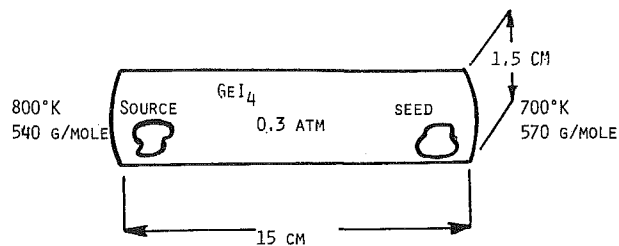
Emphasis will be given to single crystals herein although some mention of epitaxial layers will be made.

Vapor, melt, and solution growth, the three main types of crystal growth techniques, will first be described in order to identify the nature of the fluid flow problems. Then, the most recent research done on relevant flow aspects will be described.

Crystal-Growth Techniques

For each of the growth methods there are a variety of geometric configurations and physical and chemical processes possible. It is beyond the scope of the present paper to discuss them all in detail. The descriptions of the three basic techniques to follow will, therefore, be limited to convey the essence of each method so that the primary fluid dynamics aspects can be clearly identified.

Vapor Growth. Closed-Tube Vapor Transport. Single crystals can be grown from vapor by sublimation and by chemical transport wherein the source material is solid so that the processes can be performed in sealed ampoules. These processes have recently been reviewed by Rosenberger [5]. For the present purposes a representative closed-tube chemical vapor transport process will be described. Crystals grown in this way are mostly used for research purposes rather than production. In such a system crystal material is transported



$$\frac{\Delta T}{T} = 0.13 \qquad \frac{\Delta M}{M} = 0.06$$

$$Gr_T = 5000$$

$$Pr = 0.5$$

$$Sc = 0.5$$

Fig. 1 Typical closed-tube vapor deposition configuration

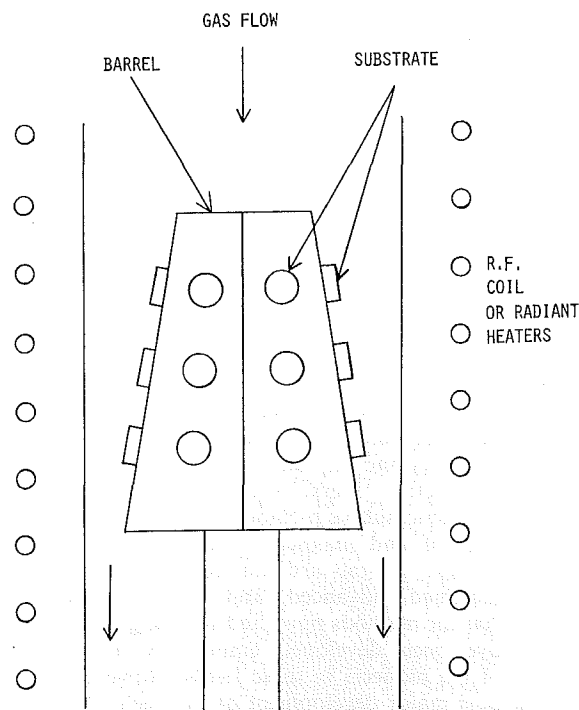


Fig. 2 Open-reactor vapor transport

inside a closed tube from a solid source to the growing crystal by counter diffusion of gaseous compounds formed by the reaction of a gaseous transporting agent with the crystal solid. The driving potential for the transport is a temperature difference between the source and the crystal, which causes a shift of the equilibrium composition of the gas mixture between the two ends and, thus, generates a concentration, i.e., partial pressure, gradient. A typical example of this process, which is depicted in Fig. 1, is the growth of germanium selenide (GeSe) crystals in an iodine environment. This system has been extensively studied (see Wiedemeier et al. [6], for example) including growth in the low-gravity environment of a spacecraft (Wiedemeier et al. [7]). Note that the configuration is essentially a shallow enclosure and that the temperatures at the two ends of the ampoule are different as are also the compositions and, for the conditions given, the composition differences are of the same order as the temperature differences. In a gravity field the simultaneous occurrence of temperature and concentration differences will lead to natural convection.

Open Reactor Vapor Deposition. Chemical vapor deposition is another growth technique in which the vapor provides one or more components of the phase to be crystallized. To maintain the nutrient supply this method is, of necessity, an open-tube flow system. This method is widely used in the semiconductor industry for the epitaxial growth of silicon and other compounds such as gallium arsenide. Open reactors of various geometric configurations are used as are many different carrier gases, the most common being hydrogen. The various types of reactors are described by Curtis [8]. Most of the fluid flow aspects of importance can be identified by considering a barrel reactor which is schematically shown in Fig. 2. It can be seen that there is a forced flow of gas past a body on which wafers or substrates are placed as growth sites. The walls of the reactor are subjected to radiant, resistance, or radio-frequency heating and the barrel can be water cooled so that large radial temperature gradients result (on the order of hundreds to thousands of degrees Centigrade per centimeter). Obviously, there are numerous types of mixed (combined forced and free) convection flows possible in such configurations depending on the gas flow direction and the location of the substrates. Furthermore, very often the dimensions of practical reactors are such that the flow and temperature profiles never become fully developed so that the flow and temperature vary axially. Thus, the substrates in various locations can be subject to different flow conditions and axial temperature gradients occur as well as the radial ones mentioned above. Clearly then, the flow and convection effects may differ considerably depending on the geometric configuration of the reactor. Flow separation at the top of the barrel can also be important. To add to the complexity the barrel is also sometimes rotated.

Although there is now a good understanding of the complex reaction kinetics in open-tube vapor systems (see Laudise [9], for example) there is little detailed information on the complex fluid dynamics. Furthermore, the relation between the convection and crystal quality has not, as yet, been established as clearly as it has for other crystal growth methods.

Melt Growth. Czochralski Technique. Nearly 80 percent of all commercially available crystals are grown from melts. There is a large variety of crystals (such as silicon and germanium semiconductors) grown in this way and the methods of growing them are diverse. The most common technique is that of crystal pulling, known as the Czochralski technique, and it is schematically shown in Fig. 3. The material to be crystallized is heated to above its melting point in the crucible. A pull rod which has a seed crystal at its lower end is placed into the melt and the melt temperature is adjusted until a meniscus is supported. The pull rod is then slowly rotated and lifted to yield a crystal with a desired diameter. (The lift rates are usually between 0.1 and 100 mm/hr and the rotation rates 1 to 100 rpm.) The entire apparatus is enclosed in such a way that the ambient gas be controlled and that the crystal can be visually observed.

Temperature fluctuations are often encountered in this process and these are believed to be the cause of chemical inhomogeneities that are undesirable in many applications. These temperature fluctuations are attributed to time-dependent fluid motions. Thus, among the various factors important in this mode of crystal growth (such as pulling rate, crucible size, heater configuration, etc.) the effect of convection in the melt on crystal quality is crucial. However, the flows are extremely complex and not well understood. The convection can be generated by several mechanisms which can occur simultaneously. Gradients in density (in horizontal or vertical directions or both simultaneously) induce natural convection whereas rotation of the crystal as it is pulled causes forced convection in the melt. Rotation of the crucible, which

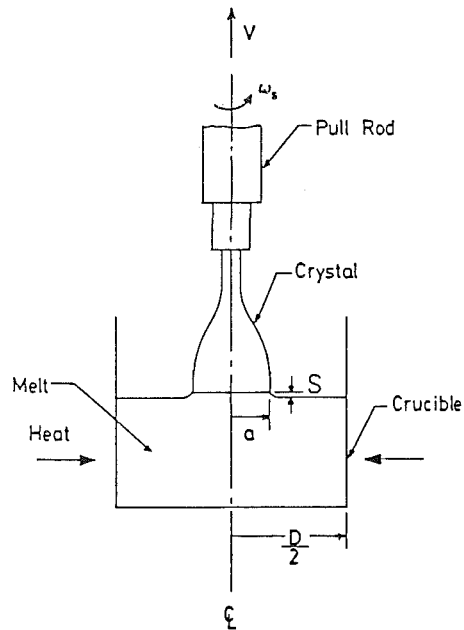


Fig. 3 Idealized schematic of Czochralski growth

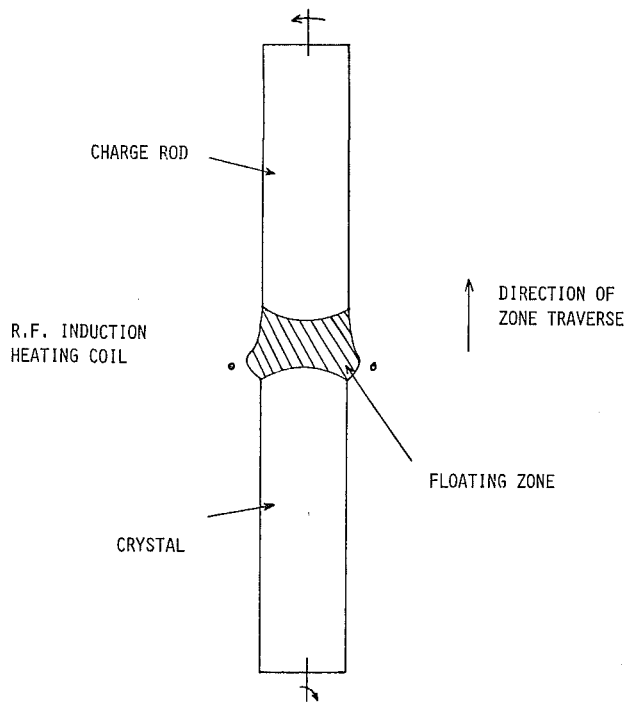


Fig. 4 Schematic representation of floating-zone melting

is sometimes utilized, can also induce forced flows. Because free surfaces are inherent to this technique, surface-tension gradient driven flows can also be of significance.

Floating Zone Technique. To obtain crystals of high ϵ and controllable purity it is necessary that the crucible material is not attacked by the molten charge. Since this is not always possible, a floating-zone technique is sometimes used e.g., to grow silicon crystals that contain no oxygen. This method is depicted schematically in Fig. 4. A molten zone is established between two rods, viz., a charge (or feed) rod of polycrystalline material and a crystalline rod. The molten zone can be established in a variety of ways depending on the material to be crystallized. For example, radio-frequency

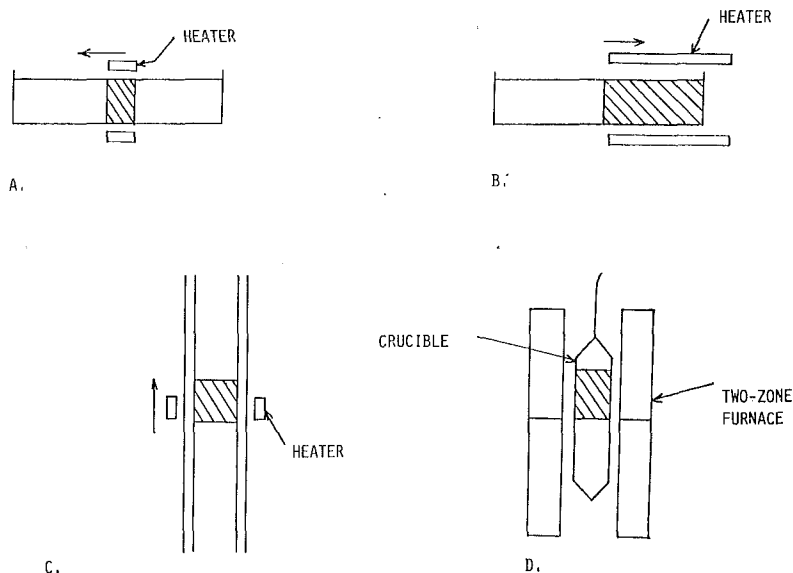


Fig. 5 Horizontal and vertical confined-crystal growth techniques. (A) Horizontal zone-melting, (B) Horizontal-normal freeze (Chalmers technique), (C) Vertical zone melting, (D) Vertical normal freeze (Bridgman-Stockbarger technique).

induction heating is commonly used for silicon whereas electron beam melting is employed to zone-melt refractory metals. The two rods are often differentially rotated to maintain axial thermal symmetry and to exert some control over the shape of the solid-liquid interface as the entire apparatus moves through the heater. The zone length on earth is limited by the gravitational force and this indirectly limits the crystal diameter. It would appear that these constraints would be less stringent in a low-gravity environment and this is the basis for current interest in experimenting with this technique aboard a spacecraft, see Carruthers et al. [10]. It should be noted that large temperature (and, possibly, concentration) gradients are imposed along the surface of the molten zone which can lead to thermo- (and diffuso-) capillary flows which mix the melt. Such flows are relatively stronger under low-gravity conditions. Forced flows due to the rotation of the rods and buoyancy-induced flows can also occur. The interaction of these various types of flow are thought to be the cause of time-dependent behavior that has been observed under some conditions, see Schwabe [11]. Again, a most complex flow situation is found to exist in such a crystal growth method which requires careful investigation.

Other Melt Methods. Other growth techniques in which both the melt and the crystal are confined in a crucible (or boat) are depicted in Fig. 5. When they involve the unidirectional motion of the solid-liquid interface from one end of the molten charge to the other they are classified as normal freezing or if a molten zone passes along a solid charge it is referred to as zone melting. The processes can be performed either horizontally or vertically. In all cases buoyancy-driven convection can occur due to the simultaneous existence of thermal gradients and concentration gradients, which result from the solute segregation at the crystallizing interface. The flow in the various configurations, however, are not necessarily of the same type because the two gradients have different orientations relative to themselves and to gravity.

Solution Growth. Some materials to be crystallized have undesirable characteristics at high temperatures (see p. 40 Laudise [9]) so that it is advantageous to grow them in a solvent at temperatures below the melting temperature:

Usually besides the crystallizing phase other components are added to lower the melting point or to increase the concentration so that the growth is a polycomponent one in a liquid phase. Such growth is considered to be growth from solution.

Crystal growth from low temperature solutions differs from melt growth in a number of ways. The lower temperatures involved permit much greater freedom in the choice of materials for the apparatus. The solutions are frequently compatible with a wide range of glasses and plastics. Another major difference from melt growth is that the growing crystals are usually nearly completely surrounded by the solution and the growth occurs on many flat faces that are at large angles to one another. Since crystal growth requires the maintenance of a supersaturated solution at the growth interface this often requires stirring of the solution. For large growing faces the stirring of solutions becomes more complicated than for growth from melts.

Although it may appear to be convenient to consider solution growth methods on the basis of the solvent used, because the equipment, range of applicability and approach are, to a large extent, determined by the choice of solvent a better delineation of the methods can be made on the basis of the method of producing the supersaturation. For the present purposes these can be considered to be evaporation methods (mainly used in aqueous and molten-salt growth), slow cooling (mainly used for liquid-metal solvents in addition to those just mentioned), and temperature-gradient methods. The first and last are isothermal methods and the second is nonisothermal.

Slow-Cooling Method. A simple example of the slow cooling technique is shown in Fig. 6. A saturated solution is heated to slightly above its saturation temperature and is poured into a screw-cap jar in which a seed crystal is located. The jar is sealed and allowed to cool to room temperature. If the solubility is high enough and the cooling rate is slow enough well-formed crystals will often grow on the seed. Other more complicated apparatuses, with stirring of the solution, are also used to obtain better control (see Brice [12] for descriptions of other devices).

Evaporation Method. The same apparatus can easily be adapted to growth by evaporation. The procedure is the same

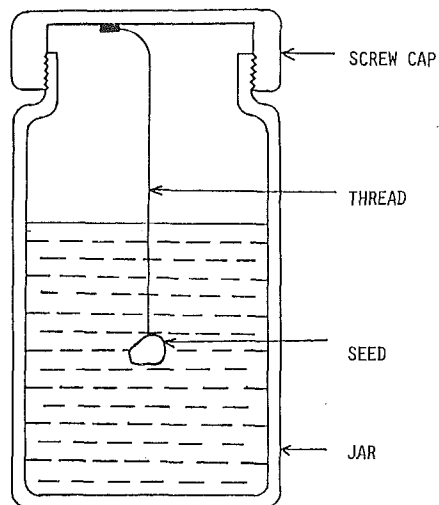


Fig. 6 Slow-cooling method

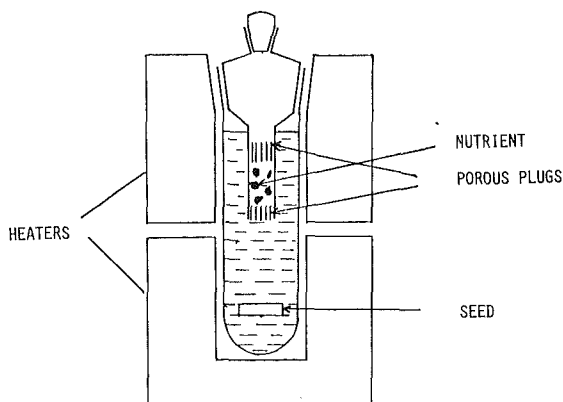


Fig. 7 A temperature gradient method using two heaters

as above except that the jar is not sealed but covered with a cloth to exclude dust and allow evaporation. The growth starts out by slow-cooling but becomes growth by evaporation after the solution reaches room temperature. Some of the crystals grown by these techniques are rock salt (sodium chloride), Rochelle salt (potassium-sodium tartrate), chrome alum, and sodium nitrate.

Temperature-Gradient Technique. In temperature-gradient methods material, the nutrient, is transported from a hot region to a cooler one where the solution is supersaturated and the crystal grows. One example of such an apparatus that utilizes two separate heaters is shown in Fig. 7. The temperature-gradient method is the only satisfactory one if really large crystals (on the order of 20 kg) are required because any other method would require prohibitive volumes of solution.

In these systems there are large concentration gradients as well as temperature gradients and even stirrers or pumps which can all generate fluid flows. Yet there seems to have been no appreciation that the fluid dynamics could be a design option in the development of the devices. Clearly, very complex flows that are not well understood occur in the configurations presently used.

Fluid Flow Phenomena

The description of the various crystal growth techniques has indicated that numerous flow phenomena are inherent to them and in many cases the geometric and flow-generating configurations are quite different from any related problems

treated to date. For example, in closed-tube vapor transport and horizontal Bridgman melt growth natural convection occurs in shallow containers, natural convection due to density variations caused by the simultaneous action of temperature and concentration gradients appears in all the methods in different forms depending on the configuration and relative orientation of the gradients to themselves and to the body-force direction, mixed forced and buoyancy flows are possible in Czochralski growth, open-reactor vapor deposition and solution growth. Surface-tension gradient driven flows are to be expected whenever there are free surfaces, such as in the floating-zone and Czochralski methods. In addition, phase changes and chemical reactions can occur with all the above. Clearly, the fluid flows influence the transport phenomena. Furthermore, as has already been said, time-dependent flows are often encountered and their associated temperature fluctuations modulate the microscopic growth rate of the crystal and are, at least, one cause of inhomogeneities in crystals. It is, therefore, important to gain as much an understanding of such flows as possible in order to answer such questions as:

- (i) What are the conditions for the occurrence of the fluctuations and what is their nature?
- (ii) What effects do they have on the crystal interface and solute distribution? and
- (iii) How can the deleterious effects be minimized or eliminated?

In addition, perhaps, other aspects will be uncovered that will lead to significant improvements in the growth of crystals.

In what follows will be a further delineation of the flow problems that are relevant to crystal growth methods and a review of the most recent work done on various aspects. Each topic will be individually treated although some of them may occur simultaneously in the actual processes.

Natural Convection in Shallow Enclosures. Since poor crystal quality is often attributed to turbulence it would be well to consider a specific example in some greater detail. To this end, consideration is given to closed-tube vapor transport in which crystals are grown in a horizontal ampoule which is subjected to a horizontal temperature gradient. Typical conditions are: ampoule diameter, $d = 1.5$ cm, length, $L = 15$ cm, mean temperature, $T = 1000^\circ\text{K}$, temperature difference, $\Delta T = 100^\circ\text{K}$, pressure 1 atm, density, $\rho = 5 \times 10^{-3}$ gm/cm³ (e.g., a mixture of GeI₄ and GeI₂), viscosity, $\mu = 5 \times 10^{-4}$ gm/(cm s), and mass diffusivity, $D = 0.2$ cm²/s. (These conditions are more severe from a convection viewpoint than those given in describing the method.) For these conditions the Grashof number $Gr = (g\Delta Td^3\rho^2)/(T\mu^2)$ is 33000, the Schmidt number, $Sc = \nu/D$ is 0.5, the Prandtl number, $Pr = c_p\mu/k$ is of the same order as the Schmidt number, and the Rayleigh number $Ra = PrGr$ is 16500, where g is the acceleration of gravity, ν the kinematic viscosity, c_p the specific heat at constant pressure, and k the thermal conductivity. From these values it would appear that the overall natural convection in the ampoule would be laminar and not turbulent as is assumed by some crystal growers. To gain some insight into possible local effects of the convective flow an equivalent Reynolds number based on the crystal size was determined by Solan and Ostrach [1] to be on the order of 10. This, too, indicates no turbulence problems. However, depending on the nature of the overall or global convection the velocity distribution in the vicinity of the growing crystals is most likely not uniform and that could be the cause of the nonuniform mass flux.

Before pursuing this point further, it must be clear that the natural convection has two effects on the crystal growth.

Firstly, it enhances the overall transport rate, which is desirable. Secondly, it has been observed that the mass flux to the growing crystal is nonuniform when convection is present, i.e., that convection adversely affects local growth conditions. Therefore, to obtain uniform growth and a high transport rate it appears that convection should be promoted over most of the ampoule volume to reduce the overall transport resistance and, at the same time, the growing crystal surface (but not the source material) should be embedded in a region of steady uniform laminar flow or in a stagnant zone. For the growth of thin layers this could possibly be achieved by embedding the substrate on the container walls where the flow is uniform. For the growth of thick crystals the seed might be positioned inside a stagnant pocket. To accomplish these ends it is necessary to know the detailed velocity distributions in the ampoule. Unfortunately, both theory and experimental data on natural convection in shallow enclosures are very limited, inexact, or cover inappropriate ranges of parameters. The deficiencies in the existing work (up to 1979) were indicated by Solan and Ostrach [1] and research topics were suggested, some of which have been started and will be described subsequently.

In the absence of gravity, the transport in closed-ampoules would be due only to molecular diffusion and a one-dimensional streaming flow would result due to the nonequimolar nature of the reaction (i.e., for mass conservation) as depicted in Fig. 8(a). In the presence of gravity, density differences would lead to natural convection. For the case shown in Fig. 1 the density difference results from the temperature difference, $\Delta T/T = 0.13$ and from the difference in mean molecular weight, $\Delta M/M = 0.06$ (which depends strongly on pressure). These two effects can reinforce or oppose each other. Very little work exists for natural convection due to the combined action of temperature and concentration gradients, particularly for enclosures, as was indicated in a review of such problems by Ostrach [13]. Thus, the prediction of the flow patterns is even more difficult than for the simpler case of pure thermal convection. It is clear, however, that convection will occur for all values of the Grashof number for a horizontal ampoule with a horizontal density gradient. There is no value of Gr (i.e., $\Delta \rho$ or g) so small that the gas would remain strictly stationary. Unfortunately, it is not possible to predict a priori the natural convection flow pattern that will occur in a completely confined enclosure (see Ostrach [14] and [15]). Therefore, it is necessary to resort to experiments for information. Ostrach et al. [16] performed experiments in shallow rectangular enclosures heated and cooled at the respective ends and with linear horizontal wall temperatures over a range of parameters appropriate to crystal growth, viz., $0.05 \leq A \leq 0.5$, $27.7 \leq Gr_H \leq 10^6$, and $0.72 \leq Pr \leq 1.38 \times 10^3$, where the aspect ratio, A , is the ratio of the enclosure height, H , to its length, L , and the subscript H indicates that the height is the reference length. Although the Prandtl number for vapor transport is included in this range, the low values (on the order of 10^{-2}) appropriate to liquid metals is not. It was found that:

(a) The overall flow patterns are predominantly unicellular.

(b) For aspect ratios below approximately 0.1 the flow is essentially parallel to the enclosure geometry as shown in Fig. 8(b). The flow pattern is inclined relative to the enclosure (skewed or nonparallel) for aspect ratios greater than approximately 0.1, Fig. 8(c).

(c) The skewness of the streamlines and the flow velocities are proportional to the Grashof number and aspect ratio.

(d) Secondary cells are observed near the enclosure ends (as shown in Fig. 8(c)) when the aspect ratio is 0.2 and $(Gr_H Pr A)^2$ is of the order of 10^{13} .

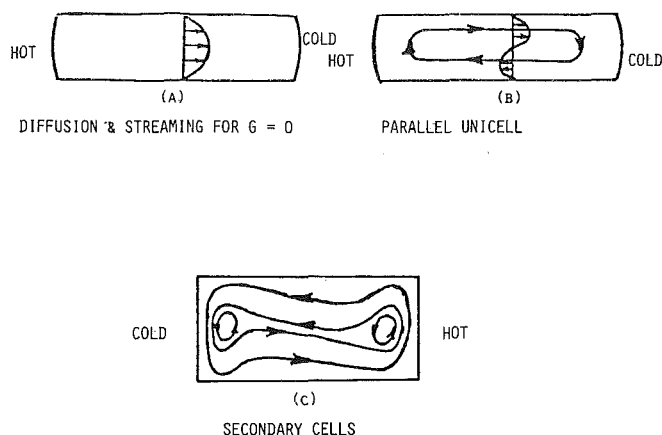


Fig. 8 Possible flow patterns

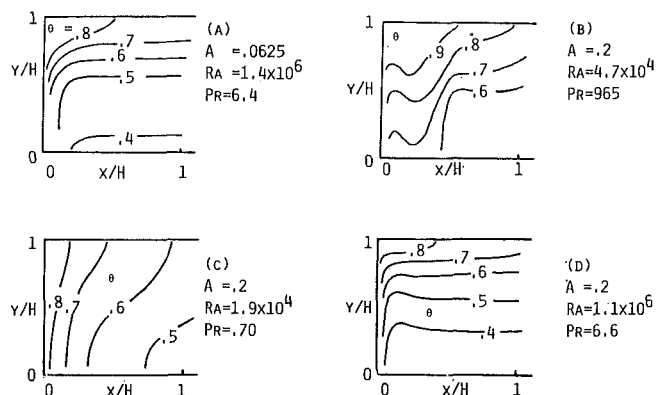


Fig. 9 Isotherms near hot wall for $A = 0.2$ and 0.0625

In Al-Houmoud's experiments with water [17] it is found that in the range $2 \times 10^8 < Ra_H < 2 \times 10^9$ with $A = 0.0625$ the core flow is nonparallel and is dominated by horizontal intrusions flowing along each of the two horizontal walls of the enclosure. The fluid embraced by the two horizontal jets is practically stagnant and thermally stratified.

Sernas and Lee [18] and [19] investigated rectangular enclosures with air both experimentally and numerically over a lower Grashof number range. The horizontal boundaries are either isothermal or adiabatic. For $A = 1.0$ and $A = 0.4$ the flow patterns for the two different thermal boundary conditions are very similar. In contrast, for $A = 0.1$ the streamlines and isotherms are significantly different for the two cases, with the core flow being nearly parallel with adiabatic walls whereas with isothermal walls there is almost no fluid motion in the core except near the enclosure ends. The numerical results of Tseng [20] over a wide range of Prandtl number also indicated the lack of sensitivity of the flow and heat transfer to the horizontal wall boundary conditions for $A = 0.5$.

Kamotani et al. [21] in a comprehensive experimental study of the heat transfer in shallow rectangular enclosures indicated how the secondary cells, that occur for $A > 0.1$ and higher Prandtl numbers, significantly influence the end region temperature distributions and, thereby, the heat transfer. Representative isotherm patterns near the hot end of enclosures are presented in Fig. 9. For $A = 0.0625$, $Ra = 1.4 \times 10^6$ and $Pr = 6.4$ (Fig. 9(a)) the fluid outside the thermal boundary layer is stably stratified and no noticeable secondary cells were present. For $A = 0.2$, $Ra = 4.7 \times 10^4$ and $Pr = 965$ (Fig. 9(b)) the isotherms are severely distorted due to the presence of a secondary fluid motion with clockwise

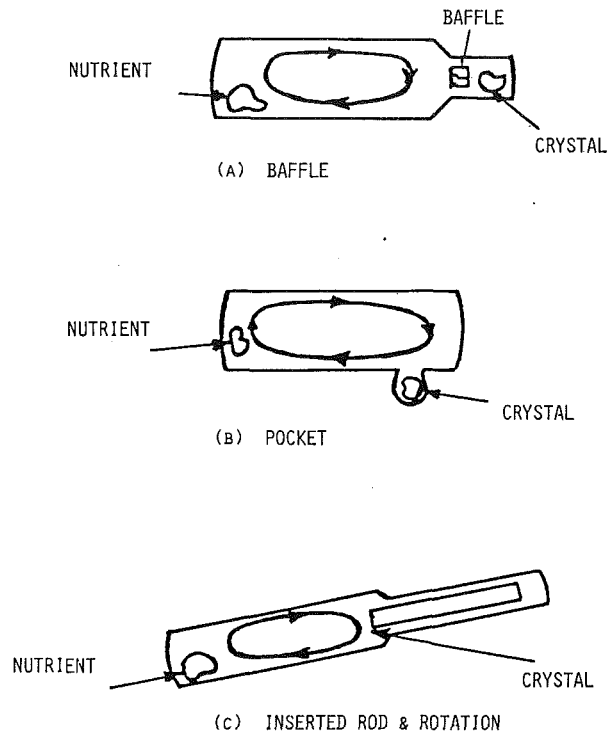


Fig. 10 Possible improved configurations

rotation outside the boundary layer. At a comparable Ra for air ($Pr = 0.72$) the isotherms are much less distorted (Fig. 9(c)), which implies no or very weak secondary cells. Secondary cells were also observed at $A = 0.2$, $Ra = 1.1 \times 10^6$ and $Pr = 6.6$ but as can be seen in Fig. 9(d) the isotherm pattern is not distorted substantially. The results of this work indicate that the influence of the secondary cells on the temperature distributions is a complex function of Pr , Ra , and A . More extensive discussion of natural convection in enclosures is presented by Ostrach [15].

From the work presented it would appear that the problems associated with the secondary cells are of no consequence for crystal growth because they seem to be important only at Prandtl numbers greater than those appropriate to those processes. However, Jhaveri and Rosenberger [22] in focusing specifically on the closed-tube transport method made a numerical study of thermal convection in a horizontal rectangular enclosure with $A = 0.1$, $Sc = 0.5$, $Pr = 0.7$, and $Gr \leq 3.3 \times 10^4$. Although the buoyancy is considered to be due only to temperature differences the effects of the mass flux from the source to the crystal are also simulated. The boundary conditions, thus, differ from those for pure thermal convection flows because of the imposition of a concentration difference at the ends and by specifying a mass average velocity at the interfaces (enclosures ends) in terms of mass flux by means of Fick's law. The flow profiles determined in this way indicate a recirculation cell near each interface (similar to those shown in Fig. 8(c)) for $Gr_H = 3.3 \times 10^4$. The cell formation is due to the coupling of the mass flux at the interfaces with the transport equations.

Recently Schiroky and Rosenberger [23] studied the natural convection in a horizontal cylinder with differentially heated ends with laser Doppler anemometry. The cylinder wall temperature was maintained linear. Interesting three-dimensional flows were observed near the ends which are in contrast to those found in rectangular enclosures.

The work presented thus far indicates the sensitivity of the flow and, hence, the transport to the geometry and imposed thermal boundary conditions. In accord with the concept mentioned previously, viz., that improved crystal quality

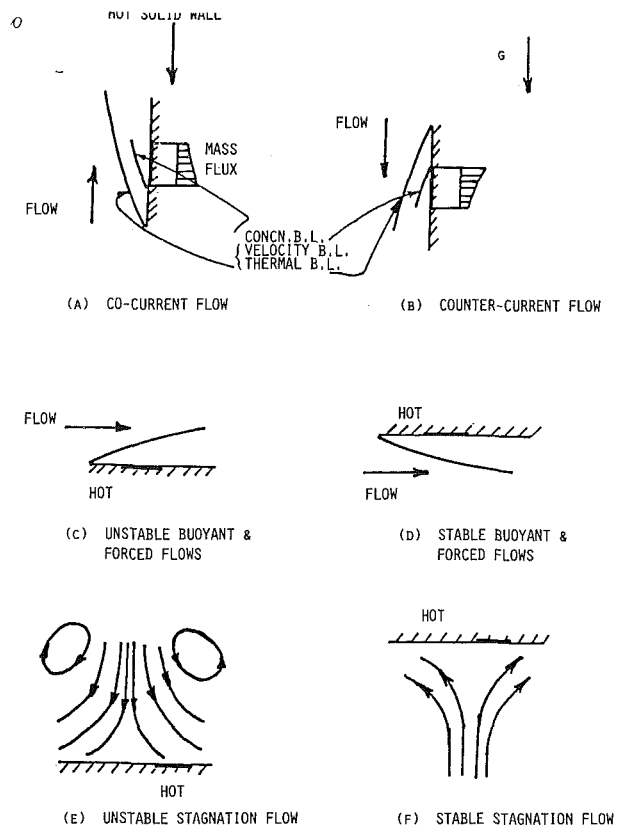


Fig. 11 Types of mixed convection flows

could be obtained if the convection were promoted to increase the overall transport while the crystal is positioned in such a way that the flux over it is uniform, it would be necessary to know the local flux distribution in the vicinity of the crystal. Unfortunately, no studies of local fluxes seem to have been made. The current situation in which a crystal is permitted to grow in an uncontrolled region of the enclosure seems to be far from optimal. Schematic sketches of some conceptual configurations in which the overall transport is enhanced by convection but the local convection is suppressed are shown in Fig. 10. An interesting configuration, depicted in Fig. 10(c), was used by Mughal and Ray [24]. A graphite rod was inserted in the narrow end and the entire ampoule was rotated in an attempt to eliminate natural convection. It perhaps would have been better to control the convection by growing the crystal at the end of the rod farthest from the larger section rather than at the end adjacent to the main flow. Clearly, there are many other configurations that could be considered to control the local convection, but little work of this type seems to have been done.

Mixed Forced and Free Convection. In open-reactor vapor deposition and some solution growth methods there are many different possible types of flows and flow regimes that need to be understood. Near the crystal the flow is due to both forced and free convection. These flows can be parallel or opposing, laminar or turbulent, or of a viscous or boundary-layer type. Growth sites (substrates) at different locations on the barrel of an open reactor will most likely experience different flow conditions. It must also be noted that in the boundary-layer regime there can be distinct layers of velocity, temperature, and concentration. The fundamental parameter that indicates the relative importance of thermal convection and forced flows is Gr/Re^2 , where Re is the Reynolds number, $U_\infty l/\nu$, and U_∞ is the forced-flow velocity and l is a characteristic length. If $Gr/Re^2 > 1$ free convection will dominate, if

$Gr/Re^2 < 1$ the flow will be primarily forced, and if Gr/Re^2 is of unit order magnitude the flow will be of a mixed free- and forced-convection type. For the flow over vertical surfaces Sparrow et al. [25] refined those criteria as:

	Co-current Flow	Counter-current Flow
Free Convection	$Gr/Re^2 > 16$	-----
Mixed Convection	$0.3 < Gr/Re^2 < 16$	$Gr/Re^2 > 0.3$
Forced Convection	$0 < Gr/Re^2 < 0.3$	$0 < Gr/Re < 0.3$

Some typical flow configurations are shown in Fig. 11. Cocurrent combined forced- and free-convection flows are depicted in Fig. 11(a). If the gaseous reaction products at the wall are more dense than the incoming gas a counterflow would tend to be established which would lead to instabilities. The counterflow depicted in Fig. 11(b) could be unstable or irregular if the free convection were strong relative to the forced flow. A potentially unstable buoyant flow combined with a forced flow is shown in Fig. 11(c) which could also lead to instabilities whereas in Fig. 11(d) stable stratification is superposed on the forced flow. Similar situations for stagnation-type flows are sketched in Figs. 11(e) and 11(f). Relatively little is known about the detailed nature of the last four types of flows.

The use of the above criteria for actual reactors has been successful in some cases, Fujii et al. [26] and Wahl [27]. However, Curtis and Dismukes [28] from measurements found that the temperature stability in a system with $Gr/Re^2 = 0.3$ decreased as the gas velocity increased. This is a surprising result if one attributes temperature fluctuations to buoyancy effects, as is seemingly inferred from the work of Curtis and Dismukes [29]. However, there are several other reasons for this apparent discrepancy. Firstly, it could be that if the flow were indeed essentially forced, it might be undergoing transition to turbulence. Also, it should be remembered that the criteria given above are developed for thermal convection with heat flow normal to the direction of gravity. However, in the real system it is possible that there is heat flow both in the radial and axial directions and, also, that solutal convection (i.e., due to concentration gradients) plays a role. The latter two topics will be discussed subsequently. Thus, it is clear that to determine the true contributions of convective effects to the growth process all the real complexities have to be considered more carefully.

Convection With Heat Flux in More Than One Direction.

In almost all existing work on natural convection the buoyancy was induced by imposing a heat flux in one direction (horizontally, i.e., normal to gravity). In many practical situations including crystal growth, however, heat fluxes are imposed simultaneously in more than a single direction. Also, crystal growers have expressed interest in reducing or eliminating natural convection to improve crystal quality. Imposition of a stabilizing (vertical) heat flux on the driving (horizontal) heat flux would seem to offer a design option for that purpose. One would then wonder as to the magnitude and effects of such a retarding flux. It should also be said that such a configuration or one in which the vertical heat flux is destabilizing occurs, in some cases, in actual growth processes.

To obtain information on the effect of stabilizing thermal gradients on natural convection in rectangular enclosures experiments were first made by Ostrach and Raghavan [30]. The flows investigated corresponded to Prandtl numbers on the order of 10^4 and unit order Grashof number. It was found that the reduction in the flow velocity depended on the aspect ratio, Gr (based on the horizontal temperature difference),

and the ratio of the horizontal to vertical temperature differences. It was not possible to stop the flow completely within the range of stabilizing gradients investigated. A more detailed continuation of that work was made by Fu and Ostrach [31] for the same range of conditions in a square cavity. Representative results are shown in Figs. 12 and 13. The streamlines and isotherms with no stabilizing gradient are shown in Fig. 12. The corresponding patterns with an imposed vertical gradient, $\Delta T_V/\Delta T_H = 3$ are presented in Fig. 13, where ΔT_V is the imposed vertical temperature difference and ΔT_H is the horizontal temperature gradient. It can be seen that the stabilizing temperature gradient causes the streamlines to skew into a parallelogram-like pattern and the isotherms to be more stably stratified in the core. Two cells appear in the corners in which the flow is counterclockwise. From the values of the streamfunction and the time for a complete circuit of the particle, which are indicated in the figures, the strong retardation effect of the stabilizing gradient is evident. At a Rayleigh number of 2.29×10^4 a decrease in the maximum velocity of more than 28 percent was obtained with $\Delta T_V/\Delta T_H = 6$ and a decrease of nearly 35 percent was obtained with $\Delta T_V/\Delta T_H = 3$ with a Rayleigh number of 4.57×10^4 . Although no work has been done on the effect of a superposed destabilizing gradient (i.e., heating from below) it could be anticipated that such configurations could lead to time-dependent flows such as are encountered in some crystal growth systems.

Convection Due to Combined Buoyancy Forces. In almost all of the crystal growth techniques there are both temperature and concentration gradients in the fluid that can lead to buoyancy-driven flows. There is little in the existing literature to indicate the nature and extent of such flows, because, for the most part, in studies of natural convection the buoyancy driving force has been considered to be due solely to temperature differences or gradients. Less attention has been given to situations in which concentration gradients alone are the cause of buoyancy.

Many transport processes that occur in nature and

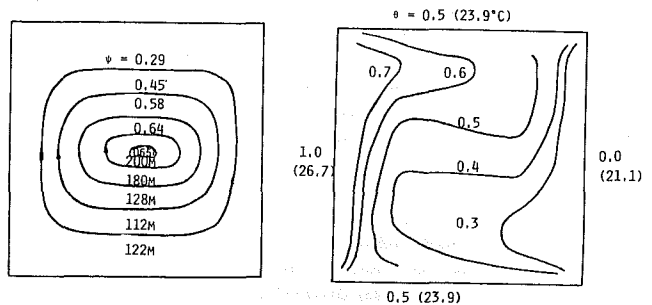


Fig. 12 Streamlines and isotherms for $Ra_H = 4.57 \times 10^4$ and $T_V/T_H = 0$.

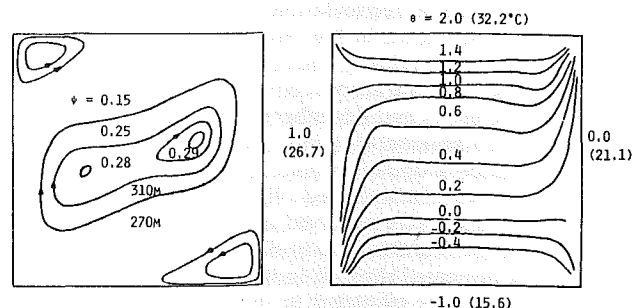


Fig. 13 Streamlines and isotherms for $Ra_H = 4.56 \times 10^4$ and $T_V/T_H = 3$

technology involve flows which are driven or modified by the simultaneous occurrence of temperature and concentration gradients. In nature, flows in bodies of water are driven by the effects of temperature, concentration of dissolved materials, and suspended particulate matter on density. In oceanography, wherein thermal and salinity gradients are important the process is called thermohaline convection. In more general contexts the term double-diffusive convection is used to encompass a wider range of phenomena. Major emphasis on problems of this type has been focused on oceanographic situations and some unusual and unexpected phenomena, such as salt fountains and fingers, have been identified in configurations with opposing thermal and salinity gradients aligned with the gravity vector, see Turner [32]. The highly organized salt convection in tall thin columns of fluid alternately ascending and descending occurs because the stabilizing effect of the thermal gradient is overcome by lateral diffusion of heat. Thus, the unstable salinity gradient (heavier fluid above lighter) provides the driving force for convection.

In vertical crystal growth techniques, such as Bridgman-Stockbarger melt or liquid-phase epitaxy (LPE), the melt or solution is subjected to vertical density gradients due to temperature and concentration variations. Generally, the thermal conditions are statically stable (cooled from below) but the solute conditions can be stable or unstable depending on whether the rejected fluids are more or less dense than the surrounding fluid. If the overall density variation due to the combined thermal and solute effects is unstable, the situation is analogous to the thermal (Rayleigh-Benard) instability. In practice, crystals are grown under statically stable conditions which are analogous to those just described in the oceanographic problem. Thus, unusual results can be expected as a result of the interaction between a stable temperature gradient and an unstable concentration gradient due to differences in the thermal and solutal diffusivities, even if the system is gravitationally stable. Hurler [33] pointed out that the conditions exist in solution and Bridgman-Stockbarger growth for the occurrence of such double-diffusive phenomena and that some crystal imperfections found in those systems could have been caused by that phenomenon. No detailed consideration has been given to this problem as yet. Because of the importance of vertical growth systems it would, therefore, seem worthwhile to investigate the possible importance of double-diffusive convection in crystal growth.

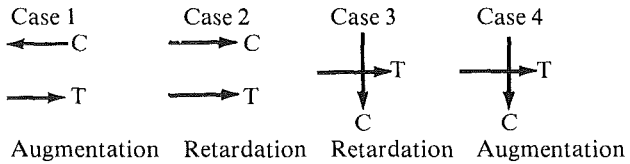
The configuration just discussed wherein the temperature and concentration gradients are parallel to gravity is just one of the many possible configurations with simultaneous temperature and concentration gradients. In order to obtain a more comprehensive appreciation of the problem Ostrach [13] considers free and natural convection with combined driving forces in general and identifies all the possible configurations. He then derives the relevant dimensionless parameters in order to categorize the various problems. Finally, he presents a critical evaluation of existing work to show what is known and what fruitful research areas remain.

Problems that involve the interaction of temperature and concentration gradients are considerably more complicated than ones in which the driving force is due only to one of them. In the latter case, two distinct modes of convection have been identified by Ostrach [34]. When a component of the density gradient is perpendicular to the body-force direction a flow ensues immediately and is called conventional convection. On the other hand, if the body force and the density gradient are parallel and opposed the configuration is unstable (heavier fluid above lighter) and convection occurs only after a critical value of the density gradient is exceeded. Of course, if the density gradient and the body force are aligned

and in the same direction the flow is stably stratified and no convection is possible.

Clearly, with the simultaneous action of both temperature and concentration gradients many more configurations are possible because the two gradients can have different orientations relative to each other as well as relative to the body force direction. Mention has just been made of the unstable situations so the discussion will now be directed to cases in which convection occurs as soon as there is a density difference.

Four distinct cases can be delineated corresponding to the conventional mode:



In Case 1 the density gradient is increased by the combined temperature and concentration gradients, whereas in Case 2 it is decreased by the opposing effects. In Case 3 the stabilizing influence of the vertical gradient tends to retard the flow and in Case 4 the superposition of the unstable vertical gradient should enhance the flow. In the above temperature and concentration can be interchanged.

The fundamental dimensionless parameters were derived by Ostrach [13] to be

$$\begin{aligned}
 Gr &= \beta g \Delta T L^3 / \nu^2 && \text{(Thermal) Grashof number} \\
 Pr &= \nu / \alpha && \text{Prandtl number} \\
 Sc &= \nu / D && \text{Schmidt number} \\
 N &= \beta \Delta C / \beta \Delta T && \text{Buoyancy ratio}
 \end{aligned}$$

where β and $\bar{\beta}$ are the thermal and concentration volumetric expansion coefficients, respectively, and α is the thermal diffusivity. Note for N positive the combined driving forces enhance the flow and for negative N they retard it. Various ratios or products of these fundamental parameters are used in existing work. Thus, four parameters describe the phenomena due to combined buoyancy forces as compared to two for a single driving force. This is another of the complexities associated with problems of this type. It should be noted, as mentioned previously, that there exist three distinct boundary layers in problems of this type, viz., those of velocity, temperature, and concentration and their relative extents are determined by the relative orders of Pr and Sc .

Very little work has been done on confined convection with combined buoyancy forces. The configuration that has received attention is one in which a stable salinity gradient was established in distilled water in a rectangular tank and then a horizontal temperature difference was imposed across the two ends, (see Chen et al. [35]). Thus, the problem is of the Class 3 previously described. A layered cell pattern developed after a period of time which was attributed to an instability. A more detailed investigation of the formation and growth of the layered convection cells in the same configuration is presented by Wirtz et al. [36]. The experimental and numerical work was directed to define the mechanisms that led to the complex multi-layered flow patterns. Additional numerical work was done by Wirtz [37]. The details are not important for the present purposes because the parametric values covered in those investigations are appropriate for geophysical problems. Research for more appropriate conditions would be of interest.

Since there was not research on Cases 1 and 2, in which temperature and concentration gradients are horizontal and can be augmenting or opposing as in horizontal crystal growth methods Wang [38] designed an electrochemical system to investigate those cases. The apparatus, Fig. 14, is a low-aspect

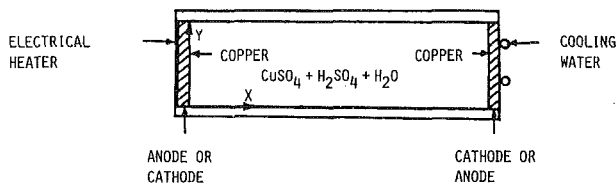


Fig. 14 Electrochemical system to impose concentration and temperature gradients

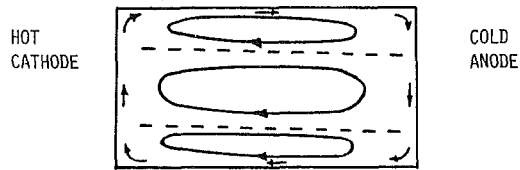


Fig. 15 Sketch of typical flow structure produced at a certain time, showing the layers formed by heating from side for an augmenting case

$$Gr_T = 6.2 \times 10^5, Gr_S = 5.8 \times 10^6$$

$$A = 0.55, Sc = 2.1 \times 10^3$$

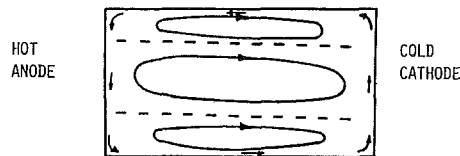


Fig. 16 Sketch of typical flow structure produced at a certain time, showing the layers formed by heating from side for an opposing case

$$Gr_T = 6.2 \times 10^5, Gr_S = 5.8 \times 10^6$$

$$A = 0.55, Sc = 2.1 \times 10^3$$

ratio rectangular cavity with the vertical end walls being the electrodes which can be maintained at fixed temperatures. All the other walls are insulated. The fluid is a copper sulphate (CuSO_4)–acid (H_2SO_4) solution. When a current is applied to the electrodes electrolysis takes place and copper dissolves into the solution at the anode and is deposited at the cathode so that the concentration there is lower than at the anode. In this way a horizontal density difference due to composition differences is established. The simultaneous imposition of augmenting and opposing concentration and temperature differences is achieved by heating the cathode and cooling the anode and vice versa, respectively. The apparatus has the additional flexibility of being able to obtain purely solutal (concentration) convection or purely thermal convection. The range of parameters covered in the experiments are $A = 0.08$ to 0.55 , $Pr = 5$ to 7 , Schmidt number, $Sc = 2.1 \times 10^3$, thermal Grashof number, $Gr_T = 0$ (pure solutal convection) to 1.1×10^6 , and solutal Grashof number, $Gr_S = 0$ (pure thermal convection) and 2.4 to 10^4 to 5.8×10^6 .

The case of pure thermal convection in shallow enclosures was discussed above. Pure solutal convection is, in a number of aspects, similar to pure thermal convection. The deposition of copper ions on the cathode wall causes the fluid to be less dense there so that it rises to the top of the test section in a boundary-layer flow and moves horizontally along the top wall. The heavier fluid near the anode moves downward along the bottom of the test section. As a result, the fluid in the core (outside the end wall boundary layers) is stratified in a manner similar to that in pure thermal convection. Although the overall flow structures are similar there are some important differences. Since the ratio $Sc/Pr = \alpha/D$ (sometimes called the Lewis number) is about 300 in the experiments, the mass diffusion process is much slower than the thermal conduction. Thus, the thermal boundary layer is larger than the solutal

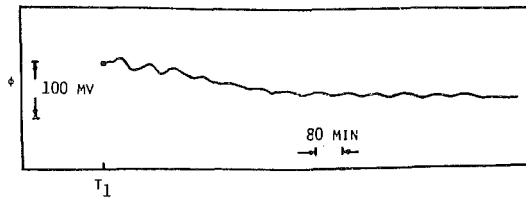


Fig. 17 The potential difference, versus time for an augmenting case

$$Gr_T = 5.1 \times 10^4, Gr_S = 1.6 \times 10^5$$

$$A = 0.17, Sc = 2.1 \times 10^3$$

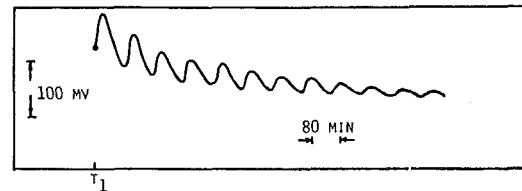


Fig. 18 The potential difference versus time for an opposing case

$$Gr_T = 6.1 \times 10^4, Gr_S = 1.6 \times 10^5$$

$$A = 0.17, Sc = 2.1 \times 10^3$$

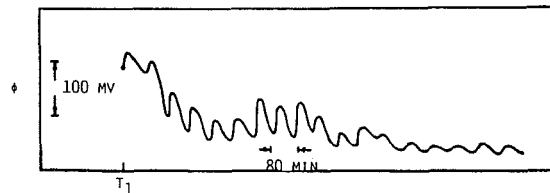


Fig. 19 The potential difference versus time for an opposing case

$$Gr_T = 8 \times 10^3, Gr_S = 2.4 \times 10^4$$

$$A = 0.08, Sc = 2.1 \times 10^3$$

layer and the solutal convection is much slower than the thermal convection.

For the combined driving forces cases, steady thermal convection is first established before the electrochemical system (the solutal effects) are started. A sketch of a representative flow pattern observed after approximately five hours for augmenting forces (Case 1) is shown in Fig. 15. It can be seen that the fluid is layered in three cells with the sense of circulation in each layer being clockwise, i.e., it is determined by the thermal effects. The cells are slightly tilted toward the anode. The flow in the thin mass boundary layer is indicated by the arrows near the boundaries. Because of the layered structure the overall fluid flow is much slower than that for corresponding pure thermal convection and within the range of parameters covered seems to be slow enough not to cause shear instabilities at the cell boundaries.

A typical flow pattern for opposing gradients (Case 2) is sketched in Fig. 16. The overall layered structure is almost identical to that for augmenting gradients, because thermal effects determine the pattern outside the thin mass boundary layer. The boundary-layer flow, however, is opposite to that in the previous case because the initially upward flow of the heated boundary layer is reversed as dissolution takes place. The mechanisms by means of which the two flow patterns are established are fundamentally different although the patterns appear to be quite similar.

Over certain ranges of the aspect ratio and Grashof number the cell potential is found to oscillate with time (typically 1 cycle/hr). These oscillations are believed to be caused by flow oscillations in the cell due to the interaction between thermal and solutal effects. The oscillations occur for both

augmenting and opposing gradients, Figs. 17 and 18, respectively. The oscillation frequency can be modified by geometrical constraints as a comparison of Fig. 18 for $A = 0.17$ with Fig. 19 for $A = 0.08$ indicate. Rosenberger et al. [39] found similar oscillations in closed-tube chemical vapor transport.

Most of Wang's work [38] is qualitative but it represents a first step in gaining an understanding of confined flows due to both temperature and concentration gradients which have important implications for the growth of crystals.

Surface-Tension Gradient Flows. To minimize or eliminate crystal contamination by container impurities pulling techniques, like the Czochralski method, and floating zones are used for growth from melts. Inherent to those configurations are free surfaces along which are temperature and concentration gradients. The presence of an interface between two fluid phases can influence the motion of fluids when either the interface has a finite curvature different from that at equilibrium or when the interfacial or surface-tension varies from point to point. Since surface-tension is a function of temperature, composition, and electrical potential, gradients of any one of these or combinations of them can lead to surface-tension gradients. Flows generated by such gradients were generally ignored in crystal growth processes because it was (erroneously) assumed that such flows would be overshadowed in a terrestrial environment by buoyancy-driven flows. However, with the possibility of growing crystals under reduced-gravity conditions aboard a spacecraft wherein buoyancy effects would be reduced, this topic assumed new importance.

A review of the existing literature on the subject was made by Ostrach [40] to gain insights that might be relevant to crystal growth processes. It was pointed out therein that there are essentially two modes of flow generated by surface-tension flows that are analogous to those induced by buoyancy. Although this was previously indicated by Scriven [41] the distinction between the two types of flows does not always seem to be clear. If the gradients are along the interface, the surface-tension gradients act like shear stresses applied by the interface to the adjoining fluids and, thereby, induce flows or affect existing ones. These flows are analogous to conventional (stable) convection and are called thermocapillary or diffusocapillary flows according to whether they are caused by temperature or concentration gradients, respectively. These flows can of course, affect transport processes.

If one of the aforementioned gradients is perpendicular to the interface a "Marangoni instability" can occur under proper conditions that can lead to cellular flows. This situation is analogous to the thermally unstable type of buoyancy flows. Problems of this type have received more attention than those with gradients along the interface. The Marangoni instability is identified as "interfacial turbulence" by Sternling and Scriven [42] and Kenning [43] calls it a "form of interfacial turbulence." However, the analogy with unstable buoyancy flows indicates that these flows are actually laminar although they do induce greater mixing.

When surface-tension flows were considered under terrestrial conditions, the relative importance of gravity and surface-tension forces was thought to be determined by the Bond number, $Bo = \rho g d^2 / \sigma$, which is really a static Bond number, where σ is the surface-tension. On this basis it was concluded that gravity suppresses surface-tension except in configurations with very small dimensions, such as thin films, capillary tubes, and droplets and bubbles. Since there are many technologically important processes that satisfy that restrictions emphasis was given primarily to such configurations. Kenning [43] and Levich and Krylov [44] outline

the many problems treated covering such applications as boiling, spreading of oil and paint films, jet decay, and corrosion mechanism. Surface tension was also studied as a mechanism of flame spreading, see, for example, Sirignano and Glassman [45]. None of this work is particularly close to the configurations or range of parameters for crystal growth so that it is not very useful in that respect.

In dealing with new problems it was pointed out by Ostrach [46] that dimensionless parameters are most useful for obtaining qualitative features of the flows and for estimating flow velocity. They also indicate the dominant physical factors, mathematical simplifications, data correlations, and proper theoretical and experimental models. Although a physically reasonable reference velocity for surface-tension gradient flows was indicated or implied by Levich [47], Kenning [43], and Stanek and Szekely [48], no explicit derivation of the fundamental dimensionless parameters was made until recently, Ostrach [49]. It is shown therein that, in analogy to buoyancy flows, there are different reference velocities obtained from the tangential stress balance, e.g., for viscous-type thermocapillary flows the characteristic velocity U_R is

$$U_R = \frac{|\partial\sigma/\partial T|\Delta T}{\mu} \frac{D}{L}$$

where μ is the absolute viscosity and D and L are two different characteristic lengths. For boundary-layer flows

$$U_R = \left[\frac{(\partial\sigma/\partial T)^2 \Delta T^2 \nu}{\mu^2 L} \right]^{1/3}$$

Note that both reference velocities are given in terms of the physically important variables for establishing thermocapillary flows. The relevant dimensionless parameters based on those reference velocities that appear in the basic equations are the surface-tension Reynolds number, $Re_\sigma = [(\partial\sigma/\partial T)\Delta T D]/\mu\nu$, the Marangoni number, $Ma = PrRe_\sigma$, and aspect ratio $A = D/L$, a dynamic Bond number, $Bd = \rho g L^2 / (\partial\sigma/\partial T)\Delta T$, and the relative temperature variation $\beta\Delta T$. The surface-tension Reynolds number plays the same role as the conventional Reynolds number in that it appears in the equations of motion and indicates the nature of flows. The Marangoni number is equivalent to the conventional Peclet number and appears in the energy equation to give an indication of the heat transfer. The proper influence of buoyancy is determined by the coefficient of the buoyancy term which for viscous-type flows is $Bd(\beta\Delta T)$ and for boundary-layer flows is $Bd(\beta\Delta T)(A/R\sigma)^{2/3}$. Thus, it can be seen that the dynamic Bond number, Bd , and not the static one, Bo , is the correct parameter for that purpose. From the above criteria it is clear that in a sufficiently low gravitational environment surface-tension gradient flows will be significant.

In most of the work to date the interface has been assumed to be flat. However, in general, the interface can be curved or deformed as a result of the forces acting on it and, therefore, its shape must be determined as part of the solution of the problem. Proper formulation of the problem requires balances of tangential and normal stresses at the interface. Other dimensionless parameters can appear in the boundary conditions depending on the forces that act on the fluid. In the existing literature a capillary number, Ca , is often cited as another parameter for free-surface problems, where it is obtained from a balance of the viscous and curvature terms in the tangential stress equation as $Ca = \mu U_R / \sigma$. For thermocapillary flows, for which the reference velocity was previously given, $Ca = (Bd/Bo)A$ so that no new parameters are obtained from the boundary conditions except for the contact angle. When the fluid is subject to more than one driving force, e.g., rotation or buoyancy, more careful analysis is necessary to obtain the appropriate parameters.

Because surface traction is the flow motivator, the condition of the free surface is most important. Oxide formation or other surface reactions and contamination (due to dust and impurities in the environment or apparatus) can seriously inhibit or even eliminate surface-tension driven flows. This is not necessarily undesirable for practical applications but it makes the prediction and interpretation of data very difficult.

The early analyses of flows induced by surface-tension gradients dealt with steady flow in idealized configurations in which the interface was assumed to be flat. Even for the simplest configuration, viz., a doubly-infinite horizontal thin fluid layer, there was inconsistencies in the analyses, see Ostrach [40]. To avoid such difficulties and to include time-dependency Pimputkar and Ostrach [50] reconsidered the problem. A formal nondimensionalization was made which indicated an explicit ordering of the equations so that ad hoc assumptions were unnecessary. The flows and surface shapes were determined for a family of different imposed surface-temperature distributions.

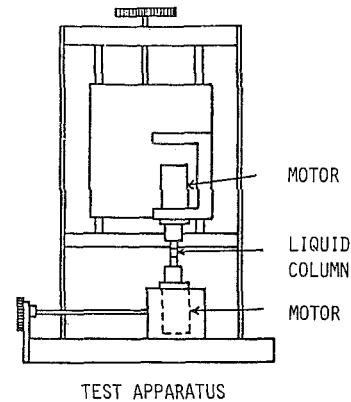
With this background the implications for crystal growth can now be discussed. The first consideration of thermocapillary flows in crystal growth was the numerical investigation of a vertical cylindrical melt contained between two rods by Chang and Wilcox [51]. This model is intended to simulate floating zone melting, which is used for purification of melts and for crystal growth. The zone is taken to be a circular cylinder with planar solid-liquid interfaces and to have radiant ring heating around the zone mid-plane. The effect of buoyancy on the results was also investigated but inappropriate parameters led to misleading interpretations, see Ostrach [40]. Clark and Wilcox [52] corrected an error in the formulation of Chang and Wilcox [51]. The physical properties of silicon were used to evaluate the parameters and the ranges covered are:

Ma	1.2 to 8.0
Re _σ	50 to 350
Gr	3 to 6200
Pr	0.023
A	1.0

In actual floating-zone processing of silicon, Ma is of the order of 10^4 to 10^5 and Re_σ ranges over 10^6 to 10^7 . Thus, the parameters investigated by Clark and Wilcox [52], which most likely were limited by numerical problems, are far too low to simulate actual situations. Also, rather than no-slip conditions at the top and bottom of the zone a constant axial velocity was assumed to simulate the crystal growth rate. This assumption is perhaps valid for the low parametric values considered. Under more realistic conditions its effects would be negligible. The main feature of this numerical work is the prediction of flow cells (toroidal vortices) that encompass the entire fluid.

Recently, Fu [53] obtained numerical solutions of the thermocapillary flow in a floating zone configuration over a more appropriate range of values for the dimensionless parameters. All the solutions indicate a single cell streamline pattern with the core located about three-quarters of the radius away from the axis. The flow is characterized into four regimes depending on the values of Re_σ and Ma. The effect of heat loss from the free surface is also investigated.

To simulate low-gravity thermocapillary flow terrestrially Schwabe et al. [54] and Chun and Wuest [55] established a bridge of transparent liquid between two disks. For the dynamic Bond number to be less than unity the fluid column had to be less than about 5 mm. The end disks or rods could be rotated and heated or the surface-temperature gradient could be imposed by a wire ring heater around the outside of the liquid zone. Particles were introduced to permit flow visualization and a thermocouple was inserted through the



TEST FLUIDS:
HEXADECANE, FLUORINERT (FC-43)

COLUMN DIAMETERS:
D = 2, 3 AND 6 MM

RANGE OF A :
A = .2 - 1.0

Fig. 20 Floating zone test apparatus

zone for temperature measurements. The test fluid used by the first group is sodium nitrate, presumably because it is a good model for silicon; the Marangoni numbers are similar but the surface-tension Reynolds numbers are not for a given set of conditions. The second group used a number of different liquids in their experiments but most of them exhibited a great deal of evaporation. The particles used by both groups for flow visualization were not neutrally buoyant. Despite these shortcomings many interesting results were obtained.

It was observed that steady flows (on the order of centimeters per second) undergo a transition to oscillatory ones above certain values of the Marangoni number, depending on the imposed conditions. This change is identified as an "instability" and the possible mechanisms are discussed by Chun and Wuest [56] and Schwabe et al. [54]. Since such flow and temperature oscillations are undesirable for crystal growth, means of suppressing them were investigated. Chun and Wuest [57] examined the effect of end rotation for that purpose. Schwabe et al. [54] show that surfactants can induce diffusocapillary flows and Schwabe et al. [58] demonstrate that surface contamination can suppress thermocapillary convection. The effects of geometry and imposed thermal conditions on the "critical" Marangoni number are examined by Schwabe et al. [59] and Schwabe and Scharmann [60].

To expand the work just described on small liquid zones and to carry out a more systematic study of the effect of the various parameters an improved version of the apparatuses was designed and tested by Vargas et al. [61], Fig. 20. Hexadecane, Fluorinert, and methyl alcohol were the test fluids although the use of the latter was limited because of its high evaporation rate. The primary aim of this work was the characterization of the temperature oscillations and the determination of how they are influenced by the basic dimensionless parameters. Temperatures inside the liquid zone were measured by a thermocouple and chalk particles observed through a microscope were used to visualize the flow. For each fluid, the zone length, L , and the supporting rods diameter, D , were the geometric variables that were varied. The temperature difference between the two rods, ΔT , was slowly increased. A simple thermocapillary flow, Fig. 21, is first observed that is like that described numerically and the

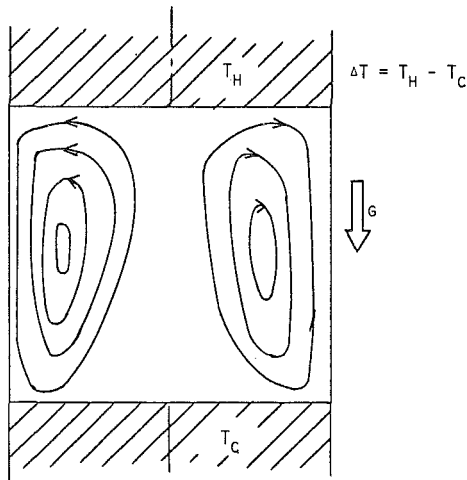


Fig. 21 Simple thermocapillary flow

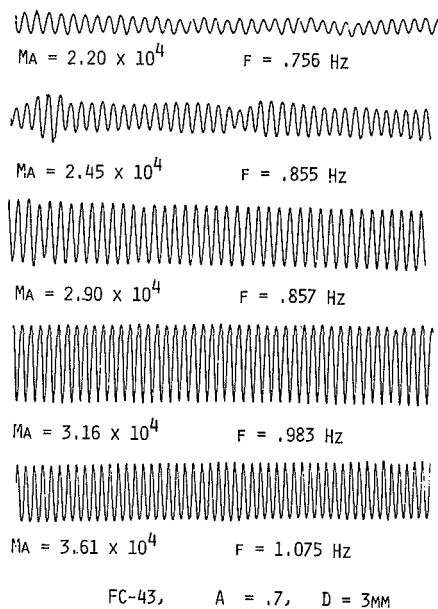


Fig. 22 Temperature oscillation patterns for fluorinert ($D = 3 \text{ mm}$)

temperature remained stationary. At a given value of ΔT the flow became oscillatory and very complex flow patterns were formed. Representative temperature oscillations are shown in Fig. 22. The form is nearly sinusoidal and the frequencies are well defined. This pattern persists over a wide range of ΔT and becomes distorted only at high values of Ma .

The value of Ma at which the oscillations start is designated as Ma_{cr} . The variation of Ma_{cr} with A is shown in Fig. 23. A linear relation between the two parameters is seen for $A > 0.4$ ($D = 3\text{mm}$), another one for $A > 0.3$ ($D = 6\text{mm}$) and still another for $A > 0.6$ ($D = 2\text{mm}$). It appears that doubling the diameter doubles the slope of the curve. With consideration of the definitions of Ma and A , this result indicates that the onset condition is independent of D and L for a given fluid, and, therefore, depends only on ΔT while Pr also seems to have some influence. Thus, Ma does not seem to be the proper parameter to characterize the onset of the oscillations. Further work is, thus, required to determine the proper parameter.

Since the flow in the liquid column is driven by the temperature distribution along the surface it was thought that measurements of it might provide a clue as to why the

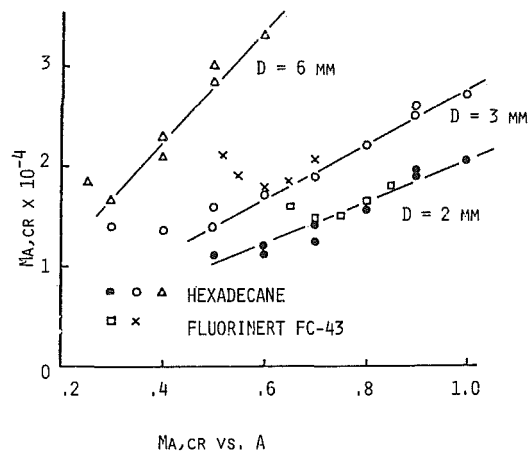


Fig. 23 Critical Marangoni number as a function of aspect ratio. Data from [61].

oscillations occur. Such measurements are shown in Fig. 24. For a given configuration as ΔT was increased the temperature distribution changed from almost the linear conduction profile to a S-shaped profile. Near the onset of oscillation a portion of the temperature profile (away from the wall) was found to be nearly flat. As ΔT was increased further, the flat portion become larger and eventually a temperature reversal appeared, i.e., the profile showed a sharp decrease in temperature near the top wall followed by a gradual increase. This temperature reversal is important in understanding the oscillation phenomenon. The sequence of events seems to be as follows: Consider that the thermocapillary convections is sufficiently strong so that a portion of the surface-temperature distribution has a part near the top wall that is nearly flat, Fig. 25. Suppose that the surface velocity is increased slightly by a small disturbance, for example. Then the flat portion is slightly extended due to the increased convection. Because of the increased flow recirculation, cooler particles are transported into the region near the top (hot) wall and tend to reduce the temperature in that region. As a result, a temperature reversal occurs temporarily, and the flow is then substantially retarded. If the flow speed is reduced below its equilibrium value, the temperature profile then has a steeper (overall) gradient than the equilibrium profile and the flow is increased, which starts the entire process again. The process is possible when convection dominates the damping effect of conduction so that the overshooting and undershooting of the surface-temperature distribution can occur. Thus, the primary mechanism that leads to flow oscillations is the coupling between the imposed surface temperature conditions and the surface convection. This coupling must be included in any meaningful analyses of this type of flow. It appears from this work that there is an inherent time-dependence in thermocapillary flows and an "instability" does not seem to be the cause of the oscillations.

By means of flow visualization and measurements of phase changes in the temperature oscillations around the liquid cylinder it was found that the oscillations produced alternately strong and weak recirculating patterns in one vertical plane and the entire flow field adjusted itself to accommodate the cycle in an optimum way.

To investigate thermocapillary flows in larger fluid volumes Schwabe and Scharmann [62] and [63] established a liquid zone of sodium nitrate 20 mm long and 12.5 mm deep between two graphite block heaters contained in a rectangular quartz boat. They postulate that the cause of oscillations in that configuration may be due to the interaction of two types of surface-tension flows, i.e., the Marangoni instability is

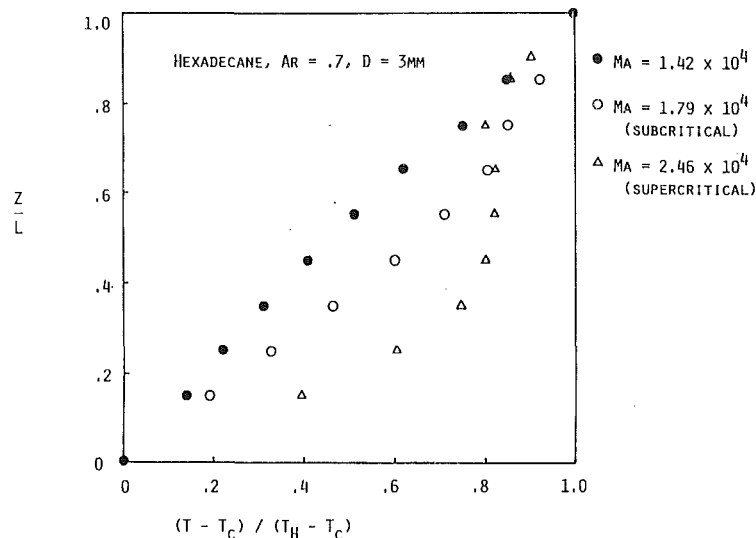


Fig. 24 Surface temperature distribution. Data from [61].

superposed on the regular thermocapillary flow. Thermocapillary flows were observed in an even larger volume of fluid by Kamotani et al. [64] by means of a rather unique experimental approach that enabled the dynamic Bond number to be small. A layer of fluorocarbon liquid (Fluorinert) 20 cm by 10 cm and 2.5 cm deep was heated from above by a thin nichrome wire to generate the flows. Detailed velocity and temperature measurements were made and oscillations were also encountered.

Until recently surface-tension gradient effects in Czochralski growth was considered as little more than a curiosity, Langlois [65]. As summarized by Pimputkar and Ostrach [2] and Langlois [65] the main driving forces for the bulk flows were considered to be buoyancy and crystal and/or crucible rotations. Thus, the melt free-surface shape was assumed to be flat and surface-tension gradient convection was neglected. The possibilities for space flight experiments enhanced interest in surface-tension effects, Langlois [66], and Langlois [67] included thermocapillary effects in his numerical studies. A more detailed review of surface-tension gradient effects in crystal growth is presented by Schwabe [11].

Balasubramaniam [68] used to proper dimensionless parameters, derived by Ostrach [49], to determine the influence of surface-tension gradients in an actual Czochralski configuration for the growth of silicon crystals. The properties of a silicon melt are:

$$\begin{aligned} d\sigma/dT &= -0.43 \text{ dyne/cm}^\circ\text{K} \\ \mu &= 0.01 \text{ gm/cm sec} \\ \rho &= 2.52 \text{ gm/cm}^3 \\ c_p &= 0.93 \times 10^7 \text{ erg/gm}^\circ\text{K} \\ \beta &= 2 \times 10^{-4} 1/^\circ\text{K} \\ Pr &= 0.031 \end{aligned}$$

The crucible is taken to be 5 cm in both depth and diameter. The diameter of the grown crystal is assumed to be 5 cm and its rotational speed is taken as 50 rpm. Estimates of the radial temperature gradients (from crucible wall to the crystal) range from 40 to 140°K/cm. For a conservative estimate the lower value is used. The calculations are made for terrestrial conditions, i.e., $g = 980 \text{ cm/s}^2$. Evaluation of the dimensionless parameters yields:

$$A = 2, Re_o = 5.42 \times 10^6, Gr = 1.94 \times 10^7$$

Since both the surface-tension Reynolds number and the

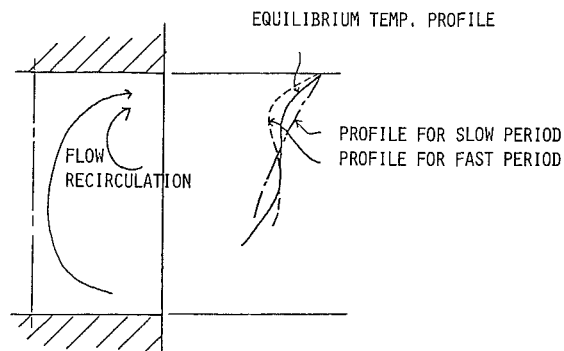


Fig. 25 Temperature profile variation with oscillation

Grashof number are large it must be determined which flow generation mechanism is dominant. Thus, the criterion for determining the relative importance of buoyancy to surface-tension gradients, given previously, for boundary-layer flows must be used, viz.,

$$Bd(\beta\Delta T)(A/Re_o)^{2/3} = Gr(A/Re_o)^{5/3}$$

If the parametric values given above are substituted into this expression it yields a value of 3.69×10^{-4} which indicates that the thermocapillary effects are dominant, even on earth. This surprising result depends on the value of $d\sigma/dT$ which could be reduced by the presence of some contaminate or film on the free surface. No real evidence for such have, as yet, been found and the value used in the above calculation is the one commonly used. Balasubramaniam [68] has determined the isotherms, streamlines, and velocity distributions for the idealized conditions of low aspect ratio and neglect of inertia, convection, and crystal rotation.

More important than the details of the flow, for the present purpose, is the implication that this result has regarding crystal imperfections. It has been observed that convection in the melt becomes irregular under certain conditions. Such irregular convection induces temperature and concentration fluctuations which result in imperfections in the crystals. In practice, to suppress these detrimental phenomena a controlled forced convection, i.e., crystal rotation, is imposed, but solute situations still occur. Despite the considerable attention given to the irregular convection phenomena, summarized by Pimputkar and Ostrach [2], they are not well

understood and are usually attributed to natural convection. In view of the fact that it now appears that thermocapillary convection is dominant relative to natural convection such an attribution may not be entirely valid, because surface-tension gradients can also cause flow oscillations. Thus, more careful investigation of such flows in Czochralski growth are necessary.

Concluding Remarks

It has been indicated herein that complex flows are inherent to crystal growth systems. The nature and extent of those flows are not well understood and have received relatively little attention. Interactions of fluid dynamics with other disciplines often helps to identify significant gaps in their knowledge. The broadening of research activities due to such stimuli usually leads to information that is even more general. Thus, some of the work done to understand the transport phenomena in crystal growth will be applicable to other technologies that involve physicochemical fluid dynamics.

With regard to the crystal growth problems the recent research reviewed herein represents a good start in the right direction in that care is being taken to use similarity concepts to model real situations, rather than using ad hoc models. It is essential for complex situations that dimensionless parameters be used for guidance if the information obtained is to be meaningful. Such an approach which is well-known and utilized by fluid dynamicists is not common in other disciplines.

Much more serious and comprehensive work needs to be done on the transport phenomena in crystal growth. The work done to date is limited by experimental methods to Prandtl numbers greater than those in real systems. Furthermore, attention has been focused on single aspects of the flows whereas, in reality, a number of them interact. Even with those limitations the flow patterns are complicated and often contain subregions, e.g., cells or multiple layers. To describe such intricate patterns experimentally or numerically requires methods with a high degree of resolution. Both theoretical and experimental approaches need to be developed to deal with such intricate flows and the more realistic low Prandtl number cases. Thus, the problems posed to fluid dynamicists by crystal growth systems are most interesting and present a great challenge to workers in this field.

Acknowledgments

The preparation of this lecture was made possible by the ASME Freeman Scholar Program and the author is thankful to the Standing Committee of the Program, Dr. A. M. O. Smith, Prof. J. M. Robertson, and Prof. J. W. Daily, for the opportunity.

NASA and the U.S. Air Force Office of Scientific Research have provided support for the author's research on the present and related topics.

The author wishes to acknowledge the help of Professor Y. Kamotani of Case Western Reserve University in most all aspects of his research. His competence, patience, and hard work contributed greatly to the work described herein.

The interactions with others in different disciplines have been both stimulating and exciting. Of the many delightful people who have been helpful special thanks are due to Profs. M. Glicksman of RPI, F. Rosenberger of the University of Utah, and D. Saville of Princeton University.

References

- 1 Solan, A., and Ostrach, S., "Convection Effects in Crystal Growth by Closed-Tube Chemical Vapor Transport," in *Preparation and Properties of Solid State Materials*, W. Wilcox, ed., Vol. 2, Marcel Dekker, Inc., 1979 pp. 63-110.
- 2 Pimputkar, S. M., and Ostrach, S., "Convective Effects in Crystals Grown from Melt," *Journal Crystal Growth*, Vol. 55, 1981, pp. 614-646.

- 3 Hurlle, D. T. J., and Jakeman, E., eds., "The Role of Convection and Fluid Flow in Solidification and Crystal Growth," *Physicochemical Hydrodynamics*, Vol. 2, No. 4, 1981, pp. 237-368.
- 4 Coriell, S. R., and Sekerka, R. F., "Effect of Convective Flow on Morphological Stability," *Physicochemical Hydrodynamics*, Vol. 2, No. 4, 1981, pp. 281-293.
- 5 Rosenberger, F., "Fluid Dynamics in Crystal Growth from Vapors," *Physicochemical Hydrodynamics*, Vol. 1, 1980, pp. 3-26.
- 6 Wiedemeier, H., Irene, E. A., and Chandhuri, A. K., "Crystal Growth by Vapor Transport of GeSe, GeSe₂, and GeTe and Transport Mechanism of GeTe*," *Journal Crystal Growth*, Vols. 13/14, 1972, pp. 393-395.
- 7 Wiedemeier, H., Klaessig, F. C., Irene, E. A., and Wey, S. J., "Crystal Growth and Transport Rates of GeSe and GeTe in Micro-gravity Environment," *Journal Crystal Growth*, Vol. 31, 1975, pp. 36-43.
- 8 Curtis, B. J., "Convective Effectives in Open-Tube Chemical Vapour Deposition," *Physicochemical Hydrodynamics*, Vol. 2, No. 4, 1981, pp. 357-365.
- 9 Laudise, R. A., *The Growth of Single Crystals*, Prentice-Hall, 1970.
- 10 Carruthers, J. R., Gibson, E. G., Klett, M. G., and Facemire, B. R., "Studies of Rotating Liquid Zones on Skylab IV.," *Prog. Astronaut. Aeronautics*, Vol. 52, 1977, pp. 207-221.
- 11 Schwabe, D., "Marangoni Effects in Crystal Growth Melts," *Physicochemical Hydrodynamics*, Vol. 2, No. 4, 1981, pp. 263-280.
- 12 Brice, J. C., *The Growth of Crystals, In Selected Topics in Solid State Physics*, E. P. Wohlfarth, ed., Vol. XII, North-Holland/American Elsevier, 1973.
- 13 Ostrach, S., "Natural Convection with Combined Driving Forces," *Physicochemical Hydrodynamics*, Vol. 1, No. 4, 1980, pp. 233-247.
- 14 Ostrach, S., "Natural Convection in Enclosures," *Advances in Heat Transfer*, Vol. 8, Chapter 3, Academic Press, 1972.
- 15 Ostrach, S., "Natural Convection Heat Transfer in Cavities and Cells," *Proc. 7th International Heat Transfer Conference*, Munich, Hemisphere, 1982.
- 16 Ostrach, S., Loka, R. R., and Kumar, A., *Natural Convection in Low-Aspect Ratio Rectangular Enclosures, In Natural Convection in Enclosures*, K. E. Torrance and I. Catton, eds., HTD-Vol. 8, ASME, 1980.
- 17 Al-Homoud, A. A., "Experimental Study of High Rayleigh Number Convection in a Horizontal Cavity with Different End Temperatures," M.S. thesis, University of Colorado, 1979.
- 18 Sernas, V., and Lee, E. I., "Heat Transfer in Air Enclosures of Aspect Ratio Less than One," *ASME Journal Heat Transfer*, Vol. 103, 1981, pp. 617-622.
- 19 Sernas, V., and Lee, E. I., "Numerical Study of Heat Transfer in Rectangular Air Enclosures of Aspect Ratio Less than One," ASME Paper 80-WA/HT-43, 1980.
- 20 Tseng, W., "Numerical Experiments on Free Convection in a Tilted Rectangular Enclosure of Aspect Ratio 0.5," M.S. thesis (Report No. NIE-050) Clarkson College, Potsdam, N.Y., 1979.
- 21 Kamotani, Y., Wang, L. W., and Ostrach, S., "Experiments on Natural Convection Heat Transfer in Low Aspect Ratio Enclosures," *AIAA Jour.*, Vol. 21, No. 2, 1983, pp. 290-294.
- 22 Jhaveri, B. S., and Rosenberger, F., "Expansive Convection in Vapor Transport Across Horizontal Rectangular Enclosures," *Journal Crystal Growth*, Vol. 56, 1982, pp. 57-64.
- 23 Shiroky, G. H., and Rosenberger, F., "Free Convection of Gases in a Horizontal Cylinder with Differentially Heated End Walls," Submitted to the *International Journal Heat Mass Transfer*, 1982.
- 24 Mughal, S. A., and Ray, B., "Preparation and Crystallization of ZnSiP₂ by the Iodine Vapor Transport Method," *Journal Crystal Growth*, Vol. 21, 1974, pp. 146-148.
- 25 Sparrow, E. M., Eichhorn, R., and Gregg, J. L., "Combined Forced and Free Convection in a Boundary Layer Flow," *Phys. Fluids*, Vol. 2, 1959, p. 319.
- 26 Fujii, E., Nakamura, H., Haruna, K., and Koga, Y., "Quantitative Calculations of the Growth Rate of Epitaxial Silicon from Silicon Tetrachloride in a Barrel Reactor," *Journal Electrochem. Soc.*, Vol. 119, 1972, p. 1108.
- 27 Wahl, G., "Hydrodynamic Description of CVD Processes," *Thin Solid Films*, Vol. 40, 1977, p. 13.
- 28 Curtis, B. J., and Dismukes, J. P., "An Investigation of Convective Effects in a Barrel Reactor," *Proc. 4th Int. Conf. on Vapour Deposition*, 1973, p. 218.
- 29 Curtis, B. J., and Dismukes, J. P., "Effects of Natural and Forced Convection in Vapour Phase Growth," *Journal Crystal Growth*, Vol. 17, 1972, p. 128.
- 30 Ostrach, S., and Raghavan, C., "Effect of Stabilizing Thermal Gradients on Natural Convection in Rectangular Enclosures," *Journal of Heat Transfer*, Vol. 101, 1979, pp. 238-243.
- 31 Fu, B.-L., and Ostrach, S., "The Effect of Stabilizing Thermal Gradients on Natural Convection Flow in a Square Enclosure," *In Natural Convection*, I. Catton and R. N. Smith, eds., ASME HTD, Vol. 16, 1981.
- 32 Turner, J. S., "Double-Diffusive Phenomena," *Ann. Rev. Fluid Mechs.*, Vol. 6, 1974, pp. 35-56.
- 33 Hurlle, D. T. S., *Hydrodynamics in Crystal Growth, In Crystal Growth and Materials*, E. Kaldis and H. J. Scheel, eds., North Holland, 1977, p. 549.
- 34 Ostrach, S., "Laminar Flows with Body Forces. In Theory of Laminar Flows," *High-Speed Aerodynamics and Jet Propulsion*, F. K. Moore, ed., Chapter 4, Vol. 4, Princeton University Press, 1964.

- 35 Chen, C. F., Briggs, D. G., and Wirtz, R. A., "Stability of Thermal Convection in a Salinity Gradient Due to Lateral Heating," *International Journal Heat Mass Transfer*, Vol. 14, 1971, pp. 56-65.
- 36 Wirtz, R. A., Briggs, D. G., and Chen, D. F., "Physical and Numerical Experiments on Layered Convection in a Density-Stratified Fluid," *Geophys. Fluid Dynam.*, Vol. 3, 1972, pp. 265-288.
- 37 Wirtz, R. A., "The Effect of Solute Layering on Lateral Heat Transfer in an Enclosure," *International Journal Heat Mass Transfer*, Vol. 20, 1979, pp. 841-846.
- 38 Wang, L. W., "Experimental Study of Natural Convection in a Shallow Horizontal Cavity with Different End Temperatures and Concentrations," Ph.D. thesis, Department of Mechanical and Aerospace Engineering, Case Western Reserve University, Cleveland, Ohio, 1982.
- 39 Rosenberger, F., DeLong, M. C., and Olson, J. M., "Heat Transfer and Temperature Oscillations in Chemical Vapor Transport Crystal Growth," *Journal Crystal Growth*, Vol. 19, 1973.
- 40 Ostrach, S., *Motion Induced by Capillarity*, In *Physicochemical Hydrodynamics*, V. G. Levich Festschrift, D. B. Spalding, ed., Vol. 2, Advance Publ. Ltd., 1977.
- 41 Scriven, L. E., "Drops and Bubbles: Their Science and the Systems They Model," In *Proc. Int. Colloquium on Drops and Bubbles*, Vol. 1., D. J. Collins, M. S. Plesset, M. M. Saffren, eds., Calif. Inst. Tech. and Jet Propul. Lab., Aug. 1974.
- 42 Sternling, C. V., and Scriven, L. E., "Interfacial Turbulence: Hydrodynamic Instability and the Marangoni Effect," *AIChE Journal*, Vol. 5, 1959, pp. 514-523.
- 43 Kenning, D. B. R., "Two-Phase Flow with Nonuniform Surface Tension," *Appl. Mech. Rev.*, Vol. 21, 1968, pp. 1101-1111.
- 44 Levich, V. R., and Krylov, V. S., "Surface-Tension-Driven Phenomena," *Ann. Rev. Fluid Mechs.*, Vol. 1, 1969, pp. 293-316.
- 45 Sirignano, W. A., and Glassman, I., "Flame Spreading Above Liquid Fuels: Surface Tension Flows," *Combust. Sci. and Tech.*, Vol. 1, 1970, pp. 307-312.
- 46 Ostrach, S., "Role of Analysis in the Solution of Complex Physical Problems," *Proc. 3rd Int. Heat Transfer Conf.*, Vol. 6, 1966, pp. 31-43.
- 47 Levich, V. G., *Physicochemical Hydrodynamics*, Prentice-Hall, 1962.
- 48 Stanek, V., and Szekely, J., "The Effect of Surface Driven Flows on the Dissolution of a Partially Immersed Solid in a Liquid-Analysis," *Chem. Eng. Sci.*, Vol. 25, 1964, pp. 699-716.
- 49 Ostrach, S., "Convection Due to Surface-Tension Gradients," in (COSPAR) *Space Research*, M. J. Rycroft, ed., Vol. 19, 1979, Pergamon Press, pp. 563-570.
- 50 Pimpulkar, S. M., and Ostrach, S., "Transient Thermocapillary Flow in Thin Layers," *Phys. Fluids*, Vol. 23, 1980, pp. 1281-1285.
- 51 Chang, C. E., and Wilcox, W. R., "Analysis of Surface Tension Driven Flow in a Floating Zone Melting," *International Journal Heat Mass Transfer*, Vol. 19, 1976, pp. 355-366.
- 52 Clark, P. A., and Wilcox, W. R., "Influence of Gravity on Thermocapillary Convection in Floating Zone Melting of Silicon," *Journal Crystal Growth*, Vol. 50, 1980, pp. 461-469.
- 53 Fu, B.-I., "Numerical Solution of Floating Zone Crystal Growth," Ph.D. thesis, Department of Mechanical and Aerospace Engineering, Case Western Reserve University, Cleveland, Ohio, 1982.
- 54 Schwabe, D., Scharmann, A., Preisser, F., and Oeder, R., "Experiments on Surface Tension Driven Flow in Floating Zone Melting," *Journal Crystal Growth*, Vol. 43, 1978, pp. 305-312.
- 55 Chun, Ch.-H., and Wuest, W., "A Micro-gravity Simulation of the Marangoni Convection," *Acta Astronautica*, Vol. 5, 1978, pp. 681-686.
- 56 Chun, Ch.-H., and Wuest, W., "Experiments on the Transition from the Steady to the Oscillatory Marangoni-Convection of a Floating Zone Under Reduced Gravity Effect," *Acta Astronautica*, Vol. 6, 1979, pp. 1973-1982.
- 57 Chun, Ch.-H., and Wuest, W., "Flow Phenomena in Rotating Floating Zones with and without Marangoni Convection," *Proc. 3rd European Symp. Materials Sciences in Space*, ESA SP-142, Grenoble, 1979.
- 58 Schwabe, D., Scharmann, A., and Preisser, F., "Studies of Marangoni Convection in Crystal Growth Melts," *Int. Astronautics Federation, IAF-80-C-140*, Pergamon Press, 1980.
- 59 Schwabe, D., Scharmann, A., and Preisser, F., "Steady and Oscillatory Marangoni Convection in Floating Zones Under 1-g," *Proc. 3rd, European Symp. Materials Sciences in Space*, ESA-SP-142, Grenoble, 1979.
- 60 Schwabe, D., and Scharmann, A., "Some Evidence for the Existence and Magnitude of a Critical Marangoni Number for the Onset of Oscillatory Flow in Crystal Growth Melts," *Journal Crystal Growth*, Vol. 46, 1979, pp. 125-131.
- 61 Vargas, M., Ostrach, S., and Kamotani, Y., "Surface-Tension Driven Convection in a Simulated Floating Zone Configuration," Department of Mechanical and Aerospace Engineering, Case Western Reserve University, Cleveland, Ohio, FTAS/TR-82-159, May 1982.
- 62 Schwabe, D., and Scharmann, A., "Thermocapillary Convection in Crystal Growth Melts," *Letters in Heat and Mass Transfer*, Vol. 7, 1980, pp. 283-292.
- 63 Schwabe, D., and Scharmann, A., "The Magnitude of Thermocapillary Convection in Larger Melt Volumes," *Adv. Space Res.*, Vol. 1, 1981, pp. 13-16.
- 64 Kamotani, Y., Ostrach, S., and Lowry, S., "An Experimental Study of Heat Induced Surface-Tension Driven Flow," In *Materials Processing in the Reduced Gravity Environment of Space*, G. E. Rindone, ed., Materials Res. Soc. Symposium Proc., Vol. 9, North-Holland, 1982, pp. 161-172.
- 65 Langlois, W. E., "Convection in Czochralski Growth Melts," *Physicochemical Hydrodynamics*, Vol. 2, No. 4, 1981, pp. 245-261.
- 66 Langlois, W. E., "Digital Simulation of Czochralski Bulk Flow in Microgravity," *Journal Crystal Growth*, Vol. 48, 1980, p. 25.
- 67 Langlois, W. E., "Conservative Differencing Procedures for Rotationally Symmetric Flow with Swirl," *Computer Meth. Appl. Mech. Engng.*, Vol. 25, 1981, p. 315.
- 68 Balasubramaniam, R., "Fluid Flow in the Czochralski Method of Crystal Growth," M.S. thesis, Department of Mechanical and Aerospace Engineering, Case Western Reserve University, Cleveland, Ohio, 1982.

Radial Vaneless Diffusers: A Re-Examination of the Theories of Dean and Senoo and of Johnston and Dean

M. Inoue

Komatsu Ltd.,
Hiratsuka, Kanagawa, Japan;
Formerly in the Whittle Laboratory,
University of Cambridge, England

There are two different but well known theories for calculating loss in the mixing process of the nonuniform flow discharged from the impeller, into the vaneless diffuser. One is by Dean and Senoo, the other by Johnston and Dean. In this paper explanations are given why these two very different theories predict similar total pressure losses. The mixing process in the vaneless diffuser based on the Dean and Senoo theory is re-examined. It is found that the reversible work exchange makes a significant contribution to the non-uniform flow becoming axisymmetric. This process is, however, greatly accelerated by wall friction and interface shear forces between the jet and wake, which lead to loss in total pressure.

1 Introduction

Dean and Senoo [1] developed a theory for the radial impeller discharge mixing process including wall friction, friction between wake and jet, and reversible work exchange. In their flow model¹, the flow out of each impeller passage was divided into two regions, the wake and the jet. The relative velocity was constant in each region with a high velocity for the jet and a low velocity for the wake. The mixing process of the jet and the wake was calculated by solving the momentum and the continuity equations for the jet and the wake simultaneously. They showed that a large part of the loss at the vaneless diffuser inlet was due to wall friction loss of an asymmetric flow. They also concluded that the asymmetric flow pattern became uniform rapidly by the reversible work exchange between jet and wake.

Johnston and Dean [2] presented a simple analysis based on an assumption of sudden expansion. In their flow model², the wake and the jet were mixed up at the inlet to the diffuser by sudden expansion and the flow was thereafter assumed axially symmetric in the diffuser. The large total pressure loss at the vaneless diffuser inlet was attributed to the mixing loss by the sudden expansion. They compared their calculations for various centrifugal blower outlet flows with those based on the Dean and Senoo model. Their simple model gave very similar predictions of total pressure loss to those by the more precise method (D-S model) over a wide range of compressor parameters. Senoo and Ishida recently tried to find out experimentally the main factor causing the mixing of the nonuniform flow in the vaneless diffuser. They came to the

conclusion that the behavior of the flow was controlled by the reversible work exchange and that the contribution of the shear force between jet and wake to the mixing was not significant. From total pressure loss measurements in a vaneless diffuser with two different wall roughness they also concluded that the large total pressure loss at the inlet was due to wall friction loss and the flow was mixed out mainly by the reversible work exchange. The prediction based on the D-S and J-D models were, however, similar for the two different wall coefficients and the reason for similarity was not made clear.

It is intended in the present paper to explain the reason why the losses predicted by the simple J-D model are so close to those based on the D-S model. To begin with, the contributions of friction and reversible work exchange towards uniformity is discussed.

2 Contributed of Friction and Reversible Work Towards Uniformity

The nonuniform flow leaving an impeller is made complicated by the combined effects of friction at the wall, shear stress at the interface between the jet and wake, and reversible work. These effects cannot properly be considered separately but some understanding can be reached by varying the individual parameters.

Reversible work exchange exists when the flow is unsteady, as it is in the jet and wake flow from a rotating impeller. In the jet and wake pattern produced by a circumferential array of stationary vanes, the flow is steady and reversible work is absent. Therefore by comparing the mixing processes of rotating and stationary jet and wake patterns, the contribution of the reversible work exchange may be observed. The wake displacement width is used here as a parameter to characterise the flow nonuniformity. It is defined by

¹For brevity, the Dean and Senoo model is called D-S in this paper.

²For brevity, the Johnston and Dean model is called J-D model in this paper.

Contributed by the Fluid Engineering Division for publication in the JOURNAL OF FLUIDS ENGINEERS. Manuscript received by the Fluids Engineering Division, May 26, 1978.

Table 1 Comparison of predicted loss in absolute stagnation pressure due to mixing for rotating and stationary jet and wake pattern (vaneless diffuser)

	Shear Coefficient ζ	Wall Friction Coefficient C_f	Mixing Loss of D-S Model			Mixing Loss of J-D Model
			Due to Shear at Interface	Due to Wall Friction	Total	
Rotating Case	0.0	0.005	0.0	0.021	0.021	0.035
	0.1	0.0	0.022	0.0	0.022	0.035
	0.1	0.005	0.019	0.018	0.037	0.035
Stationary Case	0.0	0.005	--	--	0.084	0.035
	0.1	0.0	--	--	0.058	0.035
	0.1	0.005	--	--	0.058	0.035

INLET FLOW CONDITION
FOR ROTATING PATTERN
 $\beta_0 = 0, W_{w0}/W_{j0} = 0.25, \epsilon_0 = 0.5$
FOR STATIONARY PATTERN
 $\chi_0 = 0, C_{w0}/C_{j0} = 0.25, \epsilon_0 = 0.5$

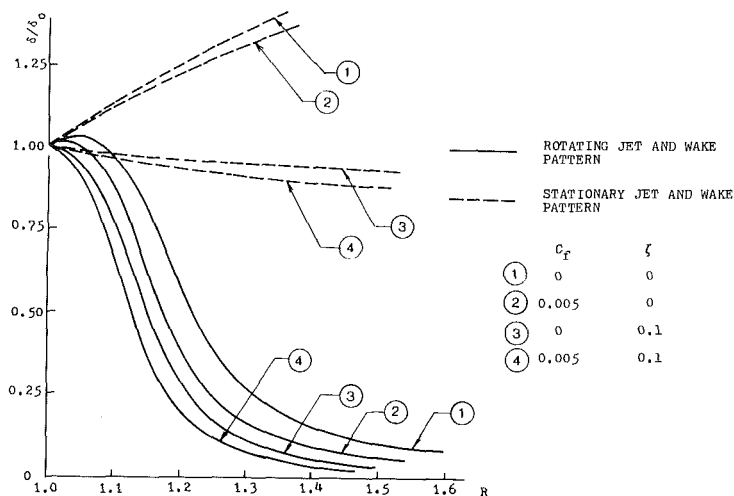


Fig. 1 Variation of displacement width based on Dean-Senoo model for various combination of C_f and ζ when χ_0 or

$$\beta_0 = 0, \epsilon_0 = 0.5, \frac{W_{w0}}{W_{j0}} \text{ or } \frac{C_{w0}}{C_{j0}} = 0.25$$

$$\delta = \epsilon \left(1 - \frac{W_w}{W_j} \right) \quad (1)$$

where ϵ is the wake width and W_w and W_j are the velocities of the wake and jet in the frame of reference generating them. Figure 1 shows the variation of δ with radius for various combinations of the wall friction, C_f , and interface shear between jet and wake coefficients, ζ . The relative flow angle for the rotating jet and wake patterns, β_0 , and the absolute flow angle for the stationary cases, χ_0 , are both zero. The solid and dotted curves are for the rotating and stationary cases, respectively.

The differences in the variation of δ between the rotating and stationary cases are large for all the combinations of C_f and ζ . This is true even for the frictionless case so that the reversible work exchange has a significant role in mixing up the flow. In the stationary case it is even possible for the value of δ to increase with radius. In the rotating case the mixing of the flow is much more rapid in the inlet region when the wall friction and the interface shear exist. (Compare the solid curves 4 with 1.) Even when only the wall friction exists ($C_f = 0.005$ and $\zeta = 0$, solid curve 2) the value of δ decreases more quickly than for the frictionless case, showing that the wall friction can assist mixing out of the flow as well as the interface shear. Curve 3 shows a significant effect of the interface shear on mixing of the flow. Dean and Senoo [1] compared the results for various shear coefficients, $C_f = 0.005$ (See Fig. 7 of reference [1].) Since there was but little

change in the static and total pressure variations with radius they concluded that the interface shear was not important for the mixing process. This was, however, incorrect. When both the wall friction and the interface shear are included, the effect of each on mixing is less than that when either one works alone; the combined effect is not a simple addition of the independent effects. If the mixing process is calculated when only the interface shear is acting, $\zeta = 0.094$ and $C_f = 0$, we can find that the mixing is actually more rapid than for the case of $C_f = 0.005$ and $\zeta = 0$.

The losses based on the D-S and J-D models for the cases of Fig. 1 are compared in Table 1 in a similar way so that used by Johnston and Dean [2]. The friction loss of the J-D model, which is the loss that a uniform flow experience in travelling a given distance, is subtracted from the overall pressure loss of the D-S model. This leaves the residual loss which is compared to the sudden expansion loss or mixing loss of the J-D model.

For the stationary cases, the predicted mixing losses by the D-S model are very different from those based on the J-D model (sudden expansion loss). For the rotating cases, the J-D model predicts mixing loss very close to the D-S model when the wall friction and the shear force exist, $\zeta = 0.1$ and $C_f = 0.005$. The mixing losses in the D-S model due solely to either the wall friction or the interface shear are very similar in this case.

The significant contribution of the shear at the interface of wake and jet and the wall friction in mixing out the flow at the inlet region provides some insight into why the sudden ex-

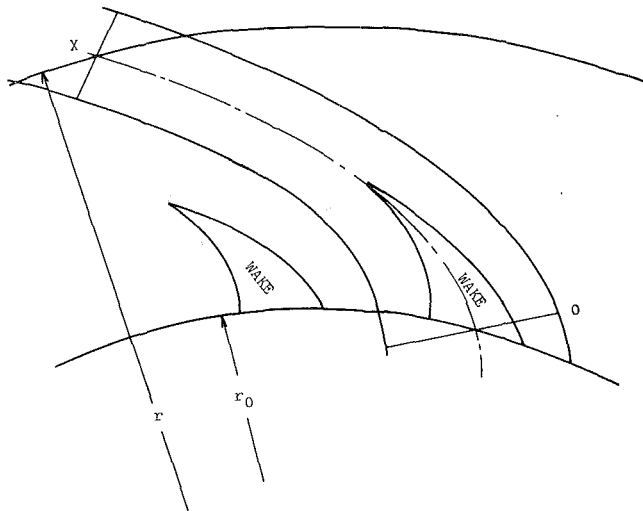


Fig. 2 Relative steam tube in vaneless diffusers

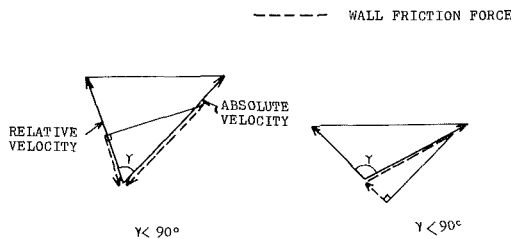


Fig. 3 Direction of wall friction force acting on relative flow

pansion model by Johnston and Dean predicts losses which are so close to those based on the D-S models.

Nevertheless, it does seem strange that the J-D model, which neglects the reversible work exchange, can predict losses so close to those by the D-S model for the rotating cases, whereas it predicts very different losses for the stationary cases where the reversible work exchange does not exist. This can be explained in the one-dimensional analysis below.

3 One Dimensional Analysis For Losses

There is a relation between absolute and relative total pressure in the vaneless diffuser as follows:

$$P = P^* - \frac{\rho}{2} (W^2 - C^2 - u^2) = P^* + \rho \Omega r C_\theta \quad (2)$$

where the relative total pressure is defined as

$$P^* = P_s + \frac{\rho}{2} (W^2 - u^2)$$

The same expression was used in the discussion of reference [4] by Mobarak.

In the absence of losses, P^* is constant along a streamline in the relative coordinate system because flow is steady and there is no energy exchange between streamlines [3]. The difference in relative total pressures of the wake and the jet is, therefore, unchanged. On the other hand, the angular momentum changes along a streamline by reversible work exchange since the flow is unsteady in the absolute coordinate system and the second terms of equation (2) of wake and jet will change.

From equation (2), the mass-averaged total pressure loss between $r = r_0$ and $r = r_1$ can be written as follows:

$$\Delta P = \bar{P}_0 - \bar{P}_1 = (\bar{P}_0^* - \bar{P}_1^*) + \rho \Omega (r_0 \bar{C}_{\theta 0} - r_1 \bar{C}_{\theta 1}) \quad (3)$$

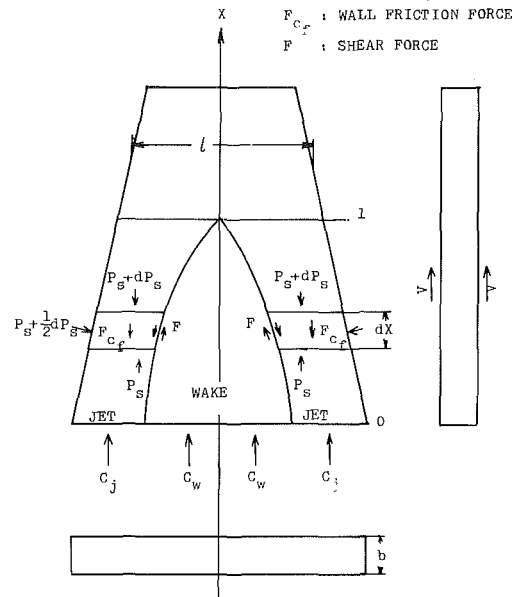


Fig. 4 Schematic mixing process in one-dimensional channel

where \bar{P}^* and \bar{C}_0 represent the mass averaged relative total pressure and absolute whirl velocity.

It is found from equation (3) that the total pressure loss in the vaneless diffuser is the sum of the loss in relative total pressure and the loss in the product of angular momentum and angular velocity $\Omega r C_\theta$. Since reversible work exchange does not exist in the mixing process of the total pressure distortion in the relative frame of reference the loss in relative total pressure may be estimated approximately from the calculation of the mixing process in a one-dimensional channel which simulates the relative streamline in the vaneless diffuser (Fig. 2).

3.1 D-S Model in One-Dimensional Channel. The flow in a one-dimensional channel is divided into the jet and the wake. These two regions are mixed up gradually by friction at the wall and interface of the jet and wake. The static pressure and the velocity of jet and wake are assumed functions only of the distance from the inlet along the centerline of the one-dimensional channel.

In the vaneless diffuser the wall friction force magnitude is determined by the absolute velocity and acts in the opposite direction to the absolute flow; a higher absolute velocity in the wake gives a higher wall friction force. When we consider the relative flow in the vaneless diffuser, the component of the wall friction force in the direction of the relative flow must be taken. If the angle between the relative and the absolute flow, γ , is larger than a right angle, the friction force works in the flow direction and acts to increase the relative total pressure and vice versa for γ smaller than a right angle (Fig. 3). These cases may be simulated in the one-dimensional channel by moving the walls at the appropriate velocity in the flow direction if $\gamma > 90$ deg and against the flow direction if $\gamma < 90$ deg.

The Momentum equations of wake and jet in the one-dimensional channel with walls moving at a velocity V are as follows (refer to Fig. 4).

For the jet

$$\frac{1}{\rho} \frac{dP_s}{dx} + \frac{dC_j}{dx} C_j + \frac{C_j}{b} \text{sign}(C_j - V) + \zeta (C_j - C_w)^2 \frac{1}{1 - \epsilon} \frac{1}{l} = 0, \quad (4)$$

and for the wake

INLET COND.	$C_f r_0/b$	$Z\zeta$	W_w/W_j	ϵ_0	$C_{\theta 0}/u_0$	$C_{r 0}/u_0$	β_0	λ_i
—○—	0.10	4.23	0.00	0.50	0.70	1.40	-6.1	0.5
—△—	0.10	4.23	0.00	0.50	0.70	0.35	-23.	2.0
—○—	0.19	0.74	0.00	0.535	0.70	0.24	-30.	2.9
—△—	0.19	0.74	0.06	0.60	0.70	0.24	-30.	2.9
—□—	0.19	0.74	0.15	0.90	0.70	0.24	-30.	2.9
—○—	0.09	0.85	0.32	0.75	0.61	0.21	-54.5	2.9
—△—	0.21	0.85	0.32	0.75	0.61	0.21	-54.5	2.9

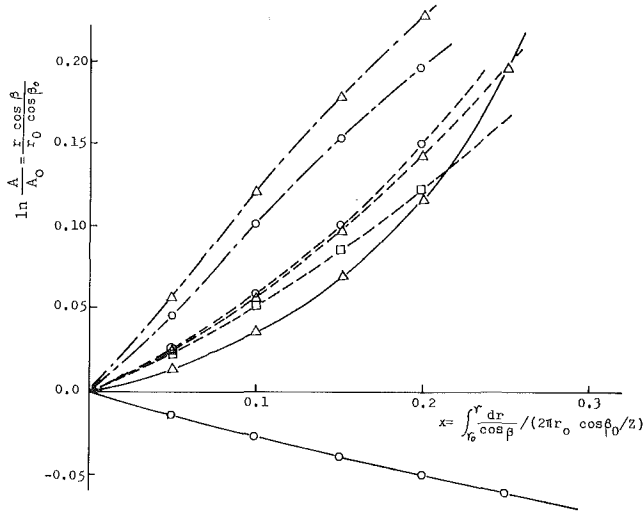


Fig. 5 Area change of relative steam tube in vaneless diffuser

$$\frac{1}{\rho} \frac{dP_s}{dx} + \frac{dC_w}{dx} C_w + \frac{C_f}{b} \text{sign}(C_w - V)(C_w - V)^2 + \zeta(C_j - C_w)^2 \frac{1}{\epsilon} \frac{1}{l} = 0. \quad (5)$$

As in Dean and Senoo's paper, C_f is assumed equal for jet and wake. It is also assumed that no friction force acts on the side walls.

The continuity equations become:

$$AC_j(1 - \epsilon) = A_0 C_{j0}(1 - \epsilon_0) \quad (6)$$

$$AC_w \epsilon = A_0 C_{w0} \epsilon_0 \quad (7)$$

for the jet and the wake, respectively, subscript zero denoting entry values.

The cross-section area variation is chosen so as to simulate the area variation of relative streamtube in the vaneless diffuser (Fig. 2).

Figure 5 shows the cross-section area variations for several cases which were considered by Dean and Senoo [1], Johnston and Dean [2] and Senoo and Inshida [4]. The abscissa

$$x = \frac{Z}{2\pi r_0 \cos \beta_0} \int_{r_0}^r \frac{dr}{\cos \beta}$$

is distance along the centerline of the relative streamtube from the inlet to the diffuser, nondimensionalised by the width of the relative streamtube at the inlet to the vaneless diffuser, $2\pi r_0 \cos \beta_0/Z$. The ordinate in Fig. 6 is the logarithm of the cross section area ratio

$$\frac{A}{A_0} = \frac{r \cos \beta}{r_0 \cos \beta_0}$$

For practical values of swirl parameter ($\lambda_i \approx 2 - 3$) the area ratio decreases monotonically. Only for a very small value of λ_i , such as 0.5, does the area ratio increase because the rate of decrease in $\cos \beta$ is smaller than the rate of increase in r . In any case, for a wide range of values of δ , $C_f r_0/b$, $Z\zeta$, W_w/W_j , and λ_i the area changes may be approximately expressed as

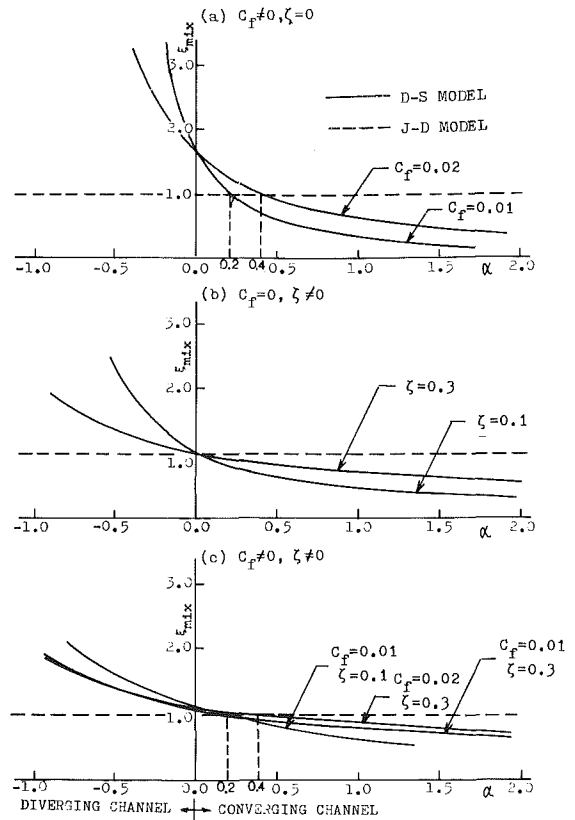


Fig. 6 Comparison of mixing loss of D-S and J-D model for one-dimensional channel; stationary wall, $V = 0$, dead wake, $C_{w0} = 0$, $\epsilon_0 = 0.5$, $A/A_0 = e^{-\alpha x}$

$$\frac{A}{A_0} = \frac{l}{l_0} = e^{-\alpha x}. \quad (8)$$

Having obtained the distribution of cross section area, the four unknowns (P_s , C_j , C_w , ϵ) may be calculated by solving the four equations (4) ~ (7) simultaneously, the final solution, after introducing equation (8) being achieved numerically by the Runge-Kutta method.

3.2 J-D Model in One-Dimensional Channel. The total pressure loss of J-D model is the sum of the sudden expansion loss and the friction loss of the mixed out flow. The sudden expansion loss is calculated by conserving momentum and continuity across the mixing process and the friction loss of the mixed out flow is calculated from

$$\Delta P_{\text{fric}} = \int_0^x \frac{2C_f}{b} \frac{1}{2} \rho (\bar{C} - V)^2 dx$$

where

$$\bar{C} = \frac{A}{A_0} C_0.$$

3.3 Comparison of D-S Model and J-D Model in One-Dimensional Channel. The D-S and J-D models are compared in the same way as in Section 2. At first we will describe the results when the duct walls as still, $V = 0$. Figure 6(a), (b) and (c) show the comparisons for the case of a "dead" wake, $C_{w0} = 0$, and $n = 1$ (i.e., $A/A_0 = e^{-\alpha x}$).

Calculations have shown that virtually identical trends are obtained for realistic values of n other than unity. When there is a nonzero flow in the wake the calculations show the same trends but with loss magnitudes which are significantly smaller. The curves in Fig. 6(a) are for various wall friction coefficients but without interface shear between jet and wake,

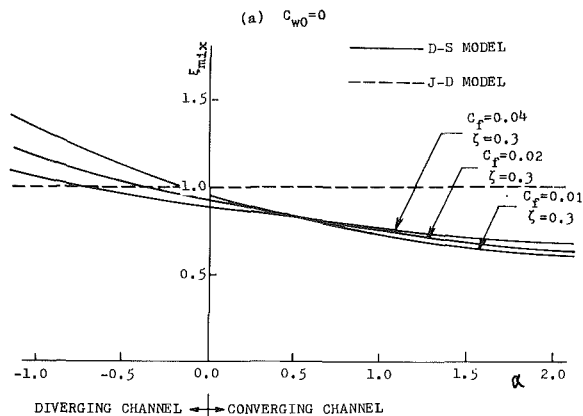


Fig. 7 Comparison of mixing loss of D-S and J-D model for one-dimensional channel; moving wall, $V/C_{j0} = 2.0$, $\epsilon = 0.5$, $A/A_0 = e^{-\alpha x}$, $C_{w0} = 0$

$\zeta = 0$. (For $\zeta = 0$, $C_{w0} = 0$ and $n = 1$ the D-S mixing process can in fact be solved analytically in closed form, Inoue [5].) The D-S model predicts higher mixing loss than the J-D model for values of a smaller than C_f . For a parallel channel, $a = 0$, the mixing losses based on the D-S model are the same irrespective of the wall friction coefficients, although larger than the sudden expansion loss due to J-D model. The flow may be mixed out without friction force, that is without loss, for the converging channel, $a > 0$, (see Appendix 1 of reference [5]). When the wall friction coefficient, C_f increases the mixing out of the flow (which is accompanied with loss) takes place in a shorter distance. Consequently the effect of convergence of the channel on the mixing becomes smaller and the mixing loss increases as the wall friction coefficient is increased. For the diverging channel, the flow is unable to be mixed out without friction force but instead the nonuniformity is amplified. As the wall friction coefficient becomes large the amplification of the nonuniformity by the effect of divergence of the channel is suppressed and the flow in the divergent channel is mixed out in a shorter distance. Therefore the mixing loss decreases for the diverging channel as the wall friction coefficient increases.

The similar tendency can be also found in Fig. 6(b), where the results are shown for various interface shear coefficients without wall friction, $C_f = 0$.

The results when both the interface shear and the wall friction exist are shown in Fig. 6(c). Compared with Fig. 6(a), the variation with respect to a is less in Fig. 6(c) because of the influence of the jet-wake interface shear on the mixing.

As indicated above, the direction in which the wall friction force acts changes with the wall velocity V . Figure 7 shows the comparison of mixing losses and the D-S and J-D models for the case of $V = 2.0 C_{j0}$ and a "dead" wake, $C_{w0} = 0$, with the wake width $\epsilon = 0.5$. In this case, the skin friction acts to increase the relative total pressure. The curves in Fig. 7, which are for various wall friction coefficients with $\zeta = 0.3$, have similar trends to those for the stationary wall, $V = 0$, shown in Fig. 6, although the loss of the D-S model is smaller for diverging channels. This smaller loss for the D-S model where $a < 0$ is because the friction is much larger than for the stationary wall and the flow is mixed out in a shorter distance.

4 Discussion

Using the results for one-dimensional channels obtained in the previous section, we will try to explain the results of the papers by Johnston and Dean [2] and Senoo and Ishida [4].

First of all, we will consider the unusually high loss of the two-dimensional D-S model for the stationary jet and wake pattern. For the stationary wake and jet pattern the values of

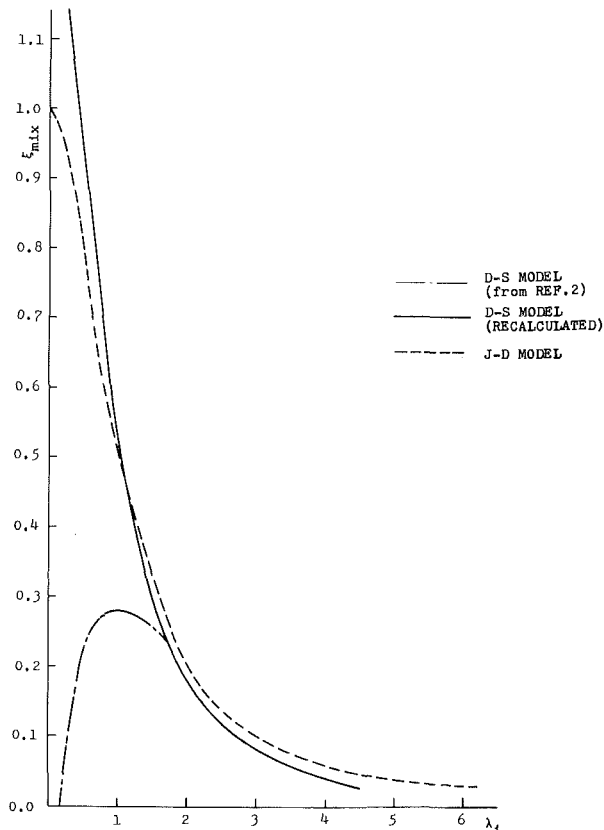


Fig. 8 Comparison of mixing loss of D-S and J-D model in vaneless diffuser; $\epsilon_0 = 0.5$, $\psi_j = 0.7$, $W_{w0}/W_{j0} = 0$, $C_f, \gamma_0/b = 0.1$, $Z\zeta = 4.23$, $R_{out} = 1.8$

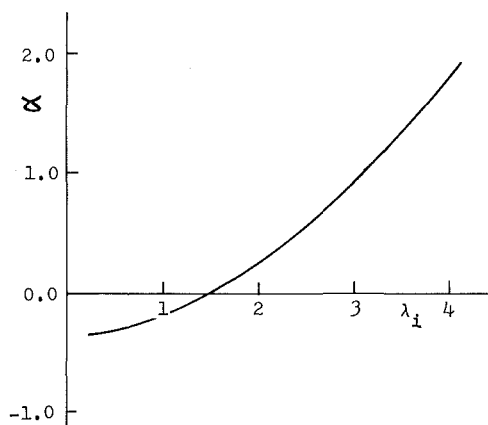


Fig. 9 Variation of α with swirl parameter λ_1 for case in Fig. 8 of reference [2], $\epsilon_0 = 0.5$,

$$\frac{C_f \gamma_0}{b} = 0.1, Z\zeta = 4.23$$

a are negative and large ($a \leq -1$). The results in Fig. 6, showing that the mixing losses based on the D-S model are then much larger than the sudden expansion loss, confirm the trend found for the stationary flow in two-dimensions.

Johnston and Dean [2] compared the prediction of loss by their method with that predicted by the earlier Dean and Senoo [1] method for a particular jet-wake pattern over a range of values of the swirl parameter λ_1 . The result (Fig. 8 of reference [2]) is reproduced here in Fig. 8. The variation of the area convergence rate, a , with λ_1 was calculated and shown in Fig. 9.

Table 2 Coefficient of predicted total pressure loss between $R = 1.014$ and $R = 1.8$ (Table 3 of reference [4])

Wall Friction Coefficient C_f	LOSS OF D-S MODEL			LOSS OF J-D MODEL		
	Due to Wall Friction	Due to Shear $(\zeta=0.094)$	TOTAL	Due to Wall Friction	Due to Sudden Expansion	TOTAL
0.005	0.110	0.018	0.128	0.082	0.070	0.152
0.012	0.206	0.009	0.215	0.161	0.070	0.231

INLET FLOW CONDITION
 $\epsilon_0 = 0.5$, $\frac{V_{j0}}{V_0} = 0.74$, $\frac{V_{w0}}{V_0} = 0.24$, $\beta_0 = -54.54^\circ$

Table 3 Comparison of predicted mixing loss for various combination of C_f and ζ

Shear Coefficient ζ	Wall Friction Coefficient C_f	MIXING LOSS OF D-S MODEL			Mixing Loss of J-D Model
		Due to Shear Force	Due to Wall Friction ^a	TOTAL	
0.094	0.005	0.029	0.016	0.045	0.070
0.094	0.012	0.025	0.028	0.053	0.070
0.300	0.005	0.044	0.010	0.054	0.070

INLET FLOW CONDITION
 $\epsilon_0 = 0.5$, $\frac{V_{j0}}{V_0} = 0.74$, $\frac{V_{w0}}{V_0} = 0.24$, $\beta_0 = -54.54^\circ$

For a large value of λ_i , the value of a is positive and large. The relative total pressure loss of the D-S model is expected from the results for one-dimensional channels to be smaller than that of the J-D model. The difference in the reductions of angular momentum of the two models will be very small because the flow rapidly becomes uniform. Therefore the one-dimensional analysis predicts that the mixing loss of the D-S model is smaller than that of the J-D model at large values of λ_i .

Since the value of a is negative, i.e., a diverging channel, at a smaller value of λ_i it may be expected that the D-S model gives larger relative total pressure loss than the J-D model. The reduction of angular momentum term, $\rho\Omega(V_0 C_{\theta 0} - V_j C_{\theta j})$, due to wall friction is also larger in nonuniform flow (D-S model) than in mixed out flow (J-D model). Therefore the one-dimensional method predicts that the mixing loss for the D-S model should be larger than that of the J-D model at small values of λ_i .

The results given by Johnston and Dean, however, show the opposite trend for small λ_i and for this reason the flow was recalculated, the solid line in Fig. 8 and differences emerged for the D-S model. For $\lambda_i > 2$, the magnitude and trend are essentially identical to those calculated by Johnston and Dean, but for $\lambda_i < 2$ the results of the recalculation are quite different to those originally given by Johnston and Dean. In the recalculation the loss predicted by the D-S model becomes larger than the prediction by the J-D model for λ_i smaller than about 1.1, whereas Johnston and Dean's calculation showed the opposite trend³. The recalculated losses show exactly the trends predicted by the one-dimensional analysis.

Since the expansion loss of the J-D model for the vaneless diffuser becomes small as λ_i becomes large, the absolute amount by which the mixing loss of the J-D model can exceed that of the D-S model is also small. At small values of λ_i , the mixing loss of the D-S model is larger than that of the J-D model; over a range of intermediate values of λ_i the two losses must therefore be comparable.

³The explanation for the erroneous trend calculated by Johnston and Dean may be that for $\lambda_i < 2$ the calculation of the D-S model using the Runge-Kutta method is very sensitive to the increment in radius (ΔR). At $\lambda_i = 1.5$ for example, the total pressure loss predicted by the D-S model is 0.421 when $\Delta R = 0.001$ and 0.500 when $\Delta R = 0.0001$. The wake width (ϵ) decreases very rapidly at $R \approx 1.095$ and $\Delta R = 0.001$ is too large to predict correct values of the next step. For $\Delta R = 0.001$ a negative value of ϵ (which cannot occur physically, of course) is predicted in the process of the calculation leading to sudden increase in the predicted wake width and decrease in the total pressure loss.

Senoo and Ishida [4] sought the major cause of the wake decay in vaneless diffusers by changing the wall roughness. They expected that if decay of the jetwake asymmetry was mainly achieved by the reversible process, the total pressure loss was mainly due to the wall friction and the influence of wall roughness on the total pressure loss would be significant. The time average prediction based on the D-S model agreed well with the experimental data for both smooth and rough diffusers. From this fact and predicted total pressure losses at radius ratio, $R = 1.8$, (shown in Table 3 reference [4] and reproduced as Table 2 in this paper), they concluded that the major part of the large total pressure loss was due to wall friction. This was misleading because in the cases they examined the flow was mixed out at about $R = 1.3$ and only the wall friction contributed to the total pressure loss downstream of this. It was therefore natural that the loss by the wall friction would be the major part of the overall pressure loss at $R = 1.8$. In fact it is the difference between the wall friction losses of the nonuniform flow for the D-S model and the corresponding wall friction loss of the axisymmetric flow which should be compared for various values of interface shear. This comparison is shown in Table 3. (The results are quite different from those by Senoo and Ishida [4] and the reason for this has not been clarified.) For a constant value of the interface shear coefficient the contribution of the wall friction to mixing loss increases as the wall friction coefficient is increased, while the contribution of the shear between jet and wake decreases. Nevertheless the interface shear does produce a large proportion of the total loss and as the interface shear coefficient is increased to $\zeta = 0.3$, keeping C_f constant at 0.005, the mixing loss by the interface shear becomes much larger than that by the wall friction, which is meanwhile dramatically reduced.

Conclusion

The papers by Dean and Senoo [1], Johnston and Dean [2] and Senoo and Ishida [4] were re-examined. From this, from the mixing process analysis of one-dimensional channels and from the relation between relative and absolute total pressure in vaneless diffusers, the following conclusions were obtained.

1 The large loss near the diffuser inlet for non-uniform flow is due to both the wall friction and the interface shear between jet and wake, both of which contribute to mixing.

2 Close to the inlet of vaneless diffusers the reversible work exchange has a significant role in mixing out the non-

uniform pattern from a rotating impeller, as shown by comparison with the stationary jet and wake pattern. Nevertheless it is the shear forces at the wall and interface which play the largest part in mixing out the flow in the rotating case.

3 Because wall and interface shear dominate the mixing of the flow, the Johnston and Dean model predicts total pressure loss in vaneless diffusers close to that based on the Dean and Senoo model when the distorted flow pattern is rotating for a wide range of inlet flow conditions. The losses are very different for the two models where the flow is non-rotating, and this can be understood by considering a one-dimensional analogy.

Acknowledgment

The author would like to thank Dr. N. A. Cumpsty of the

Cambridge University Engineering Department for much valuable advice and many helpful suggestions. The comments of Professor Senoo on an early draft, which have played an important part in this work, are gratefully acknowledged.

References

- 1 Dean, R. C., and Senoo, Y., "Rotating Wakes in Vaneless Diffusers," *ASME Journal of Basic Engineering*, Vol. 82, Sept. 1960, pp. 563-574.
- 2 Johnston, R. P., and Dean, R. C., "Losses in Vaneless Diffusers of Centrifugal Compressors and Pumps," *ASME Journal of Basic Engineering*, Vol. 88, 1966, pp. 49-60.
- 3 Dean, R. C., "On the Necessity of Unsteady Flow in Fluid Machines," *ASME Journal of Basic Engineering*, Vol. 81, 1959, pp. 24-28.
- 4 Senoo, Y., and Ishida, M., "Behaviour of Severely Asymmetric Flow in a Vaneless Diffuser," *ASME Journal of Engineering for Power*, Vol. 97, 1975, pp. 375-382.
- 5 Inoue, M., "Radial Vaneless Diffusers: A Re-Examination of the Theories of Dean and Senoo and of Johnston and Dean," Cambridge University Engineering Department Report Turbo/TR 86, 1977.

A Stall Margin Design Method for Planar and Axisymmetric Diffusers

R. C. Strawn
Research Assistant.

S. J. Kline
Professor, Fellow ASME
Thermosciences Division,
Department of Mechanical Engineering,
Stanford University,
Stanford, Calif. 94305

An inverse design method is presented which gives the user control over stall margin, or distance from detachment, along the walls of planar and axisymmetric diffusers. It is proposed that optimum diffuser designs have continuous incipient detachment along their wall boundary layers. This hypothesis is supported by experimental and computational results plus physical arguments concerning the detachment process. Several computed optimum planar diffuser shapes are presented and discussed. For short diffusers with healthy inlet boundary layers, these optimum shaped wall units can have significantly higher pressure recovery than their straight-wall counterparts (up to 40 percent higher C_p in certain favorable cases). In most cases, however, the gains from wall contouring are small when compared to optimum straight-wall designs. This paper differs from earlier discussion in two ways: (i) it employs an improved physical model and correlation of detachment, and (ii) it uses improved boundary layer procedures based on (i).

Introduction

The usual purpose of a diffuser is to decelerate a fluid flow, recovering as much as possible of the entering momentum. Often this design objective also requires that the diffuser exit velocity profiles be uniform and steady, or that the pressure recovery occur at either fixed length or area ratio.

In all of these cases, the goal of a high performance design is limited primarily by boundary layer detachment. Maximum pressure recovery typically occurs for diffuser geometries in which the wall boundary layers at exit are very close to detachment. If design is pushed beyond detachment, however, large regions of stalled fluid may accumulate in the flow passage. These stalls are relatively stagnant regions of fluid which effectively block the through flow, thereby reducing recovery markedly and creating asymmetric or very peaked velocity profiles. Gross unsteadiness may also occur.

The key to an effective diffuser design thus lies in the ability to predict whether flow detachment will occur, and to control its occurrence through appropriate design modifications. The design method presented in this paper attacks this problem directly by giving the designer control over the "stall margin" in the flow field. Stall margin is defined here as the proximity of a boundary layer to detachment in a newly defined metric. The designer is able to specify stall margin along the walls at the outset. An inverse procedure is then used to compute the required geometry for a given stall margin. The method is applicable for incompressible flows which have thin, turbulent inlet boundary layers and uniform core velocities. Although developed here for planar and axisymmetric cases, the method should extend to external flows (2-D airfoils) and annular diffusers as well.

This paper is divided into two sections. The first section

presents the basic stall margin method. It is an inverse method based on the direct methods of Bardina et al. [1] and Lyrio et al. [2]. The second section of this paper uses the stall margin concept to develop a method for computing wall contours that give optimum recovery for fixed non-dimensional length. For short units with comparable inlet conditions, these optimally shaped units show a predicted performance that can be substantially better than that of a straight-wall diffuser. In a few favorable cases, the increase in C_p is close to 40 percent, but in most cases the gains from wall contouring are small when compared to optimum straight-wall designs.

Characterization of Stall Margin

Kline, Bardina, and Strawn [3] have shown that an approximately linear relation exists between the two parameters h and Λ for two-dimensional turbulent boundary layers close to detachment. In terms of these shape parameters, Coles' wall-wake correlation [16] can be integrated to yield:

$$\frac{h}{\Lambda} = 1.5 + .179 \frac{V_T}{\Lambda} + .321 \left(\frac{V_T}{\Lambda} \right)^2 \quad (1)$$

where V_T is at most a weak function of Re_{δ^*} .

$$V_T = \frac{1 - 2\Lambda}{\ln(KRe_{\delta^*}) + \ln\left(\frac{|V_T|}{\Lambda}\right) + .05} \quad (2)$$

Moreover, as V_T approaches zero, \bar{C}_f will also go to zero; hence near detachment (or reattachment) equation (1) reduces to $h = 1.5 \Lambda$.

Kline et al. [3] also showed that the point $\Lambda = .42$ (and $h = .63$) correlates the best available data for incipient separation in boundary layer flows without strong curvature, body forces, or suction/blowing. Similarly, the point $\Lambda = 0.5$ ($h =$

Contributed by the Fluids Engineering Division of THE AMERICAN SOCIETY OF MECHANICAL ENGINEERS and presented at the Winter Annual Meeting, Phoenix, Ariz., November 14-19, 1982. Manuscript received by the Fluids Engineering Division, February 16, 1982. Paper No. 82-WA/FE-8.

0.75) correlates full detachment ($\bar{C}_f = 0$) for the same class of flows.

These two correlations, plus the linear nature of the $h - \Lambda$ relation of equation (1) for flows approaching detachment, suggest the use of either h or Λ as a stall-margin parameter. For the design method of this paper, Λ has been chosen as a stall-margin parameter, since its use considerably simplifies the analysis. However, Λ is a difficult quantity to measure, since it involves the estimation of the boundary layer thickness δ . This problem can be avoided by noting that the correlations of equations (1) and (2) define Λ in terms of the quantities h and Re_{δ^*} , which can be more accurately measured in the laboratory. Further discussion concerning experimental measurement of Λ is given by Kline et al. [3].

In terms of the parameter Λ , stall margin (S_m) can be characterized as: $S_m = 0.42 - \Lambda$. It is worth noting that the bounds on both Λ and h are 0-1, and that the linear relation between h and Λ near detachment implies that the choice of Λ or h is one of convenience rather than accuracy.

Method of Computation: General Equations

The design method presented here is basically an inversion of the diffuser prediction schemes of Lyrio et al. [2] and Bardina et al. [1]. It consists of two ordinary differential equations coupled with three algebraic relations. The equations presented below apply to the case of a two-dimensional planar diffuser. A similar set of equations can be written for the axisymmetric case. Details are presented in reference [19].

The two differential equations consist of the Von Kármán momentum integral equation (3) and the definition of boundary layer entrainment (4).

$$\frac{d\theta}{dx} + (2+H) \frac{\theta}{U_\infty} \frac{dU_\infty}{dx} = \frac{\bar{C}_f}{2} \quad (3)$$

$$\frac{1}{U_\infty} \frac{d}{dx} [U_\infty(\delta - \delta^*)] = E \quad (4)$$

The first of the algebraic relations is a one-dimensional continuity relation for internal flow (5).

$$Q = U_\infty(1 - B)W \quad (5)$$

It is implemented here as a radial source flow. Its origin is shifted so that the potential flow is always tangent to the diffuser walls. Equation (5) can be differentiated and solved simultaneously with equations (3) and (4).

The second algebraic relations is the entrainment correlation of Lyrio et al. [2]. Lyrio has shown that this correlation works at least as well for adverse pressure gradient

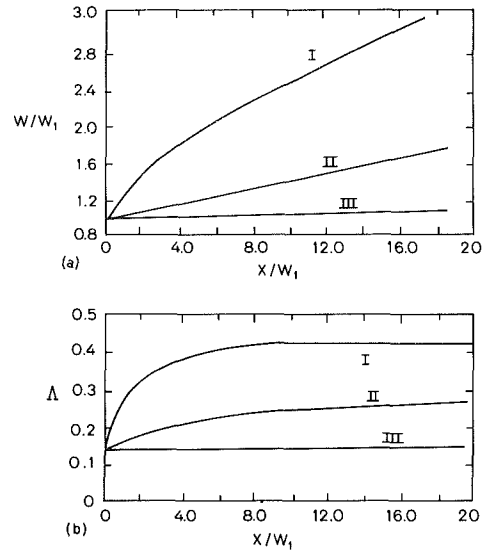


Fig. 1 Some sample geometries for specified Λ distributions

flows as the more commonly used Bradshaw correlation [17]. Lyrio's correlation is also much easier to implement computationally. The nondimensional entrainment rate given by Lyrio et al. [2] is:

$$E = .0083(1 - \Lambda)^{-2.5} \quad (6)$$

The final algebraic relation is the $h - \Lambda$ correlation of equations (1) and (2). For rapid computation, the implicit relation for V_T of equation (2) can be replaced by an explicit form (7) of essentially equal accuracy, as shown by Lyrio et al. [2]:

$$V_T = (.44)(1 - 2\Lambda)^{.885} \left(\frac{\Lambda}{Re_{\delta^*}} \right)^{.115} \quad (7)$$

With suitable algebraic manipulation, equations (1) through (7) can be combined to yield a system of two ordinary differential equations. The coefficients a_{11} , a_{12} , a_{21} , b_1 , b_2 are defined in Appendix A.

$$a_{11} \frac{d\bar{B}}{dx_N} + a_{12} \frac{dW_N}{dx_N} = b_1 \quad (8)$$

$$a_{21} \frac{d\bar{B}}{dx_N} = b_2 \quad (9)$$

These two ordinary differential equations are then solved with the integration routine ODE, which is fully described in

Nomenclature

AR = local passage width divided by throat width
 B = passage blockage for 2-D flow = $(\delta_{\text{upper}} + \delta_{\text{lower}}^*)/W$
 \bar{B} = passage half blockage = $B/2$
 \bar{C}_f = friction coefficient = $2\bar{\tau}_w/\rho U_\infty^2$
 C_p = pressure coefficient = $(P - P_1)/1/2\rho U_\infty^2$
 C_p^* = maximum pressure recovery for a straight-wall diffuser, at fixed nondimensional length
 E = nondimensional entrainment rate
 h = shape factor = $(H - 1)/H$
 H = shape factor = δ^*/θ
 K = Von Karman constant = 0.41
 L = total centerline diffuser length
 P = pressure
 Q = volume flow rate
 R = diffuser radius for axisymmetric flow
 Re_{δ^*} = displacement thickness Reynolds number = $U_\infty \delta^*/\nu$
 S_m = stall margin = $0.42 - \Lambda$
 U_∞ = boundary layer edge velocity

u_τ = shear velocity = $(\text{sign } \tau_w) \sqrt{|\tau_w|/\rho}$
 V_T = nondimensional shear velocity = u_τ/KU_∞
 W = passage width for 2-D internal flow
 x = distance along diffuser wall measured from throat
 δ = boundary layer thickness
 δ^* = boundary layer displacement thickness
 θ = boundary layer momentum thickness
 ρ = fluid density
 Λ = shape factor = δ^*/δ
 ν = kinematic viscosity
 μ = dynamic viscosity
 τ_w = wall shear stress
 2θ = total included angle for a straight-wall diffuser
 $(\bar{\quad})$ = denotes time-averaged quantity

Subscripts

1 = denotes diffuser inlet quantity
 N = denotes quantity normalized on diffuser inlet width

reference [4]. This numerical solution provides for excellent user control of stepwise errors. Typical computation times for a complete diffuser calculation are less than one CPU second on an IBM 3033 machine.

The only difference between the method of this paper and the method of Lyrio et al. [2] is in the choice of dependent and independent variables. Lyrio et al. [2] treat the diffuser geometry (W) as a known quantity and solve for the boundary layer parameter Λ . The design method of this paper treats the distribution of Λ in the flow field as a known quantity and solves for $W(x)$.

Results From the Design Method

Since no data yet exist for optimum shapes or the wall shapes generated below, a direct comparison with data to validate the method is not yet possible. However, the present design method is a mathematical inversion of the method developed by Lyrio et al. [2]. Thus an adequate test of whether the stall margin method predicts realistic diffuser flows can be found from the results of Lyrio et al. [2]. Their results demonstrate the ability to predict the diffuser flows of Ashjaee et al. [5], Carlson and Johnston [6], Chui and Kline [7], and Reneau et al. [9] to within the uncertainty of each data set. Together, these data sets cover three diffuser flow regimes: unstalled flow, transitory stall, and fully developed stall. Moreover the results of Ashjaee et al. [5] have uncertainty intervals one order lower than any other known data. The agreement of Lyrio's results with these data, particularly in the difficult transitory stall regime, leaves little room for improvement. Given these results, it is expected that the present method will have similar accuracy when used in the inverse, stall margin design mode. This accuracy of computation is important to the present purposes, as we shall show below.

Various possible planar shapes generated by the stall margin inverse method are shown in Fig. 1(a). Figure 1b shows the distribution of stall margin (Λ) in the flow field, and Fig. 1(a) shows the diffuser geometries that result from these distributions of Λ . Curve I in Fig. 1 represents a high-performance design, since the wall boundary layers are held at incipient detachment for most of the diffuser length. This design is a perilous one, since the boundary layers will be very close to the full-detachment condition. A significant change in diffuser inlet conditions owing to flow unsteadiness or to design or construction inaccuracy could lead to appreciable stall, with subsequent large degradation in performance.

Curve II in Fig. 1 represents a much more conservative design. The stall margin is significant throughout the length of the diffuser, and the designer could safely assume that stall will not be a problem in this design. The price paid for such a conservative design is a lower pressure recovery than that shown by Curve I.

The results shown in Fig. 1 are meant to be a demonstration of how the present design method works. It is a simple matter to generate a large number of diffuser shapes based on specific inlet conditions and desired stall margin. By using straightforward geometric relations, diffuser wall shapes can be converted from the wall coordinates shown in Fig. 1(a) to appropriate Cartesian coordinates. Details are given in reference [19]. Final decision on which design is best for a particular application will depend largely on the tradeoff between safety, that is, stall margin, and pressure recovery. Another factor to be considered is the construction cost of a curved-wall diffuser versus that of a straight-wall unit.

Computed wall shapes from the axisymmetric stall margin method are very similar to those generated for planar geometries. In both cases, a high-performance design consists of a rather rapid expansion just beyond the diffuser throat, followed by a straight-wall geometry of reduced opening angle.

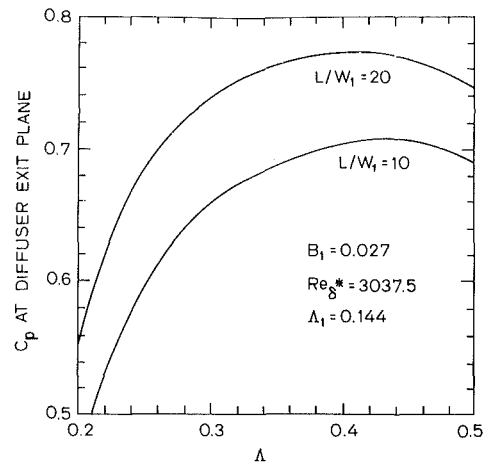


Fig. 2 Computed C_p versus constant value of Λ along diffuser walls

In general, remarks concerning the design of high-performance planar diffusers also apply for the axisymmetric cases. This paper focuses its attention on the planar units in regard to numerical results and comparison to experiments. Qualitatively, the same results are seen for axisymmetric cases, and they will not be discussed in detail here.

A Criterion for Optimum Diffuser Design

One demonstration of the power of a design method based on stall margin is in its ability to characterize an optimum performance condition. Maximum pressure recovery in diffuser flows occurs when the wall boundary layers are close to detachment. Specification of stall margin gives the designer direct control over the entire detachment process. It seems reasonable that some optimum distribution of stall margin (Λ) throughout the flow maximizes pressure recovery at fixed diffuser length.

The experimental observations of Ashjaee et al. [5] contain data that can be used to suggest this optimum distribution. In particular, quantitative data are reported for flow-direction intermittency in the boundary layers. As noted by Kline et al. [3], this time-averaged percent forward-flow measurement is a measure of boundary layer detachment state.

Ashjaee et al. [5] observed that peak pressure recovery occurs when small amounts of backflow are present along both side walls. This observation is supported by results from several earlier studies [8, 9, 10]; however the results of Ashjaee et al. [5] are more detailed and precise in their nature. The flow field at maximum recovery corresponds to a region between line a-a and the line of appreciable stall in the flow regime classifications of Fox and Kline [8]. Another observation from Ashjaee et al. [5] is that, "At maximum pressure recovery, the mean shear stress does not drop to zero at any point on either side wall." Using these two observations, it is reasonable to characterize an optimum straight-wall diffuser design as having incipient detachment at its exit plane.

This same result can be applied to the optimization of pressure recovery for a curved-wall diffuser. An optimum design should have incipient detachment ($\Lambda = 0.42$) at its exit. The question then becomes, "What distribution of stall margin, $\Lambda(x)$, will lead to maximum pressure recovery?" A one-parameter distribution of Λ along the diffuser walls is given by equation (10).

$$\Lambda(x) = 0.42 - (0.42 - \Lambda_1)(1 - x/L)^n \quad (10)$$

Thus, the value of $\Lambda(x)$ varies from its inlet value to a value representing incipient detachment at the diffuser exit ($\Lambda = 0.42$). In all cases, computed results indicate that maximum pressure recovery occurs for a large value of n (i.e., $n > 50$). Thus, the computational results indicate that maximum

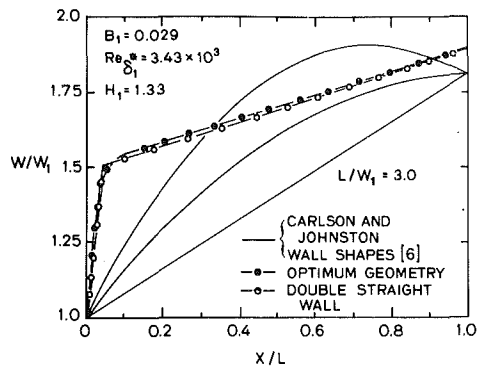


Fig. 3 Comparison of computed optimum geometry to the wall shapes of Carlson and Johnston [6] for $L/W_1 = 3.0$

pressure recovery for curved-wall planar diffusers occurs when the boundary layers on both walls are continuously maintained at incipient detachment. We call this the incipient detachment hypothesis.

Experimental support of this hypothesis is given by the data of Stratford [11]. Stratford's results indicate that minimum energy loss in a diffuser occurs when the skin friction is held at a low value all along the wall. Stratford [11] originally stated that the skin friction was zero all along the wall; however, Sandborn and Kline [12] reexamined Stratford's results and showed that C_f was not zero but rather about 10 percent of the equivalent "flat-plate value." Moreover, comparison of Stratford's data with the Sandborn-Kline criterion for incipient detachment [12] shows that Stratford's experimentally determined performance maximum has its wall boundary layer maintained near incipient detachment for roughly 70 percent of its length.

The same result is achieved by physical reasoning regarding boundary layer blockage and its effect on pressure recovery. Kline et al. [3] show that beyond $\Lambda = 0.42$, δ^* rises rapidly, and an immediate adverse effect on $C_p(x)$ then occurs.

In order to further examine the incipient detachment hypothesis, a numerical test was carried out. The results appear in Fig. 2. In this test, the boundary layers along the diffuser walls were continuously maintained at various values of stall margin. Figure 2 shows that the maximum value of C_p is insensitive to Λ in the neighborhood of incipient detachment ($\Lambda = 0.42$). Specifically, the variation in C_p over the range $0.40 < \Lambda < 0.44$ is less than 0.01 for both $L/W_1 = 10$ and $L/W_1 = 20$. Presumably, a value of Λ in the range $0.38 < \Lambda < 0.40$ might be a good design compromise for some purposes. This range gives: some residual stall margin, reduced unsteadiness compared to higher values of Λ , and only an insignificant decrease in C_p .

It should be noted that the zero skin-friction diffuser ($C_f = 0$, $\Lambda = 0.5$) does not give optimum performance. Zero skin-friction design has been previously suggested by Stratford and Tubbs [13]. However, Kline et al. [3] show that many older works confuse incipient and full detachment both in data and in computation, and, as noted above, the physical picture adduced by Kline et al. [3] suggests that incipient detachment is the appropriate criterion.

Given these results, we can tentatively accept the incipient detachment hypothesis and employ it in the present inverse procedure to examine optimum curved-wall shapes and compare them to results for straight-wall units.

Hokenson [14] also suggests that the incipient detachment condition is required for optimum diffuser performance. His design method uses a power-law distribution of C_f which drops very rapidly from its initial value to zero at the diffuser exit. Although this is clearly an improvement on the $\bar{C}_f = 0$ design, such a specified \bar{C}_f distribution lacks the direct correspondence to "degree of detachment" that is provided by the stall margin parameter S_m .

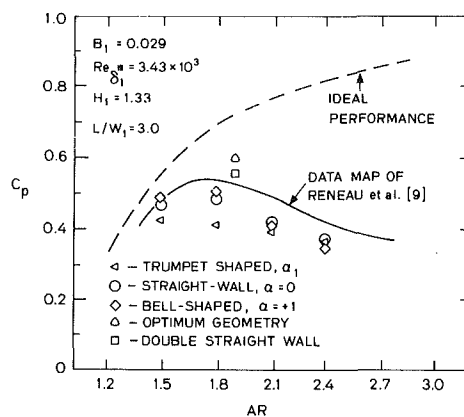


Fig. 4 Comparison of predicted performance at $L/W_1 = 3.0$ to the data of Carlson and Johnston [6] and Reneau et al. [9]

Results From Computed Optimum Planar Diffuser Shapes

Figures 3 and 4 show some calculated results for optimally configured planar diffusers. The inlet conditions were taken from the experiments of Carlson and Johnston [6]. The comparison case from the Carlson and Johnston data in Fig. 3 was chosen from the unit whose final area ratio yielded the highest pressure recovery. Additional comparisons of computed wall shapes to those of Carlson and Johnston [6] are given in Reference [19]. It is interesting to note that the curved-wall diffuser shapes tested experimentally by Carlson and Johnston [6] are distinctly different from the optimum geometries generated by the stall margin method.

The wall shape shown in Fig. 3 shows a number of trends that are common to all of the optimum diffuser designs. First, it is clear that the maximum pressure gradient should be imposed on the flow when the boundary layers are in their "healthiest state." Healthy boundary layers can be characterized through the stall margin concept as those which are far from detachment. This argument has been made much earlier by others, notably H. Eichenberger [18] and Reneau et al. [9]. Reneau et al. [9] based their reasoning on an examination of terms in the momentum integral equation.

A second observation from Figs. 3 and 4 is that the performance of optimum curved-wall shapes can be closely approximated by two straight-wall sections. This result is general for all of the optimum planar diffuser shapes. Nishi [15] used a similar idea in combining two straight-wall conical sections. Nishi's experimental results indicate an improved performance over a single straight-wall unit (the same C_p is achieved for 10 percent shorter length).

Figure 4 shows that the use of two straight-wall sections results in a calculated pressure recovery just slightly lower than the maximum attainable with an optimum curved-wall design. However, the pressure recovery is significantly higher than that which can be obtained with a single straight-wall unit. Since curved-wall shapes are expensive to manufacture, particularly in planar units, this observation suggests obvious practical possibilities when short diffusers are mandated by design constraints.

The results shown in Figs. 5 and 6 address the more general question of whether optimum curved-wall units can achieve a significantly higher pressure recovery than straight-wall units of the same L/W_1 . In these figures, data and computations for C_p^* in straight-wall diffusers are compared to the optimum pressure recovery as calculated by the present inverse method. C_p^* denotes the maximum pressure recovery at fixed length for straight-wall diffusers. Experimental data in Figs. 5 and 6 are taken from the data maps of Reneau et al. [9]. Computed C_p^* results are taken from the calculations or Lyrio et al. [2]. In

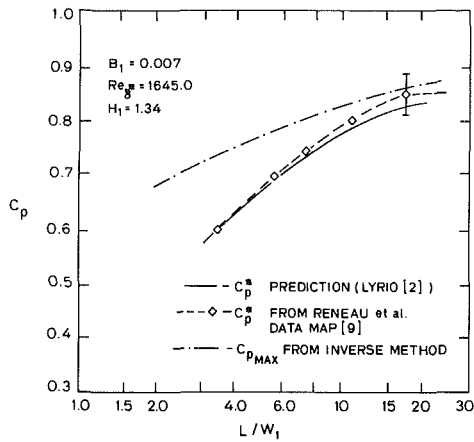


Fig. 5 Comparison of C_p^* from Reneau data map to $C_{p,max}$ from computation (low inlet blockage)

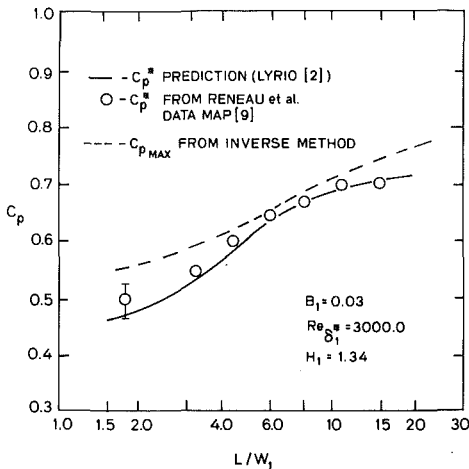


Fig. 6 Comparison of C_p^* from Reneau data map to $C_{p,max}$ from computation (high inlet blockage)

both figures, the computed optimum pressure recovery for the curved-wall diffusers is above the C_p^* line for the straight-wall units. Additional comparisons to the data maps of Reneau et al. [9] are given in reference [19].

The advantage of an optimum curved-wall diffuser is most evident for short diffusers ($L/W_1 < 4$) with low inlet blockage. If a long diffuser is used ($L/W_1 > 8$), a straight-wall unit can be expected to perform almost as well as an optimum curved-wall shape. Figures 5 and 6 indicate that, for short diffusers ($L/W_1 < 4$) and low values of B_1 , pressure recovery can be significantly increased if an optimum curved-wall shape is used instead of a straight wall. In Fig. 5, a 25 percent increase in C_p is observed for $L/W_1 = 3$ and $B_1 = 0.007$. For longer units and higher B_1 , little gain is realizable. The net gains are such that it is dubious if earlier solutions of this problem employed detachment models of sufficient accuracy to give credible results.

Discussion

Any practical design would have to be more conservative than a computed optimum. The diffuser design method presented in this paper allows one to choose a margin of safety suitable to a given design purpose. The designer is given *direct* control over the tradeoff between increased pressure recovery and the proximity of a boundary layer to detachment. Thus, in some applications, a designer can choose a final pressure recovery which is below the optimum value in order to ensure that the wall boundary layers will not detach.

In other cases, an optimum recovery can be sought where the boundary layers are very close to detachment.

If the diffuser designs such as those presented in Figs. 3-6 are to be implemented in a realistic situation, a few practical considerations must be taken into account in the final design. Most important is that Figs. 3-6 show sharp corners at the diffuser inlets. Mathematically, these sharp corners present no problems, but, physically, they may cause detachment at the diffuser throat. Corner fairing should be used in any realistic design.

This corner fairing is important when considering the high initial opening angles for the optimum wall shapes (up to $2\theta = 80$ deg). These initial regions of high opening angle are extremely short, however, typically $x/W_1 = 0.15$. Normal corner fairing should prevent detachment at the diffuser throat without significantly affecting overall performance.

Conclusions

- An inverse design method has been developed which gives the user control over stall margin along the wall in diffusers with straight centerlines and incompressible flow.
- Data to check the method directly do not exist. However, the method is a purely analytical inversion of the direct method of Lyrio et al. [2]. Lyrio's method checks all known data within their experimental uncertainties, including the particularly accurate data of Ashjaee et al. [5]. The present method can therefore be accepted as of high accuracy for the range covered by existing data, as long as a potential core exists at inlet.
- It is proposed that optimum diffusers have continuous incipient detachment along their wall boundary layers. This hypothesis is supported by: (i) results from straight-wall diffuser experiments [5, 9]; (ii) the experimental results of Stratford [11]; (iii) physical arguments based on the comments of Kline et al. [3]; (iv) results from computations using the present inverse method.
- Several optimum diffuser shapes for planar diffusers have been computed and compare favorably with the experimental results of Carlson and Johnston [6] and Reneau et al. [9]. The increase in C_p shown by an optimum curved-wall diffuser over its straight-wall counterpart can be as large as 40 percent for short diffusers ($L/W_1 < 4$) and low B_1 .
- It has been shown that performance of computed optimum curved-wall diffuser shapes can be closely approximated by a geometry consisting of two straight-wall sections. The use of two straight-wall sections makes construction easier and less expensive; no significant loss in recovery occurs even in short units.

References

- 1 Bardina, J., Lyrio, A., Kline, S. J., Ferziger, J. H., and Johnston, J. P., "A Prediction Method for Planar Diffuser Flows," *ASME JOURNAL OF FLUIDS ENGINEERING*, Vol. 103, June, 1981, pp. 315-321.
- 2 Lyrio, A., Ferziger, J. H., and Kline, S. J., "An Integral Method for the Computation of Steady and Unsteady Turbulent Boundary Layer Flows, Including the Transitory Stall Regime in Diffusers," Report PD-23, Thermosciences Div., Dept. of Mech. Engrg., Stanford Univ., Mar. 1981.
- 3 Kline, S. J., Bardina, J. G., and Strawn, R. C., "Correlation of the Detachment of Two-Dimensional Turbulent Boundary Layers," *AIAA Journal*, Vol. 21, Jan. 1983, pp. 68-72.
- 4 Shampine, L. F., and Gordon, M. K., *Computer Solution of Ordinary Differential Equations, The Initial Value Problem*, W. H. Freeman, San Francisco, 1975.
- 5 Ashjaee, J., Johnston, J. P., and Kline, S. J., "Subsonic Turbulent Flow in Plane Wall Diffusers: Peak Pressure Recovery and Transitory Stall," Report PD-21, Thermosciences Div., Dept. of Mech. Engrg., Stanford Univ., July, 1980. See also *ASME JOURNAL OF FLUIDS ENGINEERING*, Vol. 102, Sept. 1980, pp. 275-282.
- 6 Carlson, J. J., and Johnston, J. P., "Effects of Wall Shape on Flow Regimes and Performance in Straight, Two-Dimensional Diffusers," Report

PD-11, Thermosciences Div., Dept. of Mech. Engrg., Stanford Univ., June 1965.

7 Chui, G., and Kline, S. J., "Investigation of a Two-Dimensional, Fully Stalled, Turbulent Flow Field," Report MD-19, Thermosciences Div., Dept. of Mech. Engrg., Stanford Univ., Aug. 1967.

8 Fox, R. W., and Kline, S. J., "Flow Regime Data and Design Methods for Curved Subsonic Diffusers," ASME *Journal of Basic Engineering*, Vol. 84, Sept. 1962, pp. 303-312.

9 Reneau, L. R., Johnston, J. P., and Kline, S. J., "Performance and Design of Straight, Two Dimensional Diffusers," Report PD-8, Thermosciences Div., Dept. of Mech. Engrg., Stanford Univ., Sept. 1964.

10 Smith, C. P., and Kline, S. J., "An Experimental Investigation of the Transitory Stall Regime in Two-Dimensional Diffusers, Including the Effects of Periodically Disturbed Inlet Conditions," Report PD-15, Thermosciences Div., Dept. of Mech. Engrg., Stanford Univ., Aug. 1971.

11 Stratford, B. S., "An Experimental Flow with Zero Skin Friction," *Journal of Fluid Mechanics*, Vol. 5, Jan., 1959, pp. 17-35.

12 Sandborn, V. A., and Kline, S. J., "Flow Models in Boundary-Layer Stall Inception," ASME *Journal of Basic Engineering*, Vol. 83, No. 3, Sept. 1961, pp. 317-327.

13 Stratford, B. S., and Tubbs, H., "The Maximum Pressure Rise Attainable in Subsonic Diffusers," *Journal of the Royal Aeronautical Society*, Vol. 69, Apr. 1965, pp. 275-278.

14 Hokenson, G., "Inverse Design of Optimal Diffusers with Experimental Corroboration," ASME JOURNAL OF FLUIDS ENGINEERING, Vol. 191, Dec., 1979, pp. 478-482.

15 Nishi, M., "Discussion of 'Inverse Design of Optimal Diffusers with Experimental Corroboration,'" by G. Hokenson, ASME JOURNAL OF FLUIDS ENGINEERING, Vol. 102, Mar. 1980, pp. 121-124.

16 Coles, D. E., "The Law of the Wake in the Turbulent Boundary Layer," *Journal of Fluid Mechanics*, Vol. 1, 1956, pp. 191-226.

17 Bradshaw, P., Ferriss, D. H., and Atwell, N. P., "Calculation of Boundary Layer Development Using the Turbulent Energy Equation," *Journal of Fluid Mechanics*, Vol. 28, Part 3, 1967, pp. 593-616.

18 Eichenberger, H., unpublished notes, circa 1955.

19 Strawn, R. C., and Kline, S. J., "A Stall Margin Design Method for Planar and Axisymmetric Diffusers," Report PD-25, Thermosciences Division, Dept. of Mechanical Engineering, Stanford University, Aug. 1981.

APPENDIX A

Coefficients for Equations (8) and (9)

$$a_{11} = \frac{1}{\bar{B}} + \left(\frac{3-2h}{1-h} \right) \left(\frac{2}{1-2\bar{B}} \right) + \frac{C_2}{\bar{B}(1-2\bar{B})(1-h)}$$

$$a_{12} = \frac{1}{W_N} \left[1 - \frac{3-2h}{1-h} \right]$$

$$b_1 = \left(\frac{C_1}{1-h} \right) \frac{d\Lambda}{dx_N} + \frac{K^2 V_T^2}{(1-h)\bar{B}W_N}$$

$$a_{21} = W_N \left(\frac{1-\Lambda}{\Lambda} \right) \left(\frac{1}{1-2\bar{B}} \right)$$

$$b_2 = E + \frac{W_N \bar{B}}{\Lambda^2} \frac{d\Lambda}{dx_N}$$

where

$$C_2 = 0.115 V_T \left(0.179 + 0.642 \frac{V_T}{\Lambda} \right)$$

$$C_1 = 1.5 - 0.321 \left(\frac{V_T}{\Lambda} \right)^2 + \frac{C_2}{0.115} \left(\frac{0.115 - 2\Lambda}{\Lambda(1-2\Lambda)} \right)$$

J. M. Kuhlman
Associate Professor.
Mem. ASME

L.-C. Chu
Research Assistant.

Department of Mechanical Engineering and
Mechanics,
Old Dominion University,
Norfolk, Va. 23508

Reynolds Number Effects on the Nearfield Mean Characteristics of a Laboratory Model Thermal Plume

Laboratory model data are presented for the three dimensional time averaged thermal characteristics of a buoyant rectangular surface thermal plume in a crossflow. Plume trajectories and widths, as determined from dye studies and thermocouple measurements, and isotherm contours have been obtained for internal Froude numbers ranging from 0.79-1.3, for crossflow-to-jet velocity ratios of 0.56 and 1.13, at a nominal Reynolds number of 20,000 and a Froude number of 0.058. These data are compared with earlier model studies at lower Reynolds number, where a surprisingly large effect of Reynolds number upon buoyant jet development has been found.

Introduction

Recent investigations of environmental impact assessment for various means of waste heat rejection from large powerplants (e.g., cooling towers, cooling ponds, submerged diffusers, and once-through surface discharges) have indicated that the least permanent overall negative ecological impact may be caused by the surface discharge [1]. This finding is contrary to early studies and current Federal regulations, which favor the use of cooling towers or cooling ponds [2].

These findings, coupled with the great difficulty of obtaining reliable field data [3-5], and the less than completely satisfactory predictive capability of current plume numerical or theoretical models [5-10], motivated the current study of the mean characteristics of a laboratory model of a rectangular buoyant surface jet entering a uniform crossflow at a moderately high nominal jet Reynolds number of $Re=20,000$. Comparison of the current results with data at lower Reynolds number [11-14] allows investigation of the influence of Reynolds number on mean plume characteristics.

Quantification of the effects of variation of Reynolds number upon model thermal plume development is essential to the determination of the usefulness of laboratory model data for predicting full scale plume behavior. Such prototype thermal plumes typically operate at Reynolds number values one or two orders of magnitude larger than values obtainable in the laboratory. While it has commonly been assumed that free turbulent shear layers are relatively insensitive to Reynolds number above a critical Re value, certainly extrapolation of model data over such a wide range of Reynolds

numbers would not be prudent, unless at least over the range of Re values obtainable in the laboratory there is clear evidence that the mean buoyant jet behavior is independent of Re .

Also, model thermal plume data which includes velocity and turbulence data may be useful for calibration of theoretical plume models [8-10], as well as providing insight into the effects of buoyancy upon the plume turbulence field, and hence upon plume mixing [15-17]. The present study is the initial phase of a planned investigation of the turbulence characteristics of a model buoyant surface jet in a crossflow. This paper summarizes results presented in detail by Kuhlman [18], and in the thesis by Chu [19], where the report by Kuhlman gives all tabulated mean temperature data and dimensional reference quantities. Discussion of considerations necessary for the design of thermal-hydraulic laboratory models has been given by Durgin [20].

Previous Work

Before presenting the present results, a brief survey of other studies of Reynolds number effects upon the mean behavior of jets will be presented. A more complete discussion has been given in the data report by Kuhlman [18]. As discussed therein, it has often been assumed that jet behavior is independent of Reynolds number for Re values larger than one or two thousand. However, often for more complicated jet flows, with buoyancy, crossflow and free surface effects, or rectangular geometries, mean jet behavior varies with Re up to values on the order of tens of thousands. Early studies of Reynolds number effects have been summarized by Chen and Rodi [21] for vertical buoyant jets with no crossflow. Ricou and Spalding [22] found jet entrainment to be a function of Reynolds number for $Re < 25,000$ for a simple non-buoyant axisymmetric air jet. In contrast, Reister et al. [23] found no

Contributed by the Fluids Engineering Division and presented at the Joint Applied Mechanics, Fluids Engineering, and Bioengineering Conference, Boulder, Colo., June 22-24, 1981, of THE AMERICAN SOCIETY OF MECHANICAL ENGINEERS. Manuscript received by the Fluids Engineering Division, June 12, 1981. Paper No. 81-FE-7.

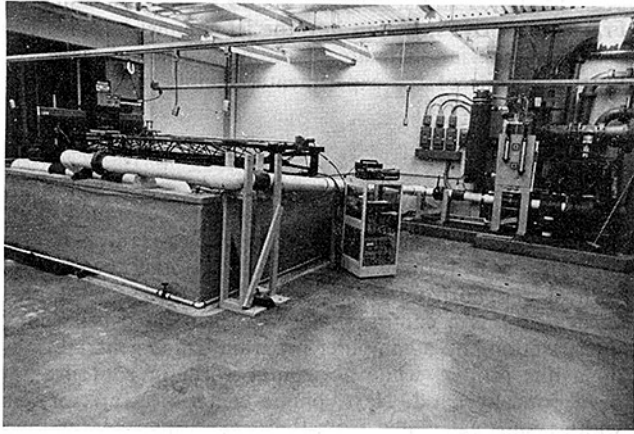


Fig. 1 Experimental facility

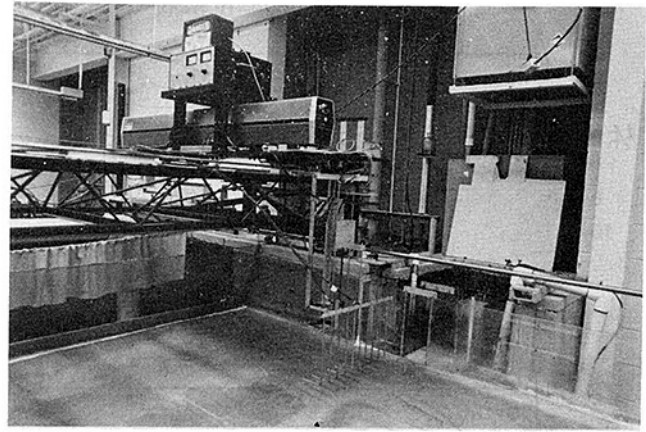


Fig. 2 Closeup view of traversing mechanism, thermocouple rake, and clear plastic thermal plume channel

noticeable effect of Reynolds number in the far field of a submerged, circular, buoyant jet entering horizontally into a still water basin, for $2000 \leq Re \leq 20,000$. Anwar [24] found a vertical, circular, buoyant jet entering still water at an internal Froude number of 4.3 to be fully turbulent for $Re > 5800$. Kuhlman and Prahl [14] found measurable effects of Reynolds number upon centerline velocity decay and width growth for a non-buoyant rectangular surface jet entering still water for Re up to 19,000. Tamai et al. [25] found dramatic Reynolds number effects upon centerline temperature decay for a buoyant, circular, surface jet entering a still basin for Reynolds numbers below 20,000. These Reynolds number effects increased as buoyancy increased, while Fr_0 was decreased from 11.3 to 2.4. In summary, a body of often contradictory studies have given values Re ranging between 2000 and 20,000 for the occurrence of a jet flow which is independent of Re . None of these studies have focused on the present, most general configuration, of a buoyant, rectangular, surface jet entering a crossflow, which is typical of the surface discharge formed using once through cooling methods.

Experimental Facility and Procedures

The flume used in the current work (Fig. 1) is rectangular, with a crossflow channel nominally 4.4m by 4.4m horizontally, and of uniform depth. The channel depth may be varied up to 0.3m. The present data have been taken at a nominal depth of 0.18m. The buoyant jet channel is rectangular, being

0.15m wide and of the same depth as the crossflow. The crossflow is fed from a concrete sump in the lab floor by a $0.1 \text{ m}^3/\text{s}$ (1500 GPM) pump to a 7m high by 0.9m diameter steel constant head tank, from which it flows to a manifold, through a series of wood baffles, screens, and a smooth half-nozzle. A smaller $0.003 \text{ m}^3/\text{s}$ (50 GPM) sump pump feeds the buoyant jet settling chamber through a 125kW electric circulation water heater with an on-off setpoint controller. The heated jet water flows through a smooth half-contraction to a jet channel of length 0.33m, and then enters perpendicular to the crossflow. Steady state operation of the facility has been achieved by simultaneous addition of colder city supply water and removal of an equal volume of warmer crossflow water from the sump. Volume flowrates have been measured using commercially calibrated rotameters, or orifice plate and flow tube sensors and mercury manometers, and have been controlled manually by globe and gate valves.

A three degrees of freedom motorized traversing mechanism (Figs. 1 and 2) which spans the flume is used to position a rake of 10 - 0.1mm diameter chromel-alumel thermocouples (Fig. 2) to determine the plume mean thermal field. Plume reference temperatures are monitored by a calibrated digital thermocouple indicator (precision = $\pm 0.06^\circ\text{C}$; accuracy = $\pm 0.17^\circ\text{C}$). Plume 3-D mean temperature distribution data have been obtained using a second calibrated digital thermocouple indicator (precision = $\pm .56^\circ\text{C}$; accuracy = $\pm 0.33^\circ\text{C}$) having an analog output, which is averaged using a DC-true RMS averaging

Nomenclature

\bar{b}_0 = jet channel width, m(ft)

e = fractional error

Fr = Froude number, $\bar{U}_j/\sqrt{g\bar{h}}$

Fr_0 = internal Froude number,

$$\bar{U}_j/\sqrt{(\Delta\rho/\rho_j)g\bar{h}}$$

\bar{g} = acceleration of gravity, m/s^2 (ft/s²)

\bar{h} = jet channel depth, m(ft)

R = crossflow to jet velocity ratio, \bar{U}_c/\bar{U}_j

Re = Reynolds number based on jet channel width, $\bar{U}_j\bar{b}_0/\bar{\nu}_j$

s = arc length along the plume centerline normalized by the initial jet width

\bar{T}_j = jet initial temperature, K(R)

\bar{T}_c = crossflow temperature K(R)

\bar{U}_c = crossflow velocity, m/s (ft/s)

\bar{U}_j = jet velocity, m/s (ft/s)

\bar{W} = ratio of crossflow channel width to jet channel width

x = coordinate along the near shoreline normalized by the initial jet width

y = coordinate normal to the shoreline normalized by the initial jet width

z = vertical coordinate normalized by jet channel depth

γ = ratio of jet channel width to depth, \bar{b}_0/\bar{h}

θ = nondimensional temperature, defined as $(\bar{T} - \bar{T}_c)/(\bar{T}_j - \bar{T}_c)$

$\Delta\rho$ = difference between crossflow and jet densities, kg/m^3 (slug/ft³)

$\bar{\nu}_j$ = jet kinematic viscosity, m^2/s (ft²/s)

$\bar{\rho}_j$ = jet density, kg/m^3 (slug/ft³)

Subscripts

j = jet

c = crossflow

Superscripts

— = denotes dimensional quantity

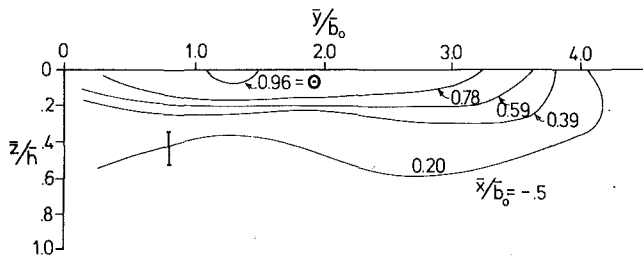


Fig. 3(a) $x = -0.5$

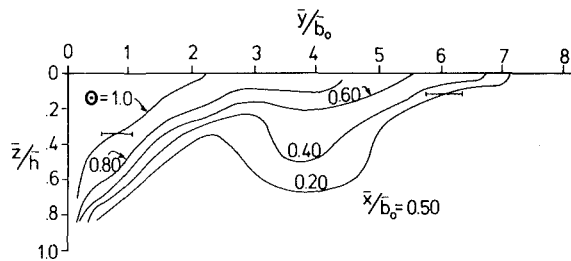


Fig. 3(b) $x = 0.5$

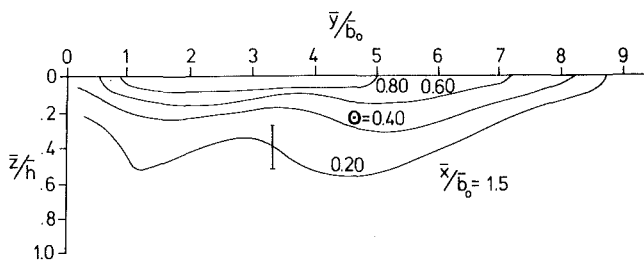


Fig. 3(c) $x = 1.5$

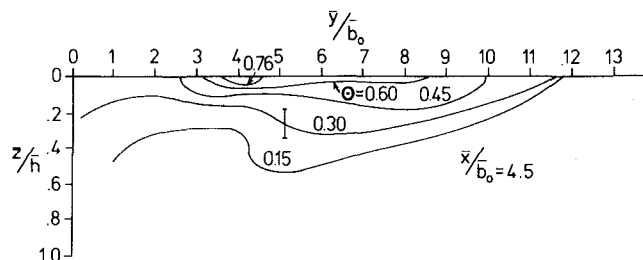


Fig. 3(d) $x = 4.5$

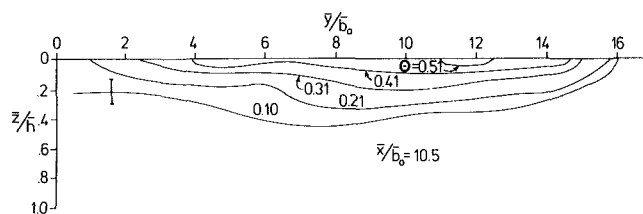


Fig. 3(e) $x = 10.5$

Fig. 3 Average isotherm contours in vertical $y-z$ planes at various x stations; $Fr_0 = 0.84$, $R = 0.56$, $Re = 22,700$, $Fr = 0.059$, $\gamma = 0.84$, $W = 27.1$

digital voltmeter. Jet and crossflow temperature versus time has been recorded to account for any slow time variation of the jet or crossflow temperatures, \bar{T}_j and \bar{T}_c , in the calculation of local average nondimensional temperatures, θ . Effects of variation of \bar{T}_j , \bar{T}_c and $\bar{T}_j - \bar{T}_c$ upon the mean values of internal Froude number and Reynolds number have

been computed statistically, to quantify any unsteadiness in Fr_0 and Re . Dye injection into the jet channel has also been used to obtain an estimate of plume width and trajectory. Further details of the experimental facility and procedures may be found in [18].

Results

In this section, examples of the time averaged plume temperature data, taken from reference [18], are first presented in the form of nondimensional isotherm contours in vertical and horizontal planes. As described in [18], these vertical isotherm contours have been generated using linear interpolation and a computer program which generates plots on a line printer, while horizontal isotherm contours have been done by hand. Next, plume centerline trajectory and width results calculated from the temperature measurements are compared with similar results obtained from dye injection studies. Finally, the isotherm data are compared with earlier data at a lower Reynolds number.

Isotherm Contours. Isotherm contours in vertical ($y-z$) planes normal to the shoreline are presented in Fig. 3 for various x stations for a rectangular surface thermal plume configuration having an internal Froude number of $Fr_0 = 0.84$, a crossflow-to-jet velocity ratio of $R = 0.56$ at a Reynolds number of 22,700 and a Froude number of 0.059. All values of Reynolds numbers for the present results have been calculated based upon the initial jet channel total width, b_0 . Jet flow rate is nominally $0.002 \text{ m}^3/\text{s}$ (33 GPM) and crossflow rate is $0.032 \text{ m}^3/\text{s}$ (500 GPM) for this jet configuration. See the appendix for discussion of the accuracy of these results. The jet channel width is 0.15m and jet channel aspect ratio, $\gamma = 0.84$, while the ratio of crossflow channel width to jet channel width, $W = 27.1$. Data presented in reference [11] (Figs. 2-5 through 2-7 in that report) have shown there is little effect of the crossflow channel width on the nearfield ($s \leq 15$) mean plume trajectory and width for values of W in this range. The x and y coordinate origins are located at the jet channel mouth in mid-channel, while $z = 0.0$ corresponds to the free surface, and $z = 1.0$ corresponds to the channel bottom.

These data show that the plume becomes wider (y increasing) as x increases, and becomes shallower (z decreasing) due to buoyancy. More interesting is the consistent appearance of a deep region of warm plume fluid relatively far from the near shoreline for all x stations except $x = 10.5$. This has been determined by dye injection to be the result of the formation of a weak vortex structure due to the action of the crossflow fluid as it turns downward to flow beneath the plume fluid very near the plume mouth. This vorticular flow persists far downstream, even after the plume fluid has turned to flow largely in the direction of the crossflow. This phenomena is similar to the dual vortex structure present in a round air jet in a crossflow [26, 27]. However, stratification of the present flow appears to damp out this secondary vortex flow before $x = 10.5$ [15, 16]. The plume temperature distribution is asymmetrical with maximum surface temperatures outboard of the plume geometric centerline.

These results have been replotted in horizontal ($x-y$) planes at various depths in Fig. 4, again at $Fr_0 = 0.84$, $R = 0.56$, $Re = 22,700$, $Fr = 0.059$, $\gamma = 0.84$, $W = 27.1$. Very little of the warm plume fluid is present below $z = 0.4$, and isotherm contour areas become much smaller as z increases. The deep region of warm plume fluid mentioned above is visible at $z = 0.2$ (Fig. 4(b)) and $z = 0.4$ (Fig. 4(c)), as a ridge of warmer fluid near the upstream edge of the plume. A similar pattern is sometimes visible in field infrared images of thermal plumes [28, 11, 12].

For completeness, additional horizontal isotherm contours

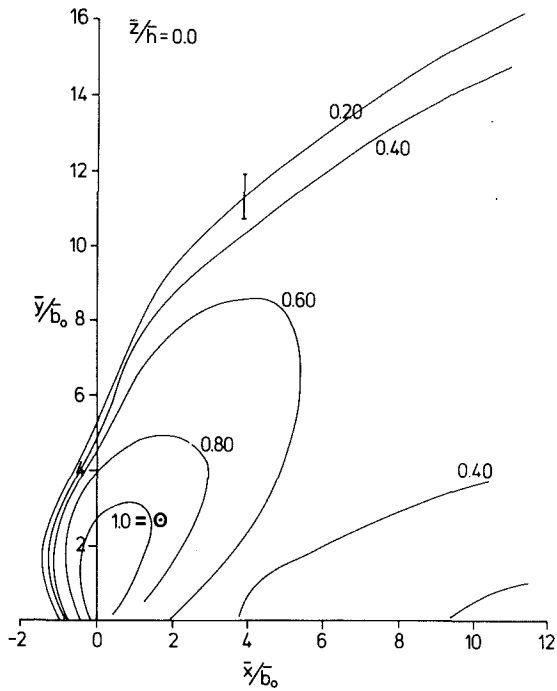


Fig. 4(a) $z=0$

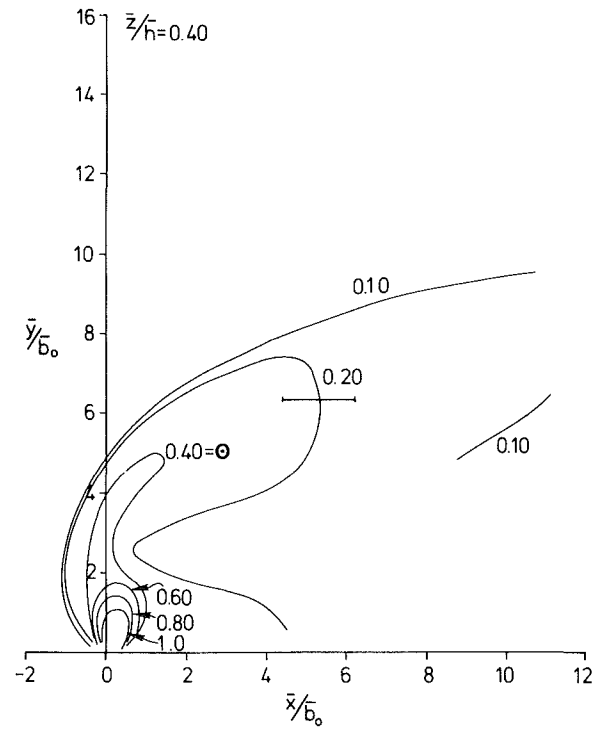


Fig. 4(c) $z=0.4$

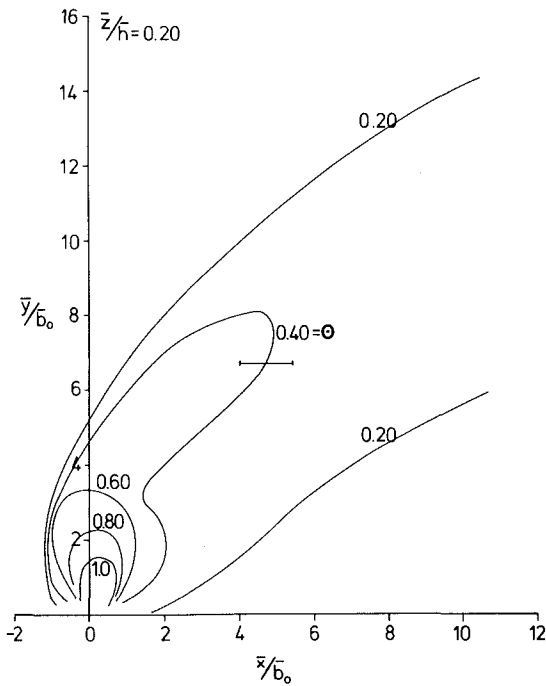


Fig. 4(b) $z=0.2$

Fig. 4 Average isotherm contours in horizontal x-y plane at various z stations; $Fr_0 = 0.84$, $R = 0.56$, $Re = 22,700$, $Fr = 0.059$, $\gamma = 0.84$, $W = 27.1$

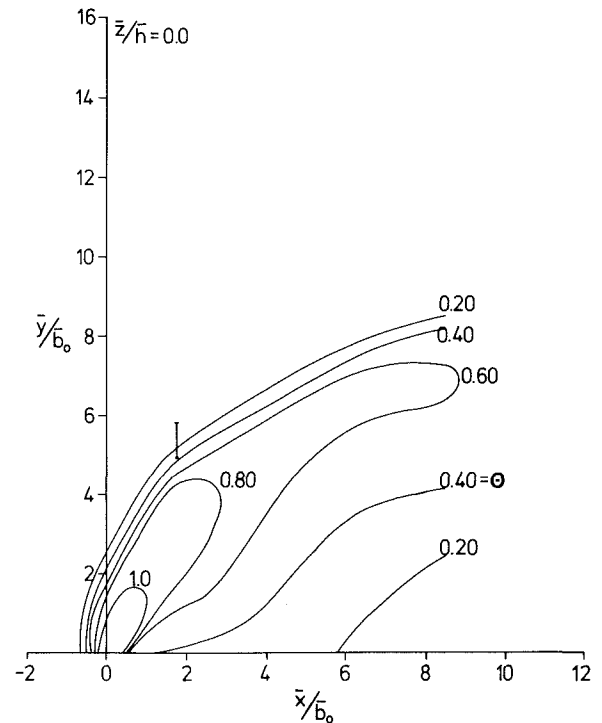


Fig. 5 Average isotherm contours in horizontal x-y plane at $z=0.0$; $Fr_0 = 1.26$, $R = 0.57$, $Re = 18,800$, $Fr = 0.058$, $\gamma = 0.84$, $W = 27.1$

near the free surface are shown in Figs. 5-7 for various values of internal Froude number and velocity ratio, all at a nominal Reynolds number of 20,000, and $Fr = .058$, $\gamma = 0.84$, $W = 27.1$. Actual values of Fr_0 , R , and Re are given on the figures and accuracy of these values is discussed in the appendix. Comparison of Figs. 4-7 shows that as R increases, the plume turns more rapidly in the direction of the crossflow, while as Fr_0 increases (buoyancy decreasing), again the plume turns more rapidly and is narrower. Vertical isotherm contours, and horizontal isotherm contours for $z \geq 0.2$, for these three additional plume configurations again reveal the presence of a vortex structure on the upstream side of the plume [18]. In all four of these plumes, dye injection has

shown the jet to be attached to the near shoreline, with a clearly visible recirculation zone. Criteria developed recently by Jirka et al. [29] indicate that for the range of velocity ratios and internal Froude numbers herein, all buoyant jets studied should be attached to the near shoreline, as well as being relatively uninfluenced by the crossflow channel bottom.

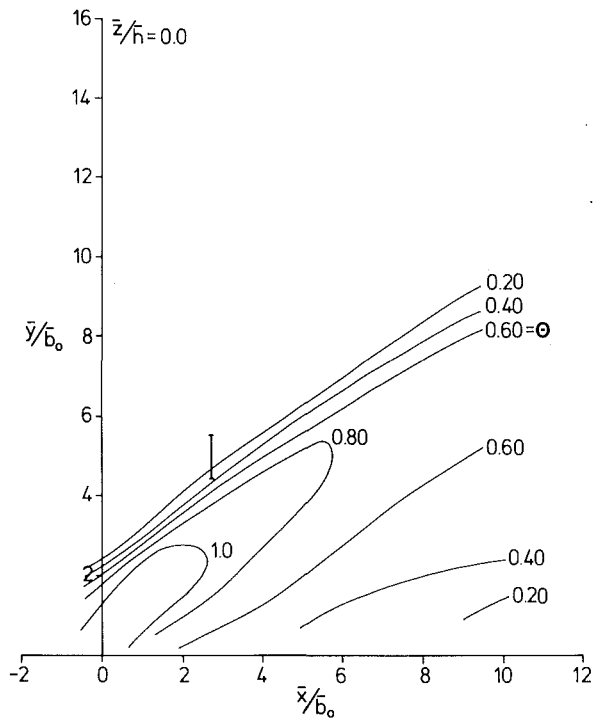


Fig. 6 Average isotherm contours in horizontal $x-y$ plane at $z=0.0$; $Fr_0 = 0.79$, $R = 1.10$, $Re = 22,700$, $\gamma = 0.059$, $\gamma = 0.84$, $W = 27.1$

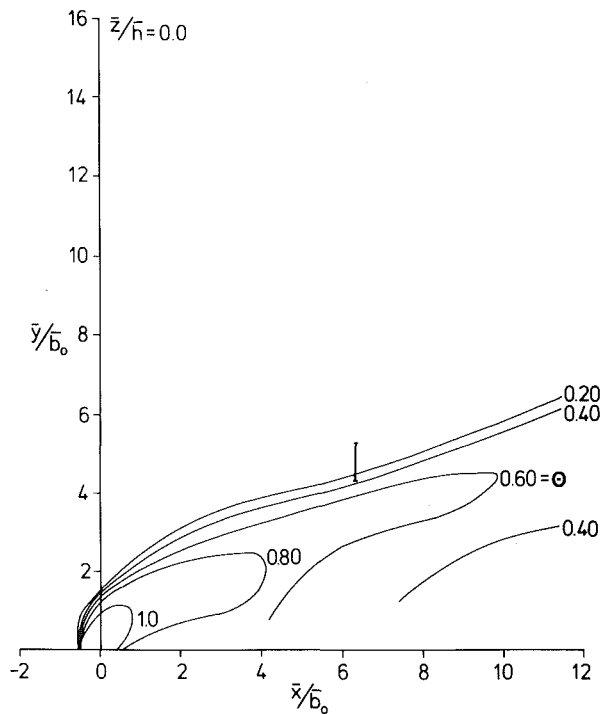


Fig. 7 Average isotherm contours in horizontal $x-y$ plane at $z=0.0$; $Fr_0 = 1.31$, $R = 1.13$, $Re = 18,700$, $\gamma = 0.058$, $\gamma = 0.84$, $W = 27.1$

Plume Trajectory and Width. Plume surface centerline trajectories determined graphically from the surface isotherms of Figs. 4-7 appear in Fig. 8. Also shown for comparison are centerline results obtained by injecting dye into the jet channel. Note that no dye injection results were obtained for $Fr_0 = 0.79$, $R = 1.10$. These centerline curves have been determined such that the centerline lies mid-way along plume widths measured normal to the local trajectory.

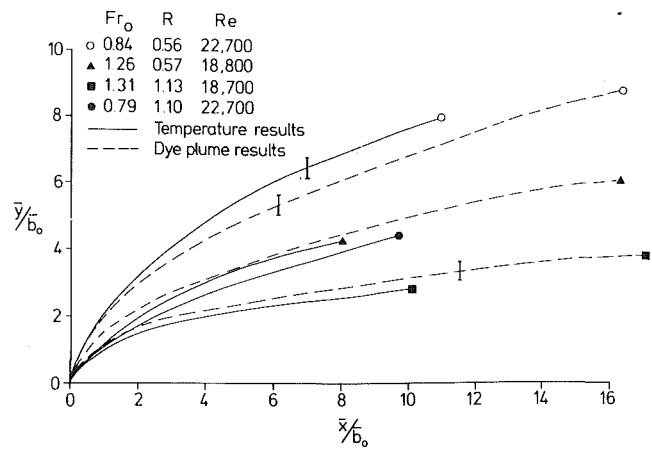


Fig. 8 Thermal plume centerline trajectories, compared with dye plume centerline trajectories for various Fr_0 , R , Re ; all results for $Fr = 0.058$, $\gamma = 0.84$, $W = 27.1$

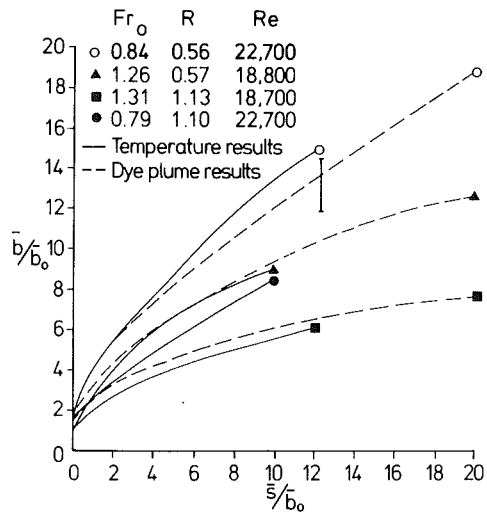


Fig. 9 Thermal plume total width, compared with dye plume total width for various Fr_0 , R , Re ; all results for $Fr = 0.058$, $\gamma = 0.84$, $W = 27.1$

Centerline results lie appreciably inboard of the trajectory of maximum surface temperature, due to the asymmetrical nature of temperature profiles normal to the plume centerline [18, 19, 29-31]. Dye results are judged to compare well with the temperature results. Local plume total widths as determined from surface isotherm data have been compared in Fig. 9 with dye plume widths, again for the buoyant jet configurations of Figs. 4-7. Dye injection is seen to be a simple means of determining mean plume characteristics such as trajectory and width. Similar results have been presented in [18] for other values of Fr_0 , R , and Re . Further, results of preliminary investigations into the effects of surface heat transfer, and of turbulence levels in the crossflow, have been described therein.

Discussion

In an effort to determine whether or not the present data have been obtained for Re values which are high enough to ensure that mean plume behavior be independent of Re , comparisons have been made between the present data and earlier data [11-13] taken at a lower nominal Reynolds number of $Re = 2,500$. Two examples of such comparisons, taken from [18], are presented in Figs. 10-13. There are very large differences between horizontal isotherm contours for

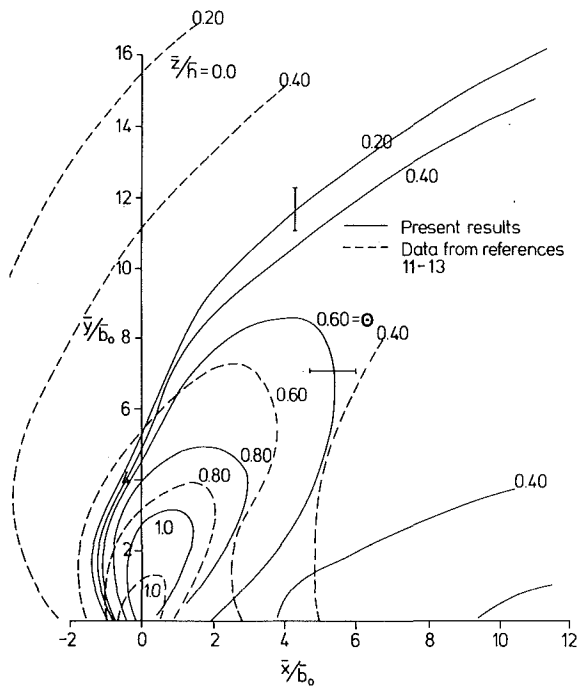


Fig. 10 Comparison of surface isotherms for $Fr_0=0.84$, $R=0.56$, $Re=22,700$ (from Fig. 4) with results for $Fr_0=0.825$, $R=0.6$, $Re=2,500$, $Fr=0.05$, $\gamma=1.0$, $W=36.5$ from [11-13]

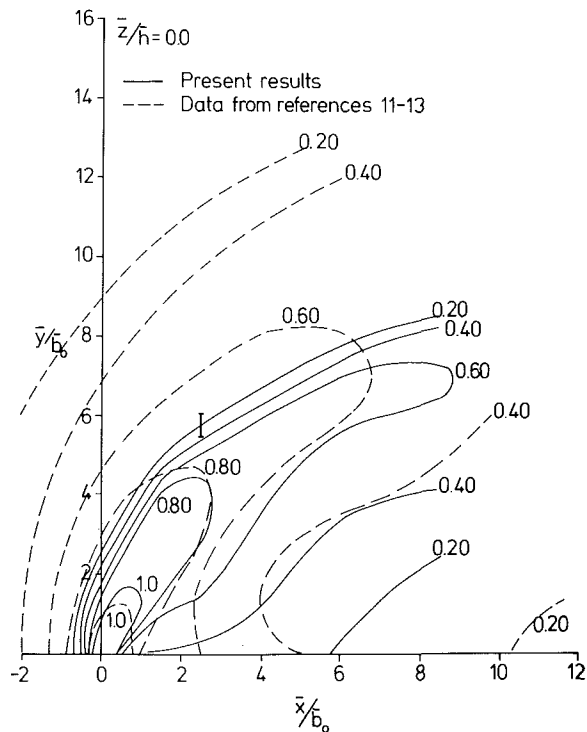


Fig. 11 Comparison of surface isotherms for $Fr_0=1.26$, $R=0.57$, $Re=18,800$ (from Fig. 5) with results for $Fr_0=1.31$, $R=0.6$, $Re=2,500$, $Fr=0.05$, $\gamma=1.0$, $W=36.5$ from [11-13]

these two sets of data at similar values of Fr_0 and R (Figs. 10, 11). Variation in vertical isotherm contours along trajectories of maximum surface temperature is much less dramatic (Figs. 12, 13), being confined to very near to the plume origin, $s < 4$, with the present results rising toward the free surface more slowly than the earlier, low Re results. Horizontal isotherm contours move markedly inward toward the near shoreline as Re is increased, both at $Fr_0=0.84$ (Fig. 10), and at $Fr_0=1.26$

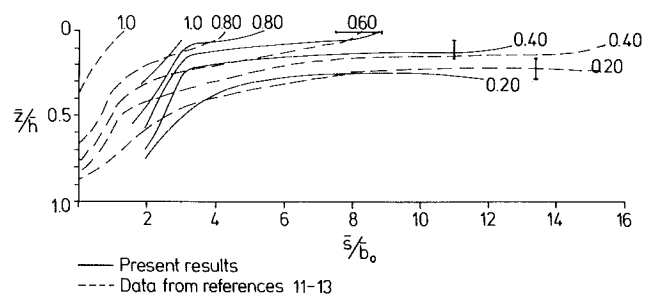


Fig. 12 Comparison of isotherms in vertical plane along temperature maximum centerline for $Fr_0=0.84$, $R=0.56$, $Re=22,700$ (from Fig. 3) with results for $Fr_0=0.825$, $R=0.6$, $Re=2,500$, $Fr=0.05$, $\gamma=1.0$, $W=36.5$ from [11-13]

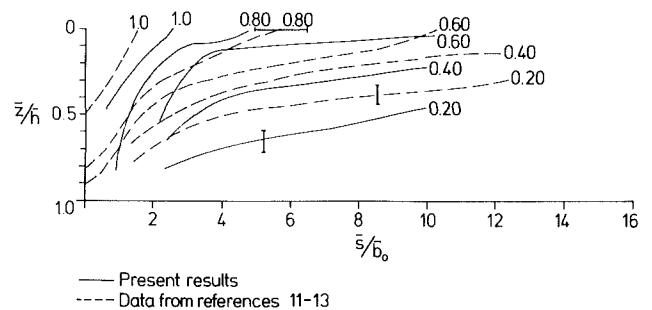


Fig. 13 Comparison of isotherms in vertical plane along temperature maximum centerline for $Fr_0=1.26$, $R=0.57$, $Re=18,800$ with results for $Fr_0=1.31$, $R=0.60$, $Re=2,500$, $Fr=0.05$, $\gamma=1.0$, $W=36.5$ from [11-13]

(Fig. 11). However, much of this inward shift of isotherms with increasing Re is confined to the windward or upstream region of the plume, for $\theta < 0.5$. Warmer plume fluid surface area ($\theta \geq 0.6$) changes very little or actually increases as Re increases (Fig. 10), at the same time that the horizontal extent of the plume is decreasing. Similar behavior has been observed in [18] for other values of Fr_0 , R , and Re , where Re values between those shown in Figs. 10-13 resulted in plume sizes intermediate to those shown herein. Also, in [18], the temperature difference between the room air and crossflow fluid was varied, with the tentative conclusion that surface heat transfer is not important in the nearfield region of the present plume configurations. It is believed that the decrease of the horizontal extent of the upstream side of the plume must have been due to a strengthening of the weak longitudinal vortex in the windward side of the plume as Re was increased. This vortex structure led to increased mixing between crossflow and buoyant jet fluid, leading to more rapid turning of the jet, as well as deepening the outer part of the plume. Although jet and crossflow velocity profiles were not documented for the present study, data presented in [11] show that for the low Re results the jet channel exit velocity profiles were turbulent, and little or no inflow of crossflow fluid along the jet channel bottom occurred.

In [23], Reister et al. discovered that the nonlinear variation with temperature of the coefficient of thermal expansion of water can lead to scatter of trajectory and centerline temperature decay results obtained at the same value of Fr_0 but at different values of \bar{T}_c . It was found in [23] that such data nearly collapsed to a single curve when results were compared for equal values of an effective internal Froude number, based upon the actual temperature difference, $\bar{T}_j - \bar{T}_c$, and the coefficient of thermal expansion evaluated at the crossflow temperature. As described in [18], comparison of these effective internal Froude numbers showed that this effect could not have led to the present deviation in horizontal isotherm contours (Figs. 10, 11). It is thus concluded that

Table 1 Estimated accuracy of measured and derived results (20:1 odds)

Quantity	Estimated Accuracy (20:1 Odds)
\bar{b}_0, \bar{h}	$\pm 1\text{mm}$
\bar{T}_j, \bar{T}_c	$\pm 0.22^\circ\text{C}$
$\bar{x}, \bar{y}, \bar{z}$	$\pm 5\text{mm}$
\bar{Q}_c	$\pm .0013\text{ m}^3/\text{s}$ ($\pm 20\text{ GPM}$)
\bar{Q}_j	$\pm 6.3 \times 10^{-5}\text{ m}^3/\text{s}$ ($\pm 1\text{ GPM}$)
$\bar{T}(\bar{x}, \bar{y}, \bar{z})$	$\pm .61^\circ\text{C}$
dye plume edge	$\pm 66\text{mm} = \pm 0.44 \bar{b}_0$
dye plume centerline	$\pm 33\text{mm} = \pm 0.22 \bar{b}_0$
$\theta(x, y, z)$	$\pm 5\%$, for $\text{Fr}_0 \cong 0.85$
	$\pm 10\%$, for $\text{Fr}_0 \cong 1.3$
Fr_0	$\pm 9\%$
R	$\pm 5\%$
Re	$\pm 5\%$
Fr	$\pm 2\%$
γ	$\pm 2\%$
W	$\pm 1\%$
isotherm locations	as shown on figs.

variation with Reynolds number of either the plume turbulence field, or more likely, of the strength of the windward longitudinal vortex, is the cause of the observed differences in horizontal isotherms as Reynolds number was varied.

Conclusion

An experimental study of the effects of Reynolds number upon the nearfield development of a buoyant, rectangular, surface jet in a crossflow has been described, where examples of dye plume and thermocouple data have been presented for various values of internal Froude number, velocity ratio and Reynolds number. Comparison of horizontal isotherm contour results with previous low Reynolds number data at the same internal Froude number and velocity ratio has shown a large Reynolds number effect, where as Reynolds number increased from 2500 to nominally 20,000 the horizontal extent of the plume decreased. This decrease in plume horizontal extent has been found to be due to the development or strengthening of a longitudinal vortex secondary flow in the upstream edge of the plume. Plume temperature distributions were found to be highly three dimensional and asymmetrical.

The observed large variation in plume horizontal extent as Reynolds number varied indicates that laboratory model plume results are not directly applicable to the quantitative prediction of full scale plume behavior for the rectangular, buoyant, surface jet in a crossflow, at least for Reynolds numbers below 20,000. Further studies at higher Reynolds numbers would be necessary to determine values above which such flows become independent of Reynolds number.

Acknowledgment

This study has been supported by the National Science Foundation under grants ENG78-00815 and CME78-00815.

References

- 1 Reynolds, J. Z., "Power Plant Cooling Systems: Policy Alternatives," *Science*, Vol. 207, No. 4429, Jan., 1980, pp. 367-372.
- 2 Croley, T. E., III, Giaquinta, A. R., Lee, R. M.-H., and Hsu, T.-D., "Optimum Combinations of Cooling Alternatives for Steam-Electric Power Plants," Iowa Inst. of Hydraulic Research, Report No. 212, July 1978.
- 3 Silberman, E., and Stefan, H., "Physical (Hydraulic) Modeling of Heat Dispersion in Large Lakes: A Review of the State of the Art," Report ANL/ES-2, Argonne National Laboratory, Aug. 1970.
- 4 Frigo, A., and Frye, D., "Physical Measurements of Thermal Discharges into Lake Michigan," Report ANL/ES-16, Argonne National Laboratory, Oct. 1972.
- 5 Dunn, W. E., Policastro, A. J., and Paddock, R. A., "Surface Thermal

Plume: Evaluation of Mathematical Models for the Near and Complete Field," Report ANL/WR-75-3, Parts I and II, Argonne National Laboratory, May 1975.

- 6 Policastro, A. J., and Tokar, A. J., "Heated Effluent Dispersion in Large Lakes: State-of-the-Art of Analytical Modeling," Report ANL/ES-11, Part I, Argonne National Laboratory, Jan 1972.
- 7 Shirazi, M., and Davis, L., "Workbook of Thermal Plume Prediction, Volume 2, Surface Discharge," Report EPA-R2-72-005b, Pacific Northwest Environmental Research Laboratory, Corvallis, Oregon, May 1974.
- 8 McGuirk, J. J., and Rodi, W., "Calculation of Three-Dimensional Heated Surface Jets," in *Heat Transfer and Turbulent Buoyant Convection*, Vol. 1, D. B. Spalding and N. Afgan, editors, Hemisphere, 1977, pp. 275-287.
- 9 Chien, J. C., and Schetz, J. A., "Numerical Solution of the Three-Dimensional Navier-Stokes Equations with Applications to Channel Flows and a Buoyant Jet in a Cross-Flow," *ASME Journal of Applied Mechanics*, Vol. 42, Sept. 1974, pp. 575-579.
- 10 Paul, J. F., and Lick, W. J., "A Numerical Model for a Three-Dimensional, Variable-Density Jet," Case Western Reserve University report FTAS/TR 73-92, January 1974; also *Proc. 16th Conference Great Lakes Research*, 1973, pp. 818-830.
- 11 Kuhlman, J. M., and Prah, J. M., "Laboratory Modeling of Surface Thermal Plumes," Case Western Reserve University report FTAS/TR-74-103, Aug. 1974.
- 12 Kuhlman, J. M., and Prah, J. M., "Observations of the Kelvin-Helmholtz Instability in Laboratory Models and Field Examples of Thermal Plumes," *Journal of Great Lakes Research*, Vol. 1, No. 1, Oct. 1975, pp. 101-115.
- 13 Kuhlman, J. M., and Prah, J. M., "Buoyant Rectangular Surface Thermal Plumes," *Journal of Great Lakes Research*, Vol. 2, No. 2, 1976, pp. 340-356.
- 14 Kuhlman, J. M., and Prah, J. M., "Laboratory Modeling of River Entrance Flows with Bottom Friction," Case Western Reserve University report FTAS/TR-73-89, 1973; also presented at 16th Conference on Great Lakes Research, Huron, Ohio, Apr. 16-18, 1973.
- 15 Stuhmiller, J. H., "Theoretical Considerations of Turbulent Buoyant Flow," in *Heat Transfer and Turbulent Buoyant Convection*, Vol. 1, D. B. Spalding and N. Afgan, editors, Hemisphere, 1977, pp. 3-14.
- 16 Hossain, M. S., and Rodi, W., "Influence of Buoyancy on the Turbulence Intensities in Horizontal and Vertical Jets," in *Heat Transfer and Turbulent Buoyant Convection*, Vol. 1, D. B. Spalding and N. Afgan, editors, Hemisphere, 1977, pp. 39-51.
- 17 Gibson, C. H., "Buoyancy Effects on Turbulent Mixing," paper number AIAA-80-1334, presented at AIAA 13th Fluid & Plasma Dynamics Conference, July 14-16, 1980, Snowmass, Co.
- 18 Kuhlman, J. M., "Effect of Reynolds Number on the Nearfield Region of a Buoyant Rectangular Surface Jet in a Crossflow," Final Technical Report, National Science Foundation Grants ENG78-00815 and CME78-00815, Old Dominion University Research Foundation, Norfolk, Va., Jan. 1982.
- 19 Chu, L.-C., "Experimental Investigations of a Rectangular Surface Thermal Plume," Master's thesis, Dept. of Mechanical Engineering and Mechanics, Old Dominion University, Norfolk, Va., Dec. 1981.
- 20 Durgin, W. W., "The Design and Operation of Physical-Thermal Models," ASME Paper 81-FE-16, presented at joint ASME/ASCE Fluids Engineering, Bioengineering and Applied Mechanics Conference, Boulder, Co., June 22-24, 1981.
- 21 Chen, C. J., and Rodi, W., *Vertical Turbulent Buoyant Jets—A Review of Experimental Data*, Pergamon Press, 1980.
- 22 Ricou, F. P., and Spalding, D. B., "Measurements of Entrainment by Axisymmetrical Turbulent Jets," *Journal of Fluid Mechanics*, Vol. 11, 1961, pp. 21-32.
- 23 Reister, J. B., and Bajura, R. A., and Schwartz, S. H., "Effects of Water Temperature and Salt Concentration on the Characteristics of Horizontal Buoyant Submerged Jets," *Journal of Heat Transfer*, Vol. 102, No. 3, Aug. 1980, pp. 557-562.
- 24 Anwar, H. O., "Appearance of Unstable Buoyant Jet," *Journal of the Hydraulics Division, Proceedings of the ASCE*, Vol. 98, No. HY7, July 1972, pp. 1143-1155.
- 25 Tamai, N., Wiegel, R. L., and Tornberg, G. F., "Horizontal Surface Discharge of Warm Water Jets," *Journal of the Power Division, Proceedings of the ASCE*, Vol. 95, No. P02, Proc. Paper 6847, Oct. 1969, pp. 253-276.
- 26 Fearn, R., and Weston, R. P., "Vorticity Associated with a Jet in a Crossflow," *AIAA Journal*, Vol. 12, Dec. 1974, pp. 1666-1671.
- 27 Kuhlman, J. M., and Warcup, R. W., "Effects of Jet Decay Rate on Jet-Induced Loads on a Flat Plate," *Journal of Aircraft*, Vol. 15, No. 5, May 1978, pp. 293-297.
- 28 Scarpace, F. L., and Green, III, T., "Dynamic Surface Temperature Structure of Thermal Plumes," *Water Resources Research*, Vol. 9, No. 1, 1973, pp. 138-153.
- 29 Jirka, G. H., Adams, E. E., and Stolzenbach, K. D., "Buoyant Surface Jets," *Journal of the Hydraulics Division, Proceedings of the ASCE*, Vol. 107, No. HY11, Proc. Paper 16660, Nov. 1981, pp. 1467-1487.
- 30 Natalizio, A., and Baines, W. D., "Simplified Analysis of Surface Buoyant Jet," *Journal of the Hydraulics Division, Proceedings of the ASCE*, Vol. 103, No. HY2, Proc. Paper 12737, Feb. 1977, pp. 123-132.
- 31 Kapur, S., Sambuco, E., and Sundaram, T. R., "Laboratory Studies on the Behavior of Thermal Plumes," presented at 20th Conference on Great Lakes Research, Ann Arbor, Mich., May 10-12, 1977.

APPENDIX

Error Estimation

Table 1, of percent error at 20:1 odds, taken from [18], summarizes the estimated accuracy of results presented herein. Estimated errors in dimensional quantities include measurement errors in lengths, temperatures, and flow rates, as well as statistical error due to unsteadiness due to the turbulent nature of the plume, or due to slow drifting of the plume reference state (primarily the result of slow variation in the jet temperature as the heater cycled off and on). Estimated accuracy of nondimensional parameters such as internal Froude number and mean nondimensional temperature have been computed by propagating the estimated errors in measured quantities. Accuracy of the dye injection results has

been estimated by comparing multiple photographs of the dye plume.

Estimated accuracies of the locations of the isotherm contours have been displayed on the figures, generally with regions having the largest error shown. Details of the methods used to estimate this accuracy have been given in [18]. Briefly, the dominant error source in isotherm location is the 5-10 percent uncertainty in the mean nondimensional temperature measurements. Error due to thermocouple rake positioning of $\pm 0.5\text{cm}$ has been found to be minor. These uncertainties in θ values have been used to graphically estimate error in isotherm location, by noting the positions where the $(\theta + e_\theta)$ and $(\theta - e_\theta)$ versus y curves crossed various levels of θ . Here, e_θ is the uncertainty estimate for θ . Thus, the regions of maximum uncertainty in isotherm location tended to be where θ changed most gradually with position.

Regular Structures in a Plane Triple Jet

G. Schweiger

Fachbereich 7/Thermodynamik,
Universität Duisburg,
4100 Duisburg,
West Germany

The mixing process in the near field of a triple rectangular jet (air-CO₂-air-jet) has been investigated in this paper by number density measurements (Laser-Raman-scattering) and schlieren pictures. The mixing process was found to be dominated by the rolling-up mechanism of the free shear layer into regular vortices. Four basic types of this process could be observed and are described here. Pulsed schlieren technique was applied to measure the vortex shedding frequency. The results are presented as a function of nozzle geometry and flow conditions. Finally a second vortex system oriented perpendicular to the main system could be detected.

Introduction

The mixing of jets is used in a wide variety of engineering applications, ranging from thrust augmenting equipment to fuel mixing in combustion processes. Relatively complete information of the jet properties in the far field is available, but most of the mixing processes of technical interest are taking place in the near field. Although the number of investigations in this part of the flow has increased remarkably in the last few years, very few investigations have been reported regarding the structure of multiple jets. Nevertheless no reliable theoretical prediction scheme is available today to describe the mixing of multiple jets in the near field satisfactorily. At present, the most effective way for the development of a quantitative prediction method is presumably the experimental investigation of some basic configuration and the generalization of the experimental results by some scaling laws. One of the basic arrangements is an array of rectangular nozzles. Economic reasons suggest to use nozzles of moderate dimensions. In addition for a given mass flow rate several small nozzles yield a better mixing than a few large ones. For these reasons the triple nozzle shown in Fig. 1 was built. Whereas the length of the nozzles was kept constant, the width of the nozzles could be varied.

Measurements on similar arrangements were made by Laurence and Benninghoff [1] and Laurence [2] with emphasis on noise generation. Some measurements were made on twin slit jets by Tanaka [3, 4], Murai, Taga and Akagawa [5] and Marsters [6]. The interaction of three or more jets was investigated for example by Edler von Bohl [7] and more recently by Komar and Petrie in a supersonic flow [8] and Leipertz and Fiebig [9], Marsters [10, 11] and Krothapalli, Baganoff, and Karamcheti [12] have investigated the flow of jets with comparable dimensions and velocities to this investigation. In the present study the center nozzle was supplied with CO₂, whereas the two outer nozzles were operated with air. The velocity of the CO₂-jet and the air-jet was varied in the range from 2 to 9 m/s (peak velocity) and three slit nozzles were used having a slit width of 4, 6 and 8 mm

respectively. The Reynolds-number-range (based on the CO₂-nozzle) was of an order of 10^3 to $5 \cdot 10^3$. The measurements were made using the Laser-Raman-Scattering technique for CO₂ number density measurements. For a qualitative analysis of the flow patterns a pulsed schlieren setup was applied.

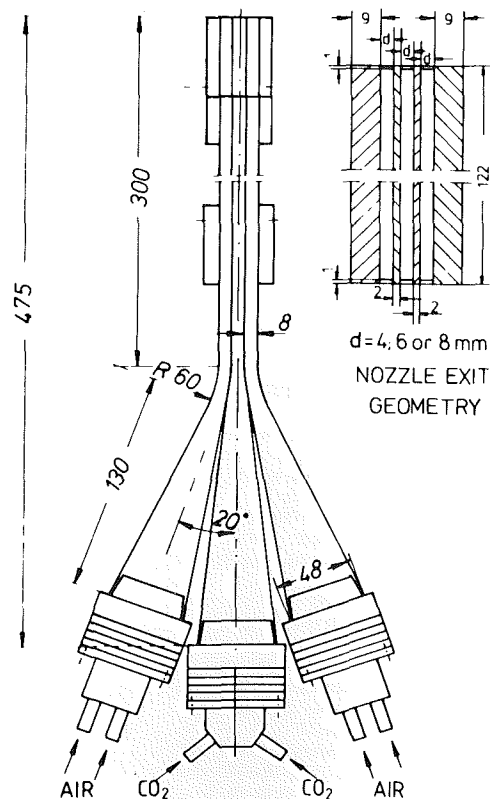


Fig. 1 Nozzle configuration

Contributed by the Fluids Engineering Division for publication in the JOURNAL OF FLUIDS ENGINEERING. Manuscript received by the Fluids Engineering Division, November 11, 1981.

Apparatus and Instrumentation

A sketch of the experimental setup is shown in Fig. 2. The air for the two outer jets was taken from a pressure vessel through pressure regulation valves and flow meters. The CO₂ was supplied by pressure bottles through pressure regulation valves, a heater and a flow meter. Special emphasis was put on the construction of the triple nozzle to generate a homogenous flow. Measurements in the exit plane showed, that the velocity and pressure was constant to ± 1 percent over 90 percent of the nozzle length. A suction cone was mounted above the triple nozzle. The distance to the nozzles and the suction velocity was chosen in such a way, that no measurable influence could be observed in the range from the nozzle exit at least 20 times the nozzle width downstream.

For the number density measurements a 4 W (single line) Argon ion-Laser was used. A scattering volume of 1 mm length (parallel to the long side of the triple-nozzle) and less than 0.1 mm in diameter was achieved by using an appropriate imaging system. The CO₂ vibration line was filtered out from the scattered light by a Spex double-monochromator and a photoncounting technique was used for signal processing. For qualitative flow analysis and vortex frequency measurements a conventional schlieren setup with a pulsed flashlamp was used. A part of the schlieren pictures was made with "dark field illumination", which means that a rectangular stop having the size of the image of the light source was used in place of the schlieren edge.

Experimental Results and Interpretation

Figure 3 shows the time averaged axial density distribution for different flow conditions and nozzle widths. The accuracy in the number density measurement was approximately ± 2 percent rising to ± 5 percent in the most turbulent regions. The axial position could be determined with an accuracy of ± 0.2 mm. The most striking result is the minimum in the number density approximately 4 to 7 slit widths downstream of the onset of the triple jet. To the author's knowledge such a minimum was observed never before, neither for a single nor for a multiple jet. One would expect a more or less exponential decay as reported in a number of publications. Assuming a fully turbulent flow, the observed number density would be even in contradiction to conservation of mass law. It will be shown later in the text, that the observed minimum can be explained by the existence of highly coherent structures in the flow and the peculiarities of the Raman-technique applied for the number density measurements. In addition the mixing process seems to be enhanced by the outer jets. The decay of the CO₂-concentration in the near field is faster than in the case of a single rectangular jet.

Figures 4 and 5 show typical schlieren pictures of the flow. The long edge of the nozzle is arranged parallel and perpendicular to the optical path respectively. The schlieren pictures reveal a very pronounced vortex system aligned parallel to the nozzle exit edge (Fig. 5) and a second system consisting of narrow-spaced vortices aligned perpendicular to the first system (Fig. 6).

The main system is caused by the rolling-up of the free shear layer between inner and outer jets. The second system seems to be due to instabilities of the Taylor type and the vortex spacing is approximately equal to the initial jet

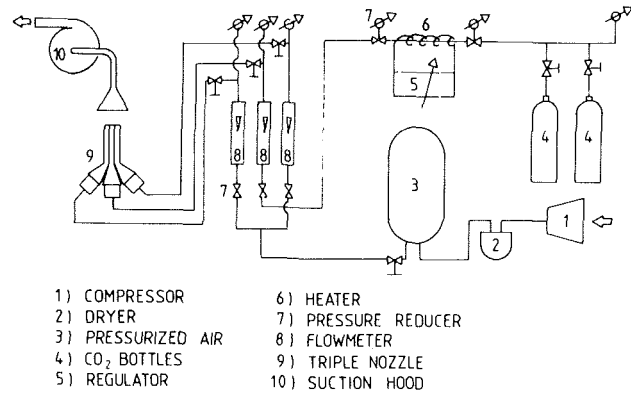


Fig. 2 Sketch of the experimental setup

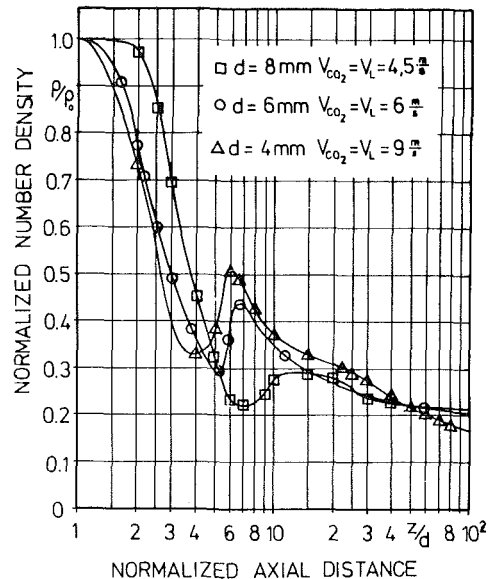


Fig. 3 Axial concentration distribution measured at three different nozzle sets, having a slit width of 4 mm, 6 mm and 8 mm, respectively, and a Reynolds-number based on the CO₂-jet between $2 \cdot 10^3$ and $6 \cdot 10^3$ approximately, $Re = (U \cdot d/\nu)_{CO_2}$. (Uncertainty in $\rho/\rho_0 \leq 5$ percent in z and $d = \pm 0.2$ mm.)

separation (thickness of the walls separating the individual nozzles). The existence of vortex lines orientated parallel to the mean flow direction was observed recently by Bernal, Breidenthal, Brown, Konrad, and Roshko [13] in a free shear layer.

Analyzing a great number of schlieren pictures, four basic types of rolling-up process of the shear layer can be distinguished, two symmetrical and two antisymmetrical patterns, which are shown in Fig. 7. At high, $V_L/V_{CO_2} > 2$, or small velocity ratios, $V_L/V_{CO_2} < 0.5$, the symmetrical vortex formation predominates, whereas at no or smaller velocity differences the antisymmetrical, vortex-street like pattern prevails. The interpretation of the schlieren pictures, in the case of the long jet edge aligned parallel to the optical path, suffered especially at low speed ratios from the lack of parallelity of the vortex lines due to instabilities in the flow.

Nomenclature

d = slit width of the rectangular nozzle	V_L = central exit velocity of the air-nozzle	ν = vortex shedding frequency
V_{CO_2} = central exit velocity of the CO ₂ -nozzle	ρ = CO ₂ number density	ν_0 = vortex shedding frequency at $V_{CO_2} = V_L$
	ρ_0 = CO ₂ number density at the jet origin	

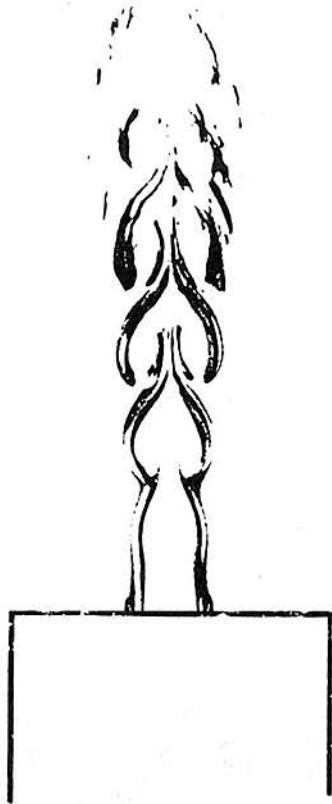


Fig. 4 Typical schlieren picture of the flow with the optical path parallel to the long edge of the nozzle. The two air-jets, one on each side of the CO₂-jet, are not visible.

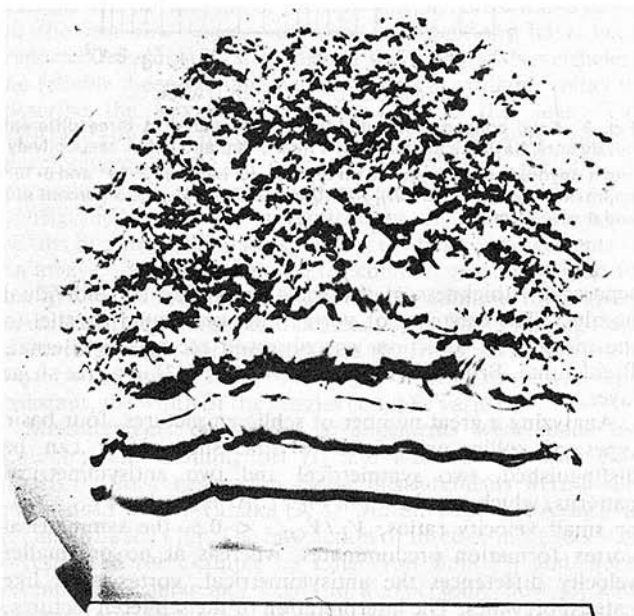


Fig. 5 Typical schlieren picture with the optical path orientated orthogonal to the long edge of the nozzle; the air jets are not visible

Nevertheless the results of the axial concentration measurements support the existence of the prescribed configurations. The strong entrainment of ambient fluid into the core of the center jet in the antisymmetrical case explains the fast concentration decay along the centerlines. The average concentration on the centerline increases farther downstream, where the regular structure collapses and the highly turbulent motion caused by this collapse enhances the mixing, ap-

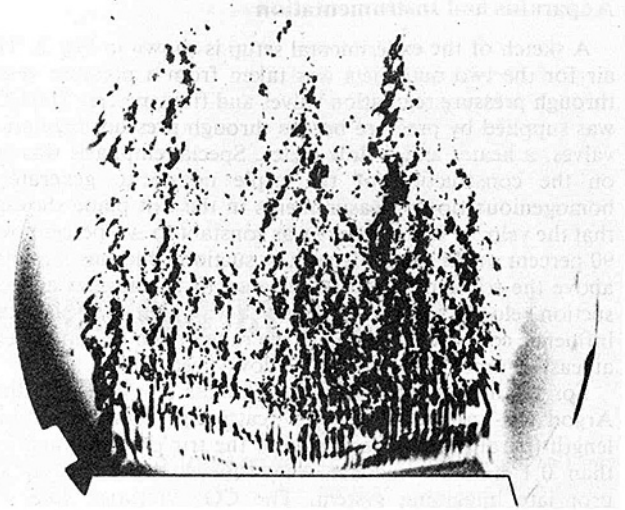


Fig. 6 Schlieren picture with the schlieren edge parallel to mean flow direction. The density gradients parallel to the nozzle edge are made visible.

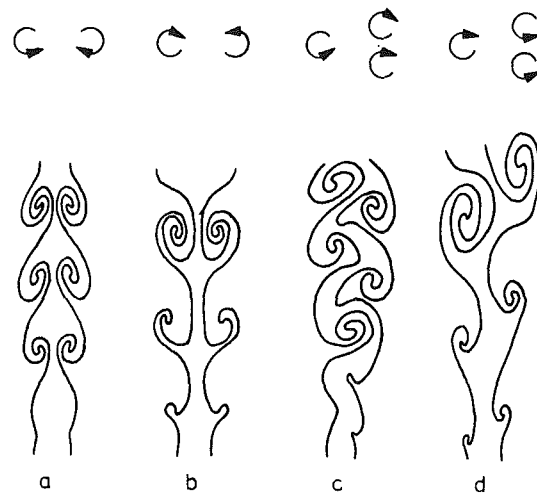


Fig. 7 Basic rolling-up configurations of the mixing layers between inner and outer jets; the arrows symbolize the vorticity

preciably. This results in an increase in the average CO₂-concentration.

The pulsed schlieren apparatus was also used to measure the vortex shedding frequency. The frequency measurements were made accurate to 0.1 Hz, but the shedding frequency showed instabilities of the order of ± 1 percent. Presumably the largest uncertainties are introduced by variations of the flow conditions during the measurements. In some cases the exit velocity of the CO₂-jet showed variations up to ± 2 percent. The stability of the air-jets was an order of magnitude better. That measurements were carried out at three different slit widths: 4, 6 and 8 mm. In all cases the nozzle length remained unchanged and all three nozzles had the same size and the velocity of the two outer jets was kept equal. Figure 8 shows some of the results. The shedding frequency is a function of slit width, relative and absolute velocity. A more unified picture can be achieved by plotting the relative shedding frequency as a function of the velocity difference or the relative velocity as shown in Fig. 9.

The pulsed schlieren pictures also revealed a remarkable difference between the vortex behaviour of a single jet and the

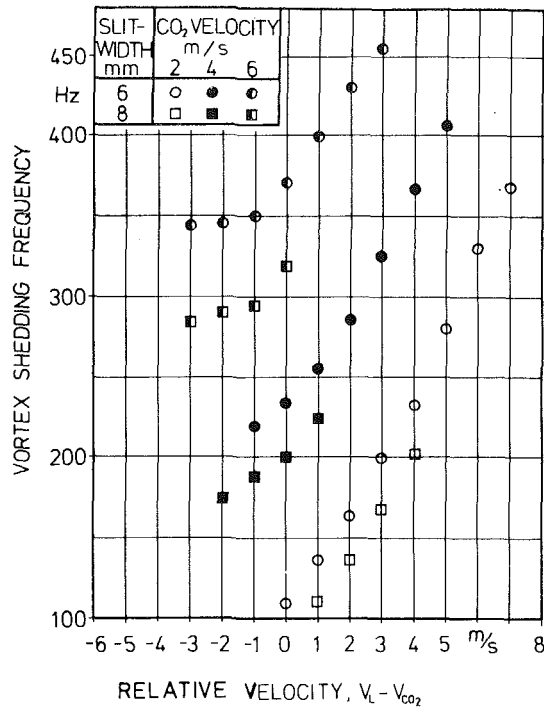


Fig. 8 Vortex shedding frequency as function of the relative jet velocity for two different nozzle widths and different CO₂ exit velocities. (Uncertainty in frequency measurements $\nu = \pm 0.1$ Hz, in velocity V_L or $V_{CO_2} = \pm 0.2$ percent.)

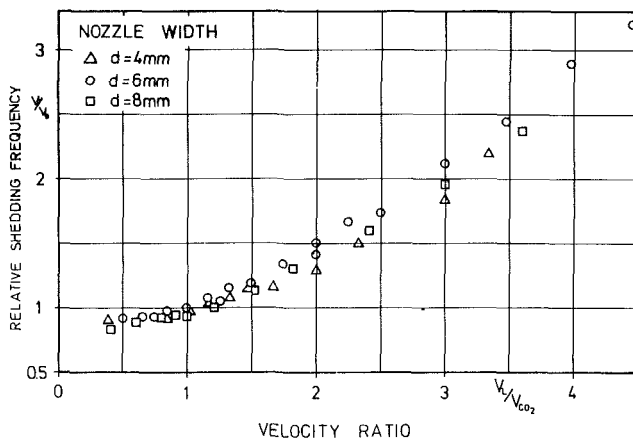


Fig. 9 Relative shedding frequency as function of the relative jet velocity. (Uncertainty same as in Fig. 8.)

triple jet. For the single jet no stroboscopic frequency could be found, which showed a stable schlieren picture. Nevertheless the schlieren apparatus made visible, that the vortex shedding frequency for a single jet depends on the distance from the jet origin and covers a certain frequency range. Similar results were found by a number of other authors [14, 15]. Contrary to the single jet the shedding frequency in the case of the triple jet remained very stable over the range of existence of the vortex rollers.

Provided that the exit velocities for all three jets were chosen equal, the shedding frequency was a linear function of the Reynolds-number as shown in Fig. 10. But the Reynolds-number is obviously not the only parameter of importance. The shedding frequency also depends on the slit width as shown in Fig. 10. Similar results have been reported for a single jet by Clark and Kit [16] for example. The comparison of the present results with Strouhal numbers available in the literature shows, that the triple jet data found in this investigation are in the range of Strouhal numbers published for

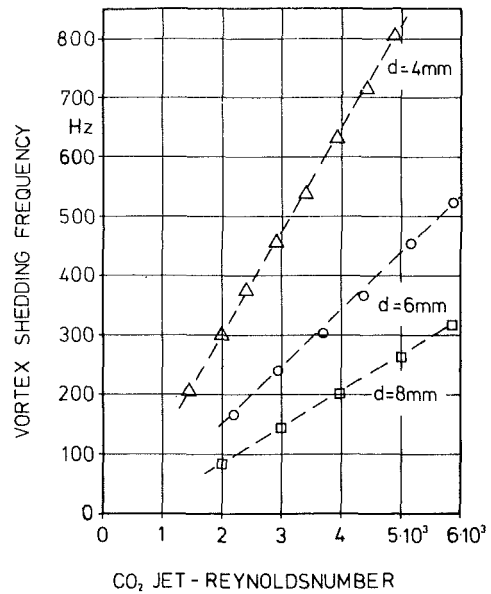


Fig. 10 Vortex shedding frequency as function of the Reynolds-number at three different nozzle widths. (Uncertainty same as in Figs. 8 and 9.)

Table 1 Strouhal numbers under different flow conditions

Strouhal number	Reynolds number 1)	Zero Ambient Velocity	Channel width/diameter (mm)	Working-medium	Comment	Author
1,35	$1 \cdot 10^3 \sim 3 \cdot 10^3$	yes	13	Water	single plane jet	Clark (16)
2,8	$2 \cdot 10^3 \sim 7 \cdot 10^3$	"	25	"	"	"
3,7	$4 \cdot 10^3 \sim 1 \cdot 10^4$	"	38	"	"	"
4,25	$4 \cdot 10^3 \sim 1,6 \cdot 10^4$	"	51	"	"	"
5,8	$7 \cdot 10^3 \sim 1,7 \cdot 10^4$	"	76	"	"	"
1,65	$2,65 \cdot 10^4$	"	25,4	Air	"	Rajagopalan (14)
4,2	$2,1 \cdot 10^4$	"	50,8	"	round jet	Yule (17)
0,62 - 0,63	350 ~ 1600 700 ~ 2800	"	8,13; 15,9	Water	"	Beavers (18)
0,4	350 ~ 1600	"	10,8	"	single plane jet	"
0,43	350 ~ 1500	"	7,6 ; 15,2	"	"	"
0,42	350 ~ 1500	"	5,6	"	"	"
0,33 2)	~3880 2)	no	25,4	"	"	Oseberg (19)
0,35	~1580	"	"	"	"	"
0,41	~1670	"	"	"	"	"
0,22	$4,5 \cdot 10^4$	yes	12,7	Air	round jet	Narayanan (20)
0,31	$1,5 \cdot 10^3 \sim 5 \cdot 10^3$	no	4	CO ₂ /Air	multiple rectangular jet	present investigation
0,39	$2 \cdot 10^3 \sim 6 \cdot 10^3$	"	6	"	"	"
0,43	$2 \cdot 10^3 \sim 6 \cdot 10^3$	"	8	"	"	"

1) based on central exit velocity and nozzle dimensions (diameter, slit width)

2) calculated using available data

free jets, see Table 1, but the variety of published Strouhal numbers seems to be as broad as the details of the flow condition under which they have been found. However, two general conclusions can be drawn:

(a) For a given nozzle configuration the Strouhal number based on exit velocity and nozzle geometry is independent of Reynolds number based on the same data.

(b) The Strouhal number depends on the slit width. For nozzles with different slit width the Strouhal numbers differ also ($S = \nu \cdot d/U$).

Conclusion

Under the condition investigated during the course of this work the results show that the rolling-up of the free shear layer dominates the mixing process from the nozzle exit to a

distance 5 to 7 times the nozzle width downstream. Information on this rolling-up process therefore is of primary interest. The available knowledge is far from being sufficient for a quantitative prediction of the mixing of multiple jets. Nevertheless the following statement can be made on the basis of this work.

1. In the rectangular triple jet investigated two vortex systems exist: one orientated parallel to the flow direction, the other one perpendicular.

2. Four basic vortex configurations have been observed: two symmetrical and two antisymmetrical systems.

3. The instantaneous concentration can have large deviation from the time averaged concentration even on the centerline of the jet. This is caused by the rolling-up process of the free shear layer.

4. The vortex shedding frequency is a function of Reynolds number (based on the exit conditions of the center jet), slit width and velocity ratio (or relative velocity) between inner and outer jets.

To improve the insight into the mixing process, more quantitative data are needed. The role of the density ratio on the vortex formation has to be investigated. Although the work of Roshko (21) indicates that the density ratio is of minor importance for the formation of the main structure, the density ratio controls possibly the formation of the fine structure. One important parameter not considered in this work is the width of the wall between the rectangular ducts. An increase in wall thickness shifts the onset of jet merging downstream and at a sufficient ratio of wall thickness to nozzle length the jets will behave in the developing region like a row of single jets but no data are available to quantify "sufficient". Therefore experiments are in preparation in our institute to investigate the influence of the wall thickness.

This project was sponsored in part by the "Forschungskommission" of the University of Duisburg.

References

1 Laurence, C. J., and Benninghoff, N. J., "Turbulent Measurements in Multiple Interfering Air Jets," NASA TN 4029, 1957.

2 Laurence, C. J., "Turbulence Studies of a Rectangular Slotted Noise Suppressor Nozzle," NASA TND-294, 1960.

3 Tanaka, E., "The Interference of Two-Dimensional Parallel Jets (1st Report, Experiments on Dual Jet)," *Bulletin of the JSME*, Vol. 13, No. 56, 1970, pp. 272-280.

4 Tanaka, E., "The Interference of Two-Dimensional Parallel Jets (2nd Report, Experiments on the Combined Flow of Dual Jet)," *Bulletin of the JSME*, Vol. 17, No. 109, 1974, pp. 920-927.

5 Murai, K., Taga, M., and Akagawa, K., "An Experimental Study on Confluence of Two Two-Dimensional Jets," *Bulletin of the JSME*, Vol. 19, No. 134, 1976, pp. 958-964.

6 Marsters, G. F., "Interaction of Two Plane, Parallel Jets," *AIAA J.*, Vol. 15, No. 12, 1977, pp. 1756-1762.

7 Edler von Bohl, J. G., "Das Verhalten paralleler Luftstrahlen," *Ing. Archiv XI. Band*, 1940, pp. 295-314.

8 Komar, J. J., and Petrie, S. L., "Investigation of Fluid Dynamic Interactions within Multiple Nozzle Arrays," *AIAA Pap.*, No. 76-342, 1976.

9 Leipertz, A., and Fiebig, M., "Experimental Investigation of Small Single and Multiple Jets by Laser-Raman-Spectroscopy," *European Electro Optical Conf. 4th Utrecht, Netherlands, Oct. 10-13, 1978, Proc. Bellingham Wash Society of Photo-Optical Instr. Engin.*, pp. 100-108.

10 Marsters, G. F., "Measurements in the Flow Field of a Linear Array of Rectangular Nozzles," *AIAA Paper*, No. 79-0350, 1979, p. 8.

11 Marsters, G. F., "An Experimental Investigation of Spanwise Velocity Distributions in Jets from Rectangular Slots," *AIAA Paper*, No. 80-0202, 1980, p. 8.

12 Krothapalli, A., Baganoff, D., and Karamcheti, K., "Development and Structure of a Rectangular Jet in a Multiple Jet Configuration," *AIAA J.*, Vol. 18, No. 8, 1980, pp. 945-950.

13 Bernal, L. P., Breidenthal, R. E., Brown, G. L., Konrad, J. H., and Roshko, A., *On the Development of Three-Dimensional Small Scales in Turbulent Mixing Layers Turbulent Shear Flows 2*, L.J.S. Bradbury, et al., Springer, Berlin, 1980, pp. 305-313.

14 Rajagopalan, S., and Antonia, R. A., "Characteristics of a Mixing Layer of a Two-Dimensional Turbulent Jet," *AIAA J.*, Vol. 18, No. 9, 1980, pp. 1052-1058.

15 Cervantes De Cortari, J., and Goldschmidt, V. W., "The Apparent Flapping Motion of a Turbulent Plane Jet-Further Experimental Results," *ASME JOURNAL OF FLUID ENGINEERING*, Vol. 18, 1981, pp. 119-126.

16 Clark, J. A., and Kit, L., "Shear Layer Transition and the Sharp-Edged Orifice," *ASME JOURNAL OF FLUID ENGINEERING*, Vol. 102, 1980, pp. 219-225.

17 Yule, A. J., "Investigation of Eddy Coherence in Jet Flows," *Int. Conf. on the Role of Coherent Structures in Modelling of Turbulence and Mixing*, Madrid, June 1980.

18 Beavers, G. S. and Wilson, T. A., "Vortex Growth in Jets," *Journal Fluid Mechanics*, Vol. 44, Part 1, 1970, pp. 97-112.

19 Oseberg, O. K., "The Near Field of a Jet with Several Initial Conditions," Ph. Dr. thesis, Stanford University, Dept. Mechanical Engineering, 1971.

20 Narayanan, M. A. B., "Experiments on the Large Scale Structure of Turbulence in The Near Jet Region," NASA TM-78567, 1979.

21 Roshko, A., "Structure of Turbulent Shear Flow: A New Look," *AIAA J.*, Vol. 14, No. 10, 1976 pp. 1349-1357.

D. W. Kuntz

NSF Fellow and Graduate Research Assistant,
Department of Mechanical
and Industrial Engineering,
University of Illinois at Urbana-Champaign,
Urbana, Ill. 61801

J. C. Dutton

Assistant Professor,
Department of Mechanical Engineering,
Texas A&M University,
College Station, Texas

S. H. White

Formerly Graduate Research Assistant,
University of Illinois;
Currently with E. I. duPont
de Nemours & Company,
Carolina Beach, N.C.

A. L. Addy

Professor and Associate Head,
Department of Mechanical
and Industrial Engineering,
University of Illinois at Urbana-Champaign,
Urbana, Ill.

Supersonic Diffusers With Reverse Flow Injection

In applications such as airborne high energy chemical lasers, diffuser size and weight can be critical parameters. This paper summarizes the authors' research concerning the effects of flow injection into a supersonic diffuser in a direction opposite to that of the main flow. Experimental studies were conducted concerning the effect of diffuser performance, particularly length and pressure recovery, of this reverse flow, and a quasi-one-dimensional control volume analysis was performed to predict some of the diffuser flow properties. Single-stream, dual-stream, and sudden enlargement configurations were considered. This work has shown that a reverse flow can reduce the length of a diffuser while causing only a small decrease in overall pressure recovery.

Introduction

The supersonic diffuser is a critical component in many systems involving high velocity compressible flows. Various types of diffusers are essential to the proper operation of such devices as high speed jet aircraft engines and supersonic wind tunnels. In recently developed devices such as high energy chemical lasers, new demands have been placed on diffuser systems. The corrosive nature of the working fluid dictates simplicity of design and in those cases where the laser is intended for airborne use, the size and weight of the diffuser are also critical factors in the overall design. Previous experiments [1, 2] have indicated that a constant area diffuser must have a length-to-diameter ratio on the order of ten for the shock structure within the diffuser to diffuse the flow to subsonic speeds with a nearly complete pressure rise. Various attempts have been made to reduce this length by such techniques as subdividing the diffuser into a number of smaller channels [3, 4] and by adding vanes to the diffuser to help dissipate the flow within the supersonic core [5].

The subject of this paper is a series of studies concerning flow injection into a diffuser in a direction opposite to that of the main flow [6, 7]. This reverse flow is intended to reduce the size of the diffuser without introducing the complexity

associated with variable geometry configurations. The injected stream dissipates the supersonic core flow in a manner conceptually similar to that promoted by the vanes of Reference 5. Theoretical and experimental investigations were conducted concerning the effects of this reverse flow on the performance of single-stream and dual-stream constant area diffusers as well as sudden enlargement configurations. The sudden enlargement is a special case of the dual-stream diffuser with the flow rate of one stream reduced to zero. Special attention was paid to the effects of this reverse flow on both the length required for diffusion and the maximum pressure rise attained by the diffuser.

Analysis

The effects of reverse flow on some aspects of diffuser performance were predicted by quasi-one-dimensional control volume analyses of the configurations under consideration. Because of the similarity between the single- and dual-stream diffuser configurations, a single analysis, sufficient for both cases, predicts the exit conditions of the diffuser. A second analysis for the sudden enlargement configuration predicts the base pressure rather than the exit conditions. Although the sudden enlargement diffuser could have been considered a special case of the dual-stream diffuser with one of the Mach numbers reduced to zero, the

Contributed by the Fluids Engineering Division and presented at the Winter Annual Meeting, Phoenix, Ariz., November 15-19, 1982, of THE AMERICAN SOCIETY OF MECHANICAL ENGINEERS. Manuscript received by the Fluids Engineering Division, December 28, 1981. Paper No. 82-WA/FB-7.

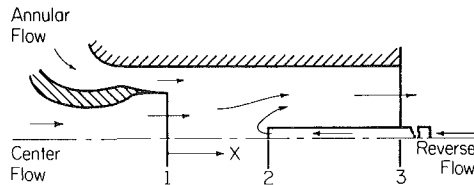


Fig. 1(a) Flow configuration for the dual-stream diffuser with reverse flow

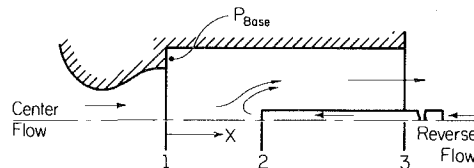


Fig. 1(b) Flow configuration for the sudden enlargement with reverse flow

Fig. 1 Diffuser flow configurations

importance of predicting the base pressure dictated a separate analysis for this case.

The basic flow configuration for the dual-stream supersonic diffuser with reverse flow is shown in Fig. 1(a). The two supersonic streams are introduced into the diffuser at station 1. At station 2 the reverse flow is introduced into the diffuser, and the resultant mixed flow exits the diffuser at station 3. The basis for this one-dimensional analysis is the solution of the conservation equations of mass, momentum, and energy. The assumptions made in this analysis are typical of most one-dimensional approaches and include such factors as steady, uniform flow at stations 1, 2, and 3, negligible shear stresses and heat transfer at the diffuser walls and ideal gas properties.

The independent variables which are assumed to be known include the geometry of the configuration and the properties of the three entering streams. Since this analysis is one-dimensional, the diffuser length and reverse flow tube location do not enter into the equations. Combining the three basic conservation equations results in a quadratic equation for M_3 , the exit Mach number, with a supersonic and a subsonic solution. The values of these solutions differ by that of a normal shock wave occurring at the supersonic solution. It should be noted that all of the necessary input quantities can be either measured or determined in an experimental apparatus with the exception of the reverse flow Mach number M_{R2} . Based on a Fanno flow analysis of the reverse flow tube, the reverse flow Mach number was taken equal to unity as a result of frictional choking within the reverse flow tube. The exit conditions of the reverse flow tube are considered in greater detail in the sudden enlargement analysis.

The theoretical analysis for the sudden enlargement configuration is similar to the analysis described previously. Figure 1(b) shows the basic flow configuration. The one-dimensional assumptions and the conservation equations of mass, momentum, and energy are used. The remaining assumptions are the same except that the flow at station 3 is

assumed to be subsonic and shock waves may exist within the diverging portion of the converging-diverging nozzle supplying the main stream. The parameters which are assumed to be known include the basic geometry, pressure ratios, and reverse flow Mach number. For a converging-diverging nozzle and sudden enlargement diffuser combination, three nozzle operating regimes are possible: subsonic flow throughout the nozzle, choked flow in the nozzle throat with a normal shock wave standing in the diverging portion, and totally supersonic flow within the nozzle. Because of these various operating regimes, the theoretical analysis must determine which nozzle operating regime exists in order to predict the base pressure. In situations in which the flow expands upon entering the sudden enlargement and attaches to the enlargement walls, the flow is highly two-dimensional and dominated by viscous effects. Thus, this one-dimensional analysis cannot deal with this flowfield, and no attempt is made to predict the base pressure under these conditions.

For the dual-stream diffuser analysis, the reverse flow Mach number is assumed to have a value of unity. For the sudden enlargement configuration, a more detailed Fanno flow analysis is applied to the reverse flow tube. In order to determine the reverse flow exit pressure and Mach number, additional properties of the reverse flow and reverse flow tube, including the friction factor of the flow in the tube and the stagnation pressure of the flow entering the tube, must be known. With these quantities, which must be determined experimentally, an improved estimate of the reverse flow properties is obtained. A comparison of these two analysis techniques is presented with the results of the experimental program.

Further details concerning the diffuser analyses may be found in references [6 and 7].

Experiments

The experimental portion of this investigation was conducted utilizing a test facility which provided compressed air for continuous flow operation. For the single- and dual-stream diffuser experiments, the test apparatus consisted of concentric, continuous-slope nozzles used in conjunction with constant area diffuser tubes. Figure 2(a) shows a half section view of the experimental apparatus. One of the streams accelerated from a stagnation chamber through the center nozzle while the other stream accelerated from a separate stagnation chamber through the annular outer nozzle. Mach number combinations of $M_{C1}=2.5$, $M_{A1}=2.5$, and $M_{C1}=2.5$, $M_{A1}=2.0$ were possible. Table 1 lists the dimensions of the various experimental components. In all cases the stagnation pressures were adjusted so that the static pressures of the entering streams were matched at the nozzle exit. Thus for the $M_{C1}=2.5$, $M_{A1}=2.5$ case, the two nozzles essentially provided a single stream entering the diffuser tube except for the effect of a small nozzle base area. Several diffuser tubes of different length-to-diameter ratio were used with static pressure taps located along the walls. A back pressure control valve located at the exit of the diffuser tube was utilized to control the exit pressure.

Nomenclature

A = area
 D = diffuser tube diameter
 L = diffuser tube length
 M = Mach number
 P = absolute pressure
 Re = nozzle throat Reynolds number based on diameter

W = mass flow rate
 X = flow direction coordinate
Subscripts
 A = annular nozzle flow property

BASE = base region property
 C = center nozzle flow property
 R = reverse flow property
 RT = reverse tube
 0 = stagnation state
 $1,2,3$ = system locations

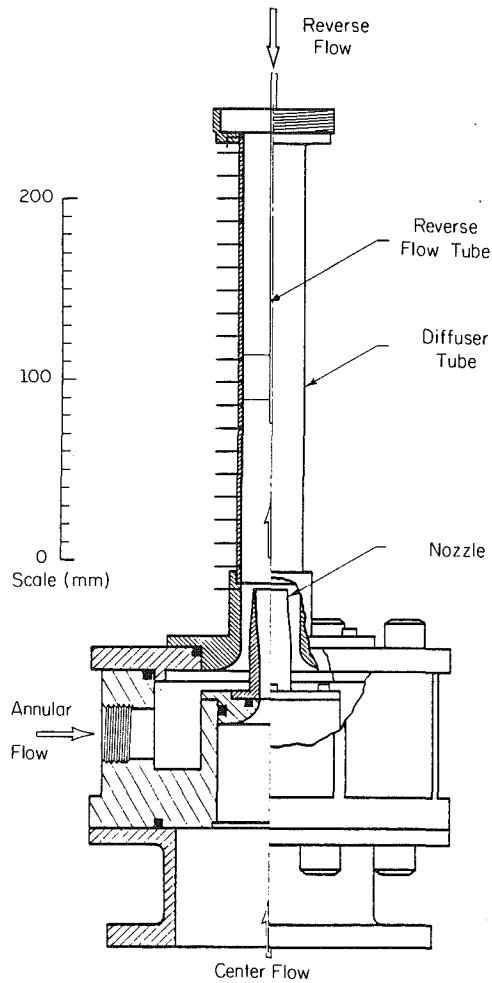


Fig. 2(a) Half section view of the dual-stream diffuser experimental apparatus

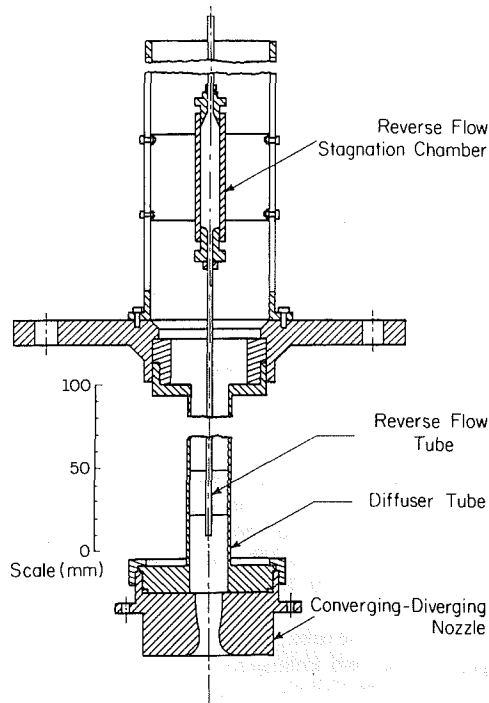


Fig. 2(b) Section view of the sudden enlargement experimental apparatus

Fig. 2 Experimental diffuser apparatus

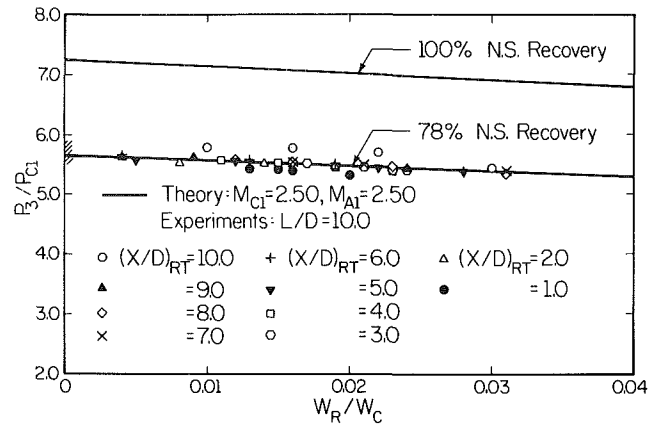


Fig. 3(a) Theoretical and experimental pressure recovery for the single-stream diffuser. (Uncertainty in $P_3/P_{C1} = \pm 0.2$, in $W_R/W_C = \pm 0.002$)

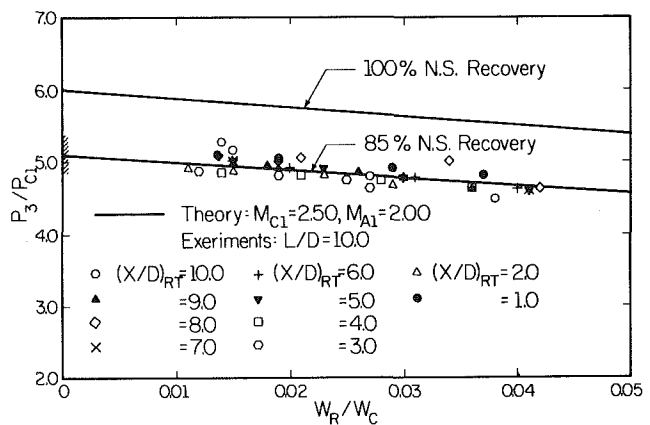


Fig. 3(b) Theoretical and experimental pressure recovery for the dual-stream diffuser. (Uncertainty in $P_3/P_{C1} = \pm 0.2$, in $W_R/W_C = \pm 0.002$)

The reverse flow was injected through a small diameter tube which entered through the back pressure control valve and was held in place by three equally spaced guide vanes near its exit. The mass flow rates were measured with standard VDI measurement sections and are believed to be accurate to within five percent. The two primary mass flow rates were regulated with automatic control valves, while the reverse flow was regulated with a manually operated needle valve. Pressures were measured to within an accuracy of three percent using either unbonded strain-gage pressure transducers, precision pressure gages, or mercury manometers. No boundary layer measurements were attempted in this series of experiments.

For the single- and dual-stream diffuser experiments, the stagnation pressures were maintained at values of $P_{OC} = 376.7$ kPa and $P_{OA} = 153.4$ kPa for the $M_{C1} = 2.5$, $M_{A1} = 2.0$ configuration and $P_{OC} = 286.0$ kPa and $P_{OA} = 279.1$ kPa for the $M_{C1} = 2.5$, $M_{A1} = 2.5$ configuration. These values yielded nozzle throat Reynolds numbers of $Re_C = 5.49 \times 10^5$, $Re_A = 7.90 \times 10^5$ and $Re_C = 4.29 \times 10^5$, $Re_A = 9.06 \times 10^4$, respectively. With these values, the static pressures at the confluence point of the two streams were matched. Data were taken with different reverse mass flow rates and reverse tube positions for each diffuser tube. In all cases, the back pressure control valve was adjusted such that the beginning of the shock structure was located at the exit plane of the annular nozzle. This flow condition may be thought of as the diffuser maximum compression condition and it was determined by

Table 1 Experimental apparatus configurations

Configuration	Single stream	Dual stream	Sudden enlargement
Center Stream			
Mach number	2.50	2.50	2.05
Nozzle throat diameter	11.18	11.18	11.95
Nozzle exit diameter	18.16	18.16	15.85
Annular Stream			
Mach number	2.50	2.00	---
Nozzle throat inner diameter	22.99	21.59	---
Nozzle throat outer diameter	25.27	25.27	---
Diffuser tube inner diameter	25.27	25.27	18.97 or 22.20
Reverse tube inner diameter	2.77	2.77	2.77

Note: All dimensions in millimeters, with uncertainty of ± 0.05 millimeters.

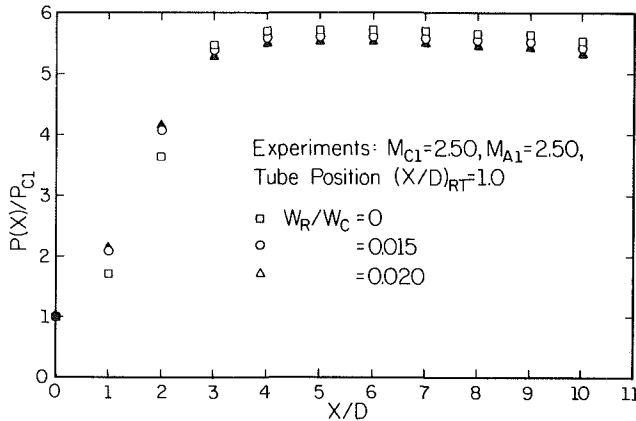


Fig. 4 Pressure profiles for the single-stream diffuser configuration. (Uncertainty in $P(X)/P_{C1} = \pm 0.2$, in $X/D = \pm 0.01$)

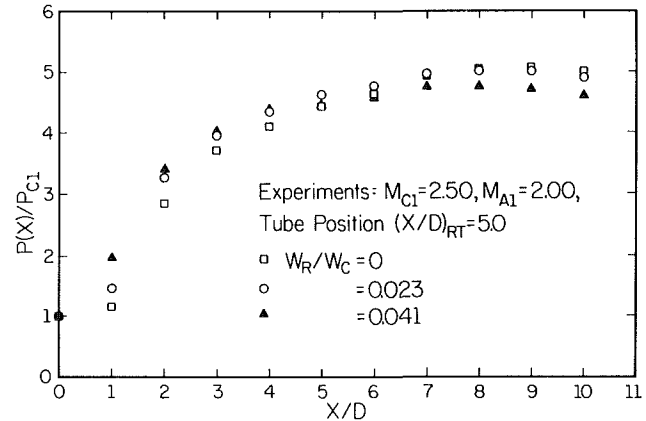


Fig. 5 Pressure profiles for the dual-stream diffuser configuration. (Uncertainty in $P(X)/P_{C1} = \pm 0.2$, in $X/D = \pm 0.01$)

the appearance of a slight pressure rise at the nozzle exit pressure tap. The maximum reverse flow used for these experiments was the flow rate which caused the shock structure to be located at the nozzle exit plane when the back pressure control valve was fully open.

The sudden enlargement experimental configuration consisted of a converging-diverging nozzle with design Mach number of 2.05 supplying the primary stream and a constant-area diffuser tube with inner diameter greater than the nozzle exit diameter forming the enlargement section. Figure 2(b) shows a section view of this test apparatus. Two diffuser tubes were used to provide two diffuser-to-nozzle exit area ratios. The dimensions of these components are also listed in Table 1. Pressure taps were located at the nozzle exit, in the base region, and longitudinally along the diffuser tubes. For this series of experiments, a stagnation chamber was attached to the reverse flow tube. Thus, it was possible to determine the reverse flow stagnation pressure and, when combined with the measured reverse mass flow, it was possible to use a Fanno flow analysis to estimate the reverse flow tube exit static pressure and Mach number. Because of the location of this stagnation chamber and its supporting structure, it was not possible to use the back pressure control valve.

Two series of experiments were conducted with the sudden enlargement diffuser configuration. In the first series, the primary stagnation pressure was maintained at a value which yielded the pressure ratio $P_3/P_{0C} = 0.5$ and a nozzle throat Reynolds number of approximately $Re_C = 3.5 \times 10^5$. This pressure ratio ensured that the nozzle flow was entirely supersonic without the flow being attached to the diffuser wall. Various reverse tube positions and reverse mass flow rates were used which included the no-reverse tube con-

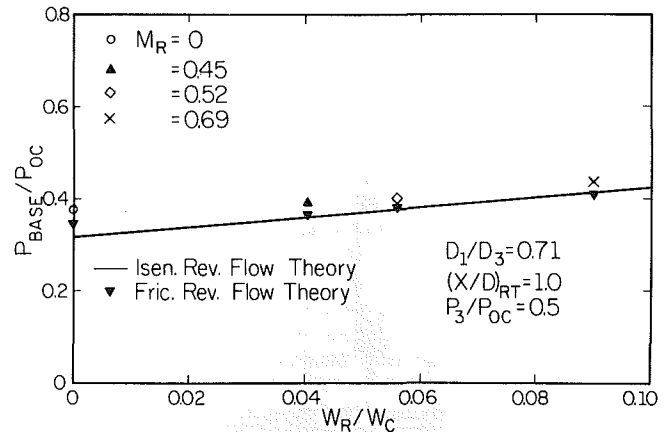


Fig. 6 Theoretical and experimental base pressure for the sudden enlargement configuration. (Uncertainty in $P_{BASE}/P_{0C} = \pm 0.015$ in $W_R/W_C = \pm 0.005$)

figuration. Both enlargement tubes were used in this series of experiments. In the second series, the primary stagnation pressure was maintained to yield the pressure ratio $P_3/P_{0C} = 0.2$ and a nozzle throat Reynolds number of approximately $Re_C = 8.0 \times 10^5$. For this pressure ratio, the flow was attached to the diffuser wall. Again, several reverse flow rates and reverse tube positions were used, however, only the larger of the two enlargement tubes was used for this series.

Results

Figure 3 compares the results of the quasi-one-dimensional

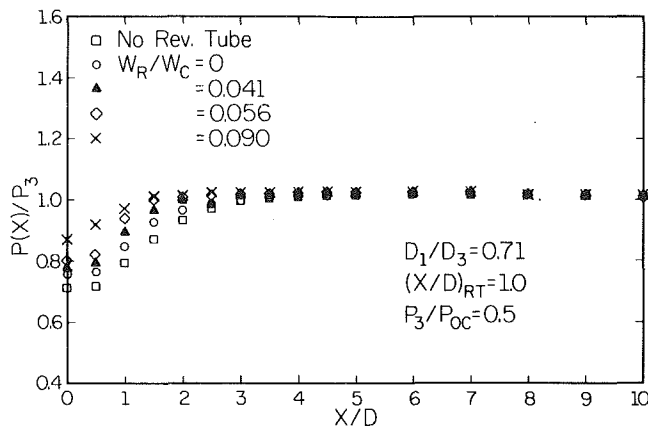


Fig. 7 Pressure profiles for the sudden enlargement configuration. (Uncertainty in $P(X)/P_3 = \pm 0.03$, in $X/D = \pm 0.01$)

analysis to the experimental data for typical cases of the single-stream and dual-stream diffuser configurations. The results are presented as the diffuser compression ratio P_3/P_{C1} as a function of the reverse flow tube-to-center nozzle mass flow ratio W_R/W_C . Data points for various reverse tube positions are shown. Due to the amount of data taken with no reverse flow, only the ranges of these data are shown plotted on the vertical axes. The lines denoted by "100 percent Normal Shock Recovery" represent the results of the theoretical analysis while the other curves on this figure represent the theoretical results modified with an empirical normal shock recovery factor. Thus, it can be seen that, when modified with an empirical recovery factor, the analyses represent well the experimental data. It can also be seen from these figures that with increasing reverse flow the pressure recovery decreases although this decrease is not large. In all cases, the empirical normal shock recovery factor has been found to range from 0.77 to 0.85. The introduction of an oblique shock system by the reverse flow should act to reduce losses over that for the equivalent normal shock, but this effect is apparently more than offset by increased losses due to shock wave boundary layer interactions. By comparing Figs. 3(a) and 3(b) it is seen that the pressure recovery factor is somewhat higher for the dual-stream configuration than it is for the single-stream case although the dual-stream data are somewhat more scattered.

Experiments were conducted in which the back pressure valve was fully open and the reverse flow was increased until the shock structure was located in the nozzle exit plane. For the equivalent single-stream configuration, ($M_{C1} = 2.5$, $M_{A1} = 2.5$), this maximum reverse mass flow ratio (W_R/W_C) varied from 0.02 to 0.04. For the dual-stream configuration ($M_{C1} = 2.5$, $M_{A1} = 2.0$), the maximum reverse mass flow ratio varied from 0.03 to 0.05. In a number of cases, particularly with short diffuser tubes, shock instabilities were present which, in some cases, rendered data acquisition difficult.

Figures 4 and 5 show typical wall static pressure profiles for the single- and dual-stream diffusers. For these figures the pressures have been nondimensionalized with the center stream nozzle exit plane static pressure, P_{C1} . As can be seen in these figures, the effect of the reverse flow is to increase the initial rate of axial pressure rise while, as indicated previously, the diffuser exit static pressure is somewhat reduced. Thus it becomes apparent that a trade-off is made between a steeper axial pressure gradient (and thus shorter diffusers) and higher pressure recovery. Figure 5 shows that near the exit of the reverse flow tube, local expansion can occur as a result of an effective blockage produced by the reverse flow. This is seen as a drop in static pressure near the exit of the reverse tube at a

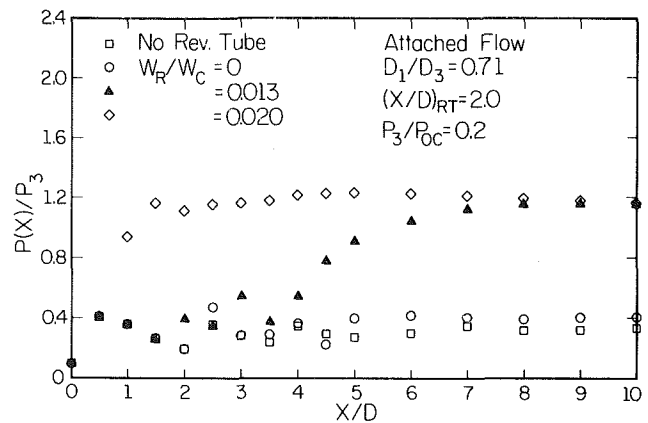


Fig. 8 Pressure profiles for the sudden enlargement configuration with the flow attached to the diffuser wall. (Uncertainty in $P(X)/P_3 = \pm 0.03$, in $X/D = \pm 0.01$)

value of X/D equal to 5 or 6. It should be noted that from a survey of all of the experimental data obtained, the single-stream diffusion processes, ($M_{C1} = 2.5$, $M_{A1} = 2.5$), require less tube length for full pressure recovery than do the dual-stream diffusion processes ($M_{C1} = 2.5$, $M_{A1} = 2.0$).

Figure 6 shows, typically, the effect on the base pressure of the reverse mass flow ratio, W_R/W_C , on the sudden enlargement configuration with $P_3/P_{OC} = 0.5$. The base pressure has been nondimensionalized with the center stream stagnation pressure, P_{OC} . Shown in this figure are the experimental data points, the theoretical points determined from the Fanno flow analysis of the reverse flow tube, and a theoretical line which results from the assumption of choked flow at the reverse tube exit. As can be seen from the figure, the Fanno flow analysis does not significantly improve the choked reverse flow theoretical predictions. The errors between the theory using the Fanno flow analysis and experiment are on the order of 4 to 26 percent and have been found to decrease with increasing area ratio, A_3/A_1 .

Figure 7 is typical of the longitudinal pressure profiles obtained with the sudden enlargement configuration when the flow is not attached to the diffuser tube wall, $P_3/P_{OC} = 0.5$. The pressure is nondimensionalized with respect to the exit pressure, P_3 . As can be seen, the effect of the reverse flow is to reduce the tube length required for full pressure recovery. In general it was found experimentally that the best reverse tube location was at a value of $X/D = 1$. With the optimum reverse flow rate, the diffusion length can be reduced from approximately five to approximately two enlargement tube diameters, which represents a significant reduction in the required diffuser length.

Figure 8 is typical of the diffusion pressure profiles obtained from the sudden enlargement configuration with the primary flow attached to the enlargement tube walls and $P_3/P_{OC} = 0.2$. As can be seen from this figure, the effect of the reverse flow is to cause the diffusion process to begin closer to the nozzle exit. The pressure in the base region and upstream of the beginning of the diffusion process is essentially unaffected by the presence of the reverse flow. Thus, it is apparent that the reverse flow has an effect similar to the back pressure control valve and can be used to regulate the position of the shock structure within the diffuser tube.

Conclusions

From the results of this investigation, it is apparent that reverse flow can be used to favorably control the supersonic diffusion process. In both the single-stream and dual-stream

diffusers, the reverse flow can be used to increase the axial pressure gradient within the diffuser while causing only a slight decrease in pressure recovery. For the sudden enlargement configuration with the flow unattached to the enlargement walls, the reverse flow can reduce significantly the length required for the diffusion process as well increase the pressure in the base region. For both configurations, it is apparent that reverse flow can also be used as a back pressure regulating device in situations where a mechanical valve arrangement is not practical.

References

1 Neumann, E. P., and Lustwerk, F., "Supersonic Diffusers for Wind Tunnels," *ASME Journal of Applied Mechanics*, Vol. 16, June 1949, pp. 195-202.

2 Merkli, P. E., "Pressure Recovery in Constant Area Supersonic Diffusers," Scientific Report 2, Department of Engineering and Applied Science, Yale University, Sept. 1974.

3 Neumann, E. P., and Lustwerk, F., "High Efficiency Supersonic Diffusers," *Journal of the Aeronautical Sciences*, Vol. 18, June 1951, pp. 369-374.

4 Neice, S. E., and Russell, D. A., "Screen Diffuser for Gas Dynamic Lasers," Report No. MSNW-73-114-1, Mathematical Sciences, Northwest, Inc., May 1974.

5 Hasinger, S. H., and Miller, D. K., "Two-Dimensional Supersonic Diffuser Experiments," *AIAA Journal*, Vol. 13, No. 4, Apr. 1975, pp. 536-538.

6 White, S. H., Dutton, J. C., and Addy, A. L., "Theoretical and Experimental Investigation of the Constant-Area, Supersonic-Supersonic Diffuser with Reverse Flow," Department of Mechanical and Industrial Engineering, University of Illinois at Urbana-Champaign, Report No. UILU-ENG-78-4016, 1978.

7 Kuntz, D. W., "Theoretical and Experimental Investigation of the Sudden Enlargement with Reverse Flow," M.S. thesis, Department of Mechanical and Industrial Engineering, University of Illinois at Urbana-Champaign, 1981.

R. E. Wilson

Professor,
Mechanical Engineering,
Oregon State University,
Corvallis, Oreg. 97331

P. B. S. Lissaman

Vice President,
AeroVironment, Inc.,
Pasadena, Calif.

M. James

Consultant,
Phoenix, Ariz.

W. R. McKie

Research Assistant,
Climatic Research Institute,
Oregon State University,
Corvallis, Oreg.

Aerodynamic Loads on a Darrieus Rotor Blade

A free-vortex analysis of a Darrieus rotor blade in nonsteady motion has been developed. The method uses the circle theorem to map a moving airfoil into the circle plane. The wake is modeled using point vortices. Nascent vortex strength and position are determined from the Kutta condition so that the nascent vortex has the same strength as a vortex sheet of uniform strength. The force on the airfoil is determined by two methods, integration of the pressure over the plate and from the impulse of the wake vortices. Both methods yield the same numerical results. A comparison with an analytical solution for a plunging airfoil gives excellent agreement. Results are shown for a one-bladed Darrieus Rotor at a tip speed ratio of three and two chord sizes. The numerical results indicate that the forces and moment on a Darrieus Rotor blade may be adequately approximated by quasi-steady relationships although accurate determination of the local velocity and circulation are still required.

Introduction

The blades of a Darrieus Rotor follow a circular path with significant cyclic variations in relative velocity and angle of attack. To date, the determination of loads and performance of Darrieus Rotors have been accomplished using quasi-steady aerodynamics [1-8]. In these approaches, the forces on the airfoil are the Kutta-Joukowski lift acting at quarter-chord and drag. Lift and drag coefficients are taken from static airfoil data. Since Darrieus Rotor blades rotating at angular velocity Ω have a pitch rate Ω as well as wake crossing and significant cyclic variations in relative velocity and angle of attack, the use of quasi-steady aerodynamics for the determination of forces and moments has been questioned [9-10]. The purpose of this investigation is to calculate the loads on a Darrieus Rotor blade and to compare these calculated loads with the loads calculated using a quasi-steady approach. The idealized case of a single blade in a two-dimensional flow covers all the significant features of the flow except stall.

The calculation of airfoil forces and moments in general unsteady motion can be performed by analytical methods given a point-vortex numerical simulation of the wake. Furthermore the best procedure is the most obvious one based on integration of the pressure equation [11]. Since a search of the literature on point-vortex numerical simulation failed to give an indication of how shed vorticity was situated in the flow, secondary objectives of this investigation were to develop a method for nascent vortex location and to check the method for accuracy.

Contributed by the Fluids Engineering Division for publication in the JOURNAL OF FLUIDS ENGINEERING. Manuscript received by the Fluids Engineering Division, March 4, 1982.

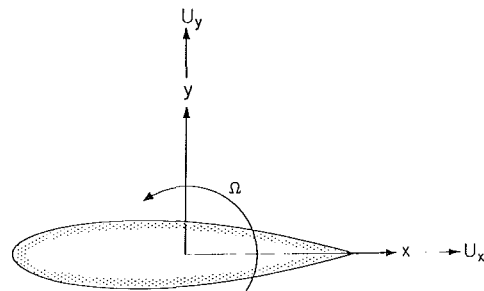


Fig. 1 Moving airfoil

Blasius Theorem for Unsteady Flow

Milne-Thomson [12] develops the expression for the conjugate force and the moment on a moving cylinder. The cylinder, which is mapped into a flat plate is shown in Fig. 1 and is fixed with respect to the x, y coordinate system. The x, y coordinate system is rotating with angular velocity Ω and the origin is translating with conjugate velocity $Q = U_x - iU_y$. The shed vorticity is represented by point vortices of strength $\kappa_n = \Gamma_n/2\pi$ where Γ_n is the circulation.

Specializing the results given by Milne-Thomson to the case of the flat plate, the conjugate force, $X - iY$, is given by

$$X - iY = \frac{i\rho}{2} \int_A \left(\frac{dw}{dz} \right)^2 dz - \Omega\rho \int_A \bar{z} d\bar{w} + i\rho \frac{\partial}{\partial t} \int_A \bar{w} d\bar{z} + i2\pi\kappa_c\rho Q \quad (1)$$

and the moment is given by

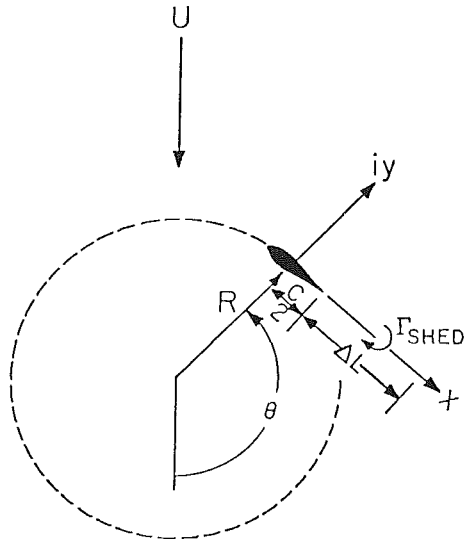


Fig. 2 Darrieus Rotor coordinate system

$$M = \text{REAL PART} \left[-\frac{\rho}{2} \int_A z \left(\frac{dw}{dz} \right)^2 dz + \rho Q \int_A z dw - \rho \frac{\partial}{\partial t} \int_A z w d\bar{z} \right] \quad (2)$$

Here A represents the bounding curve of the flat plate and w is the complex potential defined such that the derivatives dw/dz yields the conjugate velocity. The circulation about the flat plate is given by $2\pi\kappa_c$.

The integrals above may be evaluated by transforming from the z plane to the ζ plane. In the ζ plane the flat plate is transformed into a circle using $z = \zeta + r^2/\zeta$ where r is the radius of the circle. The complex potential on the boundary of the circle is given by

$$w(\zeta) = B_1(\zeta) + i\kappa \ln \zeta + \sum_{n=1}^N i\kappa_n \ln(\zeta - \zeta_n) - \sum_{n=1}^N i\kappa_n \ln(\zeta - \zeta_n^*) \quad (3)$$

Here ζ_n is the position of the n th shed vortex and ζ_n^* is the position of its image and

$$B_1(\zeta) = 2iI(Q) \frac{r^2}{\zeta} - i\Omega \frac{r^4}{\zeta^2}$$

Complex Force and Moment

The complex force may be written in terms of circle coordinates as

$$X - iY = \left\{ \begin{array}{l} \frac{i\rho}{2} \left(4\pi \Sigma \kappa_n q_n^* - i2\pi \Sigma \frac{\kappa_n^2 c^2}{8\zeta_n^3 \left(1 - \frac{c^2}{16\zeta_n^2}\right)^2} \right) \\ -\Omega \rho \left[-\frac{\pi c^2}{4} I(Q) + \Sigma 2\pi \kappa_n \left(\zeta_n^* + \frac{c^2}{16\zeta_n} \right) \right] \\ + i2\pi \kappa_c \rho Q \\ + i\rho \Omega \frac{\partial}{\partial t} \left[-\frac{\pi c^2}{4} I(Q) - 2\pi \kappa_c \frac{c}{2} \right. \\ \left. - \Sigma 2\pi \kappa_n \left(\zeta_n^* + \frac{c^2}{16\zeta_n} \right) \right] \end{array} \right\} \quad (4)$$

The above relation may be restated in dimensionless form as

$$c_F \equiv \frac{X - iY}{\rho U^2 R} \quad (5)$$

where R is an appropriate characteristic length.

The above expression may be cast into variables associated with the airfoil plane in lieu of the circle-plane. First we scale the velocities with U and the circulations with UR so that

$$q_i \equiv \frac{(\text{COMPLEX VELOCITY})_i}{U} \quad \text{and} \quad \gamma_n \equiv \Gamma_n / UR = \frac{2\pi\kappa_n}{UR}$$

Second, we define the following terms:

- q_{0_n} is the complex velocity at the origin in the airfoil plane induced by the n th vortex
- $q_{L.E.n}$ is the complex velocity at the leading edge induced by the n th vortex
- $q_{T.E.n}$ is the complex velocity at the trailing edge induced by the n th vortex

Nomenclature

- A = bounding curve of the airfoil
- B_1 = boundary function
- c = blade chord
- C_F = conjugate force coefficient
- C_L = blade lift coefficient
- C_M = blade moment coefficient (about $c/2$)
- C_N = blade normal force coefficient
- C_T = blade tangential force coefficient
- $I(Q)$ = imaginary part of Q
- I = impulse
- $i = \sqrt{-1}$
- M = moment about half chord position
- N = number of shed vortices
- Q = conjugate velocity of airfoil
- q_n^* = conjugate velocity of n th vortex in the airfoil plane

- r = radius of the circle in the circle plane
- R = scaling length; Darrieus Rotor, radius; plunging airfoil, chord
- t = time
- u_n = x -direction velocity of the n th vortex
- U = free stream wind speed
- $U_x = -R\Omega - U \sin \theta$
- $U_y = -U \cos \theta$
- V_c = conjugate velocity of the fluid relative to the blade
- W = magnitude of V_c
- x = x -direction
- X = force in the x -direction
- y = y -direction
- Y = force in the y -direction
- z = complex variable = $x + iy$

- α = angle of attack
- β = blade position = $\theta - \pi/2$
- γ = circulation = Γ / UR
- Γ = circulation of vortex
- ζ_n = position of the n th vortex in the circle plane
- ζ_n^* = position of the n th image vortex in the circle plane = $r^2 \zeta_n^{-1}$
- θ = angular position of blade
- κ = circulation = $\Gamma / 2\pi$
- ρ = fluid density
- ρ_n = radial distance in circle plane
- τ = dimensionless time = Ut/c
- ϕ = velocity potential
- ϕ_n = angular position of n th vortex in circle plane $\zeta_n = \rho_n e^{i\phi_n}$
- ω' = strength of shed vortex sheet
- Ω = blade angular velocity

γ_p is the pitching circulation $-\frac{\pi c^2 \Omega}{4} \left(\frac{1}{UR} \right)$

q_n^* is the complex velocity induced at the n th vortex by all causes.

Using these definitions and the transformation from circle to airfoil coordinates, equation (4) may be written in dimensionless form as

$$C_F \equiv \frac{X - iY}{\rho U^2 R} = \left\{ \begin{array}{l} i \Sigma \gamma_n \left(q_n^* - q_{0n} + \frac{q_{T.E.n} + q_{L.E.n}}{2} \right) \\ \gamma_p I \left(\frac{Q}{U} \right) - \frac{\Omega R}{U} \Sigma \frac{\gamma_n}{R} \left(\xi_n^* + \frac{c^2}{16 \xi_n} \right) \\ i \gamma_c \left(\frac{Q}{U} \right) \\ -i \frac{\partial}{\partial t} \left[\frac{\pi c^2}{4UR} I \left(\frac{Q}{U} \right) + \frac{c}{2U} \gamma_c \right. \\ \left. + \frac{1}{U} \Sigma \gamma_n \left(\xi_n^* + \frac{c^2}{16 \xi_n} \right) \right] \end{array} \right\} \quad (6)$$

It may be noted that two terms have been left in terms of circle coordinates. The terms are written in the same order as in equation (4). In the bottom line, which is due to the $\partial \phi / \partial t$ term in the Bernoulli equation, the time variable has not been scaled. For the plunging airfoil we take $R = c$ and use $\tau = Ut/c$. For the Darrieus case, Ω is constant and we use $\theta = \Omega t$ as the independent variable.

It may be noted that the $\partial \phi / \partial t$ term contributes only to the force normal to the airfoil and the pitching term (2nd line of equation (6)) contributes only to the force parallel to the airfoil.

Using the same method as used with the conjugate force, a moment coefficient can be expressed as

$$C_M \equiv \frac{M}{\rho U^2 R^2}$$

The moment coefficient may be expressed as

$$C_M = \text{real} \left\{ \begin{array}{l} -\Sigma \gamma_n q_n^* \frac{z_n}{R} - \Sigma \gamma_n \left(\frac{q_{T.E.n} + q_{L.E.n}}{2} \right. \\ \left. - q_{0n} \right) \frac{z_n}{R} \\ \frac{Q}{U} \left[-\frac{\pi}{4} \left(\frac{c}{R} \right)^2 I \left(\frac{Q}{U} \right) \right. \\ \left. + \Sigma \frac{\gamma_n}{R} \left(\xi_n^* + \frac{c^2}{16 \xi_n} \right) \right] \\ \frac{\partial}{\partial t} \left[\frac{\pi}{128} \left(\frac{c}{R} \right)^2 \frac{c^2 \Omega}{U} + \frac{c^2 \gamma_c}{16UR} \right. \\ \left. + \frac{R}{2U} \Sigma \frac{\gamma_n}{R^2} \left(\xi_n^{*2} + \left(\frac{c}{4} \right)^4 \frac{1}{\xi_n^2} \right) \right] \end{array} \right\} \quad (7)$$

Alternate Method for Force Calculations

The approach given above was developed by integration of the pressure on the airfoil. Since the wake is to be modeled by discrete vortices, and these vortices are supposed to be free of external forces, being convected in the local flow, an alternate method to calculate the forces using the wake vortices has been used. Theodorsen [13] has shown that the fluid

momentum of a body in an infinite fluid can be written in complex form as

$$I = -i \oint w dz \quad (8)$$

Using equation (3) for the complex potential and performing the integration around a path that is deformed into an infinite radius circle we obtain

$$I = 2\pi i \{ 2r^2 I(Q) - \Sigma \kappa_n (\xi_n - \xi_n^*) \}$$

Since the time derivative of the impulse is the force, successive evaluation of I at different positions of the airfoil can be used via numerical differentiation to determine the force on the airfoil. Equation (8) involves only the velocity normal to the airfoil and the shed vortices. The force evaluated in this manner can be compared with the pressure integration on the airfoil surface. Errors in the vortex kinematics and the positioning of the shed vortex both cause the wake not to be force-free.

Kinematics

The vortices are advanced with each time step Δt using a backward difference approach. At time t , the velocities induced at a vortex are calculated. The new x -position is determined from

$$x_n(t + \Delta t) = x_n(t) + 1/2 [3u_n(t) - u_n(t - \Delta t)] \Delta t \quad (9)$$

where u_n is the x -direction velocity of the n th vortex. A similar expression was used for $y_n(t)$. This method was found to give small but noticeable improvement over straight extrapolation. Each vortex carries the same circulation through its trajectory in the wake. The magnitude of the circulation of each external vortex is fixed at the time it is shed.

Circulation

Circulation is conserved and as a result of the system starting with zero circulation, the total circulation in the system at any time t remains zero. The total circulation given by

Sum of free vortices	$\sum_{n=1}^N \gamma_n$
Sum of image vortices	$-\sum_{n=1}^N \gamma_n$
Sum of induced center vortices	$\sum_{n=1}^N \gamma_n^c$
Quasi-steady term	$\gamma_{Q.S.}$
Pitching term	γ_p

The last three terms when transformed from the airfoil plane to the circle plane are located at the center of the circle. It may be noted that at any time t that

$$\sum_{n=1}^N \gamma_n^c + \gamma_{Q.S.} + \gamma_p = 0 \quad (10)$$

since the external and image circulations cancel each other.

Consider the system of time $t + \Delta t$ after the vortices and the airfoil have been moved to their new positions in the airfoil plane. The coordinates of each free vortex may be transformed to the circle plane where the induced center circulation corresponding to the nascent vortex may be calculated from

$$\gamma_{N+1}^c = -\gamma_{Q.S.} - \gamma_p - \sum_{n=1}^N \gamma_n^c \quad (11)$$

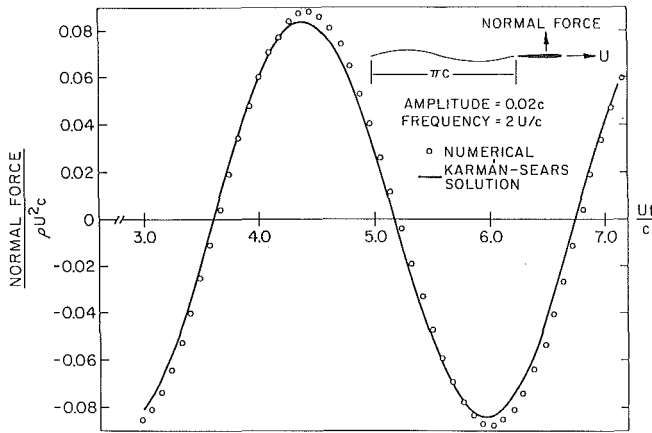


Fig. 3 Point vortex method comparison with Karman-Sears solution

Here

$$\gamma_{Q.S.} = \frac{\Gamma_{Q.S.}}{UR} = \pi \frac{c}{R} U_y/U$$

$$\gamma_p = \frac{\Gamma_p}{UR} = -\frac{\pi}{4} \left(\frac{c}{R}\right) \frac{c\Omega}{U}$$

$$\gamma_n^c = \frac{\Gamma_n c}{UR} = \gamma_n \frac{\rho_n^2 - 1}{\rho_n^2 - 2\rho_n \cos \phi_n + 1}$$

where the position of the n th vortex in the circle plane is given by $\zeta_n = \rho_n e^{i\phi_n}$. Once the magnitude of the center induced circulation of the nascent vortex is determined it remains to find both the magnitude and position of this vortex. *The vortex on the airfoil is quite sensitive to the location of the nascent vortex.*

Nascent Vortex

The relation between the strength of the nascent vortex and the center induced circulation is determined from the Kutta Condition. In the circle plane this relation is

$$\frac{\Gamma_{n+1}^c}{\Gamma_{n+1}} = \frac{\gamma_{n+1}^c}{\gamma_{n+1}} = \frac{\rho_{n+1}^2 - 1}{\rho_{n+1}^2 - 2\rho_{n+1} \cos \phi_{n+1} + 1} \quad (12)$$

If the nascent vortex is assumed to be located along the x -axis as shown in Fig. 2 the above relation can be transformed to a simple expression in the airfoil plane

$$\Gamma_{n+1}^c = \Gamma_{n+1} \sqrt{\frac{2x_{n+1} + c}{2x_{n+1} - c}} \quad (13)$$

The assumption that the nascent vortex lies on the x -axis simplifies the analysis greatly. Although we speak of a single vortex being shed from the airfoil, in reality the vorticity is being shed continuously in the form of a sheet. A first approximation to the problem is that the sheet is of constant strength $\omega' = \Gamma_{n+1}/\Delta L$. Rewriting equation (13) one obtains for a sheet of length ΔL

$$\Gamma_{n+1}^c = \int_{c/2}^{c/2 + \Delta L} \sqrt{\frac{2x_{n+1} + c}{2x_{n+1} - c}} \omega' dx$$

so that

$$\frac{\Gamma_{n+1}}{\Gamma_{n+1}^c} = \frac{\gamma_{n+1}}{\gamma_{n+1}^c} = \frac{\Delta L/c}{\sqrt{\frac{\Delta L}{c} \left(1 + \frac{\Delta L}{c}\right)} + \ln \left(\sqrt{\frac{\Delta L}{c}} + \sqrt{1 + \frac{\Delta L}{c}} \right)} \quad (14)$$

Thus if we know the value of γ_{n+1}^c and the length of the sheet ΔL , we can determine the strength of the shed vortex, γ_{n+1} .

The length of the sheet ΔL can be determined by tracking a particle shed from the trailing edge at time t using equation (9). It may be noted that the complex velocity at the trailing edge in the airfoil plane is

$$\frac{q_{T.E.}}{U} = \frac{U_x}{U} - \frac{ic\Omega}{2U} - \frac{2R}{\pi c} \sum_1^N \gamma_n \frac{\rho_n (\rho_n^2 - 1) \sin \phi_n}{(\rho_n^2 - 2\rho_n \cos \phi_n + 1)^2} \quad (15)$$

where the contribution due to the external and image vortices is expressed in terms of circle plane coordinates.

At this point, we have the strength of the nascent vortex defined, but not its position. Returning to the Kutta Condition for a discrete vortex, we may solve for the position. Thus

$$\frac{x_{n+1}}{c/2} = \frac{(\gamma_{n+1}^c)^2 + (\gamma_{n+1})^2}{(\gamma_{n+1}^c)^2 - (\gamma_{n+1})^2} \quad (16)$$

We now have a nascent vortex that

- (a) has the same strength as an element of vortex sheet situated along the x -axis
- (b) satisfies the Kutta Condition.

Calculation Sequence

Starting with the airfoil and the vortices in a given position, the induced velocities at each vortex and a particle at the trailing edge are calculated in the airfoil plane and transformed into the velocities in inertial coordinates. Using the procedure described in the kinematics section, the vortices are allowed to drift to their new positions. The airfoil is moved to its new position and the vortices' new blade and circle plane coordinates are calculated. The center induced circulation of the nascent vortex is calculated from equation (11). Equation (14) gives the strength of the nascent vortex and equation (16) its location. The force and moment are calculated using equations (6), (7), and (8). This process is then repeated for the next motion step.

Since each step introduces two new vortices, a shed and an image vortex, the computational time increases rapidly as the number of vortices increases. Cases were run with up to 130 vortices in the system.

Plunging Airfoil

In order to check the method, the normal force on a plunging airfoil was calculated and compared to the Karman-Sears solution [14]. Figure 3 shows the results. The reduced frequency, $\omega c/2U = 1$ and amplitude of the oscillation was $0.02c$. Agreement between the numerical approach and the Karman-Sears solution was considered to be good. The new vortex positions were determined from

$$x_n(t + \Delta t) = x_n(t) + u_n(t) \Delta t$$

in lieu of equation (9). As can be seen from the figure, the phase and amplitude closely approach that of the analytical solution.

Darrius Rotor

A one-bladed Darrius Rotor as illustrated in Fig. 2 was analyzed in order to examine the forces and moments on a Darrius Rotor blade. Figures 4 and 5 illustrate the normal and tangential force coefficients for the eighth revolution of a single blade at a tip speed ratio ($R\Omega/U$) of three. Chord to radius ratios of 0.200 and 0.063 were used. The value of 0.200 corresponds to operation at maximum power extraction while the chord to radius ratio of 0.063 is typical of the size of blade used on current Darrius Rotors. Two curves are shown for each chord to radius ratio. The solid line shows the con-

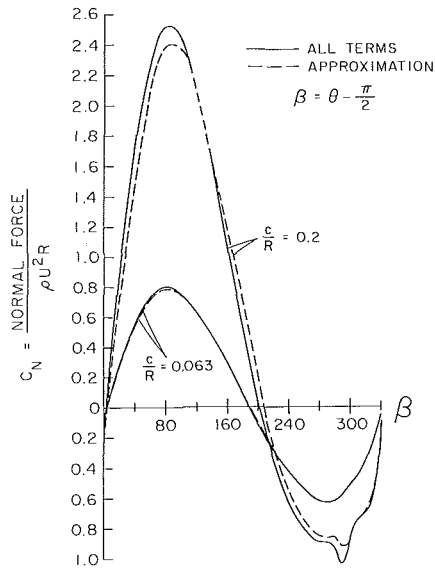


Fig. 4 Normal force variation at tip speed ratio of 3

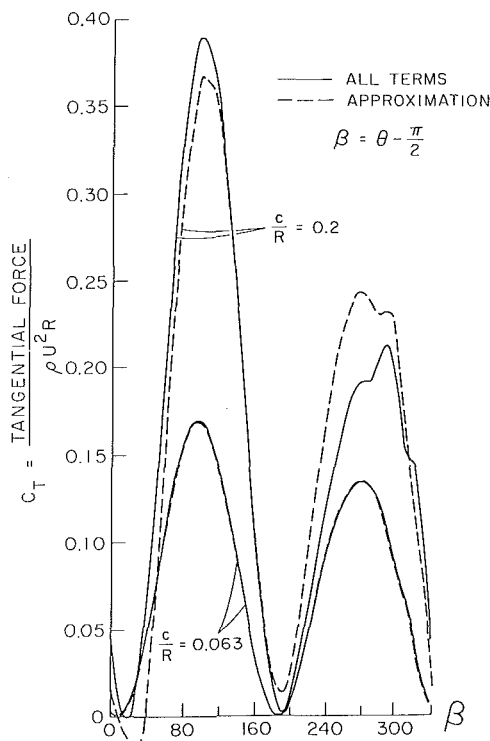


Fig. 5 Tangential force variation at tip speed ratio of 3

tribution of all terms in equation (6). The dashed line illustrates the value of

$$C_F \approx i\gamma_c \left(\frac{V_c}{U} \right) - \frac{\pi}{4} \left(\frac{c}{R} \right)^2 \frac{R\Omega}{U} e^{-i\theta} \quad (17)$$

where V_c is the local complex velocity relative to the blade origin.

The first term is a Kutta-Joukowski term and the second term is a combination of the pitching term and the apparent mass term. It can be seen that the approximate relation gives very little error at the lower chord size. The second term in the approximate relation (17) does no net work but does contribute to the loads. The keys to using equation (17) depend upon accurate determination of γ_c and V_c , both of which are intimately associated with the vortex field.

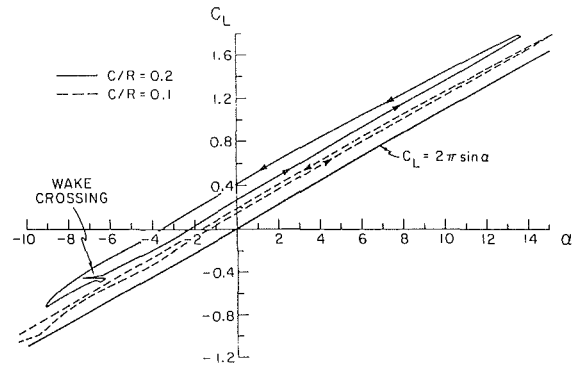


Fig. 6 Lift coefficient versus angle of attack for a one-bladed Darrieus Rotor at tip speed ratio of 3.54

The contribution of the moment to the power was quite small, even for the larger chord, typically less than 0.5 percent. The center of pressure for the flat plate airfoil was ahead of the quarter chord position on the lee side of the rotor and behind the quarter chord position on the windward side of the rotor. For a tip-speed ratio of three, the displacement of the center of pressure varied as the moment, that is as $(c/R)^2$. The magnitude of the displacement was approximately $0.08c$ for $c/R = 0.2$ and $0.01c$ for $c/R = 0.063$.

The induced velocity field was observed to vary considerably over the rotor with the largest induced velocities occurring on the lee side of the rotor. As a result, the local angle of attack experienced by the blade was greater in absolute value on the front (windward) side of the rotor.

Examination of the magnitude of the individual force contributions in equation (6) shows that the principal terms are

$$C_F \approx i\Sigma\gamma_n q_n^* + \gamma_p I \left(\frac{Q}{U} \right) + i\gamma_c \frac{Q}{U} - i \frac{\partial}{\partial t} \left(\frac{\pi c^2}{4UR} I \left(\frac{Q}{U} \right) \right) - i \frac{c}{2U} \frac{\partial \gamma_c}{\partial t} \quad (18)$$

Using the fact that $\gamma_c = -\Sigma\gamma_n$ and using the second term of equation (17) to express the second and fourth terms of equation (18) one may write

$$C_F \approx i\Sigma \left(q_n^* - \frac{Q}{U} + \frac{c}{2U} \frac{\partial}{\partial t} \right) \gamma_n - \frac{\pi}{4} \left(\frac{c}{R} \right)^2 \frac{R\Omega}{U} e^{-i\theta} \quad (19)$$

The controlling term in the moment equation is

$$C_M \approx - \frac{\pi}{4} \left(\frac{c}{R} \right)^2 \left(\frac{R\Omega}{U} + \sin\theta \right) \cos\theta \quad (20)$$

Although equations (17) and (19) are numerically quite close, it is not apparent that they are algebraically equal.

Figure 6 illustrates the variation in the lift coefficient with angle of attack for a one-bladed Darrieus Rotor at a tip speed ratio of 3.54. The difference between the calculated values and $C_L = 2\pi\sin\alpha$ is an apparent angle of attack $\Delta\alpha$ due to pitching circulation. If W is the local relative velocity then the angle is given by $\sin\alpha_p = c\Omega/4W$. For small angles and $W \approx R\Omega$

$$\alpha_p \approx \frac{1}{4} \frac{c}{R}$$

Ignoring the apparent mass term, the force on the blade for low chord to radius ratios is then well approximated by a Kutta-Joukowski lift force acting perpendicular to the relative velocity with the lift coefficient evaluated at an angle of attack equal to the sum of the geometric angle of attack α and an angle of attack due to pitching, α_p .

Conclusions

1. A free-vortex analysis of an idealized Darrieus Rotor Blade has been developed. The analysis uses a unique method for location of the nascent vortex that satisfies both the Kutta condition and the conservation of circulation.

2. The free-vortex analysis has been checked by two analytical methods, comparison with the Karman-Sears solution for a plunging airfoil and comparison with the impulse of the vortices. Both comparisons showed excellent agreement.

3. The loads on an unstalled Darrieus Rotor Blade may be adequately approximated by three terms:

- (a) the Kutta-Joukowski lift
- (b) a term due to the pitching circulation
- (c) an added mass term.

Further, since the pitching and added mass terms (the second term in equation (17)) do not produce any wake, these terms do not produce any net power extraction. Thus the Kutta-Joukowski term alone, as used in current aerodynamic performance models [1-6, 8] yields an adequately accurate representation of the power extraction mechanism for unstalled Darrieus Rotor Blades provided that accurate determination of the circulation and velocity field is obtained.

Acknowledgment

This work was supported by the U.S. Department of Energy under contract EY-76-S-06-2227. The authors wish to express their thanks to Professor W. R. Sears for his valuable suggestions.

References

- 1 Templin, R. J., "Aerodynamic Performance Theory for the NRC Vertical-Axis Wind Turbine," National Research Council of Canada, LTR-160, June 1974.
- 2 Wilson, R. E., and Lissaman, Peter, B. S., "Applied Aerodynamics of Wind Powered Machines," Oregon State University, May 1974.
- 3 Muraca, Ralph J., Stephen, S., Maria, V., and Dagenhart, Ray J., "Theoretical Performance of Vertical Axis Windmills," NASA-Langley Research Center, NASA TM TMX-72662, May 1975.
- 4 Shankar, P. N., "On the Aerodynamic Performance of a Class of Vertical Axis Windmills," National Aeronautical Laboratory, Bangalore TM AE-TM-13075, July 1975.
- 5 Strickland, J. H., "The Darrieus Turbine: A Performance Prediction Model Using Multiple Streamtubes," Advanced Energy Projects Department, Sandia Laboratory, SAND 75-0431, Oct. 1975.
- 6 Holme, Olof, "A Contribution to the Aerodynamic Theory of the Vertical-Axis Wind Turbine," International Symposium on Wind Energy Systems, Cambridge, England, Sept. 1976.
- 7 Fanucci, J. R., and Walters, R. E., "Innovative Wind Machines: The Theoretical Performance of a Vertical Axis Wind Turbine," p. III-61-95, *Proceedings of Vertical-Axis Wind Turbine Technology Workshop*, Sandia Laboratory, Albuquerque, N. Mex., SAND 76-5586, May 1976.
- 8 Strickland, J. H., Webster, B. T., and Nguyen, T., "A Vortex Model of the Darrieus Turbine: An Analytical and Experimental Study," Final Report Submitted to Sandia Laboratories, Albuquerque, N. Mex., Texas Tech University, Lubbock, Texas, Jan. 1979.
- 9 James, E. C., "Unsteady Aerodynamics of Variable Pitch Vertical Axis Windmill," AIAA Paper No. 75-649, AIAA/AAS Solar Energy for Earth Conference, Los Angeles, Calif., Apr. 21-24, 1975.
- 10 Ashley, Holt, "Some Contribution to Aerodynamic Theory for Vertical Axis Wind Turbines," 12th IECEC, Washington, D.C., Aug. 28, 1977.
- 11 Lamb, H., *Hydrodynamics*, Sixth Edition, Dover Publications, New York, 1945.
- 12 Milne-Thomson, L. M., *Theoretical Hydrodynamics*, Fifth Edition, The MacMillan Press, Ltd., London, 1968, p. 255.
- 13 Theodorsen, T., "Impulse and Momentum in an Infinite Fluid," Theodore von Karman Anniversary Volume published by The Friends of Theodore von Karman, Pasadena, California, May 1941.
- 14 von Karman, T., and Sears, W. W., "Airfoil Theory for Non-Uniform Motion," *Journal of the Aeronautical Sciences*, Vol. 5, No. 10, Aug. 1938.

W. D. Baines

W. W. Martin

D. M. Smith

Department of Mechanical Engineering,
University of Toronto,
Toronto, Canada

Development of Stratification in a Rectangular Tank by Horizontal Inflow

Introduction

The efficiency of thermal energy systems can usually be improved by providing for storage of heated and/or chilled water. For example, in solar space heating systems the excess of supply over demand which occurs in the summer months may be used to heat water in a storage tank in order to accumulate enough thermal capacity to cover the shortfall during the winter months. For the heating and air-conditioning of large buildings the energy requirements are so large that only short term storage is feasible. Nevertheless there is usually an alternating need for heating and cooling over the 24 hour night/day cycle, that is, there is a need for chilled water during the daytime and heated water at night. By storing water that is chilled partially by heating the building at night, the capacity of the chiller equipment may be significantly reduced. A similar savings can be obtained on the capital investment in heating equipment and, of course, there is an attractive energy conservation gain. For these tanks in energy systems it is desirable to keep the hot and cold fluids separate without resorting to physical separation. The largest possible temperature difference in tank without barriers can be maintained by minimizing the mixing across the density interface that occurs whenever fluid is being added to and/or withdrawn from the tank. Withdrawal from stratified tanks has been studied in some detail but information on the inflow is extremely limited. This paper describes an attempt to develop criteria for this latter aspect of the design of storage tanks. The effects of horizontal inflow into a rectangular tank were studied for the case of a multi-port manifold source spanning the bottom edge of the tank.

The storage tank is sketched in Fig. 1(a).

Water of larger density $\Delta\rho_0$ is introduced through an inlet system near the bottom at a discharge $Q=qW$ where W is the width of the tank. An equal flow rate leaves through an exhaust system near the top. When an interface exists, the volume underneath it is defined as $V=WA$ and the highest point is h above the horizontal bottom. The functional representation of the simplest case of a tank of uniform density ρ at time $t=0$ with q constant is thus

$$\frac{A}{B^2} = \phi\left(\text{Fr}, \text{Re}, \text{Pe}, \frac{gt}{B^2}\right) \quad (1)$$

for dimensional consistency.

The Froude number

$$\text{Fr} = \frac{q}{(g^1 B^3)^{1/2}} \quad (2)$$

where

$$g^1 = g\Delta_0/\rho \quad (3)$$

is the dimensionless ratio of the inertia of an ideal source to the flux of buoyancy. It defines the tendency to form an interface because the inertia controls the mixing by recirculation and turbulence and because the buoyancy is the force holding the heavier fluid on the bottom. It would be expected that the larger Fr the larger would be A at a given time. The second parameter is the Reynolds number of the source

$$\text{Re} = \frac{q}{\nu} \quad (4)$$

upon which will depend the rate of entrainment of the jets and the turbulence level.

The third parameter is the Peclet number of the flow

$$\text{Pe} = \frac{q}{\alpha}$$

which, following the studies described by Turner [3], would be expected to influence the thickness of the interface. The diffusivity α is the molecular diffusivity in for experiments using salt and is the thermal diffusivity for hot and cold water. They differ by a factor of about 100 and so the effect on the structure of the interface could be considerable. However, by using salt in lab. scale studies to represent heat in full scale the resultant Peclet number is about the same magnitude in each case. The effect of variation of Peclet number should be the focus of future studies but in this work it is apparent that the model represents heat transport at full scale.

If the interface extends over the full horizontal cross-section of the tank there is no flow across it so

$$\frac{dA}{dt} = q \quad (5)$$

The interface acts like a membrane and the design is ideal. Many tanks currently being constructed for large buildings

Contributed by the Fluids Engineering Division for publication in the JOURNAL OF FLUIDS ENGINEERING. Manuscript received by the Fluids Engineering Division, August 17, 1981.

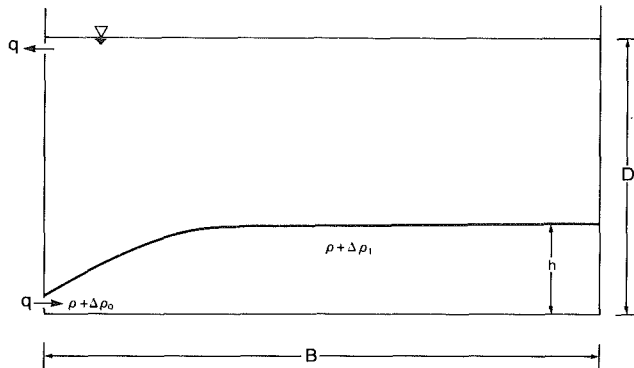


Fig. 1(a) Definition sketch of stratified storage tank

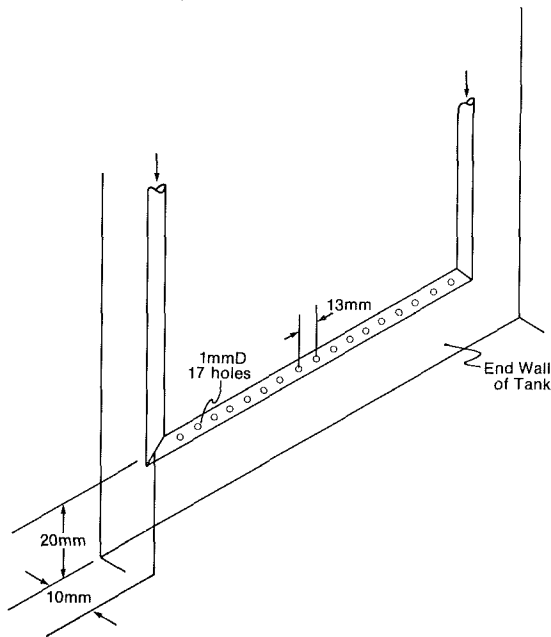


Fig. 1(b) Sketch of manifold inlet

employ a membrane of a thin plastic to ensure no vertical flow. These membranes have a limited life and are expensive to install.

The function ϕ in equation (1) obviously depends on the design of the inlet and outflow systems. The entrainment and turbulence level of the jets of the inlet system depend more directly on the velocity than the discharge per unit length and hence the elevation of interface will be higher for larger jet velocity. Outflow design should not be so critical because no turbulence is produced and the flow should approximate that due to a line sink for the outlet of width W . The flow to a line sink with an interface has been studied extensively as a problem of selective withdrawal. The results are summarized by Turner [3] who indicates that for a slot outlet the height of the opening is not a factor. A critical Froude number exists based on the elevation of interface relative to the outlet.

$$Fr_i = \frac{q}{\sqrt{g^1(D-h)^3}} \quad (6)$$

The value $Fr_i = 1.5$ was quoted by Turner [3] but a smaller value $Fr = 1.0$ was indicated by the theory of Benjamin [4].

A similar definition of critical Froude number can be made for the inlet system but the value depends on the design and Reynolds number. It must be much smaller than unity because the velocity of the jets from the inlet is much larger than that for a sink. In the study by Sliwinsky et al. [2] a single small

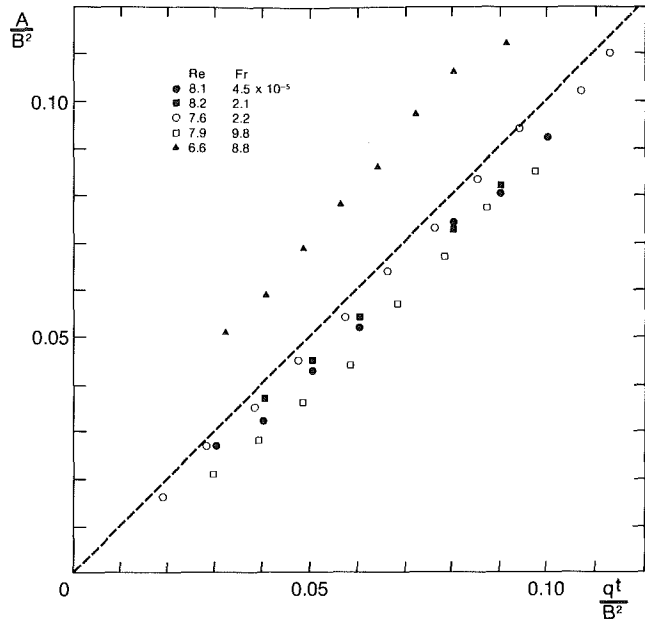


Fig. 2 Area under interface as function of time for small Reynolds number. Dashed line is area if all and only flow from source is under interface. (Uncertainty in $A/B^2 = \pm 0.005$, in $qt/B^2 = \pm 0.0002$ at 20:1 odds.)

diameter jet entered the side of a circular tank near the top and hot water was introduced at the same rate that cold water was removed from near the bottom. Stratification was observed with thick mixed layers and thick interface. No critical interface Froude number was identified although there was evidence in the results that one existed.

The laboratory investigation described herein was focused on development and maintenance of stratification produced by a multiport inlet system. Experiments were conducted in a rectangular tank of water with a constant discharge of larger density introduced across the width near the bottom. This arrangement is somewhat similar to the study of Baines and Turner [1] in which the density distribution was determined for the introduction of heavier water as a plume at the surface. A continuous density variation over the whole depth of the tank was found. This result would not be practical for energy storage.

This paper contains a brief description of the flow regimes observed for the one particular influx distributor. Measurements of the volume and density of fluid below the interface were used to determine the flow pattern throughout the tank. From the results it is concluded that both the volume and density below the interface are critically dependent on the detailed design of the source. The particular design chosen is probably not the most efficient. Better ones can be devised after analysis of the results.

Description of Experiments

The experiments were conducted in a tank 86cm long and 27.7cm wide. In flow was fed from both ends of a tube 3.2mm in diameter with 1mm diameter holes spaced at 13mm and arranged so that the individual jets emerged in the horizontal plane. The source tube was located 2cm above the tank bottom as shown in Fig. 1(b).

Common salt was dissolved in the water supplying the source to produce a predetermined density. The tank initially contained fresh water at the same (room) temperature to a depth of 30cm. The use of a salinity produced density difference instead of one produced by heat avoids loss of buoyancy effect through walls.

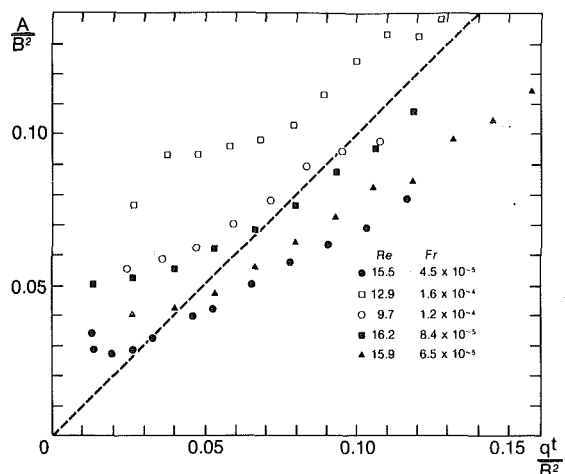


Fig. 3 Area under interface as function of time for moderate Reynolds number. Dashed line same as in Fig. 2. (Uncertainty in $A/B^2 = \pm 0.01$, in $qt/B^2 = \pm 0.0002$ at 20:1 odds.)

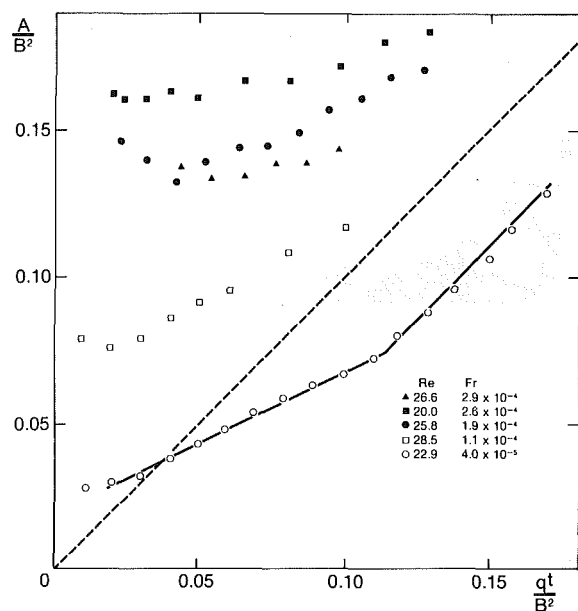


Fig. 4 Area under interface as function of time for large Reynolds number. Dashed line same as in Fig. 2. (Uncertainty in $A/B^2 = \pm 0.0005$, in $qt/B^2 = \pm 0.002$ at 20:1 odds.)

Direct measurements were made of the shape of the interface by a shadowgraph technique. A light source was located a long distance behind the tank and the shadow observed on a paper screen attached to the front. Photographs were taken periodically during the experiment and dimensions scaled for enlargements. Both the water in the tank and the salt water for the source were stored for at least a day so that each was at the room temperature and free from dissolved air. A constant head tank supplied the inflow which was metered continuously. With the available head and a range of $\Delta\rho/\rho$ from 0.001 to 0.17 it was possible to vary Fr between 3×10^{-4} and 2×10^{-5} . The range of Reynolds number was from 8 to approximately 30.

Observations of Flow

Three distinct flow patterns were observed as time progressed. Immediately after the valve was opened the inflow formed a gravity current with a characteristic head which proceeded across the length of the tank. The size of the head

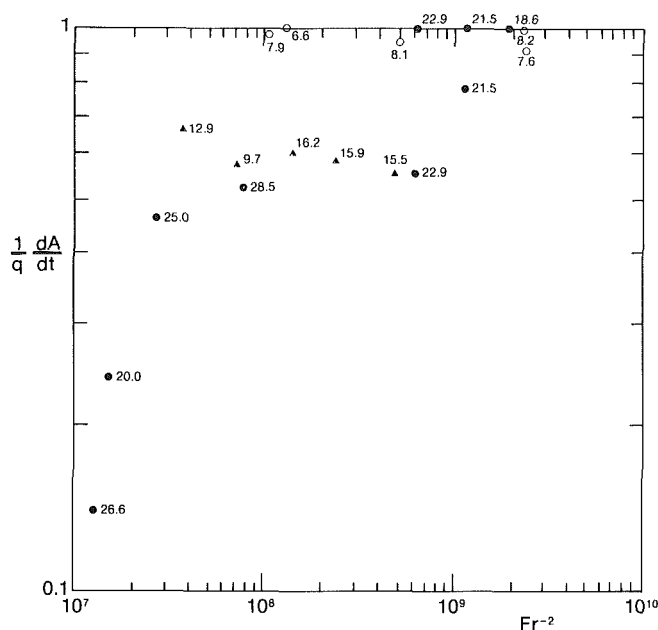


Fig. 5 Dimensionless rate of area increase as function of source Froude number. Values of Reynolds number shown beside each point. (Uncertainty in $(1/q) dA/dt = \pm 0.01$, in $Fr^{-2} = \pm 5 \times 10^6$ at 20:1 odds.)

increased with distance from the source and was higher the smaller the density difference. In the case of very small density difference the shape of the head was roughly circular and resembled a puff produced by an impulse. The head reflected from the far side of the tank and proceeded against the current back towards the source. It was reflected several times with reducing the amplitude. The time required for this regime is small, of the order of $qt/B^2 = 0.03$. Very soon an interface was established and a steady flow regime observed. The volume below the interface and the elevation of the interface at the opposite side of the tank from the source increased steadily.

Another interface was seen to develop for cases of large source Reynolds number. The mixed region above the first interface which appeared uniformly grey in the shadowgraph changed slowly in shading. A horizontal white line became evident which sharpened and defined this second interface.

Volume Below Interface

The shape of the interface was clearly defined on the photographs except for a small length near the jets. The volume was easily determined by computing the area under the white line using Simpsons rule and five values of the height. Figures 2, 3, and 4 present the results in dimensionless form for low, moderate, and large Reynolds number, respectively. It is evident that both the slope and zero intercept of the linear portion of the curves vary both with Reynolds and Froude numbers.

The dimensionless form of the slope is the ratio of the rate of volume increase to the entering volume flux. On each figure a dashed line of unit slope is drawn from the origin which defines the volume which would be found if all heavy fluid was retained below the interface. It is seen that in most cases the slope is less than unity. This means that some of the volume flux from the source escapes to the region above the interface. This effect is more clearly shown on Fig. 5 which is a plot of the dimensionless slope as a function of Froude number for all data. The magnitude of the escape increases with Reynolds number.

Inasmuch as all of the photographs show a clear interface over most of the length of the tank this out flow must occur in

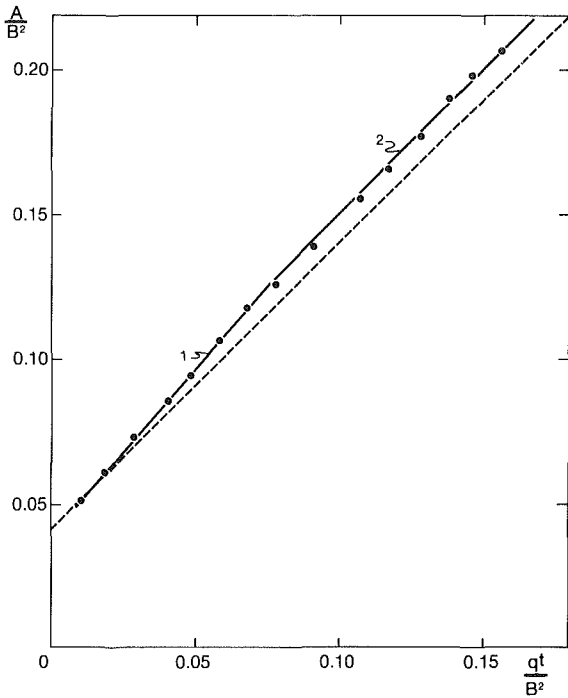


Fig. 6 Area under interface as function of time for pre-established interface. $Fr = 6.5 \times 10^{-5}$, $Re = 23.6$. (Uncertainty in $A/B^2 = 0.004$, in $qt/B^2 = \pm 0.002$ at 20:1 odds.)

the short region near the manifold where the interface is not seen. The escape flow was never observed but the mechanism is surmized from other observations. At the smallest Reynolds number a laminar jet existed for a distance of at least twenty hole diameters downstream of the manifold. The interface was flat over the length of the tank and the dimensionless slope unity. As the Reynolds number increased, the jet became turbulent at sections closer to the outlet and the interface curved downwards toward the jet. Entrainment is obviously larger in this turbulent flow and the individual jets act like hydrodynamic sinks. These draw fluid from large distances both from above and below the interface. It is surmized that the fluid is withdrawn primarily from below the interface but a larger flow was set in motion than was entrained by the jets.

The lowest curve on Fig. 4 has two distinct slopes which are plotted on Fig. 5. For dimensionless time less than 0.11 the slope is 0.53 which indicates a large escape. At this time the interface was observed to change shape to a horizontal line and after the slope is effectively unity. We conclude that at this time the critical Fr has been reached. The value could not be determined accurately in all cases because of the thick layer of salt water which the escape had produced above the interface. The critical Fr was probably also exceeded in the cases where a second interface was observed. The slope of the area-time curve of the second interface was unity in every case indicating that there was no escape. A numerical value for Fr_{ic} can be assigned in these cases if the depth is assumed to be that when first observed and if the density difference is defined by conservation of salt. The results for three cases are $Fr_{ic} = 6.36 \times 10^{-3}$, 4.28×10^{-3} and 5.09×10^{-3} at source Froude numbers of 4×10^{-5} , 3.24×10^{-5} and 2.84×10^{-5} , respectively.

A second set of experiments was conducted to determine Fr_{ic} more directly. An interface was established prior to $t=0$ by slowly leaking the heavier fluid through the inlet until a 3cm layer existed. The constant q was again started at $t=0$. Figure 6 shows the volume variation with time and two distinct slopes can be seen. For time less than 0.07 the

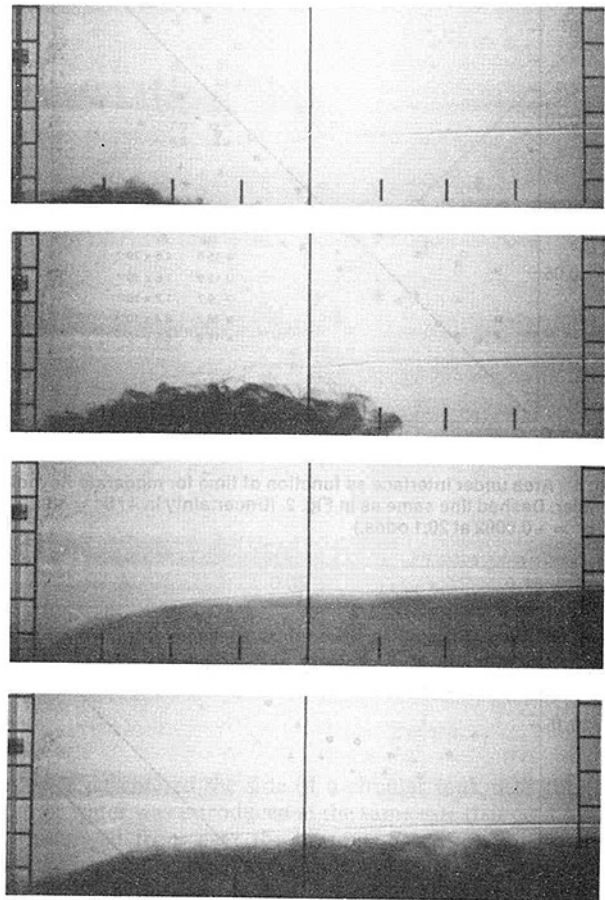


Fig. 7 Photographs of colored region produced by introduction of dye into source flow for established interface. $Re = 15.9$, $Fr = 6.5 \times 10^{-5}$, $qt/B^2 = 0.16$. (Uncertainty in $A_0/B^2 = \pm 0.005$, in $Fr^{-2} = \pm 5 \times 10^6$ at 20:1 odds.)

dimensionless slope is greater than unity indicating that more water was accumulating under the interface than is coming from the inlet. The interface was subjected to turbulent erosion from the large eddies produced by the jets. This is the process of mixing across an interface discussed by Turner [3]. The inertia in the turbulence is large enough to overcome the buoyant force existing across the interface. The phenomenon is thus also dependent on the interface Froude number Fr_i , so that when the interface is at a level such that Fr_{ic} is obtained the mixing stops and a stable interface is formed.

The critical condition occurred at time 0.07 after which the slope on Fig. 6 is unity. A value of Fr_{ic} can be calculated assuming conservation of salinity at time 0.07. For this source value of $Fr = 6.27 \times 10^{-5}$, $Fr_{ic} = 1.5 \times 10^{-3}$ and for other experiments with $Fr = 8.74 \times 10^{-5}$ and $Fr = 2.3 \times 10^{-5}$, $Fr_{ic} = 2.0 \times 10^{-3}$ and 2.8×10^{-3} , respectively. A larger critical value was found in the first set in which the interface was established by the mean flow rather than the turbulence.

A series of photographs presented in Fig. 7 were taken to illustrate the flow pattern under the interface and to verify the explanation for interface movement given above. Dye was introduced into the source at a time after the interface had been established. The shape of the dyed zone can only be the result of the closed mean stream-lines shown on Fig. 8. These are similar to those produced by a hydrodynamic quadrupole located in the corner. This, indeed, is the general effect one would expect from a jet which corresponds to the source and the entrainment which corresponds to the sink. The effect of the quadrupole is to produce a negative pressure which pulls the interface down and thus provides the reason for the lack

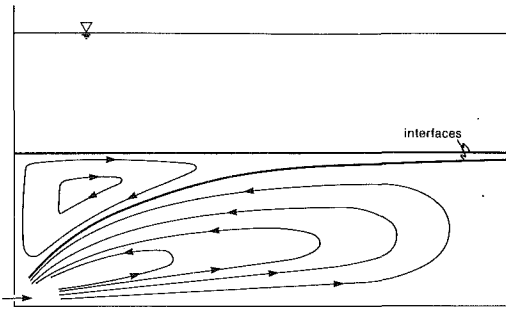


Fig. 8 Stream-line pattern inferred from Fig. 7

of definition of the interface in the first set of experiments. The flow pattern also shows that turbulent eddies are ejected from the jet and carried back toward the source by the entrainment flow, thus providing the reason for the erosion in the second set of experiments. Figure 8 also shows the circulation pattern between the two interfaces which was observed by injecting dye into this region. This circulation is driven by the shear exerted on the lower interface by the quadrupole circulation.

The intercept of the lines on Figs. 2, 3, and 4 on $qt/B^2 = 0$ is a measure of the volume initially mixed by the gravity current and reflections. This should also depend primarily on the source Froude number as demonstrated on Fig. 9. As the Froude number is decreased the initial volume decreases and approaches a small value. It should be noted that the zero and negative values of A_0 have no physical significance but are merely the result of using an intercept at time zero. A more significant measure would be the area when the interface is first discernible. This, however, occurs at different times and so these values are not readily comparable. A reasonable compromise is to use the volume at a specific time such as $qt/B^2 = 0.03$.

An effect of Reynolds number is also noted in Fig. 9. This is, no doubt, due to the laminar or turbulent entrainment during the period of the gravity current. At low Reynolds number the laminar entrainment would be small and thus result in a relatively small volume in the current.

All of the tests described above were conducted with a tank initially filled with fresh water to a depth several times the height of the gravity current. This was done purposely to avoid any effect of the free surface on the establishment of the interface. However, the depth of the tank is an important design consideration so a few tests were conducted to determine this limitation. Three tests were conducted at two values of Reynolds and Froude numbers with different initial depth. In every case the location at $qt/B^2 = 0.03$ was higher as the tank depth was decreased. The dimensionless rate of area increase did not appear to be affected. From these few measurements it was deduced that if the initial volume of the tank was larger than 4 times the area defined at $qt/B^2 = 0.03$ there was no effect of the tank depth. If the initial volume was twice this volume the observed initial value was increased about 20 percent. It was concluded that the tank volumes in practice should be at least 4 times that produced by mixing in the initial gravity current.

Density of Fluid Below Interface

The efficiency of a storage tank could be assessed either by the density or total buoyancy of the water below the interface as a ratio of the same quantity introduced by the source. The equations of conservation of mass and buoyancy can be used to predict these ratios from the data on for the linear region. The area is defined by

$$A = A_0 + mqt \quad (7)$$

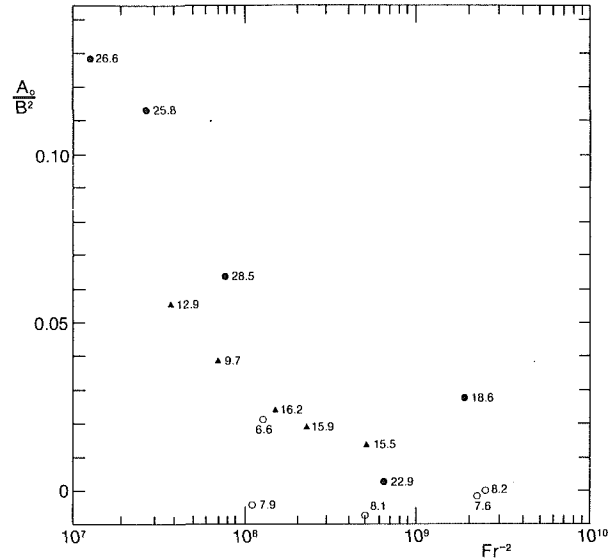


Fig. 9 Intercept of linear section of area under interface plot on axis qt/B^2 as function of Froude number. Negative values are not physically significant. Values of Reynolds number shown beside each point.

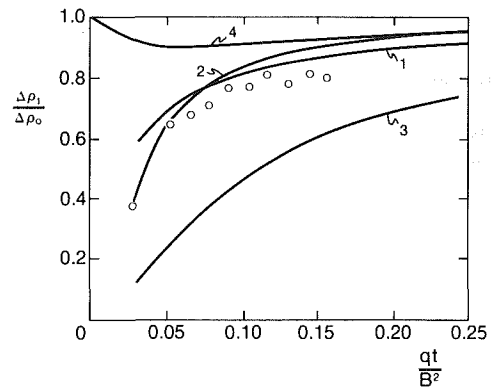


Fig. 10 Analysis and measurement of density below interface as function of time, 1. $Re = 7.6$, $Fr = 2.2 \times 10^{-5}$, 2. and Δ , $Re = 15.9$, $Fr = 6.5 \times 10^{-5}$, 3. $Re = 25.8$, $Fr = 1.9 \times 10^{-9}$, 4. $Re = 22.9$, $Fr = 4 \times 10^{-5}$. (Uncertainty in $\Delta \rho_1 / \Delta \rho_0 = \pm 0.04$, in $qt/B^2 = 0.002$ at 20:1 odds.)

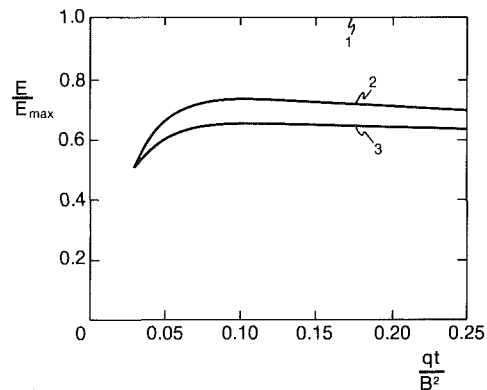


Fig. 11 Analysis of total buoyancy below interface as function of time

where

$$m = \frac{1}{q} \frac{dA}{dt}$$

and the conservation of buoyancy gives

$$q\Delta\rho_0 - q(1-m)\Delta\rho_1 = \frac{d}{dt}(A\Delta\rho_1) \quad (8)$$

It has been assumed that all of the fluid escaping to the region above the interface is of density $\Delta\rho_1$. Combining equations (1) and (2) and integrating yields

$$\frac{\Delta\rho_1}{\Delta\rho_0} = 1 - c \left[\frac{1 + mqt_1/A_0}{1 + mqt/A_0} \right]^{1/m} \quad (9)$$

with the initial condition

$$c = \frac{\Delta\rho_1}{\Delta\rho_0} \text{ at } t = t_1 \quad (10)$$

The total buoyancy below the interface is

$$E = g\Delta\rho_1 A \quad (11)$$

Or relating this to the integrated buoyancy flux from the source E_0 gives

$$\frac{E}{E_0} = \left(m + \frac{A_0}{qt} \right) \frac{\Delta\rho_1}{\Delta\rho_0} \quad (12)$$

Figure 10 presents the evaluation of equation (9) for a case from each of the Reynolds number regions. The large Reynolds number case shows a much poorer performance than the other two for which the density under the interface is greater than 90 percent of the source density for time greater than 0.2. The points plotted on the graph are measurements of density made during the course of the experiment described by the curve labeled 2. Density was measured by withdrawing samples below the interface and weighing in specific gravity bottles. There is a steady deviation between the measured and predicted values indicating that one of the conservation equations is not being satisfied. If some of the salt from the source flow proceeded directly to the region above the interface and did not participate in the circulation pattern shown on Figure 8 such a discrepancy would occur.

The consequence of leakage from below the interface is more evident on Fig. 11 which is a plot of equation (12). In evaluating the initial condition for this figure as well as for Fig. 8, it has been assumed that during the time of establishment of the interface one half of the salt has been distributed elsewhere in the tank. This is consistent with measurements made of the initial density below the interface. For both of the larger Reynolds number cases the buoyancy storage reaches a maximum and then decreases slowly with time. For the larger Reynolds number the storage does not exceed 65 percent of the inflow buoyancy at any time.

A much more efficient method of operation results from establishing an interface as was done in the second set of experiments. This is illustrated by applying the conservation equations to the two zones shown on Fig. 6. For small time the expression for mean density below the interface is

$$\frac{\Delta\rho_1}{\Delta\rho_0} = \frac{1 + qt/A_0}{1 + mqt/A_0} \quad (13)$$

and for time larger than t^* where critical conditions are passed

$$\frac{\Delta\rho_1}{\Delta\rho_0} = 1 - \frac{1 - \Delta\rho_1^*/\Delta\rho_0}{1 + q(t - t^*)/A^*} \quad (14)$$

These expressions are plotted on Fig. 8 as curve 4 for the data of Fig. 6. Dilution of the fluid occurs until t^* after which the density slowly decreases and approaches $\Delta\rho_0$ for large time. Curve 4 should be compared to 3 which gives results for approximately the same inlet conditions. There is a very much larger density if the interface is established. If critical conditions existed from time zero the density below the interface would be exactly that from the source.

In every case of a pre-established interface $E/E_0 = 1$ because there is no loss of salinity to the zone above the interface. Similarly $E/E_0 = 1$ for the second interface in the first set of experiments.

Conclusions

This study has delineated the flow pattern produced by the inlet in the storage tank and defined the critical Froude number for this manifold design. The critical interface Froude number is so much smaller than the published value for the outlet that one must conclude that the inlet design controls the effectiveness of the interface as a separator of the two fluids. For a constant volume tank the critical thickness of the layer at the inlet would be 500 times as thick as that at the exhaust.

The magnitude of the critical layer at the inlet appears to be controlled indirectly by the flow in the jets from the source. Entrainment produces a pressure field which depresses the level of the interface and the high turbulence level produces mixing which can transport fluid across the mean interface level. It is evident that the thickness of the critical layer could be reduced by reducing the jet velocity since both effects are proportional to the jet velocity. This could be accomplished by increasing the size of the holes or reducing the spacing in the manifold. However, the value of the critical Froude number would have to be determined by experiment for each design.

The best design would utilize a slot in place of a series of jets although it would be more difficult to construct. One such design has been studied in an exploratory test. It was found that the critical Froude number was about 4×10^{-2} for a slot 1mm in height in the tank described above. This value is ten times the value for the manifold and verifies the contention that in any design the inlet velocity should be minimized.

Any inlet design will function effectively and liquid of maximum density is stored if the interface is established at the critical level before the design discharge is started. This condition can be obtained either by using the critical depth as a permanent layer of storage or by introducing fluid at a low enough velocity that laminar entrainment occurs until the critical depth is reached. It appears from calculations of specific designs that both of these approaches add appreciably to the cost of an installation and so may not be feasible. If, however, the critical Froude number can be reduced the establishment and maintenance of the layer may not be a large proportion of the volume of the tank or time of utilization, respectively.

Acknowledgments

The experimental studies described herein were supported by the NSERC through grants A-1066 and A-9196 and a summer fellowship to one author (DMS). Data on pre-established interfaces was supplied by L. A. Sinclair.

References

- 1 Baines, W. D., and Turner, J. S., "Turbulent Buoyant Convection from a Source in a Confined Region," *J. Fluid Mech.*, Vol. 37, 1969, pp. 51-80.
- 2 Sliwinski, B. J., Mech, A. R., and Shih, T. A., "Stratification in Thermal Storage During Charging," 6th Intl. Heat Transfer Conference, Toronto, Vol. 4, 1978, pp. 149-154.
- 3 Turner, J. S., *Buoyancy Effects in Fluids*, Cambridge University Press, 1973.
- 4 Benjamin, T. B., "Steady Flows Drawn from a stably Stratified Reservoir," *J. Fluid Mech.*, Vol. 106, 1981, pp. 245-260.

Computer Prediction of Local Destratification Near Low-Level Release Structures of Reservoirs

A. A. Busnaina

Graduate Student.

D. G. Lilley

Professor.
Mem. ASME

School of Mechanical and
Aerospace Engineering,
Oklahoma State University,
Stillwater, OK 74708

The Garton Pump consists of a low-energy axial flow propeller placed just below the surface so as to provide a downward directed jet of fluid and thereby locally mix reservoirs near the release structure of the dam. In this way high-quality epilimnion water is transported downwards, so obtaining local destratification and improved release water quality in the vicinity of low-level release structures. The flowfield is fully three-dimensional and a simplified numerical simulation and solution procedure has been formulated in Cartesian coordinates to include species diffusion and buoyancy forces. Comparison of predictions with experimental data confirms that the main dynamic effects are modeled adequately and better than a previous two-dimensional simulation. This fundamental study with practical applications represents a low cost basic tool to show the influence of design parameters on the practical flowfield.

Introduction

During the hot months of summer, thermal stratification may occur in water reservoirs. Then the lower layers of water become severely anaerobic [oxygen deficient] with corresponding harm to water quality. When this phenomenon occurs, three main layers of water with different characteristics may be observed. The epilimnion, the top layer, contains warm low-density water (usually rich in oxygen because of atmosphere reaeration and photosynthesis, and thus considered as a high-quality water). The hypolimnion, the bottom layer, consists of cold high-density water (often poor in oxygen and thus considered as a low-quality water). The region of rapid temperature change (between the other two layers) is called the thermocline or metalimnion. This stratification presents a serious problem for reservoirs with low-level release structures in that the quality of water released, as characterized by its oxygen content, may be poor, since most of the exit flow comes from the bottom layer of water in the reservoir. Since many old reservoirs have release structures located near the bottom, there is indeed a problem of finding suitable and economically feasible alleviation techniques.

Possible approaches include artificial destratification, structural modification, and localized mixing to improve the release water quality. Artificial destratification can be either mechanical pumping (with assorted piping) or diffused-air pumping. These mixing devices, however, require a substantial amount of energy to destratify a large body of water, see Symons et al. [1]. Structural modification of the dam involves elevating the release gate position in order to allow

some of the water to be drawn from the epilimnion. This method, although effective, is extremely costly. On the other hand, localized mixing of epilimnion water into the hypolimnion has been found to be effective and economical in enhancing the quality of water release from low-level release gates. There has been a continued interest in local mechanical destratification of reservoirs to improve water quality. A low-energy axial flow propeller may be positioned just below the water surface so as to provide a downward-directed jet of water and thereby locally mix the reservoir in the vicinity of the release structure of the dam. The high-quality epilimnion water is transported downwards, and the effectiveness of a pump of this type has been illustrated in field experiments at Pine Creek Reservoir, Oklahoma [see Garton and Peralta [2]] and Lake Okatibbe, Mississippi [see Dortch and Wilhelms [3] and Garton and Jarrell [4]]. Figure 1 shows a schematic of the mixing so produced when there is no exit beneath the

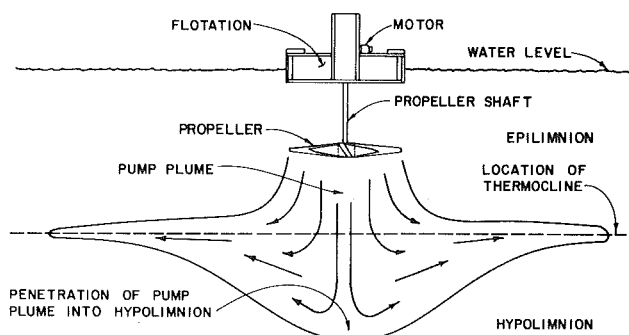


Fig. 1 Schematic of a typical propeller pump and the flowfield produced without exit flow

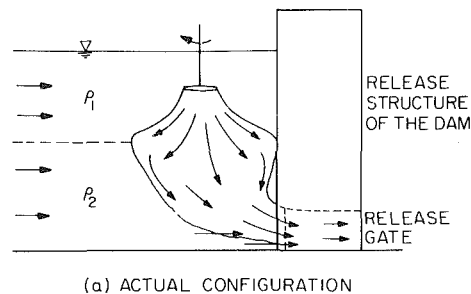
Contributed by the Fluids Engineering Division of THE AMERICAN SOCIETY OF MECHANICAL ENGINEERS and presented at the Fluids Engineering Conference, Boulder, Colo., June, 1982. Manuscript received by the Fluids Engineering Division, September 2, 1981. Paper No. 81-FE-11.

propeller. The jet or plume penetrates some distance below the level of the thermocline.

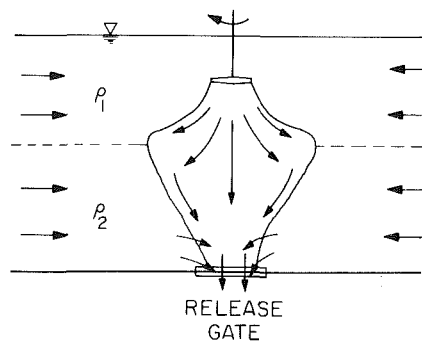
Figure 2(a) illustrates the practical application of localized mixing in the proximity of the release structure of a dam with a low-level release gate. The flowfield so produced is fully three-dimensional. However, an axisymmetric two-dimensional simulation of this phenomenon is illustrated in Fig. 2(b). In this, the release flow is represented by a circular opening at the bottom of the flowfield directly beneath the propeller. This does not represent correctly the position of the exit, since in practice it is in an off-axis position, but it provides a useful simplification of the true problem. Earlier work by the authors [5] was restricted to this axisymmetric formulation about a vertical axis, and good results were portrayed for cases in which the propeller was close to the release structure. The present work investigates a more advanced theoretical model for the enhancement of release water quality by localized mixing in thermally stratified lakes and reservoirs. To allow for the off-axis position of the outlet and the presence of a vertical dam wall, it is necessary to extend the modeling effort to a fully three-dimensional simulation. A Cartesian (x,y,z) coordinate approach is employed so that practical questions of design and sizing can be investigated in more detail and with greater accuracy than was previously possible.

In either case, the release flow can entrain some or all of the jet or plume of water from the surface. If the arrangement is successful, the release flow will consist mostly of epilimnetic water, along with some hypolimnetic water that enters the plume through mixing, and the dilution factor (as defined later) will be near one. If the velocity of the downward jet is insufficient for penetrating deeply into the stratification only hypolimnetic water will be drawn, and the dilution factor will be zero. If the jet velocity is adequate, but the propeller flow rate small compared to the release flow rate, or the plume located too far from the release gate, the dilution factor will have some intermediate value.

Hydraulic model experiments have enabled considerable success to be achieved in understanding the phenomena [see Moretti and McLaughlin [6]]. Recent numerical simulations [see Busnaina [7] and Busnaina, Lilley, and Moretti [5]] of local mixing supplement the experimental program and demonstrate substantial promise for improvement in modeling the transient mixing behavior during destratification. Advantages of being able to calculate [rather than experiment in the laboratory or in the field] are enormous in terms of their cost/benefit ratio. Such procedures confirm and extend the available experimental data to a larger set of cases, and supplement the rather limited theoretical



(a) ACTUAL CONFIGURATION
Fig. 2(a) in the release structure of the dam



(b) AXISYMMETRIC SIMULATION
Fig. 2(b) directly beneath the propeller

Fig. 2 Schematic of a typical propeller pump and the flowfield produced with exit flow via a low level release gate

treatment of associated problems, see, for example, Abraham and Eysink [8], Baines [9], and Ditmars [10]. The present work extends previous approaches and presents a fully three-dimensional numerical simulation and solution scheme.

Simulation and Solution Technique

The modeling and prediction technique are now dealt with in the context of an incompressible 3-D transient flow. Slight density variations are accounted for via the solution of a two inert component system, thereby obtaining the required buoyancy force. The computational code solves directly for the primitive pressure and velocity variables, and is based on the Marker and Cell MAC Los Alamos technique. This is one of the most well-known methods to solve time-dependent incompressible fluid flow problems; its conceptual simplicity

Nomenclature

D_p = propeller diameter	L^* = nondimensional propeller depth, $L^* = L/H$	Z_p = penetration depth (measured from the surface)
D^* = nondimensional propeller diameter, $D^* = D_p/H$	m_1 = mass fraction of fluid of density ρ_1 (epilimnion)	Z_p^* = nondimensional penetration depth, $Z_p^* = Z_p/H$
DF = dilution factor, $DF = (\rho_r - \rho_2)/(\rho_1 - \rho_2)$	m_2 = mass fraction of fluid of density ρ_2 (hypolimnion)	Z_T = metalimnion location (measured from the bottom)
Frd = densimetric Froude number, $Frd = v_p/[g(\Delta\rho/\rho_1)H]^{1/2}$	P = pressure deviation from hydrostatic pressure	Z_T^* = nondimensional metalimnion location, $Z_T^* = Z_T/H$
g = gravitational acceleration	Q_p = propeller flow rate	μ = absolute viscosity
H = total depth of model	Q_r = release flow rate	μ_t = turbulent viscosity
K = propeller axis distance from release structure	Q^* = nondimensional flow rate, $Q^* = Q_p/Q_r$	ρ_1 = epilimnion or top density
K^* = nondimensional propeller distance, $K^* = K/H$	u, v, w = velocity components in (x, y, z) coordinate directions	ρ_2 = hypolimnion or bottom density
L = propeller depth below the surface	v_p = propeller velocity	σ_{sc} = Schmidt number
	x, y, z = Cartesian coordinates	

is one of the main attributes. A 2-D version is described in reference [11], upon which the present work is based. Earlier versions of the MAC code have also been given for 3-D flows [12]. Other 3-D computational schemes have also been documented [13-15]. In the present work, an Eulerian finite difference formulation is used with pressure and velocity as the main dependent variables.

The Partial Differential Equations. The numerical simulation of the flowfield of the jet induced by an axial-flow propeller pump is performed by solving the governing equations of the flowfield—the equations of conservation of mass (continuity), momentum (in x , y , and z directions) and species diffusion. Density changes are slight and allow the flowfield to be simulated as an incompressible flow with the addition of an upward buoyancy force. The equations in Cartesian coordinates may be taken in conservative form as:

$$\begin{aligned} \frac{\partial u}{\partial x} + \frac{\partial v}{\partial y} + \frac{\partial w}{\partial z} &= 0 \\ \frac{\partial u}{\partial t} + \frac{\partial}{\partial x}(u^2) + \frac{\partial}{\partial y}(vu) + \frac{\partial}{\partial z}(wu) &= \frac{1}{\rho_1} \left[-\frac{\partial p}{\partial x} + \mu_t \nabla^2 u \right] \\ \frac{\partial v}{\partial t} + \frac{\partial}{\partial x}(uv) + \frac{\partial}{\partial y}(v^2) + \frac{\partial}{\partial z}(wv) &= \frac{1}{\rho_1} \left[-\frac{\partial p}{\partial y} + \mu_t \nabla^2 v \right] \\ \frac{\partial w}{\partial t} + \frac{\partial}{\partial x}(uw) + \frac{\partial}{\partial y}(vw) + \frac{\partial}{\partial z}(w^2) &= \frac{1}{\rho_1} \left[-\frac{\partial p}{\partial z} + \mu_t \nabla^2 w - g(\rho - \rho_1) \right] \\ \frac{\partial m_1}{\partial t} + \frac{\partial}{\partial x}(m_1 u) + \frac{\partial}{\partial y}(m_1 v) + \frac{\partial}{\partial z}(m_1 w) &= \frac{1}{\rho_1} \left[\frac{\mu_t}{\sigma_{SC}} \nabla^2 m_1 \right] \\ m_1 + m_2 &= 1 \\ \rho &= m_1 \rho_1 + m_2 \rho_2 \end{aligned} \quad (1)$$

where

$$\nabla^2 \phi = \frac{\partial^2 \phi}{\partial x^2} + \frac{\partial^2 \phi}{\partial y^2} + \frac{\partial^2 \phi}{\partial z^2}$$

is a Laplacian operator.

Several fundamental questions arise in the correct modeling of the physical phenomena. First, consider the question of modeling turbulence. Over the range of parameters studied, flow visualizations in the laboratory suggest that the controlling factor for the dilution of the release water with epilimnetic water is the entrainment of the downward plume into the release flow, rather than the mixing process in the vicinity of the plume (which is the governing mechanism for whole-lake mixing). Thus the modeling of jet penetration depth on the one hand, and critical release flow rates on the other, are key items in the representation of the physical phenomena. The viscous or turbulent mixing processes in the shear layers are less important than these items, and do not greatly affect the jet velocity at which the dilution factor increases from a low to a high value. In the numerical model, this has been confirmed by varying the viscosity from a laminar value to a *constant large viscosity* with minor effect

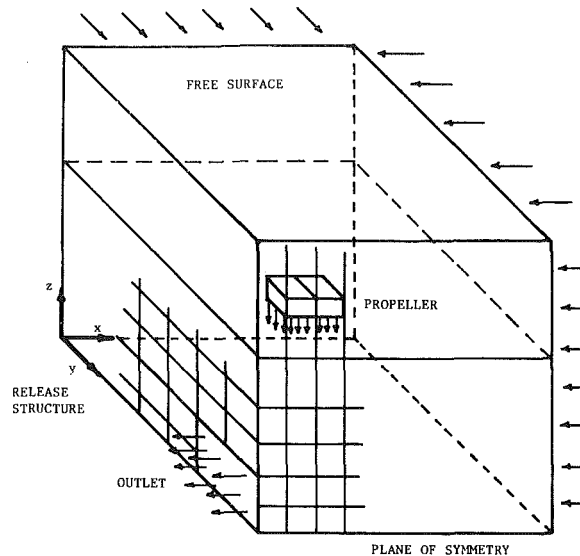


Fig. 3 Fully 3-D Cartesian grid schematic

on the results, as seen later in the discussion of results. That such a value is appropriate for a round turbulent free jet is well known [16, 17]. Hinze [16], for example, asserts that the turbulent viscosity in a round free jet is approximately constant and given by

$$\mu_t = 0.00196 \rho (x+a) u_m \quad (2)$$

in terms of station maximum axial velocity u_m . In terms of jet initial velocity u_{m0} this can be written

$$\mu_t = 0.00196 A \rho u_{m0} d \quad (3)$$

where A is a parameter between 5.4 and 6.39. Our work in general uses the latter value in accordance with the early recommendation [18]. For the particular propeller diameter and initial jet velocity used in most of the subsequent predictions, this choice gives

$$\mu_t / \mu = 142 \quad (4)$$

An indication of how susceptible computed results are to this choice is given in the results. With these equations, a vertically downward-directed jet in the stratified environment can be simulated, and proper account is taken of species mixing and buoyancy.

The Mesh System. The rectangular 3-D region to be considered is divided into rectangular cell divisions, with uniform Δx , Δy , and Δz spacings. This solution domain is complemented by a layer of cells on all sides, so as to allow easy simulation of the required boundary conditions. These fictitious cells increase the total number of cells in each direction and Fig. 3 illustrates the mesh arrangement. The pressure and m_1 are located at the center of each cell and the velocities are on the faces as follows:

$$\begin{aligned} u_{ijk} &= x\text{-direction velocity located at center of right face} \\ &\text{of the } (I, J, K)\text{-cell touching the } (I+1, J, K)\text{-cell} \\ v_{ijk} &= y\text{-direction velocity located at center of top face of} \\ &\text{the } (I, J, K)\text{-cell touching the } (I, J+1, K)\text{-cell} \\ w_{ijk} &= z\text{-direction velocity located at center of rear face} \\ &\text{of the } (I, J, K)\text{-cell touching the } (I, J, K+1)\text{-cell} \end{aligned}$$

Thus normal velocities lie *directly on* the physical boundaries of the solution domain, while the tangential velocities and pressure are *displaced half a cell interval* inside the flowfield. In this way the exterior fictitious cells are particularly convenient when applying the boundary conditions.

Figure 3 also represents the physical problem, and contains a downward flowing jet of fluid from the propeller. Initially

two fluids occupy positions above and below the interface as shown, so that their mass fractions are $m_1 = 1$ and $m_2 = 0$ (for $z > Z_T$, the height of the interface) and vice versa. Also shown is how the inlet and outlet flows are handled. The exit release flow is via a rectangular area in the release structure with the flow rate specified a priori. The available volume of the flow domain is very limited. To allow the outlet of release water without dramatically decreasing the fluid level, there is a compensating incoming flow which is distributed among the top and bottom layers in amounts equal to the epilimnetic and hypolimnetic water released. The peripheral inflow is at all elevations in such a way that epilimnetic water enters into the upper layer and does not disturb the density profile. The large area of inflow allows it to be at a low velocity in order to avoid any disturbance to the flow field. Similarly, hypolimnetic water is fed into the bottom layer.

The Finite Difference Equations. The usual intuitive estimates of one-sided first-derivatives, centered first-derivatives and centered second-derivatives are used in representing the momentum equations. Superscripts n and (blank) are used to denote values at time-level t and $t + \Delta t$, respectively. Portrayed now are equations enabling one such forward time-step to be accomplished. Thus, starting from initial field values throughout the domain of interest, a time-march process is used so as to advance toward the final steady-state solution, which is usually of special interest as opposed to the en route calculation.

In equation (1) the time-derivatives are approximated by forward one-sided derivatives; most spatial derivatives are approximated by central differences based on values at time-level t . In the representation of the convection terms, a certain amount of upstream differencing is required. The difference equations representing the partial differential equations may be written explicitly as

$$\phi = \phi^n + \Delta t [\dots] \quad (5)$$

where $\phi = u, v, w$ and m_1 , and the right-hand side is evaluated at time-level t . Convective, diffusion and other terms occur in the parentheses on the right. Donor cell differencing is used with the convection terms. The formulation is obtained in a straightforward but tedious manner as a 3-D version of the 2-D version given in references [7 and 11] for u, v , and m_1 . The w velocity component is handled in a similar manner. In all four of these forward marching equations, donor cell differencing is used with the convection terms. In this, a coefficient α takes a constant value between 0 and 1, so giving the desired amount of upstream differencing [11]. A value of 0 gives merely central differencing as in the original MAC code (19, 20) and numerical instability problems arise: a value of 1 gives the full upstream or donor cell for which, although less accurate, is stable provided among other things that the fluid is not allowed to pass through more than one cell in one time-step.

Although equation (5) accomplishes one forward time-step based on conservation of momentum principles, the newly calculated velocities will not, in general, satisfy the continuity requirement, as expressed by the central finite difference form of the continuity equation (the first of equation (1)):

$$\frac{1}{\Delta x} (u_{ijk} - u_{i-1,j,k}) + \frac{1}{\Delta y} (v_{ijk} - v_{i,j-1,k}) + \frac{1}{\Delta z} (w_{ijk} - w_{i,j,k-1}) = 0 \quad (6)$$

Terms here are evaluated at time-level $t + \Delta t$. This incompressibility condition is imposed by iteratively adjusting the cell pressure and velocities, as described elsewhere [11, 12, 21].

At each step of the time-march, application of the diffusion

equation (conservation of chemical species) to the low-density fluid 1 (initially the top layer of fluid in the solution domain) enables the respective proportions of fluid 1 and fluid 2 (the high density fluid initially forming the bottom layer of fluid in the solution domain) to be calculated, and hence the density at all locations. Convergence to the steady-state solution is established by taking many forward time-steps. The choice of time increment must be restricted (for stability) in two ways. First, fluid should not pass through more than one cell in one time step. Therefore Δt must be less than (usually 0.25 to 0.33 times) the minimum cell transit time taken over all cells. Secondly, when a nonzero value of kinematic viscosity is used, the momentum should not diffuse more than one cell in one time step. Accuracy is enhanced by using small space and time intervals, the choice being determined in an ad hoc manner as a suitable trade-off between accuracy and economy of computation.

Boundary Conditions. The time-march process is applied to all cells within the flow domain of interest. Cells touching the boundary thus utilize the value on the boundary (in the case of a normal velocity) or values half a cell distant beyond the boundary (in the case of tangential velocities). Interior normal velocity calculations take the zero normal wall values, and the given normal inlet and outlet values, as appropriate BCs during their calculations. Interior tangential velocity calculations use the fictitious values which are placed in the surrounding layer of complementary cells. Specification of these is after each time-step and after each sweep of the cells during the pressure iteration. With a coarse grid, *free-slip* BCs are appropriate for tangential velocities, and external values are set equal to their associated immediately interior values. On the other hand, with a fine grid computing through the boundary layer, *no-slip* BCs are appropriate for tangential velocities and external values are set equal to the *negative* of their associated immediately interior values. At planes of symmetry the usual zero normal velocity and free-slip tangential velocity specification are applicable. Free-slip conditions are also imposed on the free surface. This is assumed to remain at a constant height, since the propeller is located sufficiently far beneath it, as discussed in reference [5]. The flow from the propeller is modeled as a square-sectioned free jet with velocity, mass flow rate and momentum corresponding to the experimental measurements.

Predictions and Discussion

The ability to characterize the flowfield in the vicinity of low-level release structures during destratification is of prime importance in addressing questions of design and sizing of applicable propeller pumps. Comparison of results with hydraulic laboratory model data of Moon [22] shows that the numerical simulation of local destratification phenomena is a useful predictive tool. The *dilution factor DF* (release water quality) is found to be a function of turbulent viscosity μ_t , densimetric Froude number Fr_d , nondimensional metalimnion (interface) height Z_T^* , nondimensional flow rate Q^* , and nondimensional propeller diameter D^* , horizontal distance K^* and depth L^* .

A standard base case is taken with parameters

$$\begin{aligned} \mu_t / \mu &= 142 \\ K^* &= 0.211 \\ Fr_d &= 1.6 \text{ and } 2.0 \\ Q^* &= 2.6 \\ D^* &= 0.131 \end{aligned}$$

from which certain changes are made and individually assessed in the subsequent discussion. Figures 4-8 show the computed effect of variation of each of these parameters on the dilution factor DF, while the other parameters are maintained at their respective base values, with the

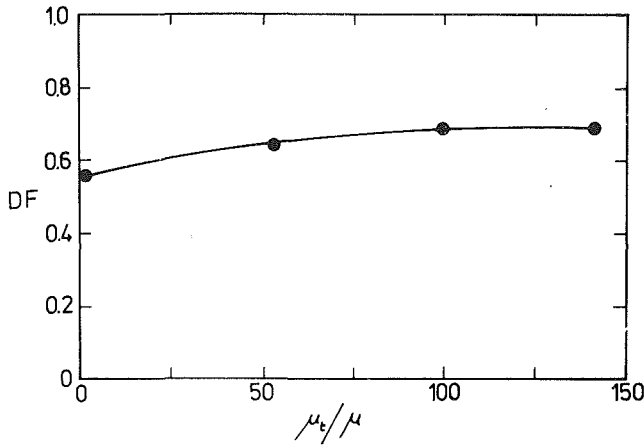


Fig. 4 Effect of turbulent viscosity μ_t on dilution factor DF [$K^* = 0.211$, $Frd = 2.0$, $Q^* = 2.6$, $D^* = 0.131$]

parameters $Z_T^* = 0.6$ and $L^* = 0.211$ held constant for all the figures. An indication of the effect of these two parameters on the axisymmetric flowfield is given in reference [5]. Appropriate experimental results are also shown where available and it is to be observed that the main dynamic effects are modeled adequately and show the same trends as the available physical data. A grid system of $10 \times 8 \times 12$ grid lines in the x , y , and z directions, respectively, is used and approximately 6 minutes of IBM 370/168 CP time is required for evolution of the final steady state solution.

Figure 4 shows the effect of varying the magnitude of the turbulent viscosity μ_t on the dilution factor DF. Only a minor effect is to be seen indicating that results are not too susceptible to the particular choice. Since the computed effects were minor, it may be concluded that precise modeling of the turbulence is not crucial to obtaining good results. The present work also incorporates a constant turbulent Schmidt number equal to unity used in the species equation. The result is a good similitude between temperature-stratified field tests, chemically-stratified laboratory tests and numerical predictions.

Another question is the difference between axisymmetric problems on which the previous theory was based [5] and asymmetric problems on which the experimental data of Moon [22] were obtained, and with which those results were compared. Identical results could not be expected, but the work reported [5] showed that similar parametric trends were to be observed in both geometries. This would undoubtedly not be the case if the geometry of the asymmetric case were no longer compact, with the release gate laterally far away from the plume. With the present 3-D prediction procedure this effect can be investigated. Figure 5 shows the effect of the nondimensional distance from the release structure to the propeller axis K^* . The figure shows that the dilution factor is maximum when the propeller is next to the wall and it decreases gradually as the propeller is moved further away from the release structure. It can be inferred from this that the previous axisymmetric simulation tends to over-predict the release water quality as compared with the practical case.

In Fig. 6 the dilution factor DF is shown to be a strong function of the densimetric Froude number Frd in both predictive and laboratory data. The general result is that release water quality (fraction of epilimnetic (top) water in the exit stream) increases with higher values of the Froude number, such conditions being achieved with higher jet velocities from the propeller and/or a lower degree of stratification in the lake. The figure clearly shows the difference between the 2-D and 3-D models: the former over-predicting the release water quality and the latter giving more

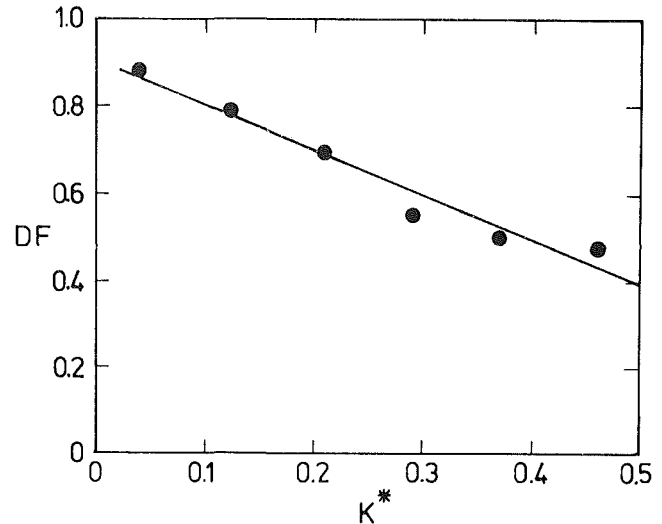


Fig. 5 Dilution factor DF as a function of nondimensional horizontal distance from release structure K^* [$\mu_t/\mu = 142$, $Frd = 2.0$, $Q^* = 2.6$, $D^* = 0.131$]

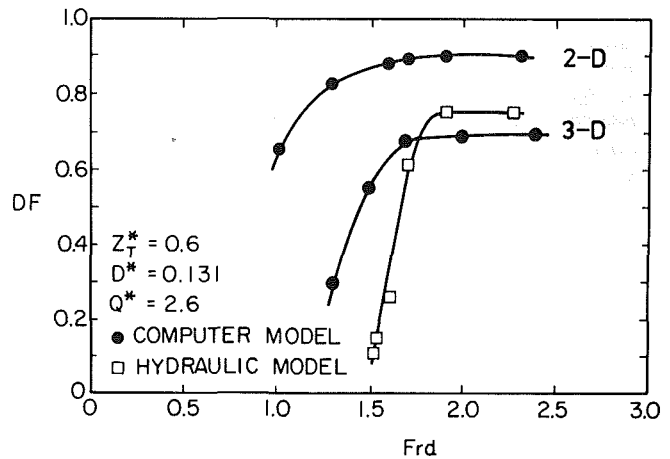


Fig. 6 Dilution factor DF as a function of Froude number Frd [$\mu_t/\mu = 142$, $K^* = 0.211$, $Q^* = 2.6$, $D^* = 0.131$]

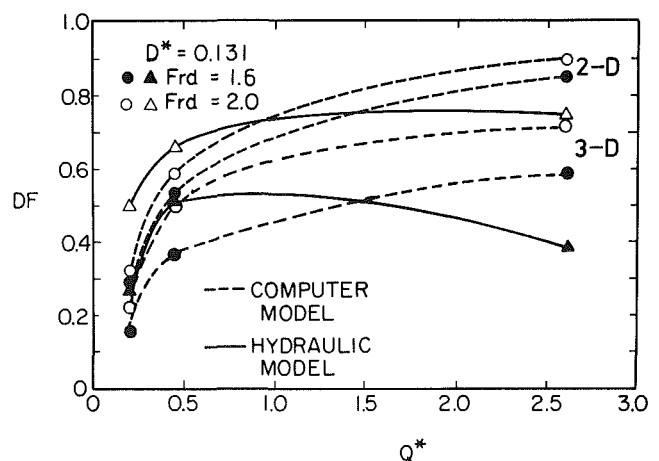


Fig. 7 Dilution factor DF as a function of nondimensional flow rate Q^* [$\mu_t/\mu = 142$, $K^* = 0.211$, $D^* = 0.131$]

accurate predictions when compared to the experimental data. From the designer's view, the important result is the Froude number at which the dilution factor rises sharply, since that determines the velocity required at the propeller for the given conditions. Clearly the 3-D simulation is superior to the 2-D

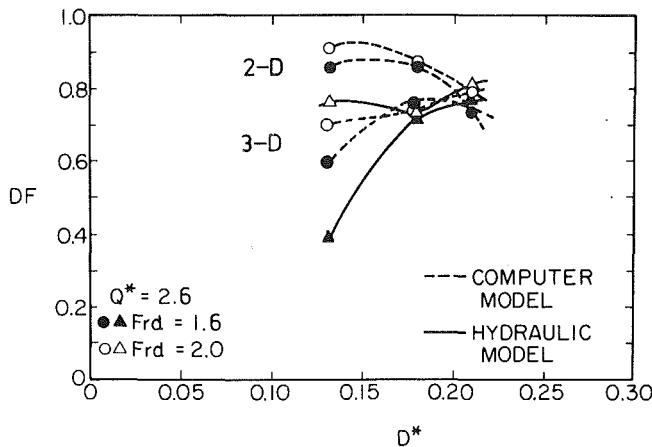


Fig. 8 Dilution factor DF as a function of nondimensional propeller diameter D^* [$\mu_t/\mu = 142$, $K^* = 0.211$, $Q^* = 2.6$]

simulation, and this Dilution Factor is predicted better via the 3-D approach.

Figure 7 illustrates that the dilution factor DF is a strong function of the flow-rate ratio Q^* . Generally, release water quality improves with increase in the value of Q^* , a condition achieved with low release rates and high propeller flow rates. The figure shows the relationship found in both hydraulic laboratory model and computer simulations. Again, the 2-D model over-predicts the dilution factor whereas the 3-D model shows more realistic results, especially at higher values of Q^* , which are better for obtaining higher water quality in the release flow.

The effect of changing the propeller diameter, but retaining the propeller flow rate Q^* the same, is shown in Fig. 8. Over-prediction with the 2-D approach was present as expected. The 3-D approach, however, shows good agreement between predicted and experimental evidence of the effect of normalized diameter D^* on dilution factor DF. These and other results show that a value of $D^* = 0.211$ gives best results at this value of $Q^* = 2.6$. At different values of Q^* , different values of D^* give optimum results [15].

Conclusions

The fully three-dimensional prediction procedure represents a low-cost basic tool to show the influence of design parameters for local destratifications in reservoirs with low-level release structures. Comparison with hydraulic models shows that this numerical simulation of the local destratification phenomenon is useful for the prediction of the dilution factor (released water quality). The main dynamic effects are modeled adequately to show the same trend as the available physical data. The dilution factor is found to be a function of the densimetric Froude number, propeller flow rate relative to the release flow rate, propeller diameter, and propeller distance from the release structure. As expected, the present three-dimensional approach gives more realistic and accurate results than previous approaches.

Acknowledgment

The authors wish to express their appreciation to the Office of Water Research and Technology and Oklahoma Water

Resources Research Institute for financial support under Cooperative Program Project A-098-OKLA.

References

- Symons, J. M., Irwin, W. H., Robinson, E. L., and Robeck, G. G., "Impoundment Destratification for Raw Water Quality Control Using Either Mechanical or Diffused-Air-Pumping," *Journal of the American Water Works Association*, Vol. 59, No. 10, Oct. 1967, pp. 1268-1291.
- Garton, J. E., and Peralta, R. C., "Water Quality Enhancement by Point Destratification, Gillham Lake, Arkansas," A special report, Feb. 1978, Oklahoma Water Resources Research Institute.
- Dortch, M. S., and Wilhelms, S. C., "Enhancement of Releases from a Stratified Impoundment by Localized Mixing, Okatibee Lake, Mississippi," Misc. Paper H-78-1, Jan. 1978, Hydraulics Laboratory, United States Army Corps of Engineers, Waterways Experiment Station, Vicksburg, Miss.
- Garton, J. E., and Jarrell, H. R., "Demonstration of Water Quality Enhancement Through Use of the Garton Pump," Supplement to the Technical Completion Report No. C-5228-A, March 1976, Oklahoma Water Resources Research Institute.
- Busnaina, A. A., Lilley, D. G., and Moretti, P. M., "Prediction of Local Destratification of Lakes," *Journal of the Hydraulics Division*, ASCE, HY3, Proc. Paper 16904, Mar. 1981, pp. 259-272.
- Moretti, P. M., and McLaughlin, D. K., "Hydraulics Modeling of Mixing in Stratified Lakes," *Journal of the Hydraulics Division*, ASCE, Vol. 103, No. HY4, Proc. Paper 12868, Apr. 1977, pp. 367-380.
- Busnaina, A. A., "Numerical Simulation of Local Destratification of Lakes," Thesis presented to the Oklahoma State University at Stillwater, Okla., in 1979, in partial fulfillment of the requirements for the degree of Master of Science.
- Abraham, G., and Eysink, W. D., "Jets Issuing Into Fluid With a Density Gradient," *Journal of Hydraulic Research*, Vol. 7, No. 2, Apr. 1969, pp. 145-175.
- Baines, W. D., "Entrainment by a Plume or Jet at a Density Interface," *Journal of Fluid Mechanics*, Vol. 68, Apr. 1976, pp. 309-320.
- Ditmars, J. D., "Mixing of Density Stratified Impoundments with Buoyant Jets," Report No. KH-R-22, Sept. 1970, W. M. Keck Laboratory of Hydraulics and Water Resources, California Institute of Technology, Pasadena, Calif.
- Hirt, C. W., Nichols, B. D., and Romero, N. C., "SOLA: A Numerical Solution Algorithm for Transient Fluid Flows," Report LA-5882, 1975, Los Alamos Scientific Laboratory and the University of California, Los Alamos, N.Mex.
- Hirt, C. W., and Cook, J. L., "Calculating Three-Dimensional Flows Around Structures and Over Rough Terrain," *Journal of Comp. Physics*, Vol. 10, 1972, pp. 324-340.
- Caretto, L. S., Gosman, A. D., Patankar, S. V., and Spalding, D. B., "Two Calculation Procedures for Steady, Three Dimensional Flows with Recirculation," *Proceedings 3rd Int. Conference on Numerical Methods in Fluid Mechanics*, Vol. 2, J. Ehlers, K. Hepp, and H. A. Weidenmuller, eds., Springer-Verlag, Germany, 1973, pp. 60-68.
- Pracht, W. E., "Calculating Three-Dimensional Fluid Flows at All Speeds with an Eulerian-Lagrangian Computing Mesh," *Journal of Computational Physics*, Vol. 17, 1975, pp. 132-159.
- Hjertager, B. H., and Magnussen, B. F., "Numerical Prediction of Three Dimensional Turbulent Buoyant Flow in a Ventilated Room," Paper presented at International Center for Heat and Mass Transfer, 1976 Int. Seminar on Turbulent Buoyant Convection, held at Dubrovnik, Yugoslavia, Aug. 30-Sept. 4, 1976.
- Hinze, J. O., *Turbulence*, 2nd ed., McGraw-Hill, New York, 1975, p. 539.
- Schlichting, H., *Boundary Layer Theory*, 6th ed., McGraw-Hill, New York, N.Y., 1968, p. 699.
- Hinze, J. O., and Van Der Hegge Zijnen, B. G., "Transfer of Heat and Matter in the Turbulent Mixing Zone of an Axially Symmetrical Jet," *Applied Science Res.*, Vol. A1, 1949, pp. 435-461.
- Harlow, F. H., and Welch, J. E., "Numerical Calculation of Time-Dependent Viscous Incompressible Flow of Fluid with Free Surface (The MAC Method)," *Physics of Fluids*, Vol. 8, 1965, pp. 2182-2189.
- Amsden, A. A., and Harlow, F. H., "The SMAC Method: A Numerical Technique for Calculating Incompressible Fluid Flows," Report LA-4379, 1970, Los Alamos Scientific Laboratory, Los Alamos, N.Mex.
- Busnaina, A. A., and Lilley, D. G., ASME Paper 81-FE-11, Boulder, Colo., June 22-24, 1981.
- Moon, J. J., "Enhancement of Release Water Quality by Localized Mixing - A Hydraulic Model Study," Thesis presented to the Oklahoma State University at Stillwater, Okla., in 1978, in partial fulfillment of the requirements for the degree of Master of Science.

Development of Magnetohydrodynamic Flow in a Parallel-Plate Channel in an Inclined Field

S. Rajaram¹

C. P. Yu

Faculty of Engineering
and Applied Sciences,
State University of
New York at Buffalo,
Amherst, N. Y. 14260

A study has been made on the steady, incompressible developing MHD flow in a parallel-plate channel. The applied magnetic field is uniform but its direction makes an arbitrary angle with the channel axis. The full Navier-Stokes equations have been employed in the analysis. Velocity development and induced magnetic fields are found. The results show that for a weak field the entrance length decreases with the magnetic field and only the transverse component of the field has an effect. However, in a strong field the entrance length is found to either increase or decrease with the field depending upon the angle of inclination.

I Introduction

In this paper, steady incompressible flow in the developing region of a parallel-plate channel under the influence of a uniform magnetic field of arbitrary direction is studied. There have been extensive efforts in the past to study the developing flow in this geometry in a transverse magnetic field [1-7]. The field was found to reduce the entrance length, and, for a very large field, the entrance length varies as $1/M^2$ where M is the Hartmann number. If the magnetic field is parallel to the channel, the field will have no effect on the fully-developed velocity profile, but the entrance length was shown to increase with the field [8]. Thus the velocity development in the channel depends upon the angle of field inclination.

II Problem Formulation

We consider an entrance flow problem as shown in Fig. 1. The fluid enters the channel with a uniform velocity u_0 . The channel has a width of $2a$ and the wall thickness is t_w . A uniform magnetic field is applied at an angle β to the channel axis. The governing equations for the fluid region are as follows:

$$\nabla \cdot \mathbf{u} = 0 \quad (1)$$

$$(\mathbf{u} \cdot \nabla) \mathbf{u} = -\frac{1}{\rho} \nabla p + \nu \nabla^2 \mathbf{u} + \frac{1}{\rho} (\mathbf{j} \times \mathbf{B}) \quad (2)$$

$$\nabla \cdot \mathbf{B} = 0 \quad (3)$$

$$\nabla \times (\mathbf{u} \times \mathbf{B}) + \frac{1}{\mu\sigma} \nabla^2 \mathbf{B} = 0 \quad (4)$$

where \mathbf{u} is the fluid velocity, p the pressure, \mathbf{B} the magnetic

field, and $\mathbf{j} = (\nabla \times \mathbf{B})/\mu$ the electric current density. Also, ρ , ν , μ , and σ are the mass density, kinematic viscosity, magnetic permeability, and electrical conductivity of the fluid, respectively.

We define vorticity ω and stream function ψ such that $\omega = \nabla \times \mathbf{u}$ and $\mathbf{u} = \nabla \times \psi$. In analogy, we define quantities ξ and ϕ such that $\xi = \nabla \times \mathbf{B}'$ and $\mathbf{B}' = \nabla \times \phi$ where \mathbf{B}' is the induced magnetic field. With the use of these new quantities and introducing a coordinate transformation

$$\eta = 1 - (1 + kx)^{-1}, \quad k = \text{constant} \quad (5)$$

which transforms x to a finite domain, η , (1)-(4) may be replaced by the following system of equations:

$$\frac{d\eta}{dx} \left[-\frac{\partial}{\partial \eta} (u_x \omega) - \frac{\partial}{\partial y} (\bar{u}_y \omega) \right] + \frac{1}{\text{Re}} \bar{\nabla}^2 \omega + \frac{M^2}{\text{ReRe}_m} \frac{d\eta}{dx} \left[\frac{\partial}{\partial \eta} (B_x \xi) + \frac{\partial}{\partial y} (\bar{B}_y \xi) \right] = 0 \quad (6)$$

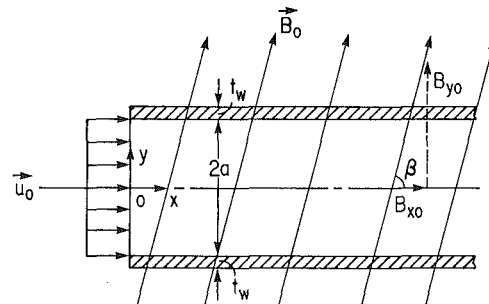


Fig. 1 Geometry of the problem

¹Present address: Western Electric Company, Princeton, N.J. 08540.

Contributed by the Fluids Engineering Division of THE AMERICAN SOCIETY OF MECHANICAL ENGINEERS and presented at the Winter Annual Meeting, Phoenix, Ariz. November 14-19, 1982. Manuscript received by the Fluids Engineering Division, March 26, 1981. Paper No. 82-WA/FE-6.

$$\frac{d\eta}{dx} \left[-\frac{\partial}{\partial \eta} (u_x \xi) - \frac{\partial}{\partial y} (\bar{u}_y \xi) \right] + \frac{1}{\text{Re}_m} \bar{\nabla}^2 \xi$$

$$+ \frac{d\eta}{dx} \left[\frac{\partial}{\partial \eta} (B_x \omega) + \frac{\partial}{\partial y} (\bar{B}_y \omega) \right] + \frac{d\eta}{dx} \frac{\partial B_x}{\partial \eta} \left(\frac{\partial u}{\partial y} - \bar{\nabla}^2 \psi \right.$$

$$\left. + \frac{\partial^2 \psi}{\partial y^2} \right) + \frac{d\eta}{dx} \frac{\partial \bar{u}_y}{\partial y} \left(\frac{\partial B_x}{\partial y} - \bar{\nabla}^2 \phi + \frac{\partial^2 \phi}{\partial y^2} \right) = 0 \quad (7)$$

$$\omega = -\bar{\nabla}^2 \psi \quad (8)$$

$$\xi = -\bar{\nabla}^2 \phi \quad (9)$$

where $\text{Re} = u_0 a / \nu$, $\text{Re}_m = \sigma \mu u_0 a$, and $M = B_0 a (\sigma / \rho \nu)^{1/2}$ are, respectively, Reynolds number, magnetic Reynolds number, and Hartmann number, and all variables have been made dimensionless by means of the following substitutions

$$x^* = x/a, \quad y^* = y/a, \quad \mathbf{u}^* = \mathbf{u}/u_0, \quad \mathbf{B}^* = \mathbf{B}/B_0$$

$$\omega^* = a\omega/u_0, \quad \xi^* = a\xi/B_0, \quad \psi^* = \psi/(a u_0), \quad \phi^* = \phi/(a B_0).$$

the asterisks in (6)-(9) have been dropped for convenience. Also, in (6)-(9) $\mathbf{B} = \mathbf{B}_0 + \mathbf{B}'$, $\bar{\nabla}^2$, \bar{u}_y , and \bar{B}_y are given by

$$\bar{\nabla}^2 = \left(\frac{d\eta}{dx} \right)^2 \frac{\partial^2}{\partial \eta^2} + \left(\frac{d^2 \eta}{dx^2} \right) \frac{\partial}{\partial \eta} + \frac{\partial^2}{\partial y^2}$$

$$\bar{u}_y = u_y / \left(\frac{d\eta}{dx} \right)$$

and

$$\bar{B}_y = B_y / \left(\frac{d\eta}{dx} \right)$$

The boundary conditions at $\eta = 0$ and $\eta = 1$ are, respectively, the uniform velocity conditions and the fully developed MHD flow solution given by Chang and Lundgren [9]. Since the developing flow is not symmetrical to the channel axis $y = 0$ in an inclined field [10], we need to find the solution of the problem in the y domain from -1 to 1 . At the channel wall, $y = \pm 1$, the boundary conditions for velocity are the no-slip condition $u_x = u_y = 0$. The electromagnetic boundary conditions require the tangential component of the electric and magnetic fields and also the normal component of the magnetic field to be continuous at the wall-fluid interface. Thus the solutions for the electric and magnetic fields must be first obtained in the wall region. If we assume that the wall is thin such that $t_w \ll a$, then \mathbf{B}' in the wall region is a linear function of y for all x . This enables us to obtain at $y = \pm 1$

$$\phi = \mp \frac{A}{2} \left(\frac{\partial \phi}{\partial y} \right) \quad (10)$$

and

$$\xi = \frac{A}{\gamma} \left(\pm \frac{1}{A} \frac{\partial \phi}{\partial y} - \left(\frac{d\eta}{dx} \right)^2 \frac{\partial^2 \phi}{\partial \eta^2} - \frac{d^2 \eta}{dx^2} \frac{\partial \phi}{\partial \eta} \right) \quad (11)$$

where $A = t_w/a$ and $\gamma = \sigma_w t_w / (\sigma_a)$. In the present analysis, a value of 0.1 for A has been used.

III Method of Solution

An inspection of the basic equations (6)-(9) reveals that they are coupled and also contain first-order nonlinear convective terms. These difficulties render the problem impossible for an analytical solution. The only means of obtaining a solution is by numerical methods. We propose a finite-difference scheme using upwind differences for the solution of the problem. Since (6)-(9) are elliptic, the most effective method of solving two-dimensional, nonlinear problems of the type is that of successive over-relaxation. Not all iterative schemes, however, are convergent. Many of the standard numerical schemes using central differences become unstable at higher Re due to the presence of the nonlinear convective terms. The maximum value of Re up to which a solution can be determined using central differences was 500, with severe under-relaxation. The increase in stability even for low Re was at the expense of a very large computing time. The upwind-differencing method was developed as the answer to this problem. By this method, the first-order convective terms are written in a finite-difference form which depends upon the direction of flow, and this formulation is termed upwind differences. This method causes the stability to the solution to be far greater than that obtained for central differences. The method is unconditionally stable up to very high values of Re .

Consider an equation in the form

$$x_i = \sum_{j, i \neq j} (a_{ij} x_j + b_i) \quad (12)$$

in which a 's and b 's are constant. This equation is a convergent successive substitute formula if

$$\sum_{j, i \neq j} |a_{ij}| \leq 1 \quad (13)$$

or each i , and, for at least one i ,

$$\sum_{j, i \neq j} |a_{ij}| < 1 \quad (14)$$

The method of upwind differences expresses the equations in a form similar to (12). These are nonlinear, however, and the a 's and b 's vary from one iteration to the next. Although the condition of linearity is slightly violated, the method tries to satisfy the necessary conditions (13) and (14) without serious loss of stability.

Table 1 Flow variables and coefficients

F	a_F	b_F	c_F	d_F
τ	$\frac{du}{dx}$	$\frac{1}{\text{Re}}$	1	$\frac{-1}{\text{Re}} \left[\frac{\partial^2 \tau}{\partial \eta^2} \left\{ \left(\frac{d\eta}{dx} \right)^2 - 1 \right\} + \frac{d^2 \eta}{dx^2} \frac{\partial \tau}{\partial \eta} \right] - \frac{M^2}{\text{Re Re}_m} \frac{d\eta}{dx} \left[\frac{\partial}{\partial \eta} (B_x \xi) + \frac{\partial}{\partial y} (\bar{B}_y \xi) \right]$
ψ	0	1	1	$-\tau - \frac{d^2 \eta}{dx^2} \frac{\partial \psi}{\partial \eta} - \frac{\partial^2 \psi}{\partial \eta^2} \left[\left(\frac{d\eta}{dx} \right)^2 - 1 \right]$
ξ	$\frac{d\eta}{dx}$	$\frac{1}{\text{Re}_m}$	1	$\frac{-1}{\text{Re}_m} \left[\frac{\partial^2 \xi}{\partial \eta^2} \left\{ \left(\frac{d\eta}{dx} \right)^2 - 1 \right\} + \frac{d^2 \eta}{dx^2} \frac{\partial \xi}{\partial \eta} \right] - \frac{d\eta}{dx} \left[\frac{\partial}{\partial \eta} (B_x \tau) + \frac{\partial}{\partial y} (\bar{B}_y \tau) \right]$ $- \frac{d\eta}{dx} \frac{\partial B_x}{\partial \eta} \left[\frac{\partial u}{\partial y} - \bar{\nabla}^2 \psi + \frac{\partial^2 \psi}{\partial y^2} \right] - \frac{d\eta}{dx} \frac{\partial v}{\partial y} \left[\frac{\partial B_x}{\partial y} - \bar{\nabla}^2 \phi + \frac{\partial^2 \phi}{\partial y^2} \right]$
ϕ	0	1	1	$-\xi - \frac{d^2 \eta}{dx^2} \frac{\partial \phi}{\partial \eta} - \frac{\partial^2 \phi}{\partial \eta^2} \left[\left(\frac{d\eta}{dx} \right)^2 - 1 \right]$

Inspection of (6)–(9) reveals that all of them can be written in one single form which contains convective terms, diffusive terms, and source terms as follows:

$$aF \left[\frac{\partial}{\partial \eta} \left(F \frac{\partial \psi}{\partial y} \right) - \frac{\partial}{\partial y} \left(F \frac{\partial \psi}{\partial \eta} \right) \right] - \frac{\partial}{\partial \eta} \left[b_F \frac{\partial}{\partial \eta} (c_F F) \right] - \frac{\partial}{\partial y} \left[b_F \frac{\partial}{\partial y} (c_F F) \right] + d_F = 0 \quad (15)$$

where the flow variable F and the coefficients a , b , c , and d for the particular flow variable F are given in Table 1.

The details of developing a finite difference equation from (15) are discussed in [11] and will not be repeated here. The final form is similar to (12) in which a_{ij} satisfy conditions (13) and (14). The computational procedure consists of a single iterative loop in which each variable is updated in a sequence. To start the procedure, values of u_x , u_y , B_x , B_y , ω , ψ , ξ , and ϕ are assumed for the entire flow field. The sequence of iterations begins with the updating of ψ using (8) and ϕ using (9). This is followed by the calculation of u_x and u_y using the new values of ψ , and B_x and B_y using the new value of ϕ . Boundary conditions for ω and ξ are calculated next, and ω and ξ are updated from (6) and (7), respectively. This completes the iterative cycle. The whole cycle of iterations is continued until convergence is attained. The solution is declared to have converged when each of the variables ω , ψ , ξ , and ϕ satisfies the criterion

$$\left| \frac{\text{New Value} - \text{Old Value}}{\text{New Value}} \right| < 10^{-4}$$

from one iteration to the next.

Among the equations in the system (6)–(9), (6) is the most illbehaved because of its strong nonlinearity. The relaxation factor for this equation was set at 1 except for a few cases where under-relaxation was required. (7)–(9) are well-behaved and were over-relaxed to obtain faster convergence. The vorticity boundary condition at the wall $\tau = -\partial u/\partial y$ is evaluated by a second-order backward difference formula. Since the velocities are 0 at the wall and ψ is constant, the condition $\partial \psi/\partial y = 0$ is also satisfied by using a second-order backward difference formula, updating the row of points Δy away from the wall. This increases the accuracy of the numerical scheme. Since the velocity gradients are steep near the wall, a logarithmic distribution is used for the grid size in the y direction. This gives closely spaced points near the wall where the gradients are large, and the grid size increases near the centerline where the gradients are smaller. This was also found to give greater accuracy. A uniform grid size is used in the η direction. Convergence in an 11×11 grid system starting from zero for the flow solution is obtained in about 350–400 iterations and for a 21×21 grid system in about 800 iterations. The converged solution for one case was usually used as the input for the next. In such cases, much faster convergence was obtained.

IV Results and Discussion

Figure 2 shows the u_x velocity profiles in the developing region of the channel. Close to the entrance, the characteristic shape of the velocity profiles includes a local minimum near the centerline and two maxima on either side. The profiles therefore show a characteristic bulge. This result was previously noted by Brandt and Gillis [3] and Wang and Longwell [12] in their studies of developing flows using the full Navier-Stokes equations. The presence of the bulges is believed to be part of the exact solution caused by the velocity singularity at the wall at $x=0$. The physical explanation of this phenomenon was given by Brandt and Gillis as follows. As the fluid enters the channel, it is brought to rest at the wall due to the nonslip condition. The core flow, therefore, has to

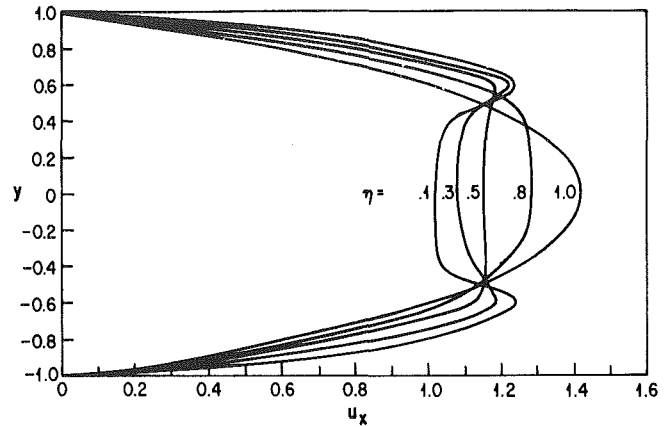


Fig. 2 Developing u_x profiles in the full channel for $Re = 100$, $M = 4$, $Re_m = 1$, $\gamma = 10$, and $\beta = 30$ deg

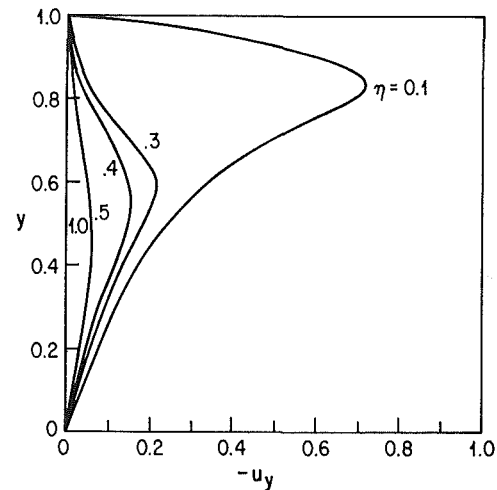


Fig. 3 Developing u_y profiles for $Re = 100$, $M = 4$, $Re_m = 1$, $\gamma = 10$, and $\beta = 30$ deg

be accelerated in order to satisfy the continuity equation. This acceleration, however, is not felt instantaneously by the entire fluid region, leading to the formation of those maxima and minimum in the velocity profile. The bulges exist up to a distance downstream and vanish thereafter as the wall shear becomes smaller. The development of u_x is qualitatively similar for all values of Re , M , Re_m , and γ . However, the magnitude of the bulges or the detailed velocity profile development depends upon these quantities. Typically, increasing Re or decreasing M will intensify the bulges, as would increasing Re_m or γ . For roughly the same value of Re , the bulges shown in Fig. 1 are considerably larger than that obtained by Wang and Longwell for $M=0$. This is caused by the Re_m and γ effect. From physical viewpoints, the appearance of the bulges may not be of great significance because a slug velocity profile at the entrance cannot be physically realizable. Indeed, when Wang and Longwell used a different upstream boundary condition, the bulges disappeared. Existing experimental data on the entrance velocity profiles so far have not confirmed the existence of these bulges.

Figure 3 shows a typical u_y velocity profile for the entrance region. Only half of the channel is shown because the asymmetry is very small for the case considered. As would be expected, the magnitude of u_y is largest near the entrance and diminishes to zero in the fully developed region. This is because the fluid is brought to rest at the walls as it enters the channel and is subjected to the greatest shear. The direction of u_y is such that the fluid moves away from the walls as the boundary layer develops. Very close to the entrance, u_x and

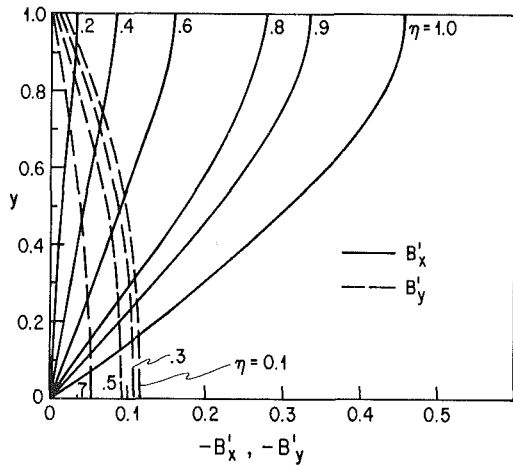


Fig. 4 Developing B'_x (solid lines) and B'_y (dotted lines) profiles for $Re = 100$, $M = 4$, $Re_m = 1$, $\gamma = 10$, and $\beta = 30$ deg

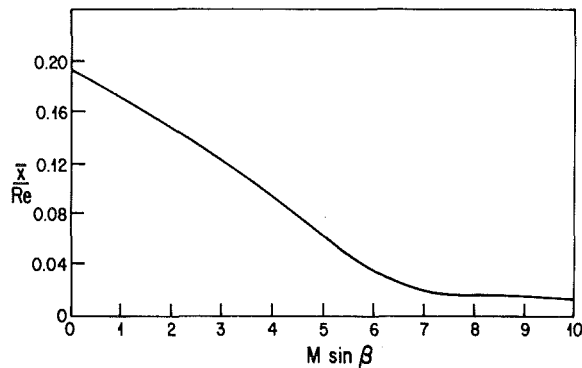


Fig. 5 Entrance length as a function of $M \sin \beta$ for $Re = 500$, $Re_m = 2$, and $\gamma = 0$

u_y can be of the same order of magnitude, depending upon the flow parameters.

The induced magnetic fields B'_x and B'_y are shown in Fig. 4. Near the entrance, B'_x and B'_y are seen to have equal order of magnitude for the flow condition studied. It is of interest to note that B'_y has its largest value near the entrance and gradually diminishes along the flow direction until it becomes zero in the fully-developed region. On the other hand, B'_x has its smallest value near the entrance and increases monotonically until the fully-developed region is reached. The distribution of B'_x depends upon the conductivity of the channel wall. For a highly conducting wall, $\gamma \gg 1$, B'_x has a maximum at the wall, which is the case shown in Fig. 4.

The entrance length is used to measure how fast the flow is developing to reach the fully-developed profile. This length is defined as the distance from the entrance at which the centerline velocity reaches 99 percent of the fully-developed value. For an inclined magnetic field, the effect of the magnetic field on flow and entrance length depends upon the parameters M , Re_m , β , and γ . However, for $M/Re \ll 1$, it is found that as β increases from 0 to 90 deg the entrance length decreases, and its value corresponds to that obtained by only a transverse field such that the Hartmann number is $M \sin \beta$. This shows that the entrance length is controlled by the transverse component of the magnetic field for $M/Re \ll 1$ and the effect of the parallel component of the field is negligible. Figure 5 shows the variation of the entrance length \bar{x}/Re for such a case with respect to $M \sin \beta$ at constant Re_m and γ . It is observed that the entrance length decreases rapidly with the increase of $M \sin \beta$. The results at $\beta = 90$ deg and $\gamma = 0$ agree favorably with those found previously by other authors. A comparison of these results is given in Table 2. The

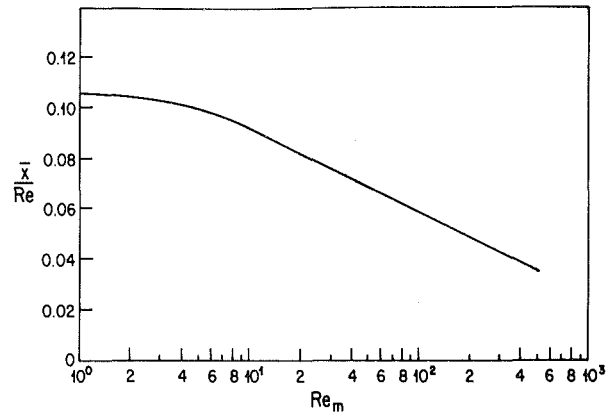


Fig. 6 Entrance length as a function of Re_m for $Re = 500$, $M \sin \beta = 4$, and $\gamma = 0$

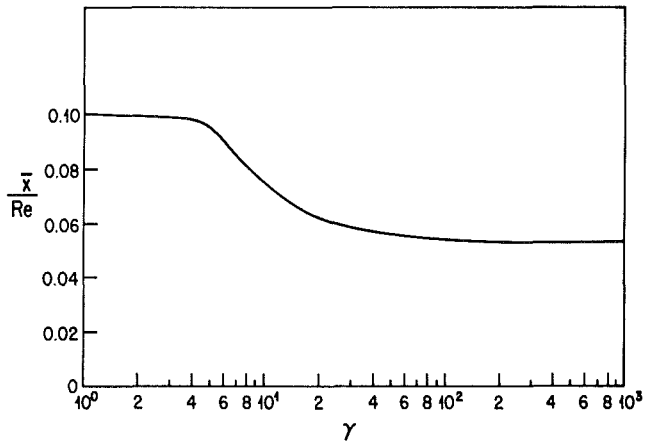


Fig. 7 Entrance length as a function of γ for $Re = 500$, $M \sin \beta = 4$, and $Re_m = 2$

Table 2 Comparison of entrance length for $\gamma = 0$ and $\beta = 90$ deg

M	2	4	10
Wu, et al. [5]	0.14	0.076	0.0106
Snyder [2]	0.145	0.077	0.009
Roidt and Cess [1]	0.1452	0.0668	—
Hwang and Fan [13]	—	0.0752	0.01216
Present Work	0.145	0.0904	0.01124

effects of Re_m and γ on the entrance length for the case $M/Re \ll 1$ are shown in Figs. 6 and 7. The entrance length is found to decrease with increasing Re_m and γ .

For the case $M/Re > 1$, the parallel component of the magnetic field becomes important to the problem and it produces an opposing effect on the entrance length from that of the transverse field. The net effect of the field in this case depends, therefore, upon the inclination angle β . At $Re = Re_m = 1$, $M = 4$, and $\gamma = 0$, Fig. 8 shows the \bar{x}/Re decreases from 2.22 to 0.35 as β increases from 0 to 90 deg. Since \bar{x}/Re has a value of 1.96 at $M=0$, we obtain from the figure that a particular angle $\beta_0 \approx 13$ deg exists such that for $\beta < \beta_0$ the entrance length is larger than the nonmagnetic value. The angle β_0 is found to vary with the parameters Re , Re_m , and γ in the problem.

In a parallel magnetic field, the fully-developed velocity profile is not affected by the field and is therefore parabolic. The velocity development in this case depends only upon the parameter $(M/Re)^2$ as noted by D'arcy and Schmidt [8].

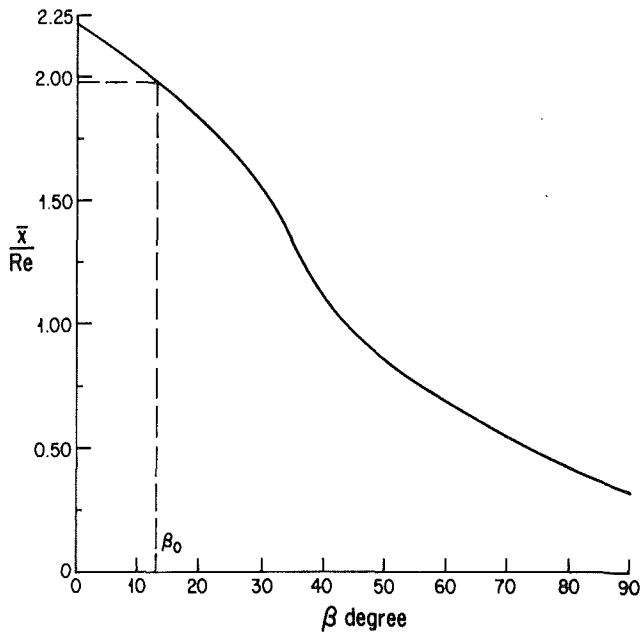


Fig. 8 Entrance length as a function of β for $Re = 1$, $M = 4$, $Re_m = 1$, and $\gamma = 0$

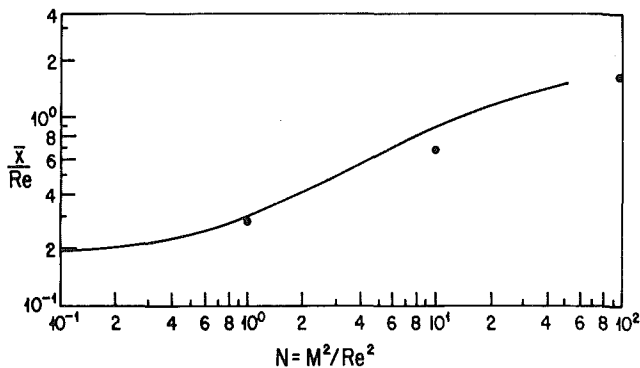


Fig. 9 Entrance length as a function of N for $\beta = 0$ deg. The dots are the results by D'arcy and Schmidt [8].

Figure 9 shows that the entrance length increases with $(M/Re)^2$. This is due to the increase of the Lorentz force which in this case acts against fluid movement in the y direction. Also, the entrance length is found to be slightly greater than that obtained by D'arcy and Schmidt using a boundary layer analysis. However, calculation shows that the pressure gradient in the y direction is significantly large, contrary to the boundary layer assumption.

Acknowledgment

This work was supported by Grant No. ENG-7721233 from the National Science Foundation.

References

- 1 Roidt, M., and Cess, R. D., "An Approximate Analysis of Laminar Magnetohydrodynamic Flow in the Entrance Region of a Flat Duct," *ASME Journal of Applied Mechanics*, Vol. 84, 1962, pp. 171-176.
- 2 Snyder, W. T., "Magnetohydrodynamic Flow in the Entrance Region of a Parallel-Plate Channel," *AIAA J.*, Vol. 3, 1965, pp. 1833-1838.
- 3 Brandt, A., and Gillis, J., "Magnetohydrodynamic Flow in the Inlet Region of a Straight Channel," *Phys. Fluids*, Vol. 9, 1966, pp. 690-699.
- 4 Hsia, E. S., "Entrance Development of the Weakly Interacted MHD Plane Channel Flow as Affected by Wall Conductances," *ASME Journal of Applied Mechanics*, Vol. 38, 1971, pp. 665-673.
- 5 Wu, S. T., Fu, T. S., and Wear, M. B., "Development of MHD Flow in the Entrance Region of a Channel," *Revue De Physique Appliquee*, Vol. 6, 1971, pp. 409-414.
- 6 Chen, T. S., and Chen, G. L., "Magnetohydrodynamic Channel Flow with an Arbitrary Inlet Profile," *Phys. Fluids*, Vol. 15, 1972, pp. 1531-1534.
- 7 Hwang, C. C., "Linearized Analysis of Magnetohydrodynamic Channel Entrance Flow," *Phys. Fluids*, Vol. 15, 1972, pp. 1852-1854.
- 8 D'arcy, G. P., and Schmidt, P. S., *Technology of Controlled Thermonuclear Fusion Experiments and Engineering Aspects of Fusion Reactors*, AEC Symposium Series No. 31, 1974.
- 9 Chang, C. C., and Lundgren, T. S., "Duct Flow in Magnetohydrodynamics," *J. Appl. Mech. and Phys. (ZAMP)*, Vol. 12, 1961, pp. 100-114.
- 10 Branover, H., *Magnetohydrodynamic Flow in Ducts*, Wiley, 1978.
- 11 Gossman, A. D., Pun, W. N., Runchal, A. K., Spalding, D. B. and Wolfshtein, M., *Heat and Mass Transfer in Recirculating Flows*, Academic Press, London.
- 12 Wang, Y. L., and Longwell, P. A., "Laminar Flow in the Inlet Section of Parallel Plates," *AICHE Journal*, Vol. 10, No. 3, 1964, pp. 323-329.
- 13 Hwang, C. L., and Fan, L. T., "A Finite Difference Analysis of Laminar Magneto-Hydrodynamic Flow in the Entrance Region of a Flat Rectangular Duct," *Appl. Sci. Res. B10*, 1963, pp. 329-343.

A Multigrid Scheme for Three-Dimensional Body-Fitted Coordinates in Turbomachine Applications

R. Camarero

M. Reggio

Ecole Polytechnique,
Montreal, Canada

An efficient numerical scheme for the generation of curvilinear body-fitted coordinate systems in three dimensions is presented. The grid is obtained by the solution of a system of three elliptic partial differential equations. The method is based on the classical SOR scheme with an acceleration of convergence using the multigrid technique. The full approximation scheme has been used and is described with the overall algorithm. A number of numerical experiments are given with comparisons to illustrate the efficiency of the method. Practical applications to typical three-dimensional turbomachinery geometries are then shown.

1 Introduction

The numerical computation of the flow in a turbine cascade requires an adequate treatment of the boundary conditions, particularly those at solid walls. These can be quite difficult to incorporate for complex three-dimensional geometries encountered in practical engineering problems. An important step in resolving this problem is the choice of an appropriate coordinate system. One characteristic of such systems is that the coordinate lines should coincide with the boundaries. This will ensure that no interpolation is required, and hence the inaccuracies that could result will not show in the solution. A second characteristic is the ability to stretch the grid in order to concentrate more nodes in regions where high gradients of flow properties are expected.

Transformations which map arbitrary physical regions into a rectangle with the above characteristics have been proposed by several authors (references [1 and 2]) and are called body-fitted curvilinear coordinate systems. The approach consists of solving a system of elliptic equations which yield the physical coordinates (dependent variables) in terms of the transformed coordinates (independent variables). There are as many equations as dimensions, and these are nonlinear and coupled.

The solution obtained is curvilinear coordinate system into which the differential equations of the problem of interest can be transformed. The main advantage is that both the mesh generation and the solution of the problem of interest are solved on a rectangular mesh. This lends itself to a very simple discretization using finite differences or finite volumes, particularly at the boundaries where all interpolations are avoided.

Another possible application is the automatic generation of a finite element mesh. Therefore it is very important that this first step of computation be very efficient and flexible. More precisely the coordinate generation should not exceed a few seconds of computer time.

Reference (1) has solved this problem using a relaxation procedure and reference (2) with an A.D.I. scheme after introducing an artificial time. Efficient multigrid schemes for the solution of such problems have also been proposed in reference [6] and reference [4] in two dimensions. The objective of the present paper to describe an extension of that work to three-dimensional configurations. The results are compared to the classical relaxation schemes and then are applied to typical turbomachinery geometries.

2 Body-Fitted Coordinate Systems

Body-fitted coordinate systems are characterized by the feature that the coordinate lines are aligned with the boundaries of the domain. In particular the bounding coordinate surface will coincide with the boundaries of the domain. The systems are generally not orthogonal and this is usually not an essential characteristic. The advantage of such systems is self-evident when incorporating boundary conditions in a finite difference computation. Using body-fitted coordinate avoids the problem of treating domains bounded by complicated boundaries by transforming the former into simple rectangular solids for which boundary conditions are easily handled. The approach consists of writing the governing equations of the problem in the transformed domain. They generally become more complicated because the shape of the domain is now included in the differential equations through the coefficients of the transformation. This however is not an inconvenience in numerical computations.

It is noted that there are in principle not limitations to the

Contributed by the Fluids Engineering Division for publication in the JOURNAL OF FLUIDS ENGINEERING. Manuscript received by the Fluids Engineering Division, December 1, 1981.

type of shapes that can be fitted and that three-dimensional systems are just as easily generated as two-dimensional systems. An additional feature of this approach is the possibility of grid line concentration. This can be particularly useful when dealing with regions of high gradients of a particular variable.

The basic idea used in generation of body-fitted coordinates can be found in several publications (references [1 and 2]) and will only be briefly described here using a physical analogy before dealing with the equations. Imagine a rectangular membrane on which a rectangular cartesian grid is drawn [Fig. 1].

To fit an arbitrary shape, one stretches this membrane over it and pegs the membrane along the boundary at a number of nodes [Fig. 2]. (This is equivalent to imposing Dirichlet boundary conditions.)

This physical situation is described by a system of elliptic equations, and unique transformation are always obtained. One can visualize the concentration as a variation of the membrane property or simply as the application of distributed point forces. The three-dimensional extension is immediate, if less easily visualized.

It is desired to map a physical region 3-D space into a cartesian computational space. Because of the intended applications to turbomachinery computations, this will be done by expressing the transformation as a set of elliptic equations written in cylindrical coordinates (r, θ, z) .

$$\xi_{rr} + \frac{1}{r} \xi_r + \frac{1}{r^2} \xi_{\theta\theta} + \xi_{zz} = P \quad (1)$$

$$\eta_{rr} + \frac{1}{r} \eta_r + \frac{1}{r^2} \eta_{\theta\theta} + \eta_{zz} = Q \quad (2)$$

$$\zeta_{rr} + \frac{1}{r} \zeta_r + \frac{1}{r^2} \zeta_{\theta\theta} + \zeta_{zz} = R \quad (3)$$

where ξ , η , and ζ are the computational or transformed coordinates. The terms P , Q , and R are forcing functions whose forms are used to introduce a stretching or concentration in the ξ , η , and ζ directions respectively. When attempting to solve these equations with some Dirichlet boundary conditions specified on six surfaces in (r, θ, z) one is confronted with the same problem that this approach was set up to avoid. That is the problem of specifying the values of the functions ξ , η , and ζ on general surfaces in the (r, θ, z) coordinate system. It will be much simpler to carry out the computations in the cartesian domain, of (ξ, η, ζ) . Thus equations (1)–(3) are inverted so that they express the transformed coordinates as functions of the physical coordinates. This is very lengthy and tedious and the reader is referred to [2]. This yields the following system

$$a_1 r_{\xi\xi} + a_2 r_{\eta\eta} + a_3 r_{\zeta\zeta} + 2a_4 r_{\xi\eta} + a_5 r_{\eta\zeta} + 2a_6 r_{\zeta\xi} - \frac{1}{r} + Pr_{\xi} + Qr_{\eta} + Rr_{\zeta} = 0 \quad (4)$$

$$a_1 \theta_{\xi\xi} + a_2 \theta_{\eta\eta} + a_3 \theta_{\zeta\zeta} + 2a_4 \theta_{\xi\eta} + 2a_5 \theta_{\eta\zeta} + 2a_6 \theta_{\zeta\xi} + P\theta_{\xi} + Q\theta_{\eta} + R\theta_{\zeta} = 0 \quad (5)$$

$$a_1 z_{\xi\xi} + a_2 z_{\eta\eta} + a_3 z_{\zeta\zeta} + 2a_4 z_{\xi\eta} + 2a_5 z_{\eta\zeta} + 2a_6 z_{\zeta\xi} + Pz_{\xi} + Qz_{\eta} + Rz_{\zeta} = 0 \quad (6)$$

where

$$a_1 = \xi_r^2 + \frac{1}{r^2} \xi_\theta^2 + \xi_z^2,$$

$$a_2 = \eta_r^2 + \frac{1}{r^2} \eta_\theta^2 + \eta_z^2,$$

$$a_3 = \zeta_r^2 + \frac{1}{r^2} \zeta_\theta^2 + \zeta_z^2, \quad (7)$$

$$a_4 = \xi_r \eta_r + \frac{1}{r^2} \xi_\theta \eta_\theta + \xi_z \eta_z,$$

$$a_5 = \eta_r \zeta_r + \frac{1}{r^2} \eta_\theta \zeta_\theta + \eta_z \zeta_z,$$

$$a_6 = \zeta_r \xi_r + \frac{1}{r^2} \zeta_\theta \xi_\theta + \zeta_z \xi_z.$$

The region that is transformed is bounded by six sides, $\Gamma_1, \Gamma_2, \dots, \Gamma_6$ which correspond to surfaces of ξ , η , and $\zeta = \text{constant}$, i.e., $\xi = \xi_1$, for Γ_1 and $\xi = \xi_2$ for Γ_2 and $\zeta = \zeta_1$ for Γ_3 and $\zeta = \zeta_2$ for Γ_6 .

The problem is to solve (4)–(6) subject to a set of Dirichlet boundary conditions which are essentially the location of the surfaces $\Gamma_1, \Gamma_2, \dots, \Gamma_6$ in the physical space, i.e., in the cylindrical system r, θ, z . These are specified as a set of equations as follows. Along the surface Γ_1

$$\begin{bmatrix} r \\ \theta \\ z \end{bmatrix} = \begin{bmatrix} f_1(\xi_1, \eta, \zeta) \\ f_2(\xi_1, \eta, \zeta) \\ f_3(\xi_1, \eta, \zeta) \end{bmatrix}$$

along Γ_2

$$\begin{bmatrix} r \\ \theta \\ z \end{bmatrix} = \begin{bmatrix} g_1(\xi_2, \eta, \zeta) \\ g_2(\xi_2, \eta, \zeta) \\ g_3(\xi_2, \eta, \zeta) \end{bmatrix}$$

Nomenclature

$(FR^K, FZ^K, F\theta^K)$ or F^K = forcing terms, equations (12)

G^K = K th grid, K varies from 0 to M , i.e., coarsest to finest grid

I_M^K = operator for interpolating from G^M to G^K

L = elliptic differential operator, equation (9)

L^K = discrete form of L on grid G^K using finite differences

(P, Q, R) = stretching functions, equations (1) to (3)

(r, z, θ) = cylindrical coordinates (continuous variables)

$(R, Z, \theta)_{i,j,k}$ = cylindrical coordinates (discrete variables)

(R^K, Z^K, θ^K) = approximate solution on G^K

Res^K = residual of (R^M, Z^M, θ^M) interpolated to G^K

(ξ, η, ζ) = transformed coordinates

Γ_i = surfaces bounding the three-dimensional domain

Indices

M = finest grid

0 = coarsest grid

K = intermediate grids

i = node in the radial direction

j = node in the axial direction

k = node in the circumferential direction

along Γ_6

$$\begin{bmatrix} r \\ \theta \\ z \end{bmatrix} = \begin{bmatrix} s_1(\xi, \nu, \zeta_2) \\ s_2(\xi, \eta, \zeta_2) \\ s_3(\xi, \eta, \zeta_2) \end{bmatrix}$$

3 Choice of a Numerical Scheme

The solution of the present problem is in general possible only by numerical methods. This consists of replacing the derivatives in equations (4) to (6) by their finite difference approximations thus yielding an equivalent system of algebraic equations. The discretization will use central differences for both first and second order derivatives yielding second order accuracy. One thus obtains for every point (ξ_j, η_i, ζ_l) one algebraic equation for each of the nodal values of R_{ij} , Z_{ij} , and ϕ_{ij} of the following form:

$$\begin{aligned} & a_1'(R_{i+1,j,k} - 2R_{i,j,k} + R_{i-1,j,k}) \\ & + a_2'(R_{i,j+1,k} - 2R_{i,j,k} + R_{i,j-1,k}) \\ & + a_3'(R_{i,j,k+1} - 2R_{i,j,k} + R_{i,j,k-1}) \\ & + 2a_4'(R_{i+1,j+1,k} - R_{i-1,j+1,k} \\ & - R_{i+1,j-1,k} + R_{i-1,j-1,k}) \\ & + 2a_5'(R_{i,j+1,k+1} - R_{i,j-1,k+1} - R_{i,j+1,k-1} + R_{i,j-1,k-1}) \\ & + 2a_6'(R_{i+1,j,k+1} - R_{i-1,j,k+1} - R_{i+1,j,k-1} + R_{i-1,j,k-1}) \\ & - \frac{1}{R_{i,j,k}} + P'(R_{i+1,j,k} - R_{i-1,j,k}) \\ & + Q'(R_{i,j+1,k} - R_{i,j-1,k}) \\ & + R'(R_{i,j,k+1} - R_{i,j,k-1}) = 0 \end{aligned} \quad (8)$$

where the coefficients a_1' to a_6' are the discrete form of equations (7). Two identical equations are written for θ and Z simply by replacing R by these variables in the above equation.

This yields for the entire problem a system of non-linear coupled equations which must be solved iteratively, in a procedure where at each step the coefficients are frozen and updated after new values of the unknowns are obtained. The nonlinearity can be better handled by updating the coefficients as soon as the new values of the variables become available (reference [1]). Essentially two approaches have been used for this class of problems: (i) Successive overrelaxation [1] and (ii) The alternating-direction-implicit scheme [2].

In the latter approach the elliptic problem is transformed into a parabolic problem by the addition of a transient term. This can be thought of as an artificial time and each time step may be associated to an iteration of the SOR method. So both methods are similar and the only criteria should be the rate of convergence, and ease of programming. No formal comparison between the two method is available and the choice was made on an intuitive basis and experience gathered by the present author on prior application of both of these methods. It is felt that a scheme based on relaxation will yield a more efficient overall scheme. But more importantly, that method lends itself better to improvements. In particular extensions to three-dimensional problems are not straightforward with A.D.I. methods. Thus the choice of the method of solution was an iterative relaxation scheme with a multigrid algorithm for the acceleration of the convergence.

4 The Multigrid Method

The multigrid method has been proposed by Brandt [3] and thoroughly detailed in that reference. The particular approach and software used are essentially derived, respectively, from reference [3] and described in detail in reference [4]. A brief summary of the method is given here.

Examination of the rate of convergence of a classical relaxation scheme shows that an initial rapid decrease in the residual, is followed by a much slower rate of decrease. This indicated that a relaxation procedure is efficient in eliminating the frequency components of the residual which are of the same order of magnitude as the mesh width. After these have been smoothed out, the remaining wavelengths are slow to disappear as the scheme discretized on a given grid is not very efficient at smoothing other wavelengths. This disadvantage is overcome by multigrid by carrying out the relaxation procedure on a series of grids representing the same problem on the same domain but with different mesh sizes. In this manner a much wider range of wavelengths in the residual is eliminated thus increasing the efficiency of the method.

The method used is a cycling algorithm based on the full approximation mode [3] where a cycle consists of relaxation sweeps on different grids starting from the coarsest to the finest. Before the start of each cycle on the coarse grid, the current solution is smoothed on the fine grid to allow its interpolation to coarse, and intermediate grids. The equation that is solved on each grid is called the residual equation and differs from the basic equation by a forcing term which effectively damps the corresponding error frequencies in the approximate solution.

The derivation for the correction equation (one per grid) for the multigrid method is given in detail in references [3 and 4] and will be briefly outlined here. The differential equations to be solved, equations (4-6) are denoted for convenience by the operator L , where

$$\begin{aligned} L \equiv & a_1 \frac{\partial^2}{\partial \xi^2} + a_2 \frac{\partial^2}{\partial \eta^2} + a_3 \frac{\partial^2}{\partial \zeta^2} \\ & + 2a_4 \frac{\partial^2}{\partial \xi \partial \eta} + 2a_5 \frac{\partial^2}{\partial \eta \partial \zeta} + 2a_6 \frac{\partial^2}{\partial \xi \partial \zeta} \\ & + P \frac{\partial}{\partial \xi} + Q \frac{\partial}{\partial \eta} + R \frac{\partial}{\partial \zeta} - \frac{1}{r} \end{aligned} \quad (9)$$

This operator is discretized on a hierarchy of grids G^0, G^1, \dots, G^M , using centered differences as in equation (8). An approximate discrete solution R^M, Z^M , and θ^M , is sought on G^M the finest grid, such that

$$\begin{aligned} L^M R^M &= 0 \\ L^M Z^M &= 0 \end{aligned} \quad (10)$$

and

$$L^M \theta^M = 0$$

where L^M is the discrete form of L , equation (9). This is carried out by a point relaxation scheme of an initial starting solution. However, before this is done on the fine grid, the solution is "skimmed" by relaxing on the coarse and intermediate grids. The full current approximation corresponding to G^K , is obtained by solving the appropriate residual equation. When a sufficient accuracy is reached on a given grid, the solution is then interpolated to the next, and so on. It is noted that the same relaxation scheme is used throughout.

The residual equation differs from the original equation by the presence of a forcing term,

$$\begin{aligned} L^K R^K &= FR^K \\ L^K Z^K &= FZ^K \end{aligned} \quad (11)$$

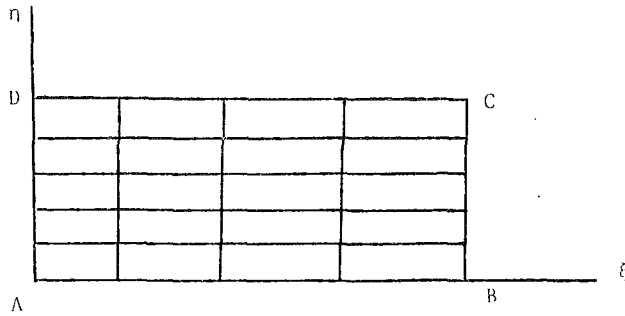


Fig. 1 Computational grid

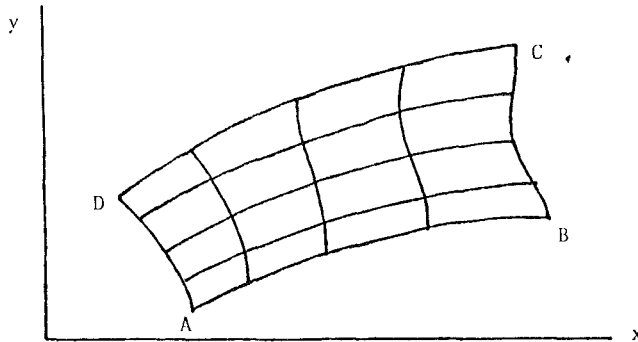


Fig. 2 Physical grid

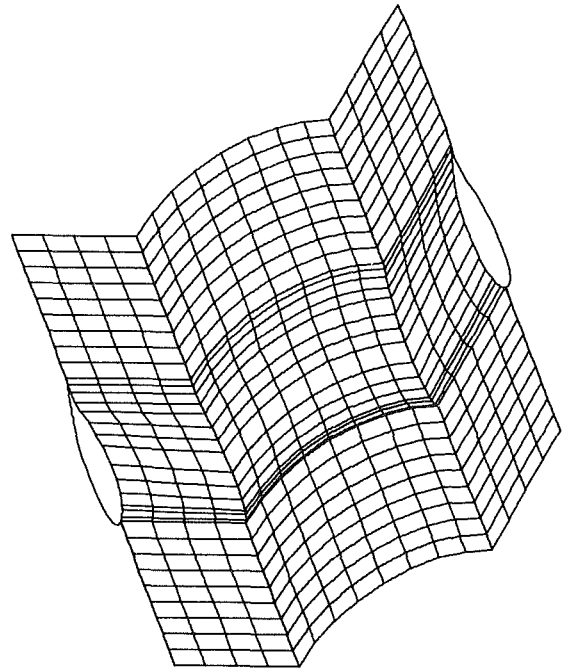


Fig. 3 Axonometric view of channel passage in test axial turbine

and

$$L^K \theta^M = F\theta^K$$

where L^K is the discrete form of L on grid G^K and the forcing terms are defined by

$$\begin{aligned} FR^K &= I_M^K L^M R^M - L^K I_M^K R^M \\ FZ^K &= I_M^K L^M Z^M - L^K I_M^K Z^M \\ F\theta &= I_M^K L^M \theta^M - L^K I_M^K \theta^M \end{aligned} \quad (12)$$

where I_M^K indicates the interpolation of a solution from grid G^M to grid G^K . One can interpret the forcing term as the difference of the discretization errors of the operator L on the fine and current grid.

The complete algorithm of a multigrid cycle for the full approximation mode is as follows:

1) An initial solution (R^M, Z^M, θ^M) is chosen on the fine grid G^M

2) The residual of this solution is computed

$$\text{Res}^M = L^M(R^M, Z^M, \theta^M)$$

3) After interpolating this solution $I_M^0(R^M, Z^M, \theta^M)$ to the coarsest grid, G^0 , the residual is computed

$$\text{Res}^0 \equiv L^0(I_M^0 R^M, I_M^0 Z^M, I_M^0 \theta^M)$$

4) The forcing term is formed

$$F^0 = (FR^0, FZ^0, F\theta^0) \equiv I_M^0 \text{Res}^M - \text{Res}^0$$

5) The residual equation is solved on G^0

$$L^0 R^0 = FR^0$$

$$L^0 Z^0 = FZ^0$$

$$L^0 \theta^0 = F\theta^0$$

and a correction $(R^0, Z^0, \theta^0) - I_M^0(R^M, Z^M, \theta^M)$ is computed.

6) The grid is increased by one to G^{K+1} and the correction is interpolated to that level

$$I_K^{K+1}(R^K - I_M^K R^M)$$

$$I_K^{K+1}(Z^K - I_M^K Z^M)$$

$$I_K^{K+1}(\theta^K - I_M^K \theta^M)$$

7) The full current approximation is computed on G^{K+1}

$$I_M^{K+1}(R^M) + I_K^{K+1}(R^K - I_M^K R^M)$$

8) The residuals of the full current approximation are computed on G^{K+1}

$$\text{Res}^{K+1} = L^{K+1}(I_M^{K+1} R^M + I_K^{K+1}(R^K - I_M^K R^M))$$

9) The forcing terms are formed

$$F^{K+1} = (FR^{K+1}, FZ^{K+1}, F\theta^{K+1})$$

$$= I_M^{K+1} \text{Res}^M - \text{Res}^{K+1}$$

10) The residual equation is solved on G^{K+1}

$$L^{K+1} R^{K+1} = FR^{K+1}, L^{K+1} Z^{K+1} = FZ^{K+1}$$

and $L^{K+1} \theta^{K+1} = F\theta^{K+1}$, and a correction is computed

$$(R^{K+1}, Z^{K+1}, \theta^{K+1}) - I_M^{K+1}(R^M, Z^M, \theta^M)$$

11) Steps (6) to (10) are repeated until the fine grid is reached.

This constitutes one multigrid cycle, and it can be repeated successively until the required accuracy on the fine grid is attained. It is seen that on the fine grid the problem reduces to the usual relaxation scheme, with the added feature that for multigrid the starting solution has had its low frequency error components removed by the sweeps on the coarser grids. Thus most of the computational effort is spent on those grids where the computational effort is low, as they contain very few points.

The interpolation from coarse to fine grids is carried out by a triquadratic formula whereas simple injection is used for fine to coarse grids. Although for highly distorted grid some other procedure may have to be used (reference [3]), this was found adequate in the present study.

This overall algorithm was used to accelerate the convergence rate of the point relaxation described in the previous section. After numerous exploratory computations the effect of certain parameters were assessed. This was carried out interactively with instantaneous graphical display of the relaxation history on a CRT terminal and/or plotter. The number of grids was varied. It resulted that little advantage is obtained from more than four grids, provided that the suc-

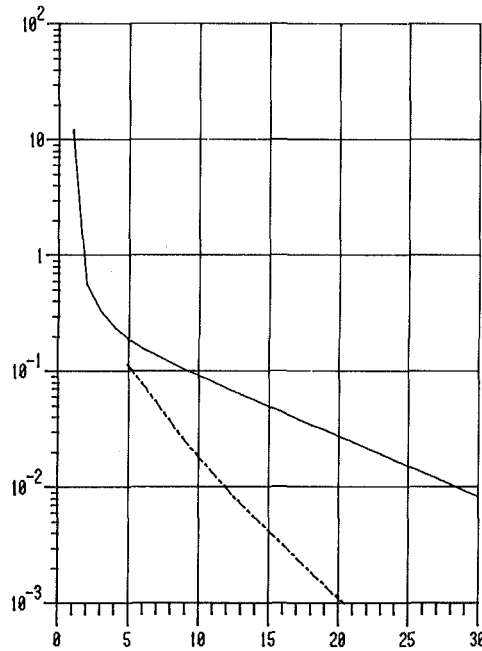


Fig. 4 Comparison of relaxation histories of point S.O.R. (solid) and multigrid (dotted) using a $17 \times 9 \times 9$ grid and a relaxation factor of 1.0

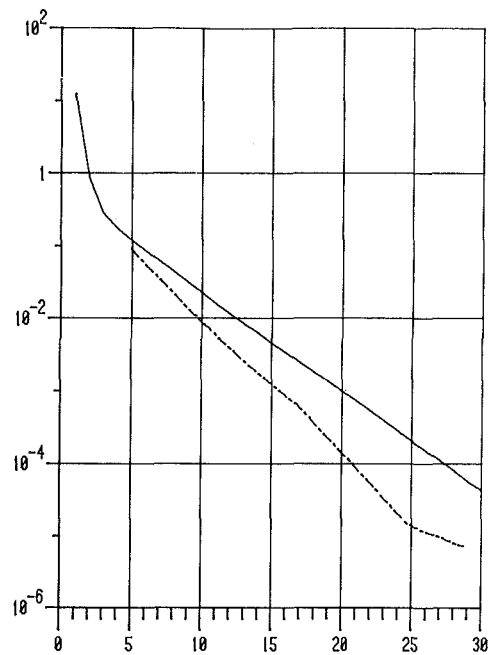


Fig. 6 Comparison of relaxation histories of point S.O.R. (solid) and multigrid (dotted) using a $17 \times 9 \times 9$ grid and relaxation factor of 1.4

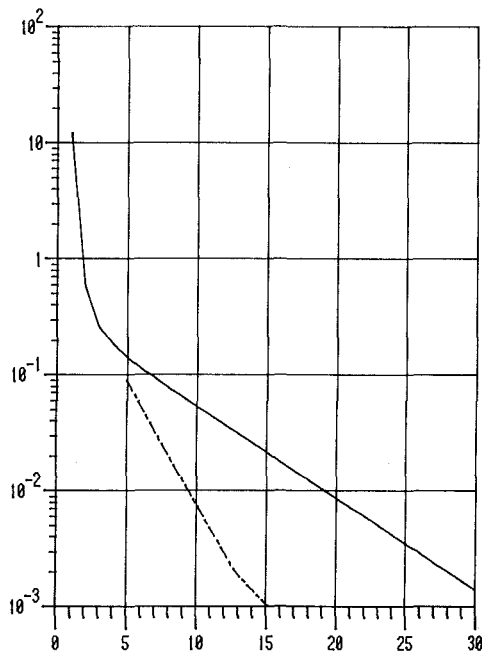


Fig. 5 Comparison of relaxation histories of point S.O.R. (solid) and multigrid (dotted) using a $17 \times 9 \times 9$ grid and a relaxation factor of 1.2

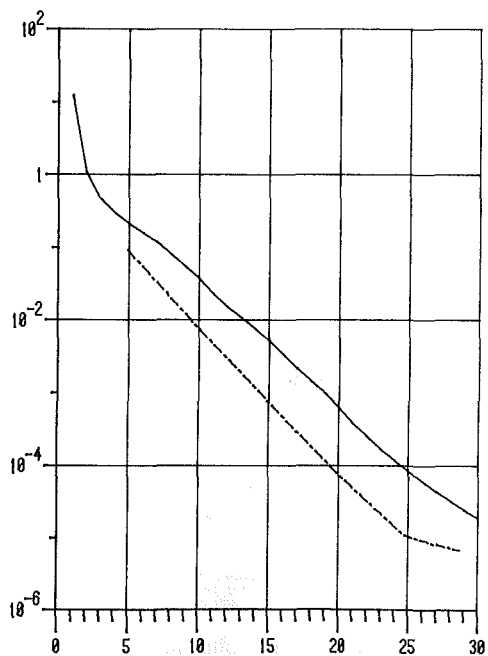


Fig. 7 Comparison of the optimum relaxation histories of point S.O.R. (solid), $W = 1.6$, and of multigrid (dotted), $W = 1.2$

cession of grids span the domain completely. Finally the number of sweeps carried out on each grid was varied and it was found that the only important factor is the number of sweeps on the finest grid. This number for the present problem was found to be 3. Using a smaller number destroyed the beneficial effects of multigrid, whereas a larger number, say 4 or 5, simply increased computer time without significantly improving the convergence rate. This clearly indicates the need to smooth the solution on G^M so that the interpolation to the coarser grid be accurate. This is important as the particular wavelength liquidated by a coarse grid relaxation depends on the interpolated solution from G^M and a "rough" solution will not be represented well on a coarser grid.

5 Comparisons and Results

The multigrid method described in the proceeding section was programmed and the results compared with these from a point S.O.R. technique. The basis for comparison is the relaxation history, that is a measure of the residual as a function of the work units. This measure of the residual or norm is chosen as the R.M.S. value of the residuals of the three operators $L^M R^M$, $L^M Z^M$ and $L^M \theta^M$ on the fine grid. The work unit is defined as the computational effort of one relaxation sweep on the fine grid. All other computations such the interpolation, the coding of the forcing functions, the solution of the residual equations of the coarse grids etc . . . are accounted for as fractions of a work unit. The numerical

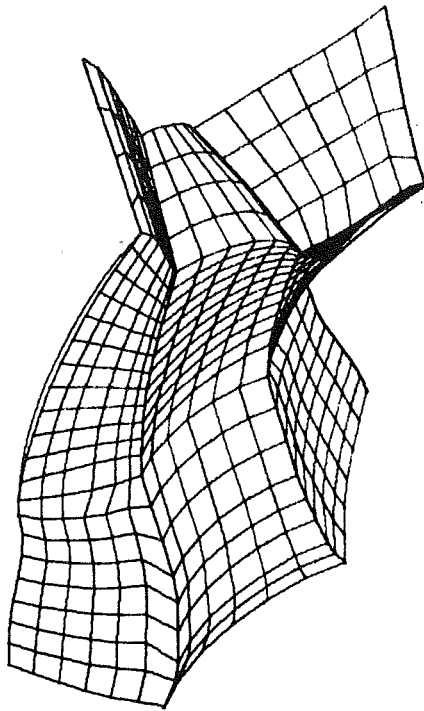


Fig. 8(a)

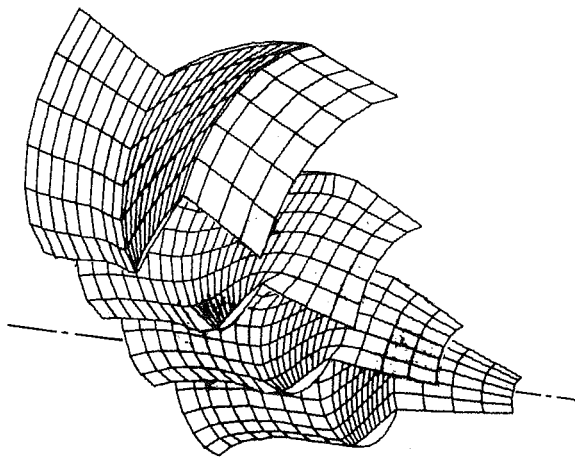


Fig. 8(b) Curvilinear coordinate grid showing four $\xi = \text{constant}$ surfaces, i.e., streamlike surfaces. Expanded view.

tests were carried out for the three-dimensional axial channel shown in Fig. 3. It represents a cylinder with two blades constructed with a constant profile in the radial direction. The fine grid was $33 \times 9 \times 9$ and two coarser grids of $17 \times 5 \times 5$ and $9 \times 3 \times 3$ were used in the multigrid program. (For clarity the $17 \times 5 \times 5$ grid is shown.) Previous experience [5] with this technique has shown that a fixed strategy is usually adequate. That is the number of relaxation sweeps on each grid level is fixed. A number of exploratory computations of the present problem have shown that the three sweeps through each grid constitutes an approximate optimum multigrid cycle. Figures 4 to 6 show comparisons of the relaxation histories of the point relaxation scheme and the present multigrid technique for the example in Fig. 3. These figures correspond to values of the overrelaxation factor of 1.0, 1.2, and 1.4. It is seen that the multigrid method yields a faster convergence in all cases. A further comparison in Fig. 7 shows the best relaxation histories of each of these methods, that is those corresponding to factors of 1.6 and 1.2 for the point S.O.R. and the multigrid schemes respectively. In this in-

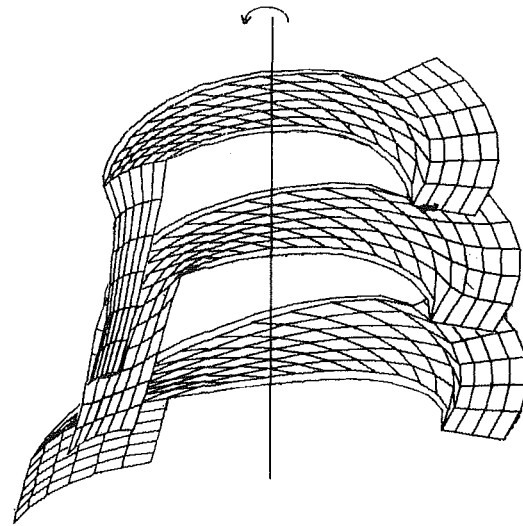


Fig. 9 Curvilinear coordinate grid showing three $\xi = \text{constant}$ surfaces, i.e., streamlike surfaces, for a radial hydraulic turbine. Expanded view.

stance the improvement is not as substantial as the previous comparisons. It should be noted however that the optimum relaxation factors are not known beforehand and vary from one problem to the next. So that one would not normally seek such an optimum and in that case of one single try, the multigrid would always yield a convergence 1.3 to 3 times faster than S.O.R. It is noted that in the present three-dimensional problem the authors did not obtain as consistent a success as for the analogous two-dimensional problem reported in reference [5]. This, it is conjectured results from the poor interpolation scheme as well as the small number of grids.

The resulting technique was then applied to the grid generation for typical hydraulic turbines. The use of the present three-dimensional program is identical, other than increased storage computer time requirements, to the previous two-dimensional versions. The essential differences (and difficulties) lie not so much in the multigrid scheme as in the preparation of the input data and in the presentation of the solution. This is particularly important as there is considerable freedom in the choice of discrete points to represent the solid blade surfaces. And these affect considerably the appearance of the grid. The distribution of points is critical and usually several trials are necessary before obtaining a solution that "looks good" or to simply detect the errors which invariably creep into the surface and channel descriptions.

Considerable help is obtained from the intended use of the resulting grid. Thus in the present application, it was found useful to identify roughly the ξ , η , and ζ coordinates with the flow field. For example ζ -curvilinear surfaces are identified to be roughly normal to the stream direction, whereas ξ -coordinates can be thought as roughly blade to blade stream sheets, somewhat similar to the $Wu S_2$ surfaces used in three dimensional flow computations.

The three-dimensional channel passage of an axial turbine was fitted and the results are shown in Fig. 8. This illustrates an axonometric projection of three ξ -surfaces (stream-like surfaces). The computation was carried out using fine grid of $17 \times 7 \times 7$. Similarly the grid for a radial runner is illustrated in Fig. 9.

6 Conclusions

An efficient numerical scheme for the generation of body-fitted curvilinear coordinate systems has been devised and

tested. Comparisons show generally a good improvement in the convergence rate over the classical point S.O.R. method. The use requires a good choice in the distribution of points used in the surface specification. By choosing these to be aligned with stream-like directions, one obtains generally a system curvilinear coordinate surfaces similar to the Wu-decomposition. This approach should be particularly well suited for the subsequent fluid mechanics problem.

Acknowledgments

The financial assistance of the National Research Council of Canada, and of the Fondation des diplômés de l' Ecole Polytechnique de Montréal is gratefully acknowledged.

References

- 1 Thomson, J. F., Thames, F. C., and Mastin, W., "Automatic Numerical Generation of Body-fitted Curvilinear Coordinate System for Field Containing any Number of Arbitrary 2-D Bodies," *Journal of Computational Physics*, Vol. 15, 1974, pp. 299-319.
- 2 Ghia, U., and Ghia, K. N., "Numerical Generation of a System of Curvilinear Coordinates for Turbine Cascade Flow Analysis," University of Cincinnati, Report #AFL75-4-17, Apr. 1975.
- 3 Brandt, A., "Multi-Level Adaptive Techniques—The Multigrid Method," IBM Research Report, RC 6026, 1976.
- 4 Camarero, R., "A Software Package for the Multigrid Method," Ecole Polytechnique, Montreal, Rapport Technique EP79-R, Feb. 1979.
- 5 Camarero, R., and Younis, M., "Efficient Generation of Body-Fitted Coordinates for Cascades using Multigrid," *AIAA Jour.*, Vol. 18, No. 5, May 1980, pp. 487-488.
- 6 Ghia, U., and Ghia, K. N., "Boundary-Fitted Coordinates for Regions with Highly Curved Boundaries and Reentrant Boundaries," NASA Publication 2166 Numerical grid generation techniques, Oct. 1980, pp. 295-306.

H. A. Dwyer
University of California,
Davis, Calif.

R. J. Kee

P. K. Barr

B. R. Sanders

Sandia Laboratories,
Livermore, Calif.

Transient Droplet Heating at High Peclet Number

The transient heating of a spherical liquid particle at high Peclet number has been calculated with the use of adaptive grids for low Reynolds numbers. The use of adaptive grids greatly enhances the efficiency of the calculations and allows for the large Peclet numbers to be studied. The results of the calculations show that the transient period of internal isotherm redistribution represents a significant part of the droplet total heating. Even for the $Pe = 1600$ case, the initial heating period caused more than 50 percent of particle heating, and the asymptotic heating results cannot be used with good accuracy. The methods employed in the study have great potential, and will be applied to unsteady droplet evaporation and burning in future studies.

Introduction

The problem of the transient heating of a spherical fluid particle at high Peclet number is one of the important areas of spray combustion. The heating and evaporation of particles play a key role in the dynamics of many practical combustion systems, and the performance of these systems is strongly influenced by the transport processes in the droplet. In this paper there will be presented the results of an investigation which calculates the heating of a spherical fluid particle for the important case of high Peclet number. The methods used are new and show very strong promise of being able to calculate the complete problem of droplet combustion. Numerical solutions have been carried out for Peclet numbers greater than one thousand and the exact equations for energy transfer have been solved. For the velocity field a Hill's spherical vortex¹ has been employed and this can be used with confidence only at low Reynolds number.

Two important studies on this problem can be found in the works of Johns and Beckmann [2] and Prakash and Sirignano [3]. The work of Johns and Beckmann has some similarities to the present investigation but it was limited to Peclet numbers of less than one hundred. The reason for this restriction was their lack of computing capacity as well as the primitive methods employed. An important conclusion of their investigation was that the transient heating could not be treated with asymptotic methods in their Peclet number regime, and that the full equations were needed to describe the majority of the heating of the particle. The limits of Peclet number for which the asymptotic results could be applied were not defined because of the lack of higher Peclet number studies.

The research of Prakash and Sirignano [3] was part of a study of droplet evaporation, and assumed that an asymptotic analysis could be applied. This assumption was based on the fact that many practical spray combustion systems have particles with Peclet numbers of one thousand. At these high values the convection processes should dominate conduction

and asymptotic approximations should be applicable. The results of the present investigation show that the asymptotic analysis is only applicable during the final half of the particle heating for the highest Peclet number case considered of 1600. As the Peclet number decreases the region of applicability of the asymptotic results becomes smaller and a full numerical treatment of the energy equation is needed over a longer time period. A discussion of the methods employed and the results will now be presented.

Analysis and Methods Approach

The basic physical problem consists of a spherical fluid particle immersed in a surrounding fluid which causes an internal circulation and also supplies the energy for the internal heating of the droplet. The Peclet number in this research will be based on the maximum velocity in the droplet and is given by

$$Pe = \frac{U_{\max} D}{\alpha}$$

where D is the particle diameter and α the fluid particle thermal diffusivity. The energy equation will be written in terms of generalized non-orthogonal coordinates with the starting point being cylindrical coordinates (axial symmetry will be employed). The transformed formulation of the incompressible energy equation in conservation form and for constant properties is

$$\begin{aligned} \frac{\partial}{\partial \tau} \left(\frac{\rho C_v r T}{J} \right) + \frac{\partial}{\partial \xi} \left\{ \frac{r}{J} \left[\rho C_v T \xi_r + (\rho u C_v T - q_r) \xi_r \right. \right. \\ \left. \left. + (\rho w C_v T - q_z) \xi_z \right] \right\} \\ + \frac{\partial}{\partial \eta} \left\{ \frac{r}{J} \left[\rho C_v T \eta_r + (\rho u C_v T - q_r) \eta_r \right. \right. \\ \left. \left. + (\rho w C_v T - q_z) \eta_z \right] \right\} = 0 \end{aligned}$$

Contributed by the Fluids Engineering Division for publication in the JOURNAL OF FLUIDS ENGINEERING. Manuscript received by the Fluids Engineering Division, January 21, 1982.

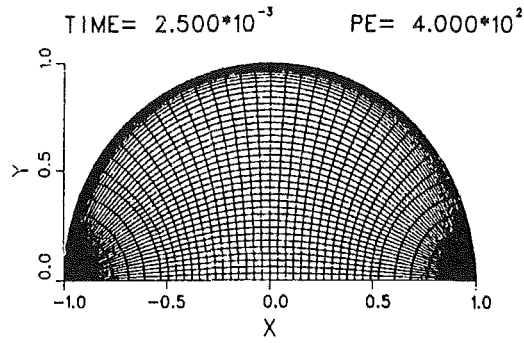


Fig. 1 Coordinate and isotherm distribution

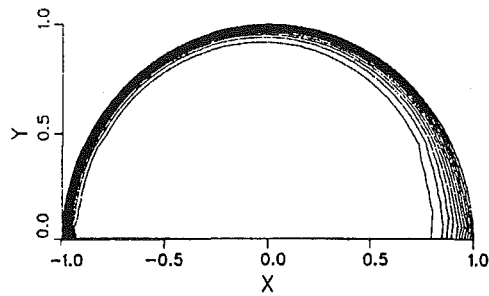


Fig. 2 Coordinate and isotherm distribution

where (r, z) , (u, w) , and (q_r, q_z) are the radial and axial coordinates, velocities, and heat flow vectors, respectively. The generalized coordinates ξ and η can be any set of orthogonal or nonorthogonal arcs inside of the particle, and the relationships between the original cylindrical coordinates z and r with ξ and η are given by the following metric relationships [4, 6]

$$J = \frac{1}{z_\xi r_\eta - z_\eta r_\xi}$$

$$\xi_z = J r_\eta \quad \xi_r = -J z_\eta \quad \xi_t = -Z_t \xi_z - r_t \xi_r$$

$$\eta_z = -J r_\xi \quad \eta_r = J z_\xi \quad \eta_t = -Z_t \eta_z - r_t \eta_r$$

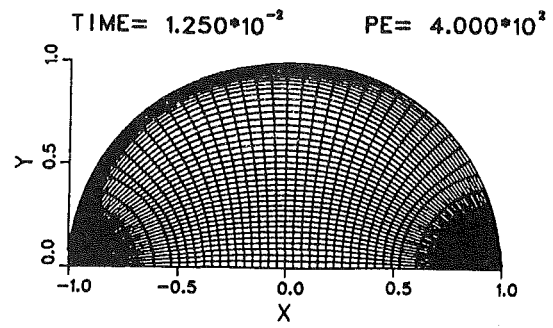


Fig. 3 Coordinate and isotherm distribution

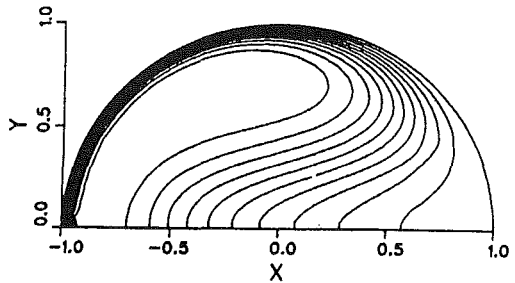


Fig. 4 Coordinate and isotherm distribution

When solving any particular problem the choice of ξ and η are of great importance to the accuracy of the solution, and care must be taken in the selection of these coordinates. In the present paper this selection process will be chosen by the geometry and the time-dependent temperature gradients in the flow field. The change in coordinate positions will develop naturally with the physics of the problems.

Criterion for Grid Placement

The basic criterion for grid placement that was employed in the present paper will now be presented. The computational space, ξ and η , has been normalized so that their numerical values go between zero and one and the grid points are fixed in time. In the physical space the grid points will be placed and

moved in time to achieve the resolution of high gradient regions. Along a given arc in the physical space the grid points will be distributed in proportion to the gradient of the dependent variable. If the distance along a given arc in physical space is denoted by S , a mathematical statement of the relationship between the computational and physical space is

$$d\xi \propto \left| \frac{\partial T}{\partial S} \right| ds$$

where S is the distance measured on the $\eta = \text{constant}$ arc, and T the dependent variable of the transport equation being solved. In order to normalize, allow for "optimization," and remove singularities, the above equation is cast into the following form

$$\xi(x, y, t) = \frac{\left[\int_0^S (1+b) \left| \frac{\partial T}{\partial S} \right| ds \right]}{\left[\int_0^{S_{\max}} (1+b) \left| \frac{\partial T}{\partial S} \right| ds \right]}$$

where b is an adjustable constant used for "optimization" of the grid distribution.

The above equation has some interesting features which will now be discussed briefly. For the case $b = 0$ a uniform distribution of points on the nonorthogonal arc is obtained, while for b becoming large constant values of the variable T , or isotherms, are selected. The coordinate location equation is solved in an explicit sense at the old time step and the details can be found in the paper by Dwyer et al. [4]. Also, it should be mentioned that the accuracy in solving the equation does not influence directly the accuracy of the finite difference solution. With the use of these generalized coordinates and an adaptive grid technique a powerful new method is available for numerical solution methods.

Results

The physical problem solved consisted of a spherical fluid particle at initial temperature T_I . The fluid flow inside the particle was described by Hill's spherical vortex for which the stream function is given by

$$\psi_0 = -\frac{1}{2} A r^2 (R^2 - r^2) \sin^2 \theta$$

where r is the radial position, R the particle radius, and θ the angular position measured from the windward axis of symmetry. At time zero the outer surface of the particle is raised to temperature T_0 , and the transient heating process begins.

A typical heating process can be observed in Figs. 1 through 4 for a Peclet number of 400. In each of these figures there are shown both the coordinate system (upper portion) and the isotherm distribution (bottom portion). In Fig. 1 the dimensionless time τ ($\tau = \alpha t / R^2$) is very small and the heating process is dominated by conduction. The isotherm distribution is confined to the region of the particle surface and the coordinate system in the top portion of the figure is also tightly packed onto the particle surface. In each of the figures are shown eleven isotherms of the dimensionless temperature defined as

$$\theta = \frac{T - T_0}{T_I - T_0}$$

Also, it should be noted that the sharp changes in the isotherms at the windward and leeward stagnation points are artifacts of the linear interpolation plot package.

In the present calculation the following locations were chosen for boundaries in the computational space.

$$\eta = 0 \quad y = 0 \quad -0.95 \leq x \leq 0.95$$

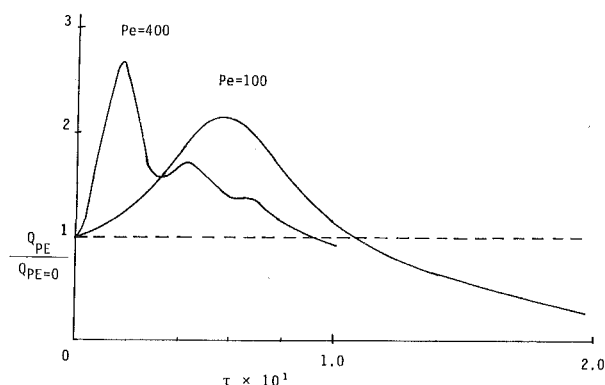


Fig. 5 Heat transfer ratio versus time

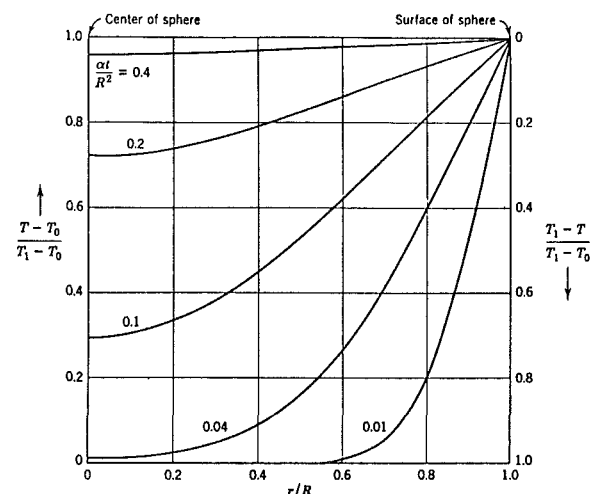


Fig. 6 Temperature distribution for pure conduction

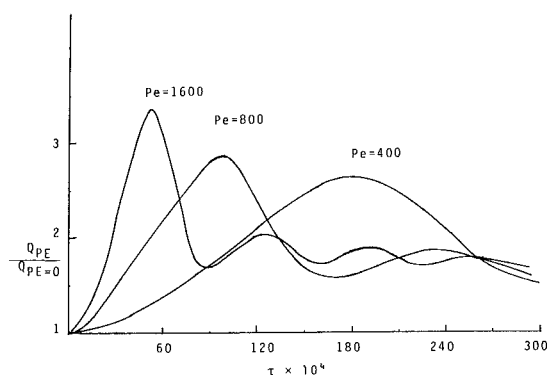


Fig. 7 Heat transfer ratio versus time

$$\eta = 1 \quad r = R$$

$$\xi = 0 \quad y = 0 \quad -1.0 \leq x \leq 0.95$$

$$\xi = 1 \quad y = 0 \quad 0.95 \leq x \leq 1.0$$

This choice is not unique and it is possible that a different choice would be more optimal. Adaption was carried out along the $\xi = \text{constant}$ lines and only the $\eta = \text{constant}$ lines were moved in physical space. Also, a value of $b = .3$ was found to give good results [4], however there is not a strong sensitivity for b between $0.2 \leq b \leq 0.5$.

The $\xi = \text{constant}$ lines in physical space were chosen to be splines (perpendicular to the surface and axis) or circular arcs (approximately perpendicular to the surface and axis). This choice worked well for the present problem, but definite improvements could be obtained by using an orthogonal

internal coordinate generation scheme. A method to accomplish this goal is now being worked out.

As time increases the convection process begins to interact strongly with conduction and the isotherm distribution becomes highly nonspherical. In Fig. 2 it can clearly be seen that the flow has convected the surface particles away from the leeward surface (right side) and along the windward surface (left side). This process causes the windward temperature gradients to remain very strong and the leeward temperature gradients to become quite weak. For relatively long times the convection process eventually carries the heated fluid particles into a pattern that causes the isotherm distribution to resemble the streamline pattern. This pattern can be seen easily in Fig. 4 where the cold unheated fluid is located in the vortex core. After the cold fluid is in the vortex core the process becomes self-similar and asymptotic methods can be employed.

The overall heating of the particle can be understood with the help of Figs. 5 through 7. In Fig. 5 is shown the ratio of the local time dependent total surface heat transfer to the pure conduction heat transfer, $Pe = 0$, for Peclet numbers of 100 and 400 (for reference the temperature distribution at various times for pure conduction⁵ is given in Fig. 6). The heat transfer ratio increases until the hot fluid from the leeward side reaches the windward side, and then decreases until the cold fluid is isolated in the vortex core. Other slight oscillations in the heat transfer ratio then occur as the fluid particles traverse the droplet. For longer times the heat transfer ratio becomes less than one because of the rapid heating of the particle in the convection case.

The physical processes described above can be grasped very clearly by comparing Fig. 5 with Figs. 1 through 4. The value of $\tau = 2.5 \times 10^{-3}$ in Fig. 1 corresponds to a very small time in Fig. 5 and it can be easily seen that the heating rate is within ten percent of its conduction value. Until a value of $\tau \approx 1.8 \times 10^{-2}$ cold fluid is being convected into the windward side of the droplet and causing the gradients to remain very steep as shown in Figs. 2 and 3. At approximately $\tau = 1.8 \times 10^2$ warm fluid from the leeward side intrudes into the windward boundary layer and causes a rapid decrease in heat transfer. The cold fluid is then convected around the droplet and the isotherm distribution quickly resembles the streamline pattern. However, the cold fluid circulates around the droplet in a nonsymmetrical fashion and this causes oscillations in the droplet surface heating at later times.

The importance of the later time oscillations is not as great as the first rise in heating rate because of the almost $t^{-1/2}$ dependence of $Q_{Pe=0}$ and the spherical geometry [5]. At $\tau = 1 \times 10^{-2}$ and $\tau = 2 \times 10^{-2}$ the total increase in energy of the particle is 38 and 64 percent of the maximum heat capacity and the later time heating rate is much slower. For pure conduction at $\tau = 2 \times 10^{-2}$ the total increase in particle energy would be 42 percent and thus it can be seen that the convection process has increased total average heating by more than 50 percent. The heating rate for $Pe = 400$ remains higher than the conduction solution until approximately $\tau = 1 \times 10^{-1}$ and then decreases below the conduction value. This behavior is due to the fact that the droplet almost reaches full heating at an earlier time for the convection case.

Also shown in Figs. 5 and 7 are the local heating rates for Peclet numbers of 100, 800, and 1600. The cases of $Pe = 100$ and 1600 exhibit the limits of some interesting physics in droplet heating. The local isotherms and coordinates for $Pe = 100$ are shown in Figs. 8 and 9. Figure 8 exhibits the heating process as the cold fluid is being convected into the windward boundary layer. This boundary layer is much thicker than the $Pe = 400$ case because of the increased relative strength of conduction. After the warm fluid from the leeward side has convected into the windward boundary layer the isotherms do

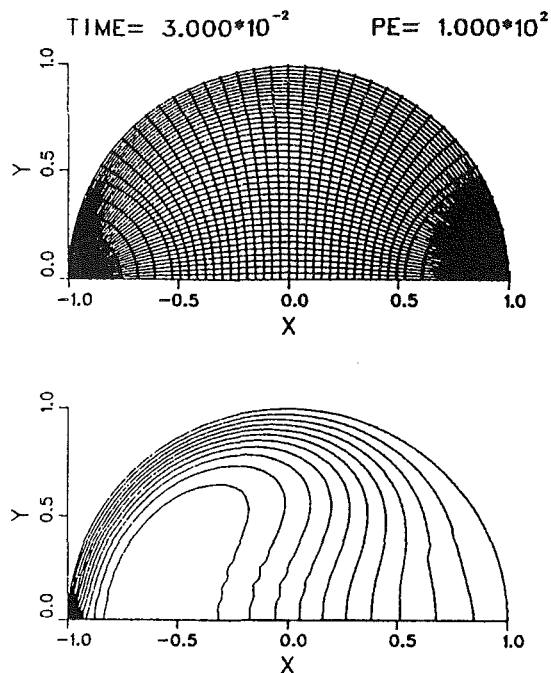


Fig. 8 Coordinate and isotherm distribution

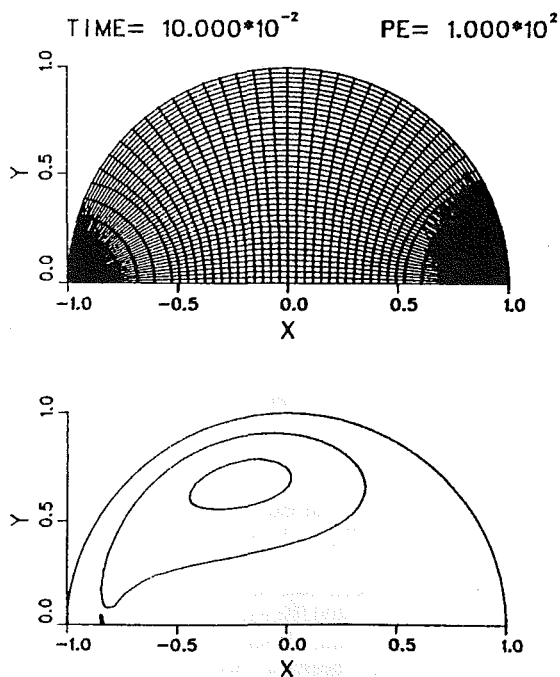


Fig. 9 Coordinate and isotherm distribution

not move quickly around the vortex core. In fact at rather long times, as shown in Fig. 9, the location of unheated fluid is not at the vortex core.

As the Peclet number is increased the time scale for the heat transfer maximum decreases and the boundary layer thickness on the windward side also decreases as shown in Figs. 5 and 7. The Peclet number case of 1600 is exhibited in Figs. 10 through 12. These figures clearly show the extreme small scaling of the windward boundary layer, as well as the rapid convection of leeward heated fluid into the windward boundary layer. Figure 12 shows that at a very early time the isotherms almost surrounded the vortex core.

From Fig. 7 for the $Pe = 1600$ case it can be seen that the

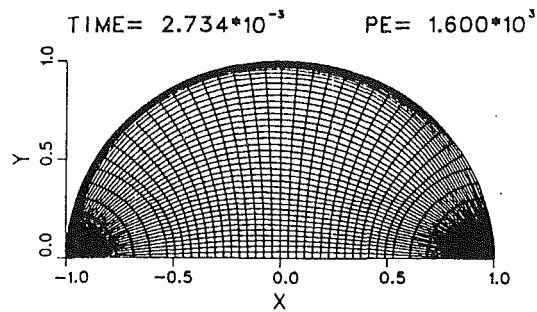


Fig. 10 Coordinate and isotherm distribution

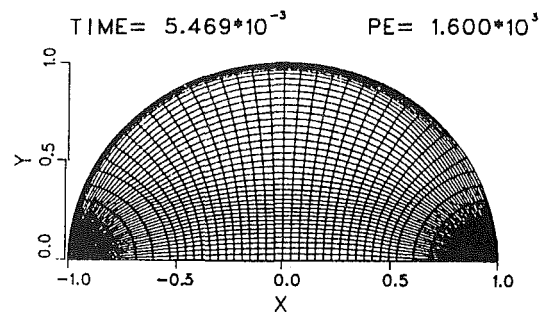


Fig. 12 Coordinate and isotherm distribution

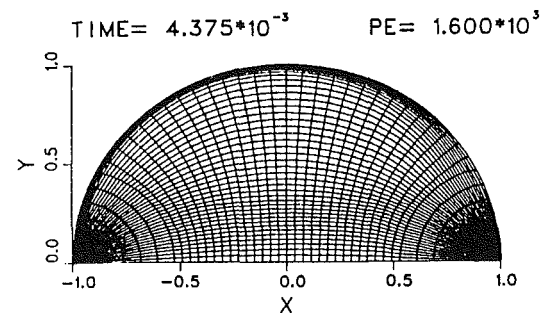


Fig. 11 Coordinate and isotherm distribution

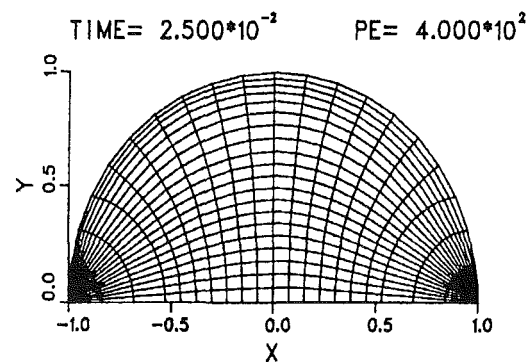


Fig. 13 Coordinate and isotherm distribution

process of leeward fluid intruding into the windward boundary layer is approximately completed at $\tau = 1 \times 10^{-2}$. At this time the energy content of the droplet has increased to 55 percent of maximum (pure conduction alone would be 30 percent), and only the later half of the droplet heating would be described by the asymptotic solution [3]. The oscillations shown in Fig. 7 are noticeable, but would not give substantial changes in the integrated total heat transfer. Therefore, although the asymptotic analysis applies at a very early time in the heating process, the nonasymptotic heating period represents more than half of the total heating process even at a Peclet number of 1600. The physical reasons for this result are the extremely large gradients in the windward side boundary layer and the r^3 volume dependence near the droplet surface. These two facts cause substantial heating during the transition to the asymptotic behavior.

Numerical Observations and Results

The results of employing the adaptive grid can be seen in their most favorable aspect in Figs. 10 through 12 for $Pe = 1600$. For this case the windward side boundary layer is extremely thin and the grid is bunched very closely near the wall. In Fig. 10 the ratio of the maximum to minimum step size normal to the surface is greater than 10/1. Adaptation was only carried out along the generalized arcs perpendicular to the droplet surface. Therefore, we have solved a problem with a 40×40 grid which would have required a 40×400 grid, and thus increased efficiency considerably.

In the boundary layer itself there were approximately eight grid points and the first four grid points near the surface are almost uniformly spaced. This uniform spacing insures that derivatives near the surface will be accurate, and this is ex-

tremely important in determining the droplet heating rate. Also, it should be mentioned that the regriding caused less than a 10 percent increase in total computation time over a 40×40 uniform grid calculation, and that regriding is not necessary every time step or during the later stages of the heating process.

Another interesting feature of the calculation is the movement of the grid with the boundary layers as they are removed during the heating process. This dynamic process can be seen most clearly in the $Pe = 400$ case where also is shown the different grid development between the windward and leeward sides of the droplet. Of particular interest is Fig. 12 for $Pe = 1600$ where the grid has its maximum size in the vortex core due to the rapid convection of leeward fluid across the symmetry axis of the particle.

Calculations were also carried out with first order windward differences to study the influence of numerical diffusion. Very little effect was noticed on the surface heat flux, since diffusion and convection are perpendicular to each other there. However, serious numerical diffusion did occur inside the particle.

Conclusions

The problem of the heating of fluid particles at high Peclet number and with internal circulation has been solved for

Peclet numbers greater than one thousand. In this regime transient processes are occurring during the major portion of the particle heating. Therefore, it is not appropriate to use asymptotic methods solely, and the physics can only be described completely with a numerical solution. The new and powerful numerical analysis techniques which have been employed have been very successful in resolving efficiently regions of high gradient. These techniques are now being extended to problems of particle evaporation and eventually to combustion.

References

- 1 Batchelor, G. K., *An Introduction to Fluid Dynamics*, Cambridge University Press, 1967.
- 2 Johns, L. E., and Beckmann, R. B., "Mechanism of Dispersed-Phase Mass Transfer in Viscous, Single-Drop Extraction Systems," *A.I.Ch.E.J.*, Vol. 12, No. 1, Jan. 1966, pp. 10-16.
- 3 Prakashh, S., and Sirignano, W. A., "Liquid Fuel Droplet Heating with Internal Circulation," *Int. J. Heat and Mass Transfer*, Vol. 21, 1978, pp. 885-895.
- 4 Dwyer, H. A., Kee, R. J., and Sanders B. R., "Adaptive Grid Method for Problems in Fluid Mechanics and Heat Transfer," *AIAA J.*, Vol. 18, No. 10, Oct. 1980, p. 1205.
- 5 Carslaw, H. S., and Jaeger, J. C., *Conduction of Heat in Solids*, Oxford University press, 1959, p. 234.
- 6 Steger, J. L., "Implicit Finite-Difference Simulation of Flow About Arbitrary Two-Dimensional Geometries," *AIAA Journal*, Vol. 16, July 1978, pp. 679-686.

Simple and Explicit Formulas for the Friction Factor in Turbulent Pipe Flow

S. E. Haaland

The Norwegian Institute of Technology,
Trondheim, Norway.
Mem. ASME

Explicit, but accurate formulas for the friction factor are given as a substitute for the more inconvenient implicit formulas which are at present considered to be the most accurate.

For computation of pressure drop in turbulent pipe flow one needs expressions for the friction factor f as a function of Reynolds number Re and the relative roughness K/D , where K is the equivalent sandroughness, and D the diameter of the pipe. The most accurate and accepted formulas are: Prandtl's formula for smooth pipes, and von Karman's formula for the fully rough regime, respectively, (f being Darcy's friction factor)

$$\frac{1}{\sqrt{f}} = 2 \log \left(\frac{Re\sqrt{f}}{2.51} \right), \frac{1}{\sqrt{f}} = 2 \log \left(\frac{3.7D}{K} \right) \quad (1),(2)$$

and Colebrook and White's universal formula

$$\frac{1}{\sqrt{f}} = -2 \log \left(\frac{2.51}{Re\sqrt{f}} + \frac{K}{3.7D} \right) \quad (3)$$

Equation (3) contains both (1) and (2) as limiting cases, Colebrook [1]. That is, (3) reduces to (1) when the parameter $t = 0.11 Re\sqrt{f} K/D \ll 1$, and reduces to (2) when $t \gg 1$. According to [1], (3) gives results which are in good agreement with experimental data for commercial pipes.

Unfortunately, the formulas (1) and (3) are implicit, that is, f appears in two places in the transcendental equations, so that either one solves the equations by iteration or one finds f from a graph (Moody's diagram), none of which is convenient. Many explicit equations have been proposed in the literature, but they all seem to suffer from some drawback, either they are simple but not accurate, or they are accurate but not simple. It is the aim of this note to present explicit formulas for the friction factor which are both simple and accurate.

The Prandtl formula (1) can be approximated by the explicit equation

$$\frac{1}{\sqrt{f}} = 1.8 \log (Re/6.9) \quad (4)$$

as was given by Colebrook [1] more than 40 years ago. Equation (4) approximates (1) within 1 percent in the Reynolds number range $5 \cdot 10^3 \leq Re \leq 5 \cdot 10^7$; the difference at $Re = 10^8$ is 1.3 percent. It is unfortunate that (4) has been largely overlooked by textbook authors, since it is simpler and

more accurate than other formulas given in the literature. The formula given by Techo et al. [2] is complicated and the stated accuracy (0.1 percent as compared to (1)) is not the true accuracy since (1) is also an empirical formula which certainly is not accurate to within 0.1 percent. Thus (4) seems to be the best one available.

The explicit formula (4) also have the advantage that it is easily combined with (2) to form the following explicit universal formula for the friction factor in turbulent flows

$$\frac{1}{\sqrt{f}} = -1.8 \log \left[\frac{6.9}{Re} + \left(\frac{K}{3.7D} \right)^{1.11} \right] \quad (5)$$

where $10/9 \approx 1.11$. The relation (5) has the same nice limiting behavior as the Colebrook-White formula, that is, it reduces to the smooth pipe formula (4) when $K/D \rightarrow 0$ and the von Karman relation (2) when $Re \rightarrow \infty$.

To establish the accuracy of (5), we have compared it with the Colebrook-White formula (3) and also with the explicit equation given by Moody [3]

$$f = 0.0055 \left[1 + \left(2 \cdot 10^4 \frac{K}{D} + \frac{10^6}{Re} \right)^{1/3} \right] \quad (6)$$

The friction factor was computed for a number of points for $(Re, K/D)$ in the range $R: [4 \cdot 10^3 \leq Re \leq 10^8, 0 \leq K/D \leq 5 \cdot 10^{-2}]$. From these calculations one finds that (5) is in very good agreement with (3), it differs with less than ± 1.5 percent. Moody's equation (6) differ with (3) between about -16 percent and $+13$ percent for the same range in $(Re, K/D)$, i.e., R .

There is another way of combining (4) with (2), that is,

$$\frac{1}{\sqrt{f}} = -2 \log \left[\left(\frac{6.9}{Re} \right)^{0.9} + \frac{K}{3.7D} \right] \quad (7)$$

but this formula has a maximum difference of nearly 3 percent in the range R compared to (3). This is twice as much as we get when using (5) so that (7) was discarded in favor of (5).

A formula similar to (7) (with 6.97 instead of 6.9) has been given by Swamee and Jain [4]. Note that the claim made that their formula is in error well within ± 1 percent is incorrect. For example, at $Re = 5000$ and $K/D = 0.01$ the difference between their formula and (3) is 2.8 percent.

A very recent paper by Barr [5] gives a formula for f which is more than twice as accurate as (5) when compared to (3),

Contributed by the Fluids Engineering Division for publication in the JOURNAL OF FLUIDS ENGINEERING. Manuscript received by the Fluids Engineering Division, September 2, 1981.

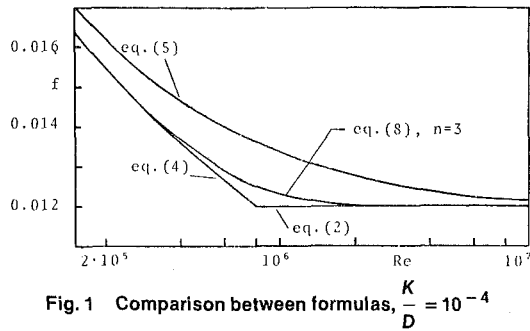


Fig. 1 Comparison between formulas, $\frac{K}{D} = 10^{-4}$

but it is considerably more complicated. Before simplicity is sacrificed for excessive accuracy, it is worth keeping in mind that the Colebrook-White formula (3) itself may be 3–5 percent, if not more, in error as compared to experimental data.

Thus, formula (5) should make a very practical substitution for (3) for the calculation of the friction factor for the following reasons: (i) it is explicit, (ii) it reduces to the appropriate limiting equations for the smooth regime and the fully rough regime, (iii) it is in very good agreement with (3).

However, more recent experiments using very smooth pipes (as in natural gas pipelines), Smith et al. [6], shows that the transition from the smooth to the rough regime is much more abrupt than is indicated by the Colebrook-White formula (3). In fact, the value one obtains by using either the smooth pipe formula (1) or the rough pipe formula (2), i.e., whichever formula that gives the largest value of f , was found to be a much better approximation than (3), [7]. To accommodate these results, we suggest the generalized formula

$$\frac{1}{\sqrt{f}} = -\frac{1.8}{n} \log \left[\left(\frac{6.9}{Re} \right)^n + \left(\frac{K}{3.75D} \right)^{1.11n} \right] \quad (8)$$

where the value $n=1$ gives the previous formula (5), i.e., we have a slow Colebrook-White type transition, whereas for larger values of n we have an increasingly abrupt transition. In Fig. 1 we have plotted, for the case $K/D = 10^{-4}$, the values

of f obtained by using formula (5), formula (8) with $n = 3$, and the result of a completely abrupt transition, i.e., respectively, formula (4) to the left and (2) to the right of the “transition” Re-number (defined as where these last two curves cross). It is seen that (8) with $n = 3$ gives values of f which are much closer to the completely abrupt transition which is recommended by the American Gas Association [7] than (5). Thus the value $n = 3$ seems to be a reasonable choice for n in case of natural gas pipelines. In addition, the numerical factor in the smooth pipe formula (1) was found [6] to be 2.8 rather than 2.51. If this is accepted, the factor 6.9 should be changed to 7.7 in (4) and (8) for pipes of very small values of K/D . Limitations of space prevents one from going further into these and other matters concerning natural gas pipelines here, see therefore [7] and [8] for further details.

It is hoped that the formulas presented herein will be of use to some of the large number of people, both practicing engineers, and students and teachers at educational institutions, who are required to make pipe flow calculations.

References

- 1 Colebrook, C. F., “Turbulent Flow in Pipes, With Particular Reference to the Transition Region Between the Smooth and Rough Pipe Laws,” *J. Inst. Civ. Eng.*, London, Vol. 11, 1939, pp. 133–156.
- 2 Techo, R., Tickner, R. R., and James, R. E., “An Accurate Equation for the Computation of the Friction Factor for Smooth Pipes From the Reynolds Number,” *ASME Journal of Applied Mechanics*, Vol. 32, 1965, p. 443.
- 3 Moody, L. F., “An Approximate Formula for Pipe Friction Factors,” *Mechanical Engineering*, Vol. 69, 1947, pp. 1005–1006.
- 4 Swamee, P. K., and Jain, A. K., “Explicit Equations for Pipe-Flow Problems,” *J. Hydraulic Div.*, Am. Soc. Civ. Eng., Vol. 102, HY5, 1976, pp. 657–664.
- 5 Barr, D. I. H., “Solutions of the Colebrook-White Function for Resistance to Uniform Turbulent Flow,” *Proc. Instn. Civ. Engrs*, Part 2, Vol. 71, 1981, pp. 529–535.
- 6 Smith, R. V. et al., “Flow of Natural Gas Through Experimental Pipe Lines and Transmission Lines,” U.S. Bureau and Mines Monograph 9, American Gas Association, New York, 1956.
- 7 Uhl, A. E. et al., “Steady Flow in Gas Pipelines,” Institute of Gas Technology Report No. 10, American Gas Association, New York, N.Y. 1965.
- 8 Haaland, S. E., “Simple and Explicit Formulas for the Friction Factor in Turbulent Pipe Flow, Including Natural Gas Pipelines,” Report IFAG B-131, The Norwegian Institute of Technology, Trondheim, Norway, 1981.

T. Makihata
 Researcher,
 Technical Research Institute,
 Hitachi Zosen Corporation
 Sakurajima, Konohana-ku, Osaka, Japan

Y. Miyai
 Professor,
 Department of Mechanical Engineering,
 University of Osaka Prefecture,
 Sakai, Osaka, Japan

Prediction of the Trajectory of Triple Jets in a Uniform Crossflow

This paper describes the results of numerical prediction of the trajectories of turbulent triple jets issuing into a uniform crossflow. The prediction technique is based on the momentum integral equation and the law of conservation of momentum, together with the interference of the triple jets under the assumption of an axially symmetrical flow pattern for each of the jets. Results are presented for both triple buoyant and nonbuoyant jets, with the velocity ratio of jet flow to crossflow ranging from 3.0 to 10.6. The numerical predictions agree well with authors' and other experimental data.

Introduction

Typical theories for calculating the trajectory of a single jet in a uniform crossflow include:

(a) Abramovich's [1] method, which takes the balance between the fluid resistance of the crossflow and the centrifugal force of the reflected jet into account the analysis,

(b) the method used by Sucec and Bowley [2] and Snel [3] based on the momentum of the jet with fluid entrainment and the fluid resistance caused by the crossflow,

(c) the method used by Keffer and Baines [4] which considers the momentum only in relation to the entrainment, and

(d) the method used by Campbell and Schetz [5] for the trajectory of a thermal effluent, which uses an integral method accounting for natural fluid mechanisms such as turbulence, entrainment, buoyancy and heat transfer.

The cross section of a jet injected into a crossflow is almost circular in shape in the region close to the nozzle outlet, but is flat due to the dynamic pressure of the crossflow in the curvilinear region where the jet is sufficiently far from the nozzle outlet. In order to handle such a complex flow field formation problem theoretically, both Campbell and Sucec assumed either an elliptical cross-section with the ratio of major to minor axes at 5:1, or a rectangular cross-section with the ratio of sides standing at 1:4. Snel and Keffer assumed a circuit cross-section, and used this assumption to calculate the width of the jet using either the momentum theory or the law of conservation of momentum. These differences in the method used to determine the width of the jet naturally result in a difference in the evaluation of the coefficient of the external force caused by the crossflow.

There have been many experimental studies on the trajectory of a single jet in a uniform cross-flow, such as experiments in wind tunnel by Schlieren's method or by smoke visualization, measurements of the velocity field by Pitot tubes, and so on. The trajectory and diffusion characteristics of a single jet have been determined, for example, by Keffer et al. for velocity ratios of $U_0/U_\infty = 2, 4, 6, 8$ and 10, Chassaing et al. [6] for $U_0/U_\infty = 2.37, 3.95,$ and

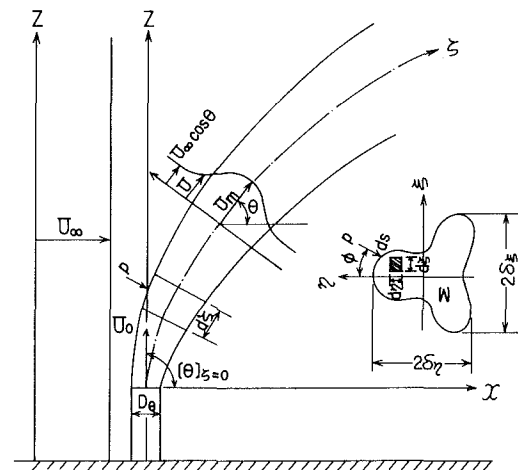


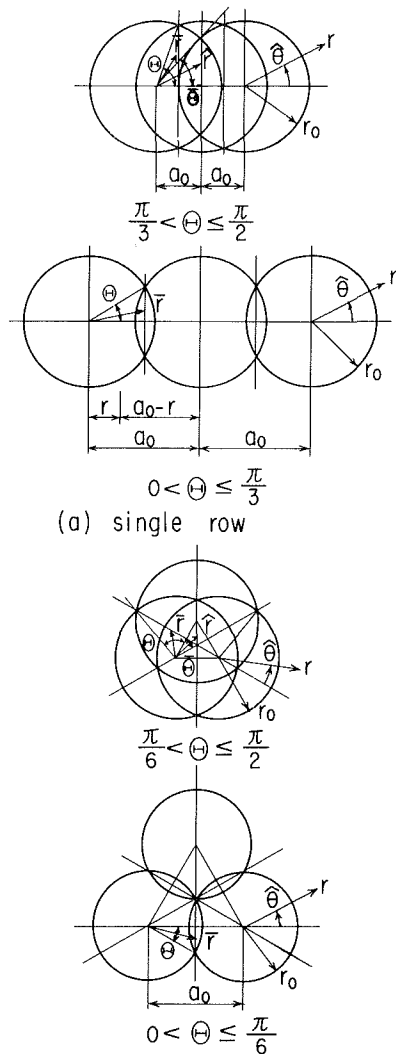
Fig. 1 Coordinate systems and nomenclature

6.35, and by Patrick [7] for $U_0/U_\infty = 11.75, 15.67, 21.19,$ and 53.76.

For buoyant jets having a momentum and buoyant flux, Bryant et al. [8] have made experiments and theoretical analysis of the results from the momentum theory derived from the centrifugal force, the buoyant flux, and the fluid resistance caused by the crossflow. Further, Campbell et al. have made numerical analysis by the finite difference method of the momentum integral equation introduced by taking the momentum with entrainment, buoyant flux, shearing force, etc. into account, and are comparing the analytical results with the available experimental data. Also, in buoyant jet analyses, the similarity of the velocity and temperature distributions in the cross section of a jet is generally explained by the assumption that these distributions are Gaussian [9, 10], this similarity has been verified experimentally by Tutu [11] and Epstein [12]. As stated above, many studies on the trajectory of single buoyant and nonbuoyant jets have been made both theoretically and experimentally, and their characteristics are now almost completely clarified.

With the rapid progress of heavy chemical industries, exhaust gases and hot waste water from various large-scale

Contributed by the Fluids Engineering Division for publication in the JOURNAL OF FLUIDS ENGINEERING. Manuscript received by the Fluids Engineering Division, October 29, 1981.



(a) single row
(b) triangular arrangement
Fig. 2 Modeling of interference phenomena

plants take the forms of multiple buoyant jets, which is a geometric assembly of a number of circular single buoyant jets. Trajectories for such multiple jets are scarce and there

Nomenclature

A_0 = total area of nozzle at the outlet
 A = cross sectional area of the jet flow at an arbitrary point
 $D_e \left(= \sqrt{\frac{4A_0}{\pi}} \right)$ = effective diameter of the nozzle
 $K_u \left(= \frac{U_0}{U_\infty} \right)$ = velocity ratio
 $K_\rho \left(= \frac{\rho_0}{\rho_\infty} \right)$ = density ratio
 $K_t \left(= \frac{T_0}{T_\infty} \right)$ = temperature ratio
 $T_0 (= 273 + t_0)$ = temperature ($^{\circ}\text{K}$) of the jet flow at the outlet
 $T_m (= 273 + t_m)$ = maximum temperature ($^{\circ}\text{K}$) of the jet flow at an arbitrary point

are only a few experimental studies by Kamotani et al. [13] reported so far, requiring more theoretical and experimental studies.

The triple jets considered in our study are multiple buoyant jets as shown in Fig. 1. To analyze their trajectory, it is necessary to model the interference of the individual jets with each other as shown in Fig. 2. In view of this, our proposed method combined the generally used momentum theory, which takes into account buoyant flux, entrainment and fluid resistance caused by the crossflow, with the law of conservation of momentum along a trajectory, as used in the analysis of Abramovich, Sucec and Snel. This method is simpler to work with than the more sophisticated analysis of Campbell et al.

In this paper we assume, as with our previous report on double jets [14], that each of the individual jets forming a multiple jet diffuses in an axially symmetric pattern. We propose a method to handle theoretically a complex multiple jet flow field as shown in Fig. 2. Using this method, triple jet trajectories are then theoretically evaluated and compared with author's and other's experimental data [13, 15], showing a fairly good comparison with the theory and experiments as we obtained for single and double jets.

Analysis

The following assumptions are used in our theoretical analysis: (1) crossflow of a uniform velocity distribution, and (2) completely turbulent, incompressible and stationary flow.

With the coordinate system and flow field as shown in Fig. 1 and taking buoyant flux, entrainment and fluid resistance caused by the crossflow into consideration, we have the momentum integral equations for the x and z components as follows [2, 3]:

$$\left\{ \int_{\Sigma} \rho U^2 A \frac{d\xi}{\sqrt{A}} \frac{d\eta}{\sqrt{A}} \cos\theta - \rho_0 U_0^2 A_0 [\cos\theta]_{\xi=0} \right\} = \int_0^{\xi} \sin\theta d\xi \int_s p \cos\phi ds + U_\infty \left\{ \int_{\Sigma} \rho U A \frac{d\xi}{\sqrt{A}} \frac{d\eta}{\sqrt{A}} - \rho_0 U_0 A_0 \right\} \quad (1a)$$

$$\left\{ \int_{\Sigma} \rho U^2 A \frac{d\xi}{\sqrt{A}} \frac{d\eta}{\sqrt{A}} \sin\theta - \rho_0 U_0^2 A_0 [\sin\theta]_{\xi=0} \right\} = - \int_0^{\xi} \cos\theta d\xi \int_s p \cos\phi ds + \int_0^{\xi} \left\{ \int_{\Sigma} (\rho_\infty - \rho) g A \frac{d\xi}{\sqrt{A}} \frac{d\eta}{\sqrt{A}} \right\} d\xi \quad (1b)$$

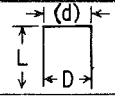
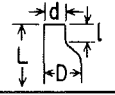
$T_\infty (= 273 + t_\infty)$ = temperature ($^{\circ}\text{K}$) of the crossflow
 $T (= 273 + t)$ = temperature ($^{\circ}\text{K}$) of the jet flow at an arbitrary point
 U_0 = velocity of the jet flow at the outlet
 U_m = maximum velocity of the jet flow at an arbitrary point
 U_∞ = velocity of the crossflow
 U = velocity of the jet flow at an arbitrary point

$$\hat{U}_m = U_m - U_\infty \cos\theta$$

$$\hat{U} = U - U_\infty \cos\theta$$

a_0 = interval between the nozzle outlets
 f = velocity distribution function in cross section of the jet flow
 g = gravitational acceleration
 h = density distribution function in the cross section of the jet flow
 n = number of multiple jets

Table 1 Shape of nozzles

$D_e(\text{mm})$	$(d/D)^2$	l/d	L/d	Remarks
60	1.0	—	10.97	
20	0.5	1.0	19.91	

The left-hand side of equation (1a) indicates the momentum change of the buoyant jet for the control volume, and \iint_{Σ} means integration over the entire area of the jet cross section. The first term of the righthand side expresses the external force due to pressure caused by the crossflow, and the second term indicates the momentum change due to the entrainment. The second term of the right-hand side of equation (1b) denotes the buoyant flux.

In order to compute the trajectory of a buoyant jet, we substitute the average velocity U and density ρ of jet fluid, the cross-sectional area A of jet control volume, and the pressure p due to the crossflow into equations (1a) and (1b), and solve them with $\cos\theta$ being the unknown quantity.

First, the velocity distribution function f in the jet cross section is given by following the analytical method by Sucec et al. The density distribution function h in the jet cross section can be introduced from the assumption by Hirst [9] and Fan [10] that $(U - U_{\infty} \cos\theta)/(U_m - U_{\infty} \cos\theta) \cong (T - T_{\infty})/(T_m - T_{\infty})$, which is experimentally confirmed by Tutu and Epstein, and the equation of state for an ideal gas [14]. Thus, we have

$$f\left(\frac{\xi}{\sqrt{A}}, \frac{\eta}{\sqrt{A}}\right) = \frac{U - U_{\infty} \cos\theta}{U_m - U_{\infty} \cos\theta},$$

$$h\left(\frac{\xi}{\sqrt{A}}, \frac{\eta}{\sqrt{A}}\right) = \frac{\rho_{\infty} - \rho}{\rho_{\infty} - \rho_m} = \frac{K_t \frac{T_m}{T_0} f}{K_t \frac{T_m}{T_0} f + (1-f)}.$$

The external force from the cross flow is given as follows [2]:

Nomenclature (cont.)

- p = dynamic pressure due to the cross flow
- $r, \hat{\theta}$ = polar coordinates of the jet flow
- r_0 = distance from the axis in the integral region of momentum
- $\bar{r}, \bar{\theta}$ = distance between the jet axis and the axis of symmetry, and angle of the weak interferential region
- $\hat{r}, \bar{\theta}$ = distance between the jet axis and the axis of symmetry, and angle of the strong interferential region
- x, z = Cartesian coordinates for the jet trajectory
- ξ, η = Cartesian coordinates in the cross section of the jet flow along the jet trajectory
- ζ = trajectory of the jet flow of maximum velocity
- ϵ = coefficient for the diffusion characteristics of the jet flow

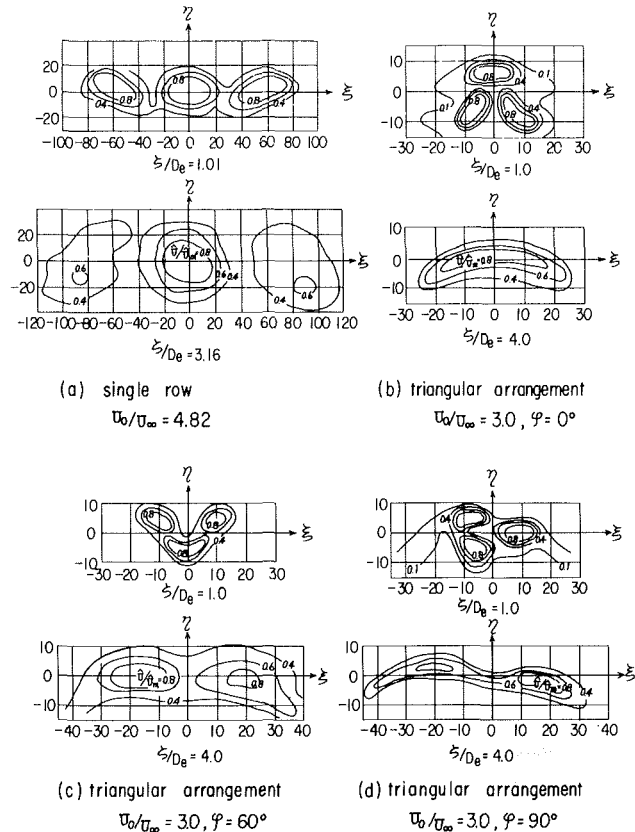


Fig. 3 Measured velocity field for triple jets [15] (Uncertainty in \hat{U}/\hat{U}_m , ξ/D_0 , ζ and $\eta = \pm 5$ percent)

$$\int_S p \cos\phi ds = \frac{\rho_{\infty}}{2} C_D \{ U_{\infty} \sin\theta \}^2 [2\delta_{\xi}]$$

The distribution functions f and h and the external force, as assumed above, are then substituted into equations (1a) and (1b), which are combined into an equation that expresses the condition along the trajectory of the jet. Both sides of this equation are multiplied by $1/(\rho_{\infty} U_{\infty}^2 A_0)$ to make the non-dimensional factors. For numerical calculation of this jet

- δ = diffusion width of the jet flow at $\frac{\hat{U}}{\hat{U}_m} = 0.5$
- ρ_0 = density of the jet flow at the outlet
- ρ_m = minimum density of the jet flow at an arbitrary point
- ρ_{∞} = density of the crossflow
- ρ = density of the jet flow at an arbitrary point
- θ = angle between the jet trajectory and horizontal x axis
- $[\theta]_{\zeta=0}$ = angle between the nozzle outlet and horizontal x axis
- φ = angle of the nozzle arrangement in the horizontal plane (direction of a crossflow)

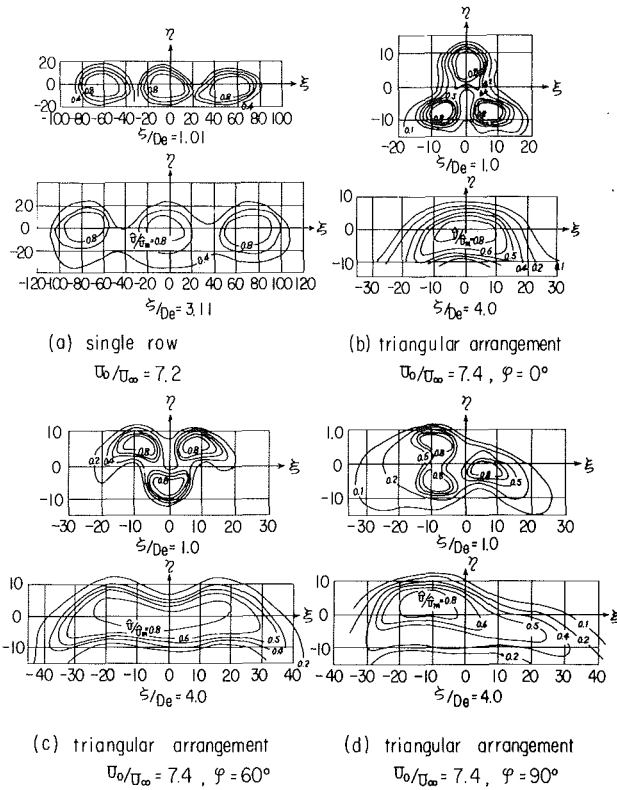


Fig. 4 Measured velocity field for triple jets [15] (Uncertainty in \hat{U}/\hat{U}_m , ζ/D_e , ξ and $\eta = \pm 5$ percent)

trajectory equation, a polynomial of order 6 with respect to $\cos\theta$, we used the finite difference method.

Experimental Results

As in the case of single and double jets [14], we used an Eiffel wind tunnel to carry out experiments on triple jets in a uniform crossflow [15]. The test section of this wind tunnel was 300 mm(B) \times 600 mm(H) \times 1500 mm(L), maximum wind velocity was 6 m/s, and turbulent intensity was 1.5 percent. Two kinds of the nozzles having a circular cross section were used in the experiments. One, with an effective diameter $D_e = 60$ mm, was composed of the triple nozzles arranged in a single row with the nozzle interval ratio $a_0/D_e = 0.876$. The other with an effective diameter $D_e = 20$ mm was composed of the triple nozzles in a triangular arrangement, with a nozzle interval ratio $a_0/D_e = 0.700$. In the former case, the nozzle had an axisymmetric configuration with a contraction ratio $(d/D)^2 = 1.0$ and an overall length: diameter ratio $L/d = 10.97$. For the latter, the locus of the center of nozzle cross-section followed a curved path as indicated in Table 1 with a contraction ratio $(d/D)^2 = 0.5$, an overall length: diameter ratio $L/d = 19.91$ and a length-diameter ratio in the uniform cross-section outlet region, $l/d = 1.0$.

The test conditions were as follows: the velocity at the outlet of the nozzle $U_0 = 10$ m/s ($Re = U_0 D_e / \nu = 1.4 \sim 4.2 \times 10^3$) constant; the velocity ratio varied $U_0/U_\infty = 3.36, 4.82, \text{ and } 7.2$ for the single row, and $U_0/U_\infty = 3, 5, \text{ and } 7.4$ for the triangular arrangement; and the heading angle of triple jet in triangular arrangement with respect to the crossflow varied $\varphi = 0, 60, \text{ and } 90$ degrees.

The velocity contour in the jet cross section was determined by using a KANOMAX 7000 Series (equivalent to DISA 5600 series) hot wire probe-operated constant temperature anemometer to travel in the cross section perpendicular to the trajectory. Its hot wire probe was a X type which was used for

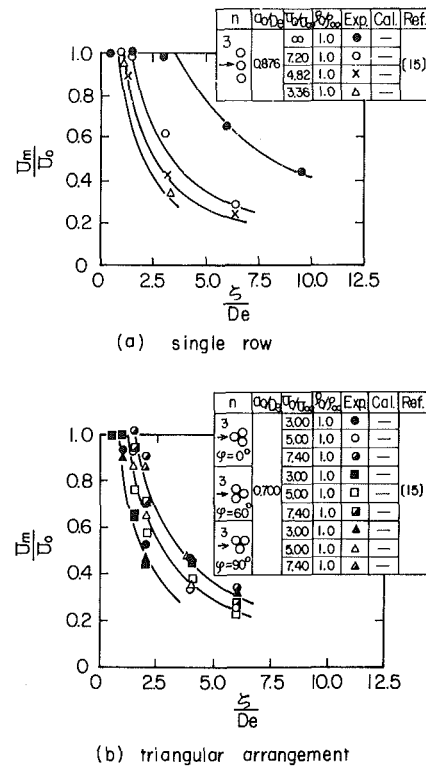


Fig. 5 Variation of jet velocity along the trajectory (Uncertainty in U_m/U_0 , U_0/U_∞ and $\zeta/D_e = \pm 5$ percent)

the field of two dimensional flow, and the final posture of the hot wire probe was set parallel to ζ axis were the out puts of each side probe were gained in the same level by trial and error method. Before starting each experiment, the relations of the jet trajectories and crossflow were obtained by the calibration of the Schlieren method using the air with 4 percent volumetric concentration of CO_2 .

The uncertainty of velocity contour and field in ξ, η Cartesian coordinates is estimated about ± 5 percent according to the technical note of Kanomax CTA 7000 Series and taking into consideration of the probe carriage having 1/20 scale vernier. Therefore, the final uncertainty shown in Figs. 3 to 7 is contained about ± 5 percent in \hat{U}/\hat{U}_m , ζ/D_e , U_m/U_0 , U_0/U_∞ and ρ_0/ρ_∞ , and about ± 15 percent in

$$\frac{x}{D_e} \left(\frac{\rho_\infty U_\infty^2}{\rho_0 U_0^2} \right) \text{ and } \frac{z}{D_e} \left(\frac{\rho_\infty U_\infty^2}{\rho_0 U_0^2} \right),$$

respectively.

Figures 3 and 4 show \hat{U}/\hat{U}_m values of the typical velocity contour diagrams measured in case of the two triple jet arrangements: $U_0/U_\infty = 4.82, 7.2$ for the single row, and $U_0/U_\infty = 3, 7.4$ and $\varphi = 0, 60, \text{ and } 90$ deg for the triangular arrangement.

Figures 3 and 4 indicate that the interference between the individual jets differs depending on the nozzle arrangement with respect to the crossflow. Since the interference in the case of the single row was not very strong, the velocity contour of the triple jet remained the same as the nozzle arrangement. With the triangular arrangement, however, strong interference is seen, which causes the velocity contour of the triple jet to become the same as that for a single jet.

The tendency to be in a kidney shape of the velocity contour becomes strong in proportion to the magnitude of the crossflow as shown in Figs. 3 and 4, and the same tendency is obtained in the previous works for a single jet [1, 4, 5].

Near-Field Region. As discussed in our previous paper for

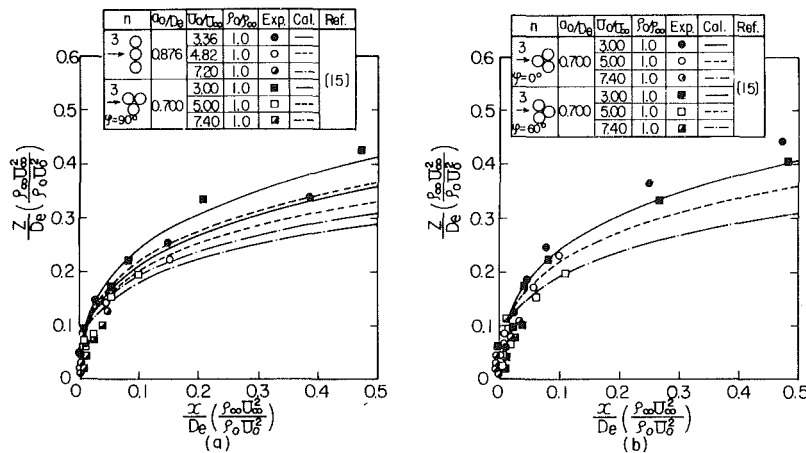


Fig. 6 Experimental and theoretical triple nonbuoyant jets trajectory (Uncertainty in

$$\frac{x}{De} \left(\frac{\rho_{\infty} U_{\infty}^2}{\rho_0 U_0^2} \right) \text{ and } \frac{Z}{De} \left(\frac{\rho_{\infty} U_{\infty}^2}{\rho_0 U_0^2} \right) = \pm 15 \text{ percent, } U_0/U_{\infty} = \pm 5 \text{ percent}$$

single and double jets, the velocity distribution function f in the potential region is given by [14].

$$\left. \begin{aligned} \frac{\sqrt{n}\zeta}{De} \left(1 + \frac{10}{K_u} \right) &\leq 6.15 \\ \left. \begin{aligned} f &= e^{-\alpha \sigma^4}, \left(\alpha = -\log_e 0.5, \sigma = \frac{\xi}{[\delta]_{n=1}} = \frac{\eta}{[\delta]_{n=1}} \right) \\ \frac{U_m}{U_0} &= 1 \end{aligned} \right\} \quad (2) \end{aligned}$$

Curvilinear Region. The velocity distribution function f in the completely turbulent flow region is given from our experimental results on the single and double jets and other available experimental data, and the U_m/U_0 reduction characteristic of the jet along its trajectory is given from the results shown in Figs. 5(a) and (b); and they are approximated as follows [14]:

$$\left. \begin{aligned} \frac{\sqrt{n}\zeta}{De} \left(1 + \frac{10}{K_u} \right) &> 6.15 \\ \left. \begin{aligned} f &= e^{-\alpha \sigma^2} \\ \frac{U_m}{U_0} &= \frac{7.8}{\frac{\sqrt{n}\zeta}{De} \left(1 + \frac{10}{K_u} \right) + 1.65}, \frac{U_m}{U_{\infty} \cos \theta} \geq 1 \end{aligned} \right\} \quad (3) \end{aligned}$$

Results and Discussion

Width of the Jet. The velocity distribution patterns of Figs. 3 and 4 clearly indicate that there is an interference between the individual jets when a multiple jet is in a crossflow, and it is extremely difficult to analyze theoretically such interference phenomena.

In our study, therefore, theoretical evaluation of the interference phenomena is approached from the law of conservation of momentum on the assumption that the individual jets forming a multiple jet diffuse axisymmetrically as shown in Fig. 2 and reference [14].

Let each of the three individual jets be a_0 (= nozzle interval) apart and diffuse axisymmetrically, then there will be two types of regions: one that involves a relatively weak interference and the other that involves strong interference.

For the single row, they are defined as $0 < \Theta \leq \pi/3$ and

$\pi/3 < \Theta \leq \pi/2$, respectively. For the triangular arrangement, they are $0 < \Theta \leq \pi/6$ and $\pi/6 < \Theta \leq \pi/2$, respectively as shown in Fig. 2.

(1) Single row, for weak interference region defined by

$$\left. \begin{aligned} 0 < \Theta &= \cos^{-1} \left[\frac{a_0}{\frac{De}{\sqrt{3}} \left(1 + \frac{\sqrt{3}\epsilon}{De} \zeta \right)} \right] \leq \frac{\pi}{3} : \\ 2 \left\{ 2 \int_{\Theta}^{\pi} \int_0^{r_0} \rho U^2 r dr d\hat{\theta} + \int_{2\Theta}^{\pi} \int_0^{r_0} \rho U^2 r dr d\hat{\theta} + 8 \int_0^{\Theta} \int_0^{\hat{r}} \rho U^2 r dr d\hat{\theta} \right. \\ &- 4 \int_0^{\Theta} \int_0^{r_0} \rho U^2 r dr d\hat{\theta} + 4 \int_0^{\Theta} \int_0^{r_0} \rho \left(U + \frac{\bar{\rho}}{\rho} \bar{U} \right)^2 r dr d\hat{\theta} \\ &- 4 \int_0^{\Theta} \int_0^{\hat{r}} \rho \left(U + \frac{\bar{\rho}}{\rho} \bar{U} \right)^2 r dr d\hat{\theta} \left. \right\} - \rho_0 \frac{\pi}{4} d^2 \left(\sum_{i=1}^3 U_{0i}^2 \right) \\ &= 2U_{\infty} \cos \theta \left\{ 2 \int_{\Theta}^{\pi} \int_0^{r_0} \rho U r dr d\hat{\theta} + \int_{2\Theta}^{\pi} \int_0^{r_0} \rho U r dr d\hat{\theta} \right. \\ &+ 8 \int_0^{\Theta} \int_0^{\hat{r}} \rho U r dr d\hat{\theta} - 4 \int_0^{\Theta} \int_0^{r_0} \rho U r dr d\hat{\theta} \\ &+ 4 \int_0^{\Theta} \int_0^{r_0} \rho \left(U + \frac{\bar{\rho}}{\rho} \bar{U} \right) r dr d\hat{\theta} \\ &\left. - 4 \int_0^{\Theta} \int_0^{\hat{r}} \rho \left(U + \frac{\bar{\rho}}{\rho} \bar{U} \right) r dr d\hat{\theta} \right\} \quad (4a) \end{aligned}$$

For strong interference region defined by

$\pi/3 < \Theta \leq \pi/2$:

$$\left. \begin{aligned} 2 \left\{ 3 \int_0^{\Theta} \int_0^{r_0} \rho U^2 r dr d\hat{\theta} - 8 \int_0^{\Theta} \int_0^{r_0} \rho U^2 r dr d\hat{\theta} + 8 \int_0^{\Theta} \int_0^{\hat{r}} \rho U^2 r dr d\hat{\theta} \right. \\ &+ 14 \int_0^{\Theta} \int_0^{r_0} \rho U^2 r dr d\hat{\theta} - 2 \int_0^{\Theta} \int_0^{\hat{r}} \rho U^2 r dr d\hat{\theta} \\ &+ 4 \int_0^{\Theta} \int_0^{r_0} \rho \left(U + \frac{\bar{\rho}}{\rho} \bar{U} \right)^2 r dr d\hat{\theta} - 4 \int_0^{\Theta} \int_0^{\hat{r}} \rho \left(U + \frac{\bar{\rho}}{\rho} \bar{U} \right)^2 r dr d\hat{\theta} \\ &\left. - 8 \int_0^{\Theta} \int_0^{r_0} \rho \left(U + \frac{\bar{\rho}}{\rho} \bar{U} \right)^2 r dr d\hat{\theta} \right\} \end{aligned}$$

$$\begin{aligned}
& + 4 \int_0^{\hat{\theta}} \int_0^{\hat{r}} \rho \left(U + \frac{\bar{\rho}}{\rho} \bar{U} \right)^2 r dr d\hat{\theta} \\
& + 2 \int_0^{\hat{\theta}} \int_0^{r_0} \rho \left(U + \frac{\bar{\rho}}{\rho} \bar{U} + \frac{\hat{\rho}}{\rho} \hat{U} \right)^2 r dr d\hat{\theta} \\
& - 2 \int_0^{\hat{\theta}} \int_0^{\hat{r}} \rho \left(U + \frac{\bar{\rho}}{\rho} \bar{U} + \frac{\hat{\rho}}{\rho} \hat{U} \right)^2 r dr d\hat{\theta} \} \\
& - \rho_0 \frac{\pi}{4} d^2 \left(\sum_{i=1}^3 U_{0i}^2 \right) = 2U_{\infty} \cos\theta \left\{ 3 \int_0^{\pi} \int_0^{r_0} \rho U r dr d\hat{\theta} \right. \\
& - 8 \int_0^{\hat{\theta}} \int_0^{r_0} \rho U r dr d\hat{\theta} + 8 \int_0^{\hat{\theta}} \int_0^{\hat{r}} \rho U r dr d\hat{\theta} + 14 \int_0^{\hat{\theta}} \int_0^{r_0} \rho U r dr d\hat{\theta} \\
& - 2 \int_0^{\hat{\theta}} \int_0^{\hat{r}} \rho U r dr d\hat{\theta} + 4 \int_0^{\hat{\theta}} \int_0^{r_0} \rho \left(U + \frac{\bar{\rho}}{\rho} \bar{U} \right) r dr d\hat{\theta} \\
& - 4 \int_0^{\hat{\theta}} \int_0^{\hat{r}} \rho \left(U + \frac{\bar{\rho}}{\rho} \bar{U} \right) r dr d\hat{\theta} - 8 \int_0^{\hat{\theta}} \int_0^{r_0} \rho \left(U + \frac{\bar{\rho}}{\rho} \bar{U} \right) r dr d\hat{\theta} \\
& + 4 \int_0^{\hat{\theta}} \int_0^{\hat{r}} \rho \left(U + \frac{\bar{\rho}}{\rho} \bar{U} \right) r dr d\hat{\theta} \\
& + 2 \int_0^{\hat{\theta}} \int_0^{r_0} \rho \left(U + \frac{\bar{\rho}}{\rho} \bar{U} + \frac{\hat{\rho}}{\rho} \hat{U} \right) r dr d\hat{\theta} \\
& \left. - 2 \int_0^{\hat{\theta}} \int_0^{\hat{r}} \rho \left(U + \frac{\bar{\rho}}{\rho} \bar{U} + \frac{\hat{\rho}}{\rho} \hat{U} \right) r dr d\hat{\theta} \right\} \quad (4b)
\end{aligned}$$

where $r_0 = \sigma_0 \delta$, $\hat{r} = \frac{a_0}{2 \cos \hat{\theta}}$, $\hat{r} = \frac{a_0}{\cos \hat{\theta}}$,

$$\text{and } \hat{\theta} = \cos^{-1} \left[\frac{a_0}{\frac{D_e}{2\sqrt{3}} \left(1 + \frac{\sqrt{3}\epsilon}{D_e} \zeta \right)} \right].$$

(2) Triangular arrangement, for weak interference region defined by

$$\begin{aligned}
0 < \Theta &= \cos^{-1} \left[\frac{a_0}{\frac{D_e}{\sqrt{3}} \left(1 + \frac{\sqrt{3}\epsilon}{D_e} \zeta \right)} \right] \leq \frac{\pi}{6} : \\
3 \left\{ \int_0^{2\pi} \int_0^{r_0} \rho U^2 r dr d\hat{\theta} - 8 \int_0^{\hat{\theta}} \int_0^{r_0} \rho U^2 r dr d\hat{\theta} + 8 \int_0^{\hat{\theta}} \int_0^{\hat{r}} \rho U^2 r dr d\hat{\theta} \right. \\
& + 4 \int_0^{\hat{\theta}} \int_0^{r_0} \rho \left(U + \frac{\bar{\rho}}{\rho} \bar{U} \right)^2 r dr d\hat{\theta} - 4 \int_0^{\hat{\theta}} \int_0^{\hat{r}} \rho \left(U + \frac{\bar{\rho}}{\rho} \bar{U} \right)^2 r dr d\hat{\theta} \} \\
& - \rho_0 \frac{\pi}{4} d^2 \left(\sum_{i=1}^3 U_{0i}^2 \right) = 3U_{\infty} \cos\theta \left\{ \int_0^{2\pi} \int_0^{r_0} \rho U r dr d\hat{\theta} \right. \\
& - 8 \int_0^{\hat{\theta}} \int_0^{r_0} \rho U r dr d\hat{\theta} + 8 \int_0^{\hat{\theta}} \int_0^{\hat{r}} \rho U r dr d\hat{\theta} \\
& + 4 \int_0^{\hat{\theta}} \int_0^{r_0} \rho \left(U + \frac{\bar{\rho}}{\rho} \bar{U} \right) r dr d\hat{\theta} \\
& \left. - 4 \int_0^{\hat{\theta}} \int_0^{\hat{r}} \rho \left(U + \frac{\bar{\rho}}{\rho} \bar{U} \right) r dr d\hat{\theta} \right\} \quad (5a)
\end{aligned}$$

For strong interference region defined by

$$\pi/6 < \Theta \leq \pi/2:$$

$$3 \left\{ \int_0^{2\pi} \int_0^{r_0} \rho U^2 r dr d\hat{\theta} - 4 \int_0^{\hat{\theta}} \int_0^{r_0} \rho U^2 r dr d\hat{\theta} + 4 \int_0^{\hat{\theta}} \int_0^{\hat{r}} \rho U^2 r dr d\hat{\theta} \right.$$

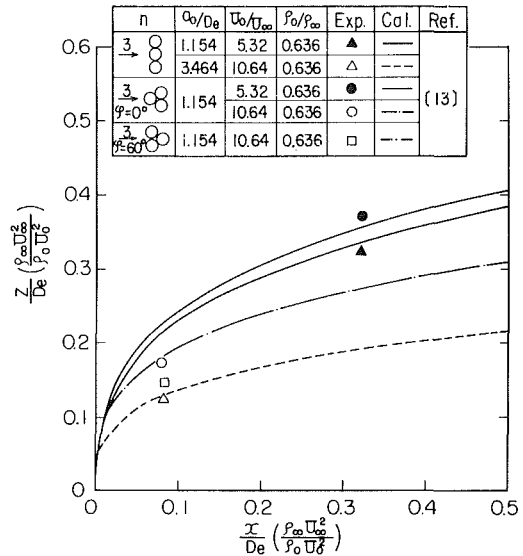


Fig. 7 Experimental and theoretical triple nonbuoyant jets trajectory (Uncertainty in

$$\frac{x}{De} \left(\frac{\rho_{\infty} U_{\infty}^2}{\rho_0 U_0^2} \right) \text{ and } \frac{z}{De} \left(\frac{\rho_{\infty} U_{\infty}^2}{\rho_0 U_0^2} \right)$$

= ± 15 percent, $U_0/U_{\infty} = \pm 5$ percent)

$$\begin{aligned}
& + 2 \int_0^{\hat{\theta}} \int_0^{r_0} \rho U^2 r dr d\hat{\theta} - 2 \int_0^{\hat{\theta}} \int_0^{\hat{r}} \rho U^2 r dr d\hat{\theta} \\
& + 2 \int_0^{\hat{\theta}} \int_0^{r_0} \rho \left(U + \frac{\bar{\rho}}{\rho} \bar{U} \right)^2 r dr d\hat{\theta} \\
& - 2 \int_0^{\hat{\theta}} \int_0^{\hat{r}} \rho \left(U + \frac{\bar{\rho}}{\rho} \bar{U} \right)^2 r dr d\hat{\theta} - 2 \int_0^{\hat{\theta}} \int_0^{r_0} \rho \left(U + \frac{\bar{\rho}}{\rho} \bar{U} \right)^2 r dr d\hat{\theta} \\
& + 2 \int_0^{\hat{\theta}} \int_0^{\hat{r}} \rho \left(U + \frac{\bar{\rho}}{\rho} \bar{U} \right)^2 r dr d\hat{\theta} + 2 \int_0^{\hat{\theta}} \int_0^{r_0} \rho \left(U + 2 \frac{\bar{\rho}}{\rho} \bar{U} \right)^2 r dr d\hat{\theta} \\
& - 2 \int_0^{\hat{\theta}} \int_0^{\hat{r}} \rho \left(U + 2 \frac{\bar{\rho}}{\rho} \bar{U} \right)^2 r dr d\hat{\theta} \} - \rho_0 \frac{\pi}{4} d^2 \left(\sum_{i=1}^3 U_{0i}^2 \right) \\
& = 3U_{\infty} \cos\theta \left\{ \int_0^{2\pi} \int_0^{r_0} \rho U r dr d\hat{\theta} - 4 \int_0^{\hat{\theta}} \int_0^{r_0} \rho U r dr d\hat{\theta} \right. \\
& + 4 \int_0^{\hat{\theta}} \int_0^{\hat{r}} \rho U r dr d\hat{\theta} + 2 \int_0^{\hat{\theta}} \int_0^{r_0} \rho U r dr d\hat{\theta} - 2 \int_0^{\hat{\theta}} \int_0^{\hat{r}} \rho U r dr d\hat{\theta} \\
& + 2 \int_0^{\hat{\theta}} \int_0^{r_0} \rho \left(U + \frac{\bar{\rho}}{\rho} \bar{U} \right) r dr d\hat{\theta} - 2 \int_0^{\hat{\theta}} \int_0^{\hat{r}} \rho \left(U + \frac{\bar{\rho}}{\rho} \bar{U} \right) r dr d\hat{\theta} \\
& - 2 \int_0^{\hat{\theta}} \int_0^{r_0} \rho \left(U + \frac{\bar{\rho}}{\rho} \bar{U} \right) r dr d\hat{\theta} + 2 \int_0^{\hat{\theta}} \int_0^{\hat{r}} \rho \left(U + \frac{\bar{\rho}}{\rho} \bar{U} \right) r dr d\hat{\theta} \\
& \left. + 2 \int_0^{\hat{\theta}} \int_0^{r_0} \rho \left(U + 2 \frac{\bar{\rho}}{\rho} \bar{U} \right) r dr d\hat{\theta} - 2 \int_0^{\hat{\theta}} \int_0^{\hat{r}} \rho \left(U + 2 \frac{\bar{\rho}}{\rho} \bar{U} \right) r dr d\hat{\theta} \right\} \quad (5b)
\end{aligned}$$

Where $r_0 = \sigma_0 \delta$, $\hat{r} = \frac{a_0}{2 \cos \hat{\theta}}$, $\hat{r} = \delta \cos \hat{\theta}$,

and $\hat{\theta} = \frac{\pi}{6}$.

In equations (4) and (5), the left-hand side is the momentum of the buoyant jet with respect to the control volume and the right-hand side is that due to the entrainment of the crossflow.

In order to evaluate the diffusion characteristic coefficient ϵ , we use the following relations:

$$\left. \begin{aligned} \delta &= \frac{D_e}{2\sqrt{3}} \left(1 + \frac{\sqrt{3}\epsilon}{D_e} \zeta \right), \left(\frac{U}{U_0} \right)^2 = \left(\frac{U_m}{U_0} \right)^2 \left(\frac{U}{U_m} \right)^2, \\ \left(\frac{\tilde{U}}{U_0} \right)^2 &= \left(\frac{U_m}{U_0} \right)^2 \left(\frac{\tilde{U}}{U_m} \right)^2, \left(\frac{\hat{U}}{U_0} \right)^2 \\ &= \left(\frac{U_m}{U_0} \right)^2 \left(\frac{\hat{U}}{U_m} \right)^2, \\ f &= \frac{U - U_\infty \cos\theta}{U_m - U_\infty \cos\theta}, \bar{f} = \frac{\tilde{U} - U_\infty \cos\theta}{U_m - U_\infty \cos\theta}, \hat{f} = \frac{\hat{U} - U_\infty \cos\theta}{U_m - U_\infty \cos\theta}, \\ h &= \frac{\rho_\infty - \rho}{\rho_\infty - \rho_m}, \bar{h} = \frac{\rho_\infty - \bar{\rho}}{\rho_\infty - \rho_m}, \hat{h} = \frac{\rho_\infty - \hat{\rho}}{\rho_\infty - \rho_m}, U = U(r), \\ \tilde{U} &= U(\tilde{a}_0 - \tilde{r}), \hat{U} = U(2\tilde{a}_0 - \tilde{r}), \rho = \rho(r), \\ \bar{\rho} &= \rho(\tilde{a}_0 - \tilde{r}), \hat{\rho} = \rho(2\tilde{a}_0 - \tilde{r}), \tilde{a}_0 = \frac{a_0}{\cos\theta}, \tilde{r} = r \frac{\cos\hat{\theta}}{\cos\theta} \end{aligned} \right\} (6)$$

By substituting equation (6) into equations (4) and (5), we obtain an equation for ϵ . Calculating this equation and the polynomial of order 6 with respect to $\cos\theta$, which is derived from equation (1), as simultaneous equations by the finite difference method, we have the width of the jet $2\delta_\xi = 2\delta + \gamma a_0$. The coefficient γ is 2 for single row; in the case of triangular arrangement, it is 1 for $\varphi = 0$ and 60 deg, and it is $\sqrt{3}/2$ for $\varphi = 90$ deg.

Jet Trajectory. Numerical calculation of the triple buoyant jet trajectory was carried out by computing the polynomial of order 6 with respect to $\cos\theta$ derived from equation (1) and the equation for ϵ obtained from equations (4) and (5) as simultaneous equations. The finite difference method was used in computations by a HITAC 8700 computer (equivalent to IBM 370-158) with the trajectory divided into 250 to 300 steps at intervals of $\Delta\zeta = 0.3705 (K_u/7.5)^2$.

For the polynomial with respect to $\cos\theta$ its approximate solution $[\cos\tilde{\theta}]$ obtained by Horner's method and, substituting this into the following equations, the triple buoyant jet trajectory was obtained.

$$\left. \begin{aligned} \frac{x}{K_\rho K_u^2 D_e} &= \frac{\zeta}{K_\rho K_u^2 D_e} [\cos\tilde{\theta}], \frac{z}{K_\rho K_u^2 D_e} = \frac{\zeta}{K_\rho K_u^2 D_e} [\sin\tilde{\theta}] \\ [\sin^2\tilde{\theta}] + [\cos^2\tilde{\theta}] &= 1 \end{aligned} \right\} (7)$$

Figures 6(a) and (b), and 7 compare the trajectories computed for triple buoyant and nonbuoyant jets with the experimental results by the authors [15] and by Kamotani et al. The experimental multiple jets compared with the calculations are nonbuoyant jets ($n = 3, K_\rho = 1$) [15] and buoyant jets in single row and triangular arrangement ($n = 3, K_\rho = 0.636$) [13]. The coefficient C_D of the external force by the crossflow used in these calculations is $C_D \cong 2.5$ for $K_u \cong 3$ and $C_D = 2.0$ for $K_u \geq 4$ [14]. Sucec et al. also used $C_D = 1.8$ for $K_u < 4.4$ and $C_D = 1.0$ for $K_u \geq 4.4$. The reason that C_D becomes a function of K_u discussed by Chan et al. [16] is presumed to be due to the fact that below $K_u \cong 4$ and this being the turning point, the width of diffusion of jet flow shows a sudden increase and negative pressure along the intersection of jets was larger than the negative pressure around the solid cylinder, which was calculated from the potential flow.

From Figs. 6 and 7, we see that the calculations and experiments for the triple jets in single row and in triangular arrangement with $\varphi = 60$ deg show a good agreement in general. While the agreement of the calculations with the experiments for the other cases is not as good as for these cases, the overall comparison indicates that the accuracy of our proposed theoretical evaluation method for the trajectory of triple jets is fairly good.

Conclusions

Our study on the trajectory of single row and triangularly arranged triple jets in a uniform crossflow has clarified the following:

1) The present method, in which the width of the jet is defined under the assumption that the individual jets forming a multiple jet diffuse axisymmetrically and by the law of conservation of momentum, and the equation derived from this and the momentum integral equation are computed as simultaneous equations by the finite difference method, is effective to evaluate complex flow fields such as multiple jets.

2) In our multiple jet trajectory analysis, the interference between the individual jets is assumed based on the momentum integral equation, that accounts for the momentum of the jet, entrainment by the crossflow and the axisymmetric diffusion of the individual jets, from which the multiple jet trajectory is evaluated. According to this analytical method, by giving the coefficient of the external force by the crossflow $C_D = 2.0$ for the velocity ratio $K_u (= U_0/U_\infty) \geq 4$ and $C_D > 2.0$ for $K_u < 4$, the multiple jet trajectory can be evaluated with a fairly good accuracy.

References

- 1 Abramovich, G. N., *The Theory of Turbulent Jets*, The MIT Press Cambridge, Mass., 1963.
- 2 Sucec, J., and Bowley, W. W., "Prediction of the Trajectory of a Turbulent Jet Injected into a Crossflowing Stream", *ASME JOURNAL OF FLUIDS ENGINEERING*, Vol. 98, Dec. 1976, pp. 667-673.
- 3 Snel, H., "A Semi-Empirical Model for the Development of a Round Turbulent Jet in a Cross Flow," NLR TR71107U, 1971.
- 4 Keffer, J. F., and Baines, W. D., "The Round Turbulent Jet in a Cross-Wind," *Journal of Fluid Mechanics*, Vol. 15, 1963, pp. 481-496.
- 5 Campbell, J. F., and Schetz, J. A., "Flow Properties of Submerged Heated Effluents in a Waterway," *AIAA Journal*, Vol. 11, No. 2, Feb. 1973, pp. 223-230.
- 6 Chassaing, P., George, J., Claria, A., and Sananes, F., "Physical Characteristics of Subsonic Jets in a Cross-Stream," *Journal of Fluid Mechanics*, Vol. 62, Part 1, 1974, pp. 41-64.
- 7 Patrick, M. A., "Experimental Investigation of Mixing and Flow in a Round Turbulent Jet Injected Perpendicularly into a Main Stream," *Journal of the Institute of Fuel*, Sept. 1967, pp. 425-432.
- 8 Bryant, L. W., and Cowdrey, C. F., "Effects of Velocity and Temperature of Discharge on the Shape of Smoke Plumes from a Funnel or Chimney: Experiments in a Wind Tunnel," NPL Report, 1949, pp. 371-399.
- 9 Hirst, E., "Buoyant Jets with Three-Dimensional Trajectories," *Proc. of the ASCE*, HY11, Nov. 1972, pp. 1999-2014.
- 10 Fan, L.-N., and Brooks, N. H., "Numerical Solutions of Turbulent Buoyant Jet Problems," CIT Report No. KH-R-18, Jan. 1969.
- 11 Tutu, N. K., "An Experimental Investigation of a Heated, Turbulent Round Jet," State Univ. of N.Y., 76-18, 726, 1976.
- 12 Epstein, A., and Hendrikson, V., "Some Peculiarities of Jet Flows in a Deflecting Stream," *Engineering Trans.*, Vol. 22, No. 3, 1974, pp. 421-426.
- 13 Kamotani, Y., and Greber, I., "Experiments on Confined Turbulent Jets in Cross Flow," NASA CR-2392, Mar. 1974.
- 14 Makihata, T., and Miyai, Y., "Trajectories of Single and Double Jets Injected into Crossflow of Arbitrary Velocity Distribution," *ASME JOURNAL OF FLUIDS ENGINEERING*, Vol. 101, June 1979, pp. 217-223.
- 15 Makihata, T., and Miyai, Y., "Experiments on the Characteristics of Multiple Jets in a Crossflow," *Bulletin of Univ. of Osaka Prefecture, Series A*, Vol. 26, No. 2, 1977, pp. 15-36.
- 16 Chan, D., T.-L., and Kennedy, J. F., "Turbulent Nonbuoyant or Buoyant Jets Discharged into Flowing or Quiescent Fluids," IIHR Report No. 140, Aug. 1972.

Flow Around a Normal Plate of Finite Width Immersed in a Turbulent Boundary Layer

H. Sakamoto

Professor,
Department of Mechanical Engineering,
Kitami Institute of Technology,
Kitami, 090, Japan

M. Arie

President,
Hokkaido University,
Sapporo, 060, Japan

An experimental investigation was carried out on the flow around a normal plate of finite width mounted on a smooth plane wall along which a turbulent boundary layer was fully developed. Experimental data were collected to investigate the effects of (1) the aspect ratio of the plate (2) the parameters characterizing the boundary-layer on the pressure drag and the vortex shedding frequency. The pressure drag coefficient of the plate defined by $C_{D\tau} = D / (1/2\rho u_\tau^2 hw)$ was found to be expressed by a power function of hu_τ/ν in the range $h/\delta < 1.0$ for each aspect ratio w/h , where D is the pressure drag, u_τ is the shear velocity, ρ is the density of fluid, h and w are the height and the width of the plate, respectively, ν is the kinematic viscosity, δ is the thickness of the boundary layer. Also, the Strouhal number for the plate defined by $S_f = f_c \cdot w / U_0$ was found to be expressed by a power function of the aspect ratio w/h in the range of h/δ less than about 1.0, where f_c is the vortex shedding frequency, U_0 is the free-stream velocity. As the aspect ratio was reduced, the type of vortex shedding behind the plate was found to change from the arch type to the Karman type at the aspect ratio of about 0.8.

1 Introduction

The flow of an incompressible fluid around a bluff body immersed in a turbulent boundary layer has become an important subject of study on account of problems, such as wind loads on man-made structures on the ground, the oscillation characteristics and noise of high-speed vehicles, the effects of roughness elements on boundary layer characteristics, the effectiveness of spoilers on an airfoil, etc. Especially, the aerodynamic behavior of a normal plate, cited as a typical bluff body, which is immersed in a turbulent boundary layer, has attracted the attention of many investigators. It should be noted that the great majority of the reported experiments (Good and Joubert [1], Sakamoto et al. [2], Ranga Raju et al. [3], Plate [4], among others) concern themselves with flow around the normal plate of infinite width attached to a plane wall on which a turbulent boundary layer is developed. However, since a considerable difference is noted in hydrodynamic characteristics between the normal plate of infinite width and that of finite width attached to a plane wall, as will be mentioned later, the values of aerodynamic force of the normal plate of finite width such as buildings, snow and wind fences on the ground, and spoilers on an airfoil cannot accurately be estimated from experimental results of the normal plate of infinite width.

An adverse pressure gradient will be produced by the deflection of flow by an obstacle in a flow field upstream of a normal plate of infinite width. As a result, the boundary layer

will be forced to separate from the plane boundary wall and will reattach on the front surface of the normal plate, thereby enclosing a front separation bubble. Subsequently, the flow will again separate from the top edge of the normal plate, and will reattach to the plane wall downstream of the plate, thereby forming a rear separation bubble. The flow visualization technique has shown that the mean flow inside the front and the rear separation bubble is fairly steady. On the other hand, in the neighborhood of the base of a normal plate of finite width, one or more vortices will be induced, being stretched in the shape of a horseshoe. These vortices will persist as streaming vortices far downstream, and the flow will roll up into a number of continuously generated horseshoe-shaped vortices, which are seen to wrap the plate, trailing downstream in multiple vortex pairs with their axes parallel to the direction of the main flow. Furthermore, one main feature of the flow around the normal plate of finite width is that it is separated from the top and both side surfaces and the separated flow is shed periodically downstream as arch-type vortices.

This study is intended to experimentally clarify flow around a normal plate of finite width immersed in a turbulent boundary layer. Measurements of pressure distribution on the surface of and vortex shedding frequency behind the plate were carried out by changing the height and width of the plate and the characteristics of the boundary layer. Pressure drag coefficients and Strouhal numbers of the plate were, respectively, calculated on the basis of measured values of pressure distribution and vortex shedding frequency to systematically investigate the relation between the aspect ratio

Contributed by the Fluids Engineering Division for publication in the JOURNAL OF FLUIDS ENGINEERING. Manuscript received by the Fluids Engineering Division, December 8, 1981.

of the plate and the characteristics of the boundary layer flow. Further, the flow pattern around the plate was clarified by the visualization of flow. Among the possible types of three-dimensional obstacles, a normal plate of finite width was selected as the most suitable one to establish a model law. Since a large number of natural obstacles like man-made structures, roughness elements on the surface of a solid wall, spurs in the river, etc., exhibit similar configurations, information on the present data will be found useful by structural engineers calculating wind loads, hydraulic engineers designing spur dikes for river drainage and agricultural engineers dealing with windbreaks.

2 Factors Governing Flow Around a Normal Plate

The governing parameters defining flow around a normal plate of finite width will now be considered. As already elucidated in Good and Joubert's report [1], the characteristics of the turbulent boundary layer with a zero-pressure gradient developed along the plane wall depend only on four parameters, i.e., the free-stream velocity U_0 , the boundary layer thickness δ , the shear velocity u_τ and the kinematic viscosity ν . Thus, on dimensional analysis, two independent dimensionless parameters, $\delta u_\tau / \nu$ and u_τ / U_0 , can be obtained from them.

The parameters, according to Coles [5], are related with each other by the equation

$$\frac{U_0}{u_\tau} = \frac{1}{\kappa} \log_e \frac{\delta u_\tau}{\nu} + C + \frac{2\Pi}{\kappa} \quad (1)$$

where Coles obtained $\Pi=0.55$ by assuming that $\kappa=0.4$ and $C=5.1$ for a turbulent boundary layer with a zero-pressure gradient. Therefore, one can arbitrarily choose either of the two parameters, $\delta u_\tau / \nu$ or u_τ / U_0 , to define the characteristics of such a boundary layer.

On the other hand, the geometrical shape of a normal plate must be characterized by its height h and width w . Accordingly, one can choose two dimensionless parameters, which are h/δ , the height h of the plate nondimensionalized after divided by δ the thickness of the boundary layer, and the aspect ratio w/h to define the geometrical shape of the normal plate attached to a plane wall.

From the foregoing discussions it can be concluded that flow around the normal plate immersed in a turbulent

boundary layer with a zero-pressure gradient along a smooth wall is governed by the three parameters u_τ / U_0 , h/δ and w/h . For example, concerning their functional relationships, the drag coefficients C_D based on the pressure acting on the surface of a normal plate and the Strouhal number S_t based on the vortex shedding frequency f_c , can be written, respectively, as

$$C_D = \frac{D}{\frac{1}{2} \rho U_0^2 h w} = f_1 \left(\frac{u_\tau}{U_0}, \frac{h}{\delta}, \frac{w}{h} \right) \quad (2)$$

$$S_t = \frac{f_c \cdot w}{U_0} = f_2 \left(\frac{u_\tau}{U_0}, \frac{h}{\delta}, \frac{w}{h} \right) \quad (3)$$

where D is the pressure drag and ρ is the density of the fluid. Consequently the main purpose of the present investigation is to clarify these functional relationships of equations (2) and (3) by varying the values of the above sets of three non-dimensional parameters. Only a limited range of u_τ / U_0 could be investigated.

3 Experimental Equipment and Procedure

3.1 Wind Tunnel. Measurements of pressure distribution on the surface of the plate were undertaken using a closed-circuit type of wind tunnel with a uniform test section of 0.6 m high, 0.6 m wide, and 5.4 m long. A series of four turbulence-reducing screens was installed in the settling section upstream of the contraction channel (9:1); the free-stream turbulence level in the test section was about 0.3 percent at the maximum free-stream velocity of 30 m/s, which was employed for measurement of pressure distribution. All the measurements of Strouhal number were made in another closed-circuit type of wind tunnel, which had a contraction channel (14:1); the test section had a uniform cross-section of 0.4×0.4 m and a length of 4.0 m; the free-stream turbulence level in the test section was about 0.2 percent at the free-stream velocity of 15 m/s used in these measurements.

The ceiling of the test section of each tunnel was made of a flexible sheet of stainless steel to make it shape adjustable see that the longitudinal pressure gradient was removed. Also, the test section floor of each tunnel was covered with a smooth

Nomenclature

C_D = pressure drag coefficient

$$= D / \left(\frac{1}{2} \rho U_0^2 h w \right)$$

C_{D_r} = pressure drag coefficient

$$= D / \left(\frac{1}{2} \rho u_\tau^2 h w \right)$$

C_{p_b} = pressure coefficient on downstream surface

$$= (p_b - p_0) / \left(\frac{1}{2} \rho U_0^2 \right)$$

C_{p_f} = pressure coefficient on upstream surface

$$= (p_f - p_0) / \left(\frac{1}{2} \rho U_0^2 \right)$$

C_p = pressure coefficient = $(p - p_0) /$

$$\left(\frac{1}{2} \rho U_0^2 \right)$$

D = pressure drag

$E_u'(f)$ = power spectrum of fluctuating velocity

X = longitudinal distance measured from the entrance of the test section of the tunnel

d_0 = diameter of tripping rod

f = frequency (Hz)

f_c = vortex shedding frequency

H = shape factor of boundary layer = δ^*/θ

h = height of plate

p = pressure on surface of plate

p_b = pressure on downstream surface of plate

p_f = pressure on upstream surface of plate

p_0 = static pressure of free stream

$R\theta$ = Reynolds number = $U_0 \theta / \nu$

S_t = Strouhal number

$$= f_c \cdot w / U_0$$

U_0 = velocity of free stream

u = longitudinal mean velocity component in boundary layer

u' = fluctuating velocity

u_τ = shear velocity = $(\tau_0 / \rho)^{1/2}$

w = width of plate

x, y, z = Cartesian coordinate system (see Fig. 1)

δ = thickness of boundary layer

δ^* = displacement thickness of boundary layer

θ = momentum thickness of boundary layer

τ_0 = shear stress on the plane wall

ρ = density of fluid

ν = kinematic viscosity of fluid

Table 1 Characteristics of an undisturbed turbulent boundary layer at the location of a plate

RUN	1	2	3	4	5	6	7
U_0 m/s	18	25	30	15	20	25	15
d_0 mm	5.0	1.5	0	3.5	3.5	3.5	6.0
δ mm	56.4	46.2	35.2	48.6	51.6	50.4	59.5
δ^* mm	7.71	6.49	5.42	7.58	7.94	7.61	8.15
θ mm	5.75	4.84	3.98	5.40	5.83	5.58	6.13
H	1.34	1.34	1.36	1.40	1.36	1.36	1.33
Re	6789	7601	7899	5327	8002	8925	5906
u_τ/U_0	0.0360	0.0360	0.0360	0.0371	0.0360	0.0353	0.0380

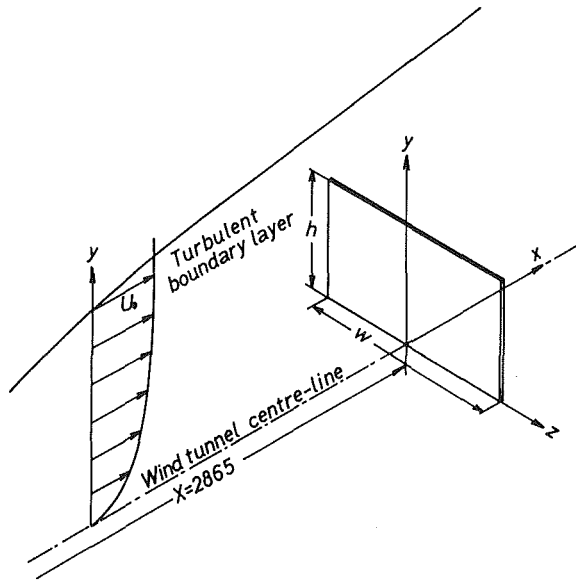


Fig. 1 Definition sketch for a test plate placed in the turbulent boundary layer

plastic plate of 10 mm in thickness in order to eliminate the effect of the roughness of the surface. The floor itself was used as the plane boundary along which a turbulent boundary layer developed.

3.2 Tests Plates. Prepared for the present experiment were several plates of finite width with a thickness of 2.5 mm. Their heights selected for measurement of pressure distribution on the plate surface were 10, 20 and 30 mm, and the aspect ratio w/h was varied in a range between 0.5 and 10.

A large number of piezometric holes 0.5 mm in diameter were drilled on the front surface of the plate, the number of holes increasing with an increase in size of the plate. It allowed to make fairly detailed measurements of pressure distribution on the surface. The plate was mounted on a disk so that it could be rotated to make possible the measurement of pressure distribution on the rear surface of the plate. Also, the heights selected for measurement of vortex shedding frequency behind the plate were 15, 20, 25, 30, 38, 48, and 58 mm, and the aspect ratio of the plate was varied in a range between 0.125 and 5.0. The square plates with various heights ($h=8\sim 80$ mm) were prepared to examine an effect of the parameter u_τ/U_0 on the drag coefficient and the Strouhal number. Figure 1 shows a definition sketch of the test plate placed in a turbulent boundary layer.

3.3 Visualizing Apparatus. A visualizing apparatus using the smoke-wire method consisted of a discharged circuit, a delay circuit, a stroboscope and a camera. A smoke wire 0.2 mm in diameter was made of Nichrome; given sufficient tension, it was fixed onto a probe made of a

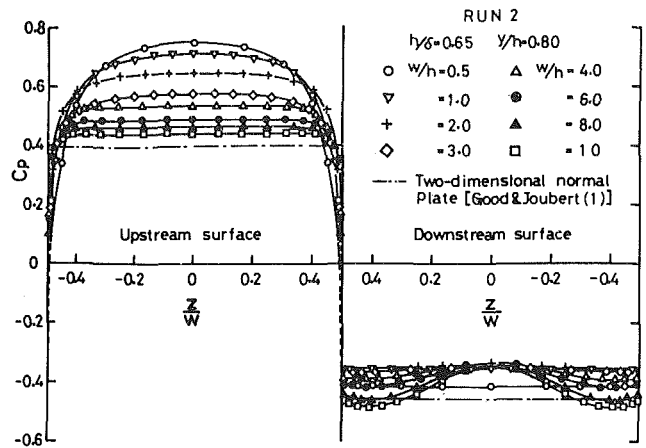


Fig. 2 Pressure distribution on the surface of a plate at relative height $y/h=0.8$. The uncertainty in the ordinate is ± 0.01 and that in the abscissa is less than ± 0.005 . Lines for visual aid only.

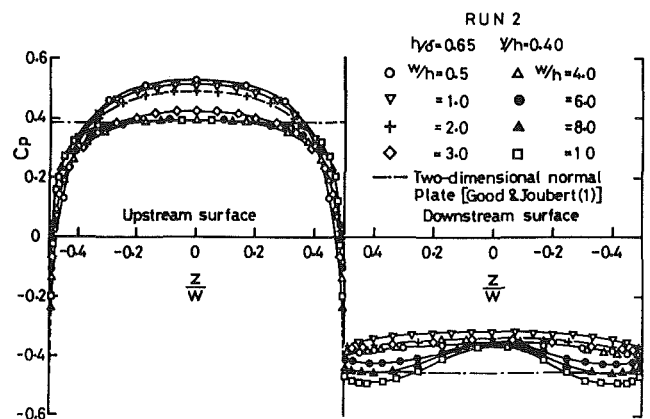


Fig. 2(b) Pressure distribution on the surface of a plate at relative height $y/h=0.4$. For further informations, see the caption of Fig. 2(a).

stainless pipe 6 mm in diameter. The oil to be smoked was a mixture of liquid paraffin and kerosene, which was painted uniformly on the Nichrome wire with a fine writing brush.

3.4 Characteristics of a Turbulent Boundary Layer. A turbulent boundary layer developing along the floor of the test section of each wind tunnel was adopted in the present investigation. The characteristics of the boundary layer were examined to ascertain that the boundary layer attained a fully developed equilibrium at the location of a test place used as a bluff body.

The mean velocity profiles of flow in the boundary layer agreed well with the experimental data of Klebanoff and Diehl [6]. Also, the mean velocity profiles of flow in the region near the wall were confirmed as following the logarithmic law suggested by Coles [5]:

$$\frac{u}{u_\tau} = 5.75 \log \left(\frac{yu_\tau}{\nu} \right) + 5.1 \quad (4)$$

The distribution of longitudinal turbulence intensity in the boundary layer at the location of the plate corresponded well with Klebanoff's data [6].

The two-dimensionality of the flow field in the test section of the two wind tunnels was examined by the measurement of velocity profiles in the direction normal to the xy -plane at various distances from the wall. The results showed that a satisfactory two-dimensionality was realized in the region about 300 mm in width including the center line in the wind tunnel with a cross-section of 0.6×0.6 m and in the region

about 150 mm in width in the wind tunnel with a cross-section of 0.4×0.4 m.

From the foregoing considerations it was concluded that the turbulent boundary layer along the floor of the test section of each wind tunnel had the same characteristics as a turbulent boundary layer in equilibrium with a zero-pressure gradient which developed fully along the smooth flat floor. The characteristics of the boundary layer at the location of the plate are summarized in Table 1.

4 Results and Discussion

4.1 Pressure Distribution on the Plate Surface. Figures 2 (a) and (b) show variations in pressure distribution for each aspect ratio w/h at the relative height $y/h = 0.8$ and 0.4 of the plate surface ($h = 30$ mm, $h/\delta = 0.65$) placed in a boundary layer shown as Run 2 in Table 1. The ordinate denotes the pressure coefficient C_D on the surface nondimensionalized by $(1/2)\rho U_0^2$; the abscissa means the location along the surface at the relative height y/h . The results of measurements of pressure distribution on the upstream surface will be examined first. The pressure distribution at the height $y/h = 0.8$ decreases gradually with an increase in w/h , and a difference in the form of pressure distribution due to a change in w/h becomes small gradually beyond the aspect ratio $w/h = 4.0$. Also, the pressure distribution on the plate surface with an increase in w/h comes closer to that of a two-dimensional normal plate [1] attached to a plane wall except in the vicinity of both sides of the plate. The pressure distribution at the height $y/h = 0.4$ on the plate surface is almost the same beyond the aspect ratio $w/h = 4.0$, and is fairly similar to that of the two-dimensional normal plate in the range of about ± 0.2 in value of z/w .

Meantime, as for the pressure distribution on the downstream surface, it is shown that the absolute value of negative pressure gradually increases with an increase in w/h except at the aspect ratio $w/h = 0.5$. Also, the values of pressure on this surface differ considerably from those of the two-dimensional normal plate because of the influence of the arch-type vortex formed in the close vicinity of the surface with an increase in w/h . The difference in the form of pressure distribution between on the plate of finite width and on the two-dimensional plate may be caused by the form of the separation vortex formed behind the plate. The flow separating from the top edge of a two-dimensional plate attaches to the plane wall downstream of the plate, thereby forming a rear separation bubble, which is fairly steady. In the plate of finite width, when the height of the plate is relatively larger than the width of the plate, the flow separating from both sides is shed periodically downstream as the Karman-type vortex street. With an increase in width of the plate, the flow separating from the top edge of the plate increases in strength; as a result, the flow separating from the top edge joins the flow separating from the sides forming and entity in the arch-type vortex and is shed behind the plate.

4.2 Pressure Force Acting on a Plate. Measurements of pressure force acting on the plate of finite width were made under the conditions shown as Runs 1, 2, and 3 in Table 1. The values of pressure drag coefficient, C_D , were obtained by means of the equation given by

$$C_D = \int_0^1 \int_{-0.5}^{0.5} (C_{pf} - C_{pb}) d\left(\frac{z}{w}\right) d\left(\frac{y}{h}\right) \quad (5)$$

where C_{pf} and C_{pb} are the pressure coefficients on the upstream and the downstream surface of the plate defined by $C_{pf} = (p_f - p_0)/1/2\rho U_0^2$ and $C_{pb} = (p_b - p_0)/1/2\rho U_0^2$, respectively. Figure 3 shows a relationship between C_D and the aspect ratio w/h , with h/δ as a parameter based on equation (2). The parameter u_τ/U_0 has a constant value for

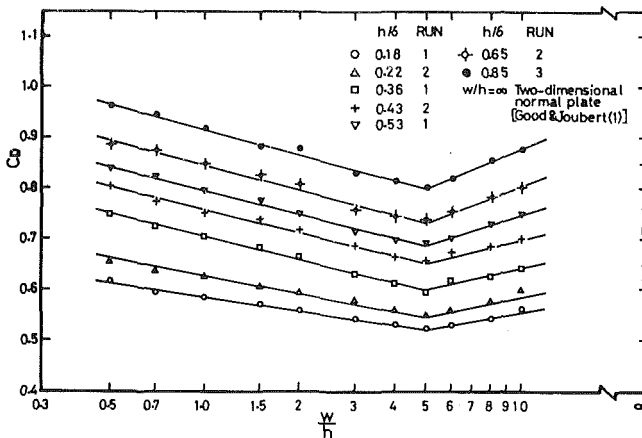


Fig. 3 Relation between C_D and w/h for a plate. The uncertainty of C_D is ± 0.02 . Lines are the best-fit line obtained by the least square averaging of the data.

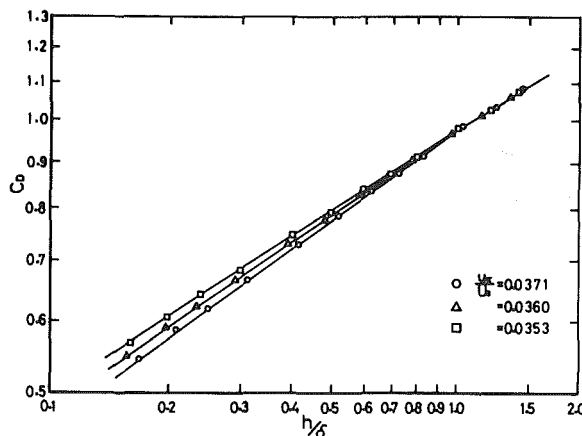


Fig. 4 Relation between C_D and h/δ for a square plate. For further informations, see the caption of Fig. 3.

all data contained in Fig. 3. As will be seen in this figure, C_D forms two groups of straight lines, each having a nodal point at about $w/h = 5.0$; i.e., C_D decreases gradually for w/h less than about 5.0, but increases again, as w/h exceeds that value. Such a recurrence of an increase in C_D when w/h exceeds 5.0 comes about from a marked decrease in pressure distribution on the downstream surface of the plate under the influence of the separation vortex formed behind the surface of the plate, because the vortex enlarges to the transverse direction of the plate and the location of the vortex approaches gradually toward the plate. Moreover, Fig. 3 shows additionally drag coefficients of a two-dimensional normal plate with $w/h = \infty$ measured by Good and Joubert [1], to which the values obtained by the present measurements gradually come closer when w/h exceeds 5.0, as seen in the figure.

As described above, it clear that, when u_τ/U_0 has a constant value, C_D of the plate of finite width depends on the two parameters, w/h and h/δ , contained in equation (2). Examined next is an effect of another remaining parameter u_τ/U_0 on C_D . Three different values of this parameter (Runs 4, 5, and 6) as shown in Table 1 were tested for the square plate, i.e., $w/h = 1$. Figure 4 shows the variation of C_D which is plotted with three values of u_τ/U_0 on a log-log scale. It can be seen in this figure that the drag coefficient C_D of the square plate is plotted on a single line representing the effect of u_τ/U_0 and fulfills the relationship of equation (2) in the range $h/\delta \leq 1.0$. In the range in which h/δ is much larger than 1.0, the drag coefficient is no longer dependent on the parameter u_τ/U_0 , but depends only on h/δ .

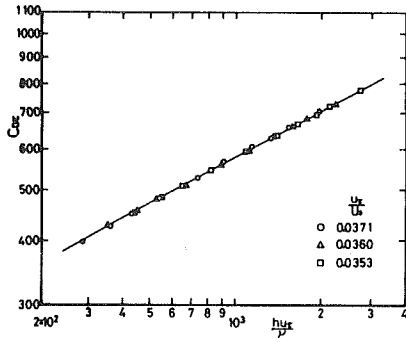


Fig. 5 Relation between $C_{D\tau}$ and hu_τ/ν for a square plate in the range of $h/\delta \leq 1.0$. The uncertainty in the ordinate is ± 0.02 and that in the abscissa is ± 0.01 . Lines are the best-fit line obtained by the least square averaging of the data.

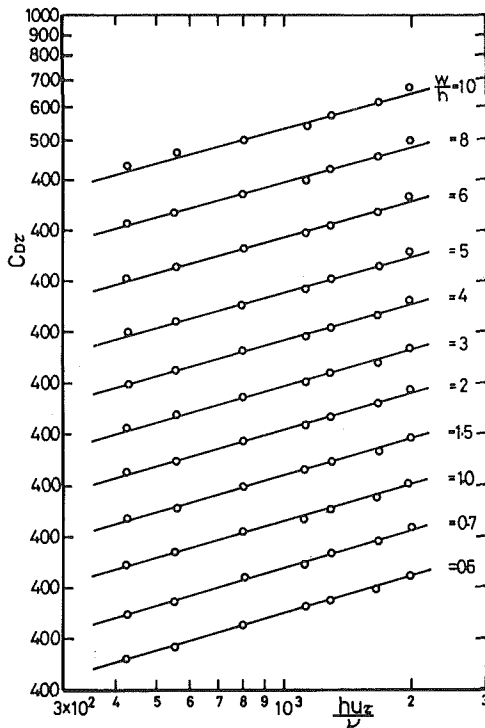


Fig. 6 Relation between $C_{D\tau}$ and hu_τ/ν against each aspect ratio of a plate. For further informations, see the caption of Fig. 5.

Next, the drag coefficient of the square plate, which is different depending on the value of u_τ/U_0 in the range $h/\delta \leq 1.0$, is plotted in Fig. 5 in a log-log scale based on the following equation (6), which was presented earlier for the drag coefficient of a two-dimensional normal plate attached to a plane wall. The drag coefficient

$$C_{D\tau} = \frac{D}{\frac{1}{2} \rho u_\tau^2 h w} = f_3 \left(\frac{hu_\tau}{\nu}, \frac{\dot{u}_\tau}{U_0} \right) \quad (6)$$

where u_τ is the shear velocity. It is clear that $C_{D\tau}$ is uniquely related to hu_τ/ν in the range $h/\delta \leq 1.0$ and can be expressed by a power function:

$$C_{D\tau} = 77.7 \left(\frac{hu_\tau}{\nu} \right)^{0.291} \quad (7)$$

This result shows that the parameter u_τ/U_0 contained in equation (6) has little influence on the drag coefficient $C_{D\tau}$ in this range.

The aerodynamic characteristics of a three-dimensional

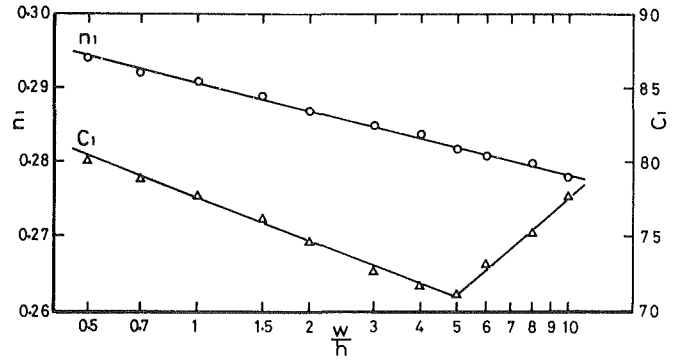


Fig. 7 Relation between coefficient C_1 and exponent n_1 and w/h

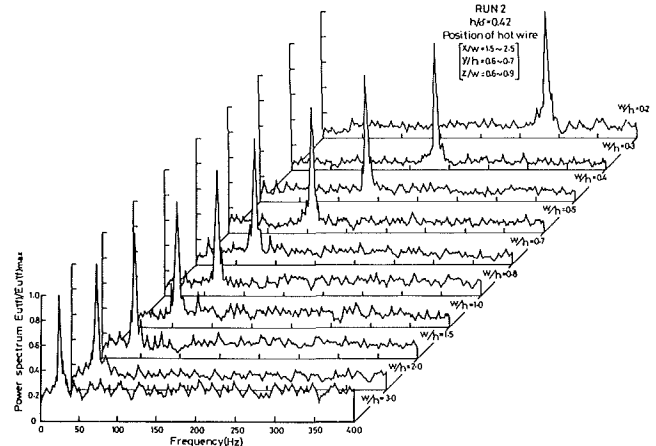


Fig. 8 An example of vortex shedding frequency and power spectrum of fluctuating velocity at downstream of a plate ($h = 25$ mm; $h/\delta = 0.42$) placed in a boundary layer shown as Run 2 in Table 1

bluff body such as a cube or a right-circular cylinder [6] immersed in a turbulent boundary layer were investigated before. It was found then that the drag coefficient $C_{D\tau}$ could be expressed by a power function using the single parameter hu_τ/ν in the range $h/\delta \leq 1.0$. Those functional relationships are written as

$$C_{D\tau} = 39.2 \left(\frac{hu_\tau}{\nu} \right)^{0.351} \quad (8)$$

$$C_{D\tau} = 44.8 \left(\frac{hu_\tau}{\nu} \right)^{0.279} \quad (9)$$

in cases of the cube and the right-circular cylinder, respectively.

From the results described above, if the drag coefficient of the plate shown in Fig. 3 is plotted in the form based on equation (6), the drag coefficient $C_{D\tau}$ will also be expressed by the function of hu_τ/ν alone for each aspect ratio w/h regardless of the values of u_τ/U_0 . Figure 6 shows the result of this examination. It is obvious that plots of $C_{D\tau}$ collapse onto a straight line with respect to hu_τ/ν in the range $h/\delta \leq 1.0$ for each aspect ratio w/h . Therefore, the drag coefficient $C_{D\tau}$ of the plate of finite width in the range $h/\delta \leq 1.0$ can empirically be expressed by a power law with the exponent n by the following equation:

$$C_{D\tau} = C_1 \left(\frac{hu_\tau}{\nu} \right)^{n_1} \quad (10)$$

where each of the coefficient C_1 and the exponent n_1 is the function of w/h alone and is given in Fig. 7.

The foregoing results show that, given the aspect ratio and the wall shear stress of an otherwise undisturbed boundary

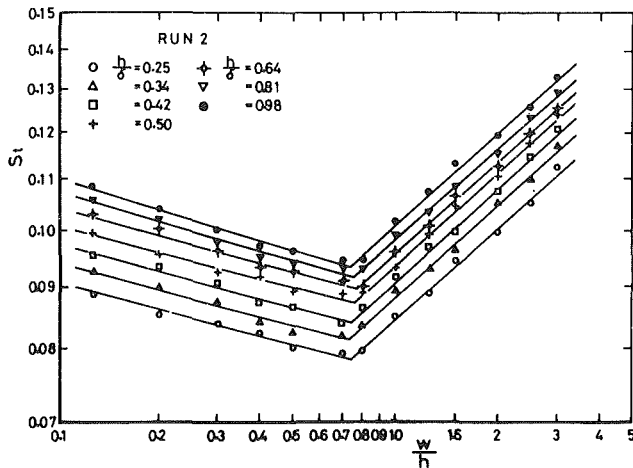


Fig. 9 Relation between the Strouhal number S_t and w/h . The parameters u_r/U_0 has a constant value for all data contained in this figure. The uncertainty of S_t is ± 0.03 . Lines are the best-fit line obtained by the least square averaging of the data.

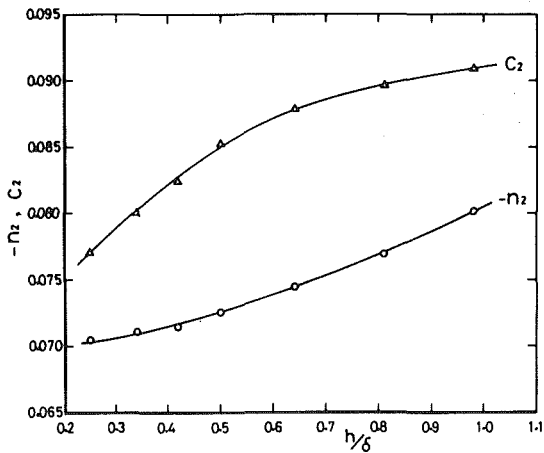


Fig. 10(a) Relation between coefficient C_2 and exponent n_2 and h/δ

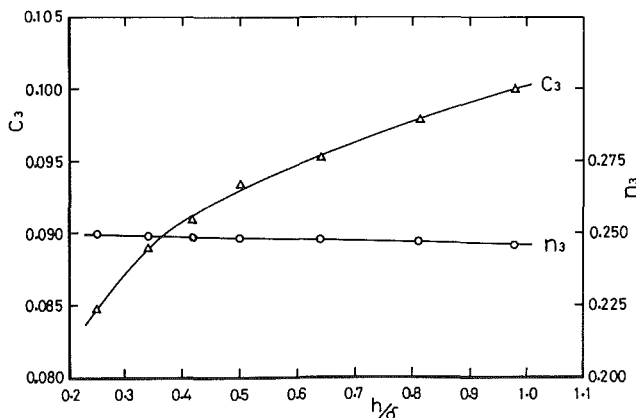


Fig. 10(b) Relation between coefficient C_3 and exponent n_3 and h/δ

layer at the location of the plate, the pressure drag can be obtained from equation (10) in the range $h/\delta \leq 1.0$.

4.3 Vortex Shedding from a Plate. It was made clear in Chapter 2 that the Strouhal number of the vortex shed behind a plate of finite width, which is almost buried in a turbulent boundary layer, is governed by three independent non-dimensional parameters u_r/U_0 , h/δ , and w/h . However, since

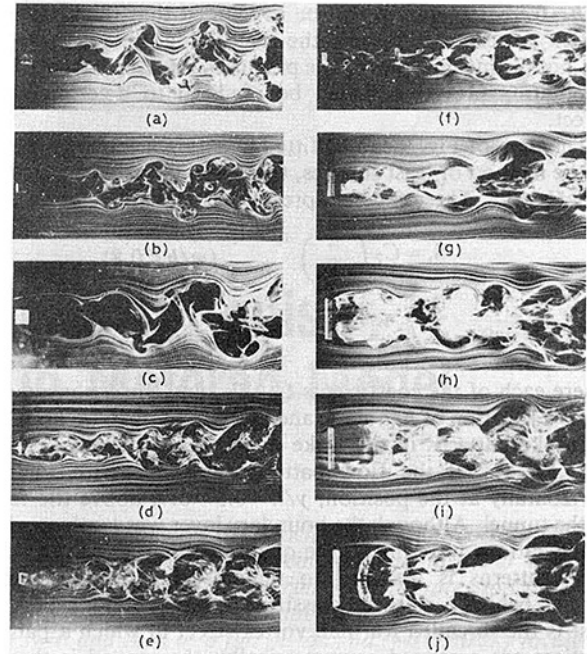


Fig. 11 The smoke patterns in the wake of a plate. The wakes vortices are the Karman type vortices in the case of (a) $w/h = 0.2$, (b) $w/h = 0.3$, (c) $w/h = 0.4$, (d) $w/h = 0.5$, and (e) $w/h = 0.7$. The wakes vortices are the arch-type vortices in the case of (f) $w/h = 0.8$, (g) $w/h = 1.0$, (h) $w/h = 1.5$, (i) $w/h = 2.0$, and (j) $w/h = 3.0$.

authors already elucidated that an effect of parameter u_r/U_0 on S_t of a three-dimensional bluff body immersed in a turbulent boundary layer is not prominent [7], this paper is devoted to looking into influences of the dimension of the plate on the Strouhal number S_t of the vortex by keeping u_r/U_0 constant and changing h/δ and w/h . Shown in Fig. 8 the power spectrum $Eu'(f)$ of the fluctuating velocity u' measured by a hot-wire probe set at a position ($x/w = 1.5 \sim 2.5$; $y/h = 0.6 \sim 0.7$; $z/w = 0.6 \sim 0.9$) behind a plate ($h = 25$ mm; $h/\delta = 0.42$) placed in a boundary layer shown as Run 7 in Table 1. In the figure the ordinate represents the value of the power spectrum $Eu'(f)$, the value being nondimensionalized using the maximum power spectrum $Eu'(f)_{\max}$, whereas the abscissa represents the frequency f (Hz). As is obvious from the figure, the prominent prevailing frequency f_c exists over the entire range in which w/h is less than 3.0; it is suggested that vortices with this prominent f_c are shed behind the plate. In a range in which w/h is larger than 3.0, however, no prominent f_c is found for the plate adopted in the present experiment. Moreover, it is shown in this figure that, with an increase in w/h , the difference between the peak spectrum at the prominent f_c and the magnitude of the spectrum at other frequencies becomes smaller gradually and, accordingly, it is then likely that the strength of the vortex shedding from the plate decreases. For w/h larger than 3.0, the power spectrum did not show any significant peak.

Shown in Fig. 9 is a relationship between the Strouhal number S_t and the aspect ratio w/h of a plate with h/δ as a parameter based on equation (3). The parameter u_r/U_0 has a constant value for all data contained in Fig. 9. It is seen that S_t varies both with h/δ and with w/h . A significant change in slope of the curves occurs near $w/h \approx 0.8$. It results from a change of the vortex pattern of the eddies shed by plate, as will become apparent from the flow visualization results to be discussed below. Surprisingly, this change in vortex pattern is not reflected in the drag coefficient, no change in the trend of the C_D curves can be recognized in Fig. 5 at a value of

$w/h=0.8$. It therefore can be concluded that the change in vortex pattern affects only the fluctuating pressure pattern, but not the mean values of the pressures. Measurements of the fluctuating pressures would be required to determine this effect.

The data of Fig. 9 can be fitted by straight lines, by means of the method of least squares, that have a kink in the vicinity of $w/h=0.8$. These can be expressed through the relations.

$$S_t = C_2 \left(\frac{w}{h} \right)^{n_2} \quad (w/h \leq 0.8)$$

$$S_t = C_3 \left(\frac{w}{h} \right)^{n_3} \quad (0.8 \leq w/h \leq 3.0) \quad (11)$$

where each of the coefficients C_2 , C_3 , and the exponents n_2 , n_3 , is a function of h/δ alone and given in Figs. 10 (a) and (b).

Smoke patterns in the wake of the plate are presented in Fig. 11. In all the flow patterns, a smoke-wire was set horizontally at the position, $y/h=0.5\sim 0.7$, above the floor of the tunnel. Although the boundary layer was laminar when visualizations were made, the qualitative nature of the wake flow patterns is assumed to remain unchanged. Vortices formed behind a plate are classified into two major types: the first is the so-called Karman vortex street in which a pair of vortices are arranged asymmetrically; the second is the so-called arch-type vortex in which a pair of vortices are arranged symmetrically [8], [9]. As is obvious from the figure for plates of w/h larger than about 0.8, the wake vortices are the second type and those for w/h less than it are the first type. This change of vortex patterns is reflected by a change in Strouhal number in the vicinity of $w/h=0.8$ (see Fig. 9).

The probable reason why this change takes place is that, when the height of a plate is relatively larger than the width of the plate, the strength of flow after separation from both sides is so much larger than that of flow from the top that the wake behind the plate is almost fully controlled by the flow from the sides. Consequently, the flow from the sides forms the Karman-type vortex street. With an increase in width of the plate relative to the height, the flow from the top increases in strength and joins the flow from the sides. As a result, they form in the arch-type vortex that is shed behind the plate.

Moreover, when the vortices are the second type, the width of the wake is much smaller than in case of the first type. Accordingly, it is conjectured that the velocity fluctuation caused by the shedding of the second type becomes smaller than that in the first type. Consequently, when vortices change from the first type to the second type, then the level of fluctuating velocity caused by the vortex shedding approaches the level of other irregular fluctuating velocities; thus the prominent prevailing frequencies are no longer detectable when w/h exceeds about 3.0.

5 Conclusions

The present paper has dealt experimentally with the

pressure drag acting on and the vortex shedding from a normal plate of finite width, which is attached to a plane wall, in a developing turbulent boundary layer. The main results of this study may be summarized as follows:

(1) The pressure drag coefficient C_D of a plate forms two groups of straight lines each with a nodal point at about 5.0 in value of the aspect ratio w/h ; i.e., C_D decreases gradually with an increase in w/h for w/h less than about 5.0 and increases again as exceeds it.

(2) The C_D of the plate defined by $C_{D\tau} = D/(1/2\rho u_\tau^2 hw)$ can be expressed by a power function using the single parameter hu_τ/ν for each value of w/h in the range $h/\delta \leq 1.0$.

(3) Two types of vortices, Karman-type and arch-type, are formed behind the plate, depending on the range of w/h . The former appears for w/h less than about 0.8, whereas the latter appears for w/h greater than it.

(4) The Strouhal number S_t decreases gradually with an increase in w/h for w/h less than about 0.8 and increases again as w/h exceeds it. This change in Strouhal number is reflected by the change of the wake vortices in the vicinity of $w/h=0.8$.

(5) Empirical equations obtained give estimates of pressure drag coefficient and Strouhal number in terms of the aspect ratio of the plate and the parameters characterizing the boundary layer.

Acknowledgments

The authors express their sincere thanks to Mr. M. Moriya and Mr. Y. Obata, Department of Mechanical Engineering, Kitami Institute of Technology, for their assistance in the construction of the experimental apparatus.

References

- 1 Good, M. C., and Joubert, P. N., "The Form Drag of Two-Dimensional Bluff Plates Immersed in Turbulent Boundary Layers," *Journal of Fluid Mechanics*, Vol. 31, Part 3, 1968, pp. 547-582.
- 2 Sakamoto, H., Moriya, M., and Arie, M., "A Study of the Flow around Bluff Bodies Immersed in Turbulent Boundary Layers (Part 1)," *Bulletin of the JSME*, Vol. 18, No. 124, 1975, pp. 1126-1133.
- 3 Raju, R. K. G., Loeser, J., and Plate, E. J., "Velocity Profiles and Fence Drag for a Turbulent Boundary Layer along Smooth and Rough Flat Plates," *Journal of Fluid Mechanics*, Vol. 76, Part 2, 1976, pp. 383-399.
- 4 Plate, E. J., "The Drag on a Smooth Flat Plate with a Fence Immersed in Its Turbulent Boundary Layer," ASME Paper No. 65-FE-17, 1964.
- 5 Coles, D., "The Law of the Wake in the Turbulent Boundary Layer," *Journal of Fluid Mechanics*, Vol. 1, 1956, pp. 191-226.
- 6 Sakamoto, H., Moriya, M., Taniguchi, S., and Arie, M., "The Form Drag of Three-Dimensional Bluff Bodies Immersed in Turbulent Boundary Layer," ASME JOURNAL OF FLUIDS ENGINEERING, Vol. 104, No. 3, 1982, pp. 326-334.
- 7 Sakamoto, H., and Arie, M., "Vortex Shedding from a Rectangular Prism and a Circular Cylinder Placed Vertically in a Turbulent Boundary Layer," *Journal of Fluid Mechanics*, Vol. 126, 1983, pp. 147-165.
- 8 Mochizuki, M., "Smoke Observations on Boundary Layer Transition Caused by a Spherical Roughness Element," *J. Phys. Soc. Japan*, Vol. 16, No. 5, 1961, pp. 995-1008.
- 9 Okamoto, T., Yagita, M., and Kataoka, S., "Flow Past Cone on Flat Plate," *Bulletin of the JSME*, Vol. 20, No. 141, 1977, pp. 329-336.

Squish and Swirl-Squish Interaction in Motored Model Engines

C. Arcoumanis

A. F. Bicen

J. H. Whitelaw

Department of Mechanical Engineering,
Imperial College of Science and
Technology,
London, England

Measurements of the three components of velocity and their corresponding fluctuations have been obtained by laser-Doppler anemometry mainly near TDC of compression in a model IC engine motored at 200 rpm with compression ratio of 6.7. The flow configurations comprised an axisymmetric cylinder head with and without upstream induced swirl and each of a flat piston and two centrally located, cylindrical and re-entrant, bowl-in-piston arrangements.

In the absence of swirl and squish, the intake-generated mean motion and turbulence decayed considerably by the end of compression. The two piston-bowl configurations, however, resulted in a compression-induced squish motion with consequent formation of a toroidal vortex occupying the whole bowl space. Interaction of swirl, carried from intake and persisting through compression, with squish generated near TDC profoundly altered the axial flow structure. In the case of the cylindrical bowl, the sense of the vortex was reversed by swirl and, in the re-entrant bowl, increased the number of vortices to two. The swirling motion inside the cylindrical bowl was close to solid body rotation while the re-entrant bowl gave rise to more complex flow patterns. Squish, in the presence or absence of swirl, did not augment the turbulent energy inside the cylindrical bowl contrary to the re-entrant configuration where turbulence generation was observed.

1 Introduction

There is evidence, for example in references [1-3], that swirl and squish influence the performance of Diesel and spark ignition engines and a number of experimental investigations such as those of references [1-8] have focused on the complex air flow field which exists prior to ignition. Swirl is generated in the intake stroke as a result of the inlet port shape and orientation and persists through to top-dead-centre (TDC) of compression developing into a mean flow pattern which approximates solid-body rotation. At the same time, the radial velocity component increases as the air is compressed between the piston and cylinder head and gives rise to a jet which issues radially into the piston bowl near TDC of compression. The interaction between swirl and squish and the resulting flow pattern inside the piston-bowl is not well understood and it is the purpose of this paper to improve this understanding by providing measurements of the three velocity components and the corresponding normal stresses in a motored model engine. The measurements are provided in sufficient detail so as to aid the appraisal and development of calculation methods such as that described in references [9 and 10].

The present measurements were obtained in a perspex piston-cylinder assembly which allowed the use of laser-

Doppler anemometry with collection of forward-scattered light. The engine rotational speed was 200 rpm, the compression ratio 6.7 and the piston-head configurations included a flat piston and a cylindrical bowl with and without a rectangular-sectioned lip. The two piston-bowl configurations were selected as idealised representations of the open and re-entrant combustion chambers widely used in Diesel engines.

An extensive background of investigations of intake generated flows obtained with open valves in the absence of compression is described in references [11 and 12]; related experimental studies in four-stroke model engines are also reported in references [13-16]. The ability of present calculation methods to predict the in-cylinder flows in model engines is demonstrated in references [17-20].

The flow configurations and instrumentation are described briefly in the following section which also considers the precision of the measurements. The results are presented and discussed in Section 3 and Section 4 provides a summary of the more important conclusions.

2 Experimental System

Line diagrams of the optical-signal processing arrangement and the piston-cylinder assembly are shown in Fig. 1. A brief description of the model engine is given in subsection 2.1 followed by discussion of the optical and signal processing arrangements in subsection 2.2 and experimental precision in

Contributed by the Fluids Engineering Division for publication in the JOURNAL OF FLUIDS ENGINEERING. Manuscript received by the Fluids Engineering Division, March 4, 1982.

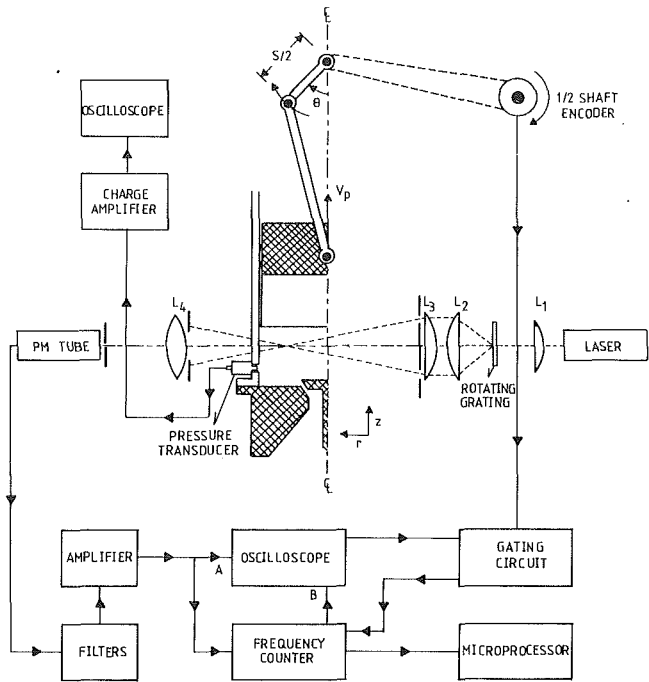


Fig. 1 Line diagram of optical-signal processing arrangement and piston-cylinder assembly

Table 1
Geometric characteristics of the model engine

Bore	75.4 mm
Stroke (S)	94.0 mm
Compression ratio (CR)	6.7
Intake-exhaust valve:	
Diameter (D)	34.0 mm
Maximum lift (L)	8.0 mm
Dimensionless lift (L/D)	0.24
Seat angle (SA)	60°
Flat piston configuration	
Diameter	75.0 mm
Clearance	16.5 mm
Cylindrical bowl configuration	
Diameter	47.0 mm
Depth	41.0 mm
Bumping clearance	0.6 mm
Re-entrant bowl configuration	
Diameter	47.0 mm
Depth	40.0 mm
Entry diameter	23.0 mm
Bumping clearance	0.6 mm

Table 2
Principal characteristics of the Laser-Doppler Anemometer

Half-angle of intersecting beams	6.4°
Fringe spacing	2.8 μm
Diameter of intersection region at the	
$1/e^2$ intensity location	58 μm
Length of intersection region at the	
$1/e^2$ intensity location	520 μm
Number of stationary fringes	21
Frequency shift	1.83 MHz

2.3. More details about the experimental system are given in references [14–16].

2.1 Flow Configuration. The three piston configurations used with the model engine were fabricated from plexiglass to provide optical access and were reciprocated, via a motor and crank, in a plexiglass cylinder. An axisymmetric cam-operated single valve with 60 deg seat angle and dimensionless lift of 0.24 was used to intake and exhaust air seeded with silicone oil to increase the rate of Doppler signals. Swirl was induced, when required, by means of 30° vanes incorporated into the inlet port and upstream of the valve. The geometric characteristics of the piston-cylinder assembly are summarized in Table 1.

2.2 Optical and Signal Processing Arrangements. The principal characteristics of the optical arrangement are summarized in Table 2.

The Doppler signals from the photomultiplier were band-pass filtered to remove low frequency pedestal and high frequency electronic noise, amplified and transmitted to a frequency counter through a gating circuit which opened and closed after a pre-set number of pulses were received from an optical shaft encoder; the encoder was geared down 2 to 1 to distinguish between the four strokes of the engine cycle.

The binary-coded-decimal frequency output from the counter was interfaced to a microprocessor which was controlled by a machine language code. A data reduction programme performed wide band filtering by accepting frequency values within three standard deviations; the percentage of rejected frequencies, corresponding to erroneous (noise-induced) measurements, was less than 1 percent. For each crank angle window, sample sizes in the range of 400–1500 were obtained depending on the cycle and the location inside the piston-bowl and cylinder, to provide ensemble-averaged mean and rms velocities.

2.3 Precision. The possible sources of experimental uncertainty have been discussed in detail and quantified for a non-compressing model engine in references [11 and 12] and

for the four-stroke engine in references [14 and 16]. In the present study the maximum uncertainties in mean and rms velocities were estimated to be less than 5 and 10 percent, respectively. Due to changes in the optical path of the laser beams and the intersection half-angle from refractions at the curved boundaries of the piston-bowl configurations and cylinder, appropriate corrections have been made to the measurement locations and velocity values according to the procedure of reference [21].

3 Results

The results for the axial, swirl and radial components of velocity at selective crank angles (θ) are presented in radial and axial profile forms; they are a representative sample of measurements chosen to show the more important flow phenomena mainly during late-compression. All mean velocities (\bar{U} , \bar{V} , \bar{W}) and their corresponding rms values (\bar{u} , \bar{v} , \bar{w}) shown in Figs. 2–11 are normalized by the mean piston speed, $\bar{V}_p = 0.627 \text{ ms}^{-1}$. In most figures, the outline of the cylinder and piston configuration is shown together with the piston position and the normalized instantaneous piston speed (V_p/\bar{V}_p) corresponding to the crank angle under consideration. The Reynolds number based on the maximum piston speed, cylinder bore and atmospheric density was calculated to be 5.2×10^3 .

3.1 Flat Piston. Figure 2 shows the mean and rms axial profiles at two crank angles late in the compression stroke obtained with the flat piston and without intake swirl. The use of a flat piston provides information on the “squish free” flow patterns which, in the absence of swirl, depend entirely on the inlet boundary conditions. As shown in Fig. 2, no flow structure is evident near TDC, either persisting from intake or generated during compression, and the associated turbulence levels have been significantly reduced, to 0.5–0.6 \bar{V}_p from those observed during intake and reported in references [15 and 16].

The addition of swirl, as shown in Fig. 3, results in higher axial velocities near the axis, which may be attributed to the radial pressure gradient associated with the swirl field.

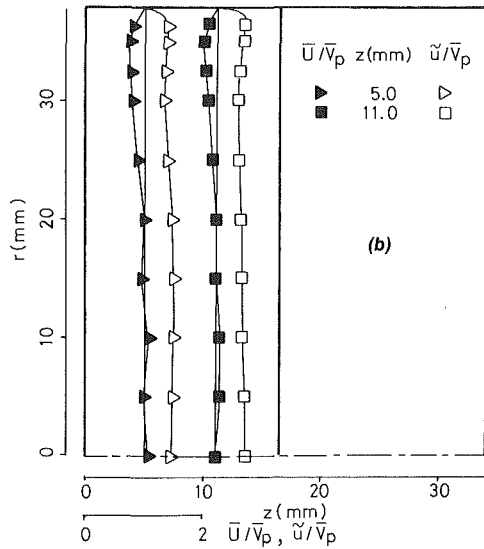
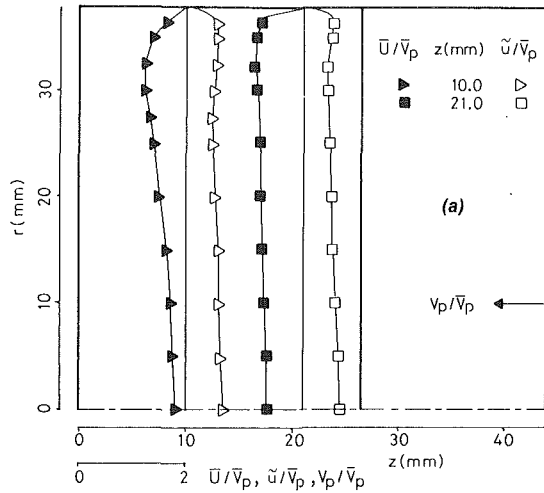


Fig. 2 Axial mean and rms velocity profiles.
 Fig. 2(a) $\theta = 324$ deg,
 Fig. 2(b) $\theta = 360$ deg.
 No swirl.

Turbulence, however, is not affected and remains almost homogeneous. Near the wall, the profile suggests a very weak vortex isolated in the corner region probably persisting from intake. The swirling motion resembles solid body rotation and corresponds to a swirl ratio of about 2; the definition of swirl ratio is given in Appendix I.

3.2 Cylindrical Bowl. Early in the intake stroke at 36 deg and without swirl, Fig. 4(a), a vortical flow structure exists inside the piston bowl as a consequence of the combined effect of jet trajectory and bowl geometry. Maximum axial mean velocities of the order of $g \bar{V}_p$ were measured close to the bowl periphery with associated turbulence levels of 3 to 4 \bar{V}_p . The vortex is no longer apparent at 324° according to Fig. 4(b), which is consistent with the findings of references [14–16]; there is, however, some indication of compression-induced squish initiation near the bowl entry plane. By TDC of compression, a squish-induced toroidal vortex is observed to occupy the whole bowl space, as shown in Fig. 5 and depicted in schematic form in Fig. 12(a); the diagrams of Fig. 12 were derived from the corresponding axial and radial mean velocity profiles. Intake-generated turbulence decays to levels comparable to those obtained with the flat piston and becomes near-homogeneous and isotropic, indicating the insignificant

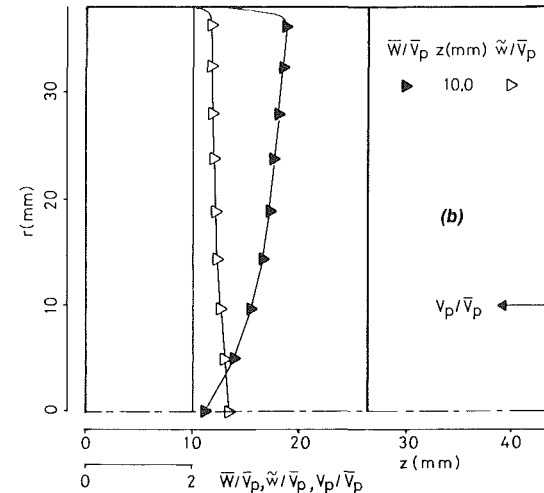
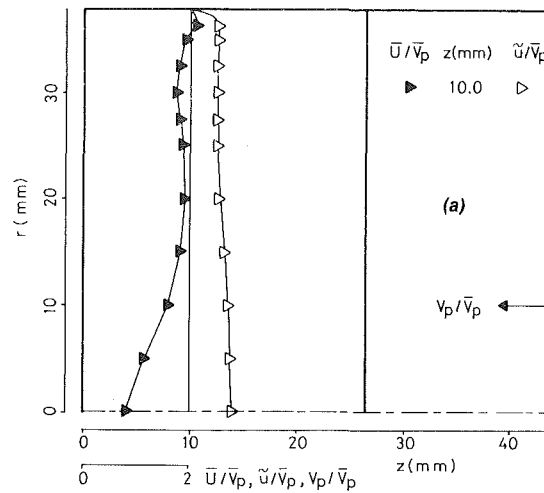


Fig. 3 Mean and rms velocity profiles at $\theta = 324$ deg.
 Fig. 3(a) Axial,
 Fig. 3(b) Swirl velocities.

effect of squish on overall turbulence in the case of the cylindrical bowl.

The effect of swirl was investigated in reference [15] and was found to affect the overall mean motion but to modify the flow structure in the axial planes only slightly. Late in the compression stroke, however, the interaction of swirl with squish has a significant effect on the axial flow patterns and results in a counter-rotating vortex (Figs. 6 and 12(c)) in contrast to the no swirl case. The mechanism responsible for this is based on the counter-acting fields of centrifugal forces, associated with swirl, and squish; the balance between the two determines the extent of the inward penetrating jet which, in this case, is confined to the bowl periphery with consequent formation of the vortex. Different levels of intake swirl may be expected, therefore, to result in different flow structures as indicated by the calculations of reference [9]. The presence of swirl, according to Fig. 7, does not have a strong influence on the turbulence levels inside the bowl, with the higher levels near the axis probably attributed to precession of the swirl center. It can be argued that, in case the precession is out of phase with the engine cycle, the observed increase of turbulence levels near the axis is rather due to overestimation of the ensemble-averaged rms values than to "true" turbulence. The swirling motion at the end of compression stroke, as shown also in Fig. 7(b), resembles solid body rotation especially near the cylinder axis and corresponds to a higher swirl ratio of about 4, compared to that obtained with the flat piston.

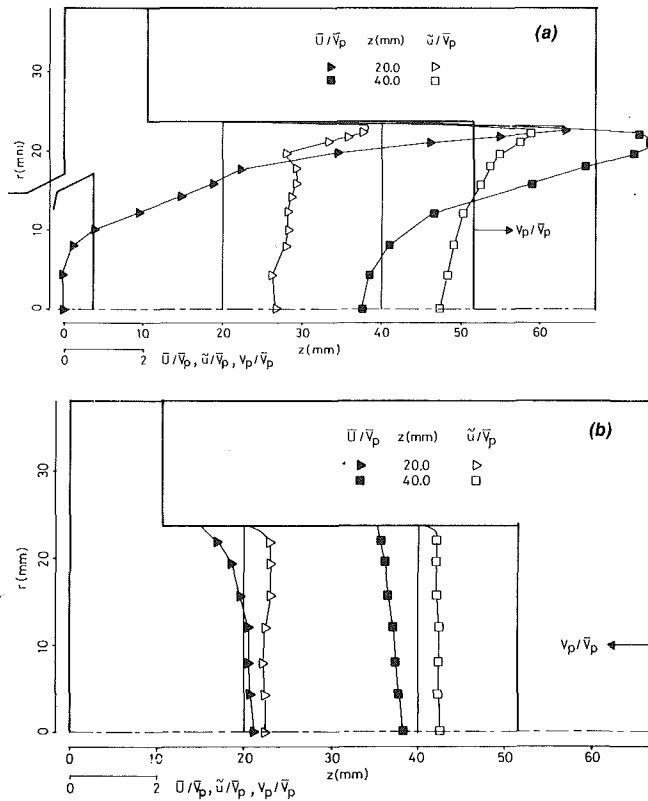


Fig. 4 Axial mean and rms velocity profiles.
 Fig. 4(a) $\theta = 36$ deg,
 Fig. 4(b) $\theta = 324$ deg.
 No swirl.

3.3 Re-Entrant Bowl. Figure 8(a) shows that at 36 deg, and in the absence of induction swirl, the fluid inside the bowl follows the piston motion contrary to the cylindrical bowl case where a vortex prevailed due to jet penetration into the bowl. Toward the end of the compression stroke, however, compression-induced velocity gradients inside the bowl result in increased turbulence levels of similar magnitude to those measured early in the intake stroke with both flat and cylindrical-bowl pistons. At TDC, according to Figs. 9 and 12(b), a flow structure similar to that in the cylindrical bowl is evident but with a stronger vortex occupying the whole bowl space due to the enhanced squish effect.

As Figs. 10 and 12(d) indicate, the swirl-squish interaction generates at TDC a system of two counter-rotating toroidal vortices inside the bowl. The flow moves towards the lower corners of the bowl and then splits either upwards over the sides or inwards over the base. Similar conclusions have been derived from the measurements of reference [7] and calculations of reference [9]. The presence of swirl results in more homogeneous turbulence than that of the no-swirl case but of similar magnitude. The swirling motion in the tangential plane, near the base of the bowl at TDC, resembles solid body rotation with deviations of a spiralling nature at the bowl entry plane, evolving from sink-type flow at 324 deg as suggested by Fig. 11(a). Calculations of the swirl ratio, based on the two mean swirl profiles of Fig. 11(b), resulted in higher local swirl ratios near the bowl entry and an average swirl ratio of about 5, which is higher than in both previous cases of flat piston and cylindrical bowl.

If we assume that the total angular momentum induced during intake is the same for the three piston configurations and the residual effects, if any, are ignored, the angular momentum at TDC of compression should provide an in-

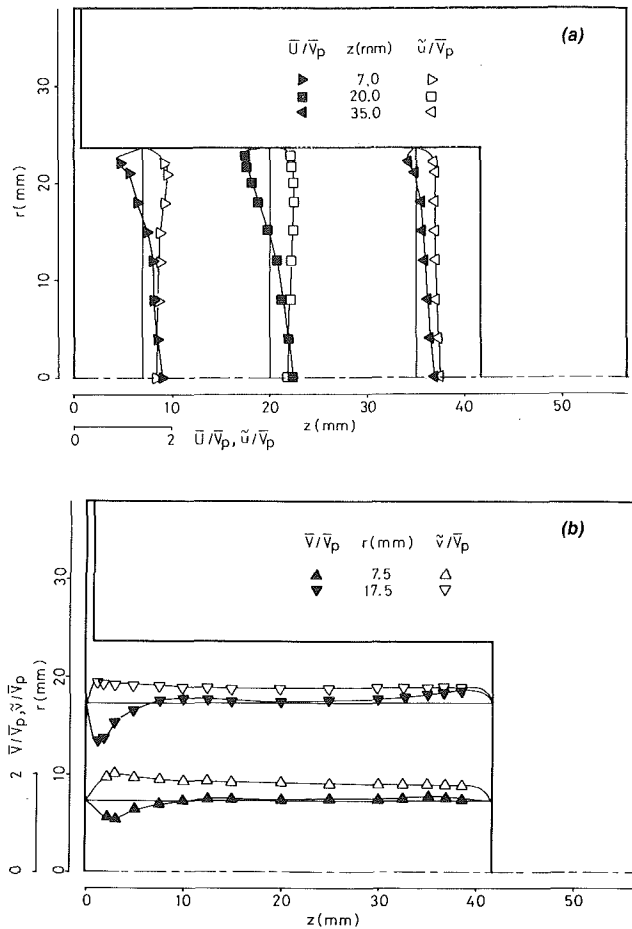


Fig. 5 Mean and rms velocity profiles at $\theta = 360$ deg.
 Fig. 5(a) Axial,
 Fig. 5(b) Radial velocities.
 No swirl.

dication of the effect of piston geometry on the swirling motion. Comparison of the angular momenta at TDC, defined according to Appendix II, showed that there is a significant loss in angular momentum in the piston-bowl cases relative to the flat piston. The calculated loss, which is about 25 percent, is mainly attributed to the increase in the surface area over which the wall shear stress acts. The average angular momenta in the two piston-bowl configurations were almost equal, within experimental and integration procedure accuracy, contrary to the swirl ratios which were not equal, as mentioned previously. This points out the relatively greater effect of piston geometry on the swirl profile inside the bowl, rather than on the total angular momentum, which is more closely associated with the intake swirl levels.

4 Concluding Remarks

The main findings of the investigation of the in-cylinder flow with a flat piston, and of squish and swirl-squish interaction inside two different bowl-in-piston configurations with one intake swirl level are summarized as follows:

1 With the flat piston, the present and previous results showed that the mean motions decayed to an insignificant level in the absence of swirl while the intake-generated turbulence initially decayed and later attained near-homogeneous levels of 0.5–0.6 \bar{V}_p . The intake-induced swirl developed into near solid body rotation augmenting the mean motions during compression but with no significant effect on overall turbulence.

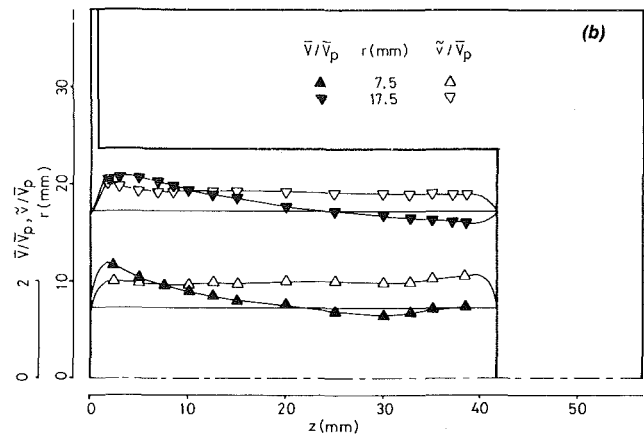
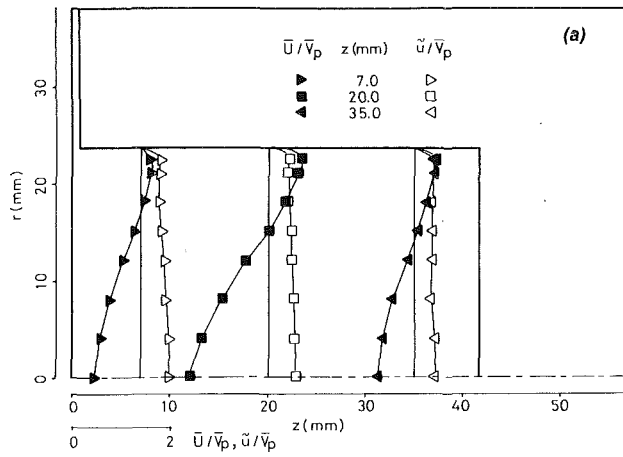


Fig. 6 Mean and rms velocity profiles at $\theta = 360$ deg.

Fig. 6(a) Axial,
Fig. 6(b) Radial velocities.
With swirl.

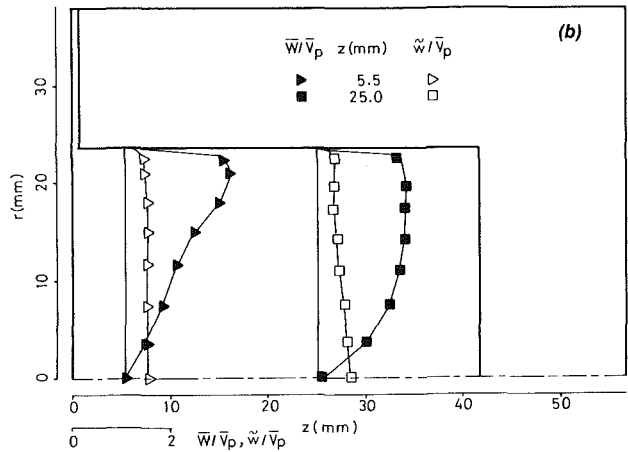
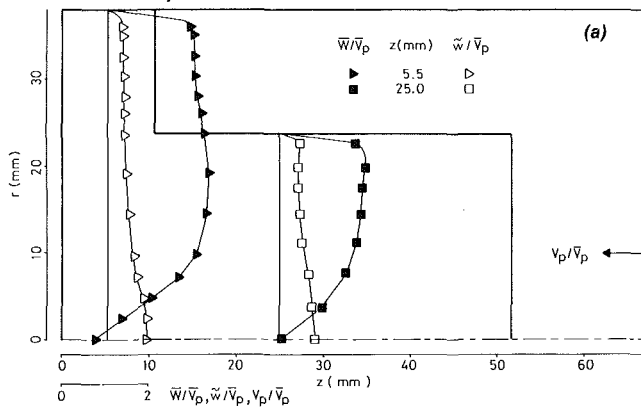


Fig. 7 Swirl mean and rms velocity profiles.

Fig. 7(a) $\theta = 324$ deg,
Fig. 7(b) $\theta = 360$ deg.

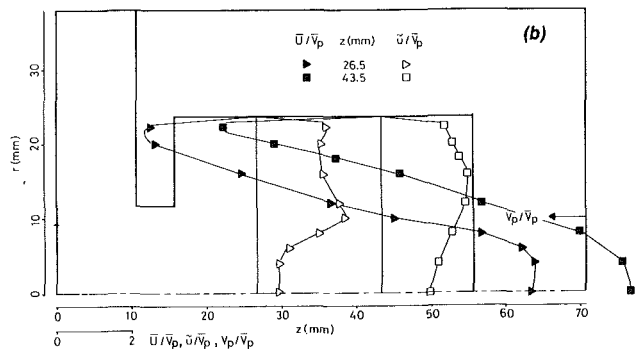
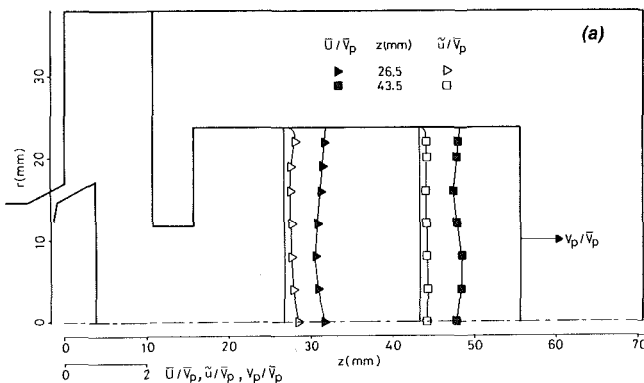


Fig. 8 Axial mean and rms velocity profiles.

Fig. 8(a) $\theta = 36$ deg,
Fig. 8(b) $\theta = 324$ deg.
No swirl.

2 For the case of the cylindrical piston-bowl and in the absence of swirl, a squish-induced toroidal vortex occupied the whole bowl space at TDC of compression. Interaction of swirl with compression-induced squish, however, resulted in the formation of a counter-rotating vortex in the axial plane in addition to the near solid body rotation of the fluid in the tangential plane. The squish, in the presence or absence of

swirl, did not alter the overall turbulence levels which remained comparable to those obtained with the flat piston.

3 In the absence of swirl and with the re-entrant bowl configuration, the squish induced a similar axial flow structure to that in the cylindrical bowl but of stronger nature. The addition of swirl, however, resulted in the formation of two vortices rotating in opposite directions. The swirling

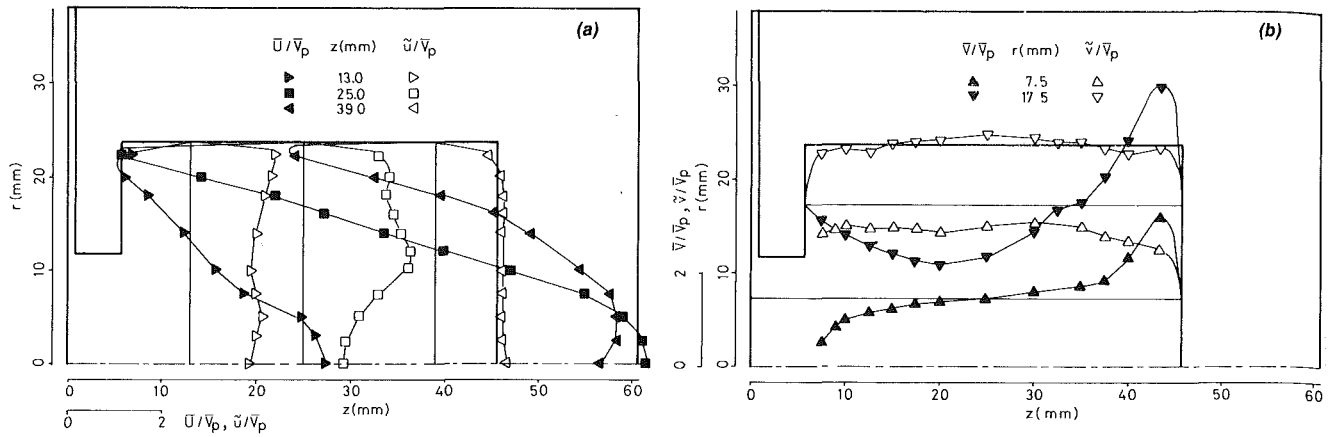


Fig. 9 Mean and rms velocity profiles at $\theta = 360$ deg.
 Fig. 9(a) Axial,
 Fig. 9(b) Radial velocities.
 No swirl.

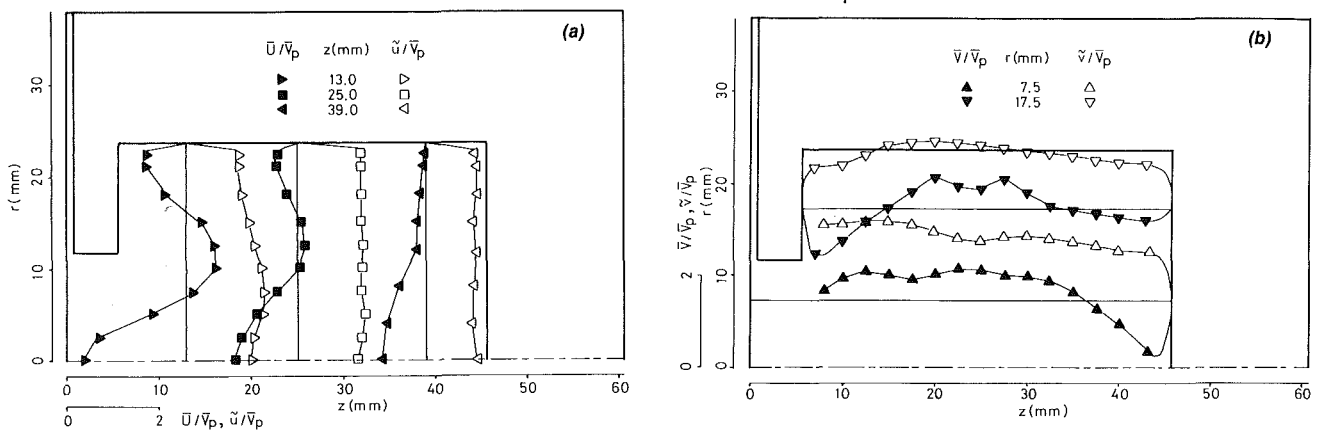


Fig. 10 Mean and rms velocity profiles at $\theta = 360$ deg.
 Fig. 10(a) Axial,
 Fig. 10(b) Radial velocities.
 With swirl.

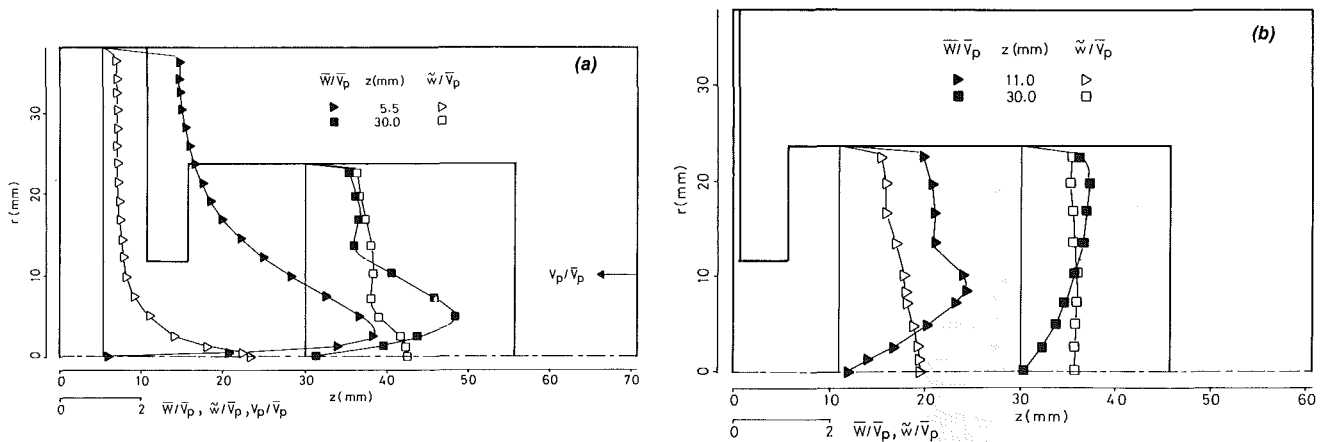


Fig. 11 Swirl mean and rms velocity profiles.
 Fig. 11(a) $\theta = 324$ deg,
 Fig. 11(b) $\theta = 360$ deg.

motion exhibited spiralling characteristics at the entry plane of the bowl and solid body type of rotation near the bowl base. Turbulence inside the bowl increased considerably, independent of swirl, to levels comparable to those generated early in the intake stroke.

4 The swirl profile at TDC of compression depended more on piston-bowl geometry rather than on the intake swirl field

which was better reflected on the final angular momentum of the bowl contents.

5 Squish and swirl have been shown to be important contributors to the mean motion rather than to overall turbulence prior to combustion, with the exception of the re-entrant bowl configuration which also resulted in significant turbulence generation.

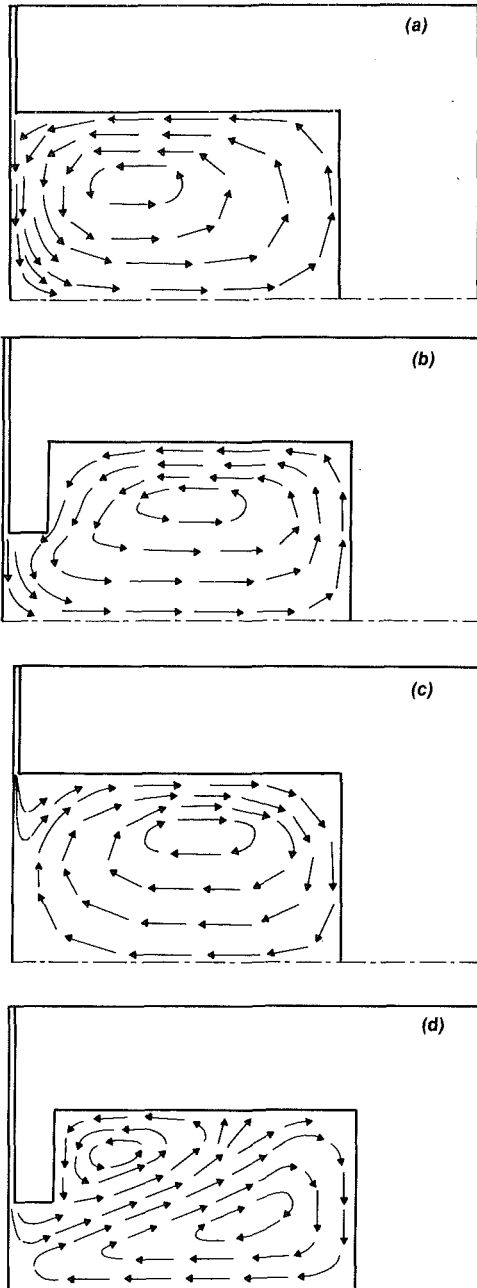


Fig. 12 Schematic diagrams of air flow in piston bowls at $\theta = 360$ deg.
 Fig. 12(a) No swirl,
 Fig. 12(b) No swirl,
 Fig. 12(c) With swirl,
 Fig. 12(d) With swirl.

Acknowledgments

The authors are glad to acknowledge the financial support provided by the U.S. Department of Energy, the U.S. Army Research Office and the Atomic Energy Research Establishment (A.E.R.E.), Harwell. They would also like to express their appreciation to Mr. N. Frost for the construction of the engine components.

References

- 1 Brandl, F., Reverencic, I., Cartellieri, W., and Dent, J. C., "Turbulent Air Flow in the Combustion Bowl of a D. I. Diesel Engine and its Effect on Engine Performance," SAE paper 790040, 1979.
- 2 Nagayama, I., Araki, Y., and Iioka, Y., "Effects of Swirl and Squish on SI Engine Combustion and Emission," SAE paper 770217, 1977.

- 3 Wigley, G., Patterson, A. C., and Renshaw, J., "Swirl Velocity Measurements in a Firing Production Diesel Engine by Laser Anemometry," *Proc. Symposium on Fluid Mechanics of Combustion Systems*, ASME, Colorado, 1981.
- 4 Alcock, J. F., "Air Swirl in Oil Engines," *Proc. I. Mech. E.*, Vol. 128, 1934, p. 123.
- 5 Fitzgeorge, D., and Allison, J. L., "Air Swirl in a Road-Vehicle Diesel Engine," *Proc. I. Mech. E. (A.D.)*, No. 4, 1962-1963, p. 151.
- 6 Witze, P. O., "Hot-Wire Turbulence Measurements in a Motored Internal Combustion Engine," Sandia Laboratories, Livermore, Calif. Report SAND 75-8641, 1975.
- 7 Williams, T. J., and Tindal, M. J., "Gas Flow Studies in Direct Injection Diesel Engines with Re-Entrant Combustion Chambers," SAE paper 800027, 1980.
- 8 Morse, A. P., and Whitelaw, J. H., "Measurements of the In-Cylinder Flow of a Motored Four-Stroke Reciprocating Engine," *Proc. Roy. Soc.*, Vol. A377, 1981, p. 309.
- 9 Gosman, A. D., and Johns, R. I. R., "Development of a Predictive Tool for In-Cylinder Gas Motion in Engines," SAE paper 780315, 1978.
- 10 Gosman, A. D., and Johns, R. I. R., "Computer Analysis of Fuel-Air Mixing in Direct-Injection Engines," SAE paper 800091, 1980.
- 11 Morse, A. P., Whitelaw, J. H., and Yianneskis, M., "Turbulent Flow Measurements by Laser-Doppler Anemometry in Motored Piston-Cylinder Assemblies," *ASME JOURNAL OF FLUIDS ENGINEERING*, Vol. 101, 1979, p. 208.
- 12 Arcoumanis, C., Bicen, A. F., Vlachos, N. S., and Whitelaw, J. H., "Effects of Flow and Geometry Boundary Conditions on Fluid Motion in a Motored IC Model Engine," *Proc. I. Mech. E.*, Vol. 198, No. 4, 1982, p. 1.
- 13 Gany, A., Larrea, J. J., and Sirignano, W. A., "Laser-Doppler Velocimetry Measurements in a Motored IC Engine Simulator," AIAA Preprint 80-0079, 1980.
- 14 Arcoumanis, C., Bicen, A. F., and Whitelaw, J. H., "Measurements in a Motored Four-Stroke Reciprocating Model Engine," *ASME JOURNAL OF FLUIDS ENGINEERING*, Vol. 104, 1982, p. 235.
- 15 Arcoumanis, C., Bicen, A. F., and Whitelaw, J. H., "Effect of Inlet Parameters on the Flow Characteristics in a Four-Stroke Model Engine," SAE paper 820750, 1982.
- 16 Arcoumanis, C., Bicen, A. F., and Whitelaw, J. H., "Application of LDA to Four-Stroke Motored Model Engines," *Proc. Symposium on Applications of Laser-Doppler Anemometry to Fluid Mechanics*, Lisbon, July 1982.
- 17 Ramos, J. I., and Sirignano, W. A., "Axisymmetric Flow Model with and without Swirl in a Piston-Cylinder Arrangement with Idealized Valve Operation," SAE paper 800284, 1980.
- 18 Ramos, J. I., Gany, A., and Sirignano, W. A., "Study of Turbulence in a Motored Four-Stroke Internal Combustion Engine," *AIAA Journal*, Vol. 19, No. 5, 1981, p. 595.
- 19 Borgnakke, C., Davis, G. C., and Tabaczynski, R. J., "Predictions of In-Cylinder Swirl Velocity and Turbulence Intensity for an Open Chamber Cup in Piston Engine," SAE paper 810224.
- 20 Ahmadi-Befrui, B., Arcoumanis, C., Bicen, A. F., Gosman, A. D., Jahanbakhsh, A., and Whitelaw, J. H., "Calculations and Measurements of the Flow in a Motored Model Engine and Implications to Open-Chamber Direct-Injection Engines," *Proc. Symposium on Three Dimensional Turbulent Shear Flows*, ASME Spring Meeting, St. Louis, 1982.
- 21 Bicen, A. F., "Refraction Correction for LDA Measurements in Flows with Curved Optical Boundaries," Imperial College Mech. Eng. Dept., Report FS/81/17, 1981. Also *TSI Quarterly*, Vol. 8, No. 2, Apr.-June 1982.

APPENDIX I

Calculation of Swirl Ratio

Average swirl ratio is defined as the rotational speed of air at TDC of compression divided by the engine speed. It is calculated by averaging the swirl ratios obtained from a number (N) of swirl profiles at various axial locations.

$$\text{Swirl ratio} = \text{SR} = \frac{\frac{1}{R} \int_0^R \frac{\bar{W}}{r} dr}{\text{engine speed}} \quad (1)$$

$$\text{Average swirl ratio} = \frac{1}{N} \sum_{i=1}^N (\text{SR})_i$$

$$= \frac{30 \cdot \sum_{i=1}^N \left| \int_0^R \frac{\bar{W}}{r} dr \right|_i}{N \cdot R \cdot \text{engine rpm} \cdot \pi} \quad (2)$$

where \bar{W} = Ensemble-averaged mean swirl velocity at radius r
 R = Bowl or cylinder radius

If it is assumed that the air rotates like a solid body at TDC, the equation above reduces to:

$$\begin{aligned} \text{Swirl ratio} &= \frac{\text{vortex speed}}{\text{engine speed}} \\ &= \frac{\bar{W} \cdot 30}{r \cdot \text{engine rpm} \cdot \pi} \end{aligned} \quad (3)$$

which has been used almost exclusively by other investigators due to the difficulty of obtaining detailed swirl velocity profiles.

APPENDIX II

Calculation of Angular Momentum

Angular momentum (or moment of momentum) of a fluid element about the cylinder axis is defined as the product of its momentum and the radial distance from the axis. It is calculated at a certain crank angle by averaging the angular momenta obtained from a number (N) of swirl profiles at various axial locations:

$$\text{Angular momentum (per unit mass)} = \text{AM} = \frac{2}{R^2} \int_0^R \bar{W} r^2 dr$$

$$\text{Average angular momentum} = \frac{1}{N} \sum_{i=1}^N (\text{AM})_i$$

Muin Baasiri

Assistant Professor of Hydraulics,
the American University of Beirut,
Beirut, Lebanon

J. Paul Tullis

Professor of Civil and
Environmental Engineering,
Utah State University,
Logan, Utah

Air Release During Column Separation

Air release caused by column separation in a pipeline was investigated in a test facility where column separation could be generated for any desired length of time. The temperature, pressure, amount of dissolved air, and the other variables affecting the process were carefully controlled. Tests were made for cases where there was no initial free air in the system and for cases where there was some initial free air. The parameters influencing air release were identified and empirical equations developed for predicting the amount of air released during each cycle of column separation.

Introduction

If the pressure during a transient in a pipeline drops below some critical pressure, air bubbles can form by convective diffusion. If the pressure drops to vapor pressure, vapor cavities are also created. During subsequent high pressure cycles of the transient, the vapor condenses but the free air remains. Since air evolves faster than it dissolves, the amount of free air increases with time if the cyclic phenomenon continues.

The presence of the free air reduces the effective bulk modulus of the liquid and consequently reduces the acoustic wave speed. Since the wave speed is a function of the void fraction and the void fraction varies with pressure, the wave speed becomes a function of pressure. This creates problems with numerical models used to solve closed conduit transients since the commonly accepted solution method (method of characteristics) requires a constant wave speed or use of interpolation which introduces numerical damping [1].

There are many real situations where free air is entrained in the system or where a local low pressure region causes degassing. If the air is ignored, transient analysis produces results which have little resemblance to the actual pressure-time response of the system. The air not only reduces the wave speed and decreases the peak pressures, but causes significant dissipation which rapidly attenuates the transient.

In a study of gas evolution in liquids and cavitation, Schweitzer and Szebehely [2] derived an expression for predicting the volume of evolved air from solution as a function of time. Their technique consisted of creating agitation by shaking a container partly filled with liquid and taking accurate pressure measurements of the air cavity above the liquid to predict the volume and the time rate of air that evolved or dissolved. In their formulation, they defined the term "half-life" as the time required to half-complete the gas evolution, which was experimentally found to be related to the gas-liquid ratio, the method of agitation, and the solubility constant (the proportionality constant in Henry's

law). The rate of gas evolution resulting from this study is a function of the half-life, the solubility constant, the gas-liquid ratio, the difference between the saturation pressure and the gas pressure above the liquid, and time. Another result of this study is that the evolution ratio between the rates of evolution obtained under agitated and quiescent conditions is in the thousands. Concerning solution rates, in all their experiments, Schweitzer and Szebehely found that the half-life for evolution was always shorter than that for solution, which meant that air evolved at a faster rate than it dissolved.

A number of studies [3, 4, 5, 6, 7, 8] have addressed the problem of how to include the influence of the free air in the numerical solutions. Brief descriptions of these and other research studies are contained in References [9] and [3]. A significant limitation in each of these studies is the need to make rather arbitrary assumptions regarding the rate that air is released. None of these studies (except [2]), made any attempt to measure the rate of air release. Most used an exponential type air release based on Reference [2].

This research project was undertaken to measure the amount and rate of air release, determine the factors which influence air release during column separation and if possible, quantify their effects.

Formulation of the Problem. From early works on air release and from preliminary tests of this study [10], it was found that the mass of released air per unit volume (ΔM) during a transient depends primarily on the following parameters: the line pressure during column separation which will be vapor pressure (P_v), the time (t) during which the system is below the critical pressure, the temperature (T), the agitation (A) created by collapse of the vapor cavities and the releasable air ($M_r - M_i$). M_r is the amount of dissolved air per unit volume at a given saturation pressure and M_i is the mass per unit volume that has already been released before the transient starts.

The determination of the prediction equation for ΔM required reduction of the number of unknowns with the aid of dimensional analysis. In completing the dimensional analysis several combinations of the parameters were considered. For each set of terms it was desired to have the mass of air released

Contributed by the Fluids Engineering Division for publication in the JOURNAL OF FLUIDS ENGINEERING. Manuscript received by the Fluids Engineering Division, March 20, 1981.

(ΔM) as the dependent variable and, of course, have the π terms independent. Details of the development are included in reference [8]. The result is the following relationship.

$$\frac{\Delta M}{M_i - M_i} = \phi \left[\left(\frac{P_v^{5/6} t}{(M_i - M_i)^5 A^{1/3}} \right), T \right] \quad (1)$$

or simply

$$\pi_1 = \phi(\pi_2, T) \quad (2)$$

The temperature could be made dimensionless by dividing by some reference temperature such as the saturation temperature. However, since the tests were conducted at saturation temperature, that π term would always be 1.0 and have little significance. It seems more reasonable to let temperature retain dimensions and not treat it as dimensionless. The problem reduces to one of experimentally determining the functional relationship of equation (2). The agitation term A will be developed subsequently.

The total mass of dissolved air M_i in g/l at a given saturation pressure which can be released when the pressure drops to vapor pressure can be measured with a Van Slyke apparatus or determined using Henry's law expressed as:

$$M_i = \frac{1602 (P_s - P_v)}{k} \quad (3)$$

in which P_s = saturation pressure, P_v = vapor pressure, k = the solubility constant.

A direct measure of the free air M_f or M_i was not possible. The Van Slyke apparatus, for example, only measures total air content (free and dissolved air) of a given sample. It cannot provide the free air content. Other methods, such as the light scattering technique, do give a measure of free air at a given point [11]. For the work reported in this paper it was necessary to know the total mass of air released in the entire pipeline. Therefore, the mass per unit volume of free air M in the pipe at the end of a test was evaluated by the wave equation for liquid-gas mixtures in an elastic pipe suggested in the paper by Tullis, Streeter, and Wylie [9]. The equation for calculating the wave speed has the form:

$$a = \left[\frac{K/\rho}{\left(1 - \frac{MRT}{P}\right) \left(1 + \frac{MRTK}{P^2} + \frac{KD}{Ee}\right)} \right]^{.5} \quad (4)$$

in which K and ρ are the bulk modulus and mass density of the water, D , e , and E are the diameter, wall thickness and modulus of elasticity of the pipe, R is the gas constant, and P and T are the absolute pressure and temperature during the test. The wave speed is measured experimentally and equation (4) is solved for M . The initial free air M_i is determined by

generating a small transient prior to creating column separation, measuring the wave speed and solving equation (4). The total amount of air released during the test is determined by measuring the wave speed after the experiment. Then $\Delta M = M - M_i$.

The absolute accuracy of the wave speed is not a critical factor in this experimental program. What is important is the change of a with the mass of free air M . Therefore, in evaluating confidence limits any errors in the pipe properties and fluid properties K , ρ , D , E , and e are of no significance.

The only other variable to be evaluated in equation (1) is the agitation term A . It has been documented that agitation is important in air release [2]. For example, the Van Slyke apparatus previously mentioned incorporates a magnetic stirrer to accelerate the air release process. In developing an empirical approach it was decided to develop an agitation term which would be expressed in terms of work acting on the free air. The work by Weyler [12, 13], in which he developed an equivalent shear stress due by the pressure of free air was used as the basis of the agitation term.

An equivalent shear stress τ_B due to the free air bubbles in the pipe was suggested by Weyler [12, 13]:

$$\tau_B = \frac{CD(P_p - P_v)V0}{L\forall} \quad (5)$$

in which D = pipe diameter, L = pipe length, $V0/\forall$ = void fraction, $(P_p - P_v)$ = pressure change acting on bubbles, and C is an experimentally determined constant. Changing the stress into work units and assuming the agitation A is equal to the work done on the air bubbles, equation (5) becomes:

$$A = \tau_B \forall = CDV0(P_p - P_v)/L \quad (6)$$

Since

$$V0 = \frac{M'RT}{P} \text{ (equation of state)} \quad (7)$$

where M' is the mass of free air just before agitation, and P is the absolute equilibrium system pressure. Equation (6) becomes:

$$A = CDM'RT(P_p - P_v)/LP \quad (8)$$

The only unknown in equation (8) is the constant C ; however, Weyler compared data obtained from the tests run in the laboratory with a computer simulation of the hydraulic transient for each test and obtained values for the constant C that resulted in agreement between the experimental results and the computer simulation. A log-log plot of Weyler's data after changing the units of free air from volume to mass per unit volume resulted in an equation for the constant C .

Nomenclature

A = agitation energy term	M_i = maximum mass per unit volume of air dissolved in the water	P_s = saturation pressure
a = wave speed	M_1 = mass of air per unit volume just before column separation cavity collapses	P_v = liquid vapor pressure
C = constant in equation (5)	ΔM = mass of air per unit volume released by column separation	R = universal gas constant
D = inside pipe diameter	M' = mass of free air in equation (7)	T = liquid temperature
E = modulus of elasticity of the pipe	P = equilibrium pressure in the pipe	t = time that water is at vapor pressure during column separation
e = pipe wall thickness	P_p = peak pressure at column collapse	\forall = volume of pipe
K = bulk modulus of water		$V0$ = volume of air bubbles in equation (5)
k = solubility constant (Henry's law)		ρ = mass density
L = pipe length		τ_B = equivalent shear stress due to air bubbles
M = mass per unit volume of free air in the pipe at any time		π_1, π_2 = dimensionless parameters, see equations (1) and (2)
M_i = initial mass per unit volume of free air before column separation		

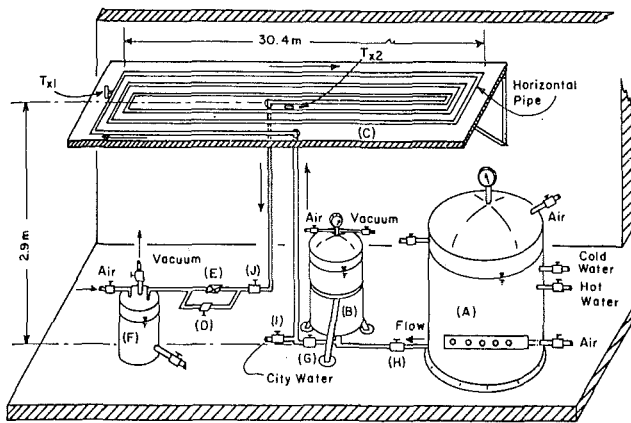


Fig. 1 Test facility

$$C = 33.6M_1^{-1.21} \quad (9)$$

Incorporating equation (9) into equation (8) and changing the total mass M' into mass per unit volume M_1 , the agitation term becomes in SI units:

$$A = 26.4M_1^{-0.21} D^3 RT(P_p - P_v) / P \quad (10)$$

Experimental Model

The approach to the problem was to investigate experimentally the amount of air released during an individual column separation event, and from the results formulate a relationship that can be used in the prediction of mass of released air for several cycles of a transient. This required an experimental set-up where the water temperature, saturation pressure, amount of initial free air, the time duration of the column separation and the agitation could be controlled. The system developed allowed each of these variables to be controlled and varied over the desired range.

The experimental facility (Fig. 1) consisted of a pressurized tank (A) with an aeration system which was used to saturate water with air; a smaller tank (B) was used as an upstream reservoir for the pipe; a 30.2 ± 0.3 mm diameter PVC pipe (C) 331.9 ± 0.1 m long; a downstream ball valve (D) which was used to generate water hammer by suddenly closing it; a solenoid valve (E); a small pressurized tank (F) which was used in controlling the pressure at the pipe downstream end; and several other accessories.

Pressure transients were monitored by two Validyne DP 15 transducers attached to the pipe and located 247.73 ± 0.2 m apart, identified as Tx_1 and Tx_2 in Fig. 1. The signals from the transducers were amplified by a Validyne Model CD 15 carrier demodulator and recorded by either a Houston Instrument OmniScribe Series B-5000 strip-chart recorder or a Honeywell Visicorder.

The procedure to generate an individual column separation event was as follows: After filling reservoir (B) (Fig. 1) with the air-saturated water and closing valves (H) and (G) the pipeline was thoroughly flushed with tap water at high velocity through valve (I) to remove any trapped air. Next the water in the pipe was replaced with the aerated water from reservoir (B). The operation was done at high pressure and low velocity to prevent de-aeration. Then valves (G) and (J) were closed.

The system was then checked to see if all the air had been flushed from the pipe by measuring the wave speed. This was done by establishing a small amount of flow from tank (B) to tank (F) and generating an initial transient by closing valve (D). Figure 2 is a record of a typical test. The transient generated by closing valve (D) produced the periodic traces at the left side of Fig. 2 (labeled initial transient). The initial

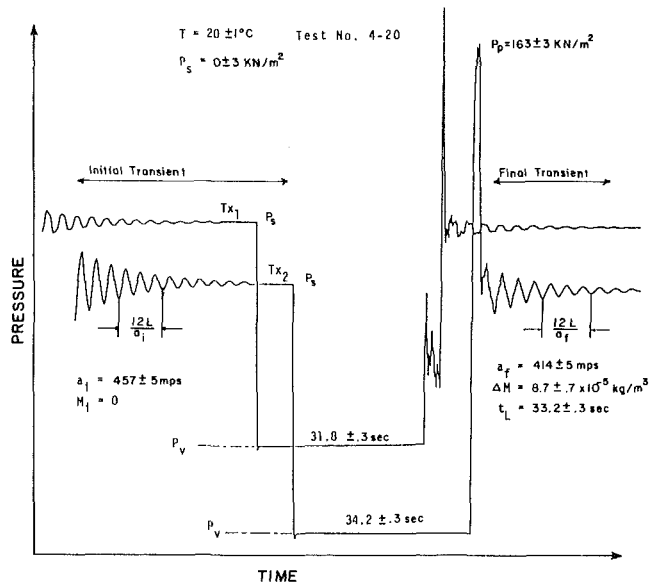


Fig. 2 Pressure traces from typical column separation tests ($M_i = 0$)

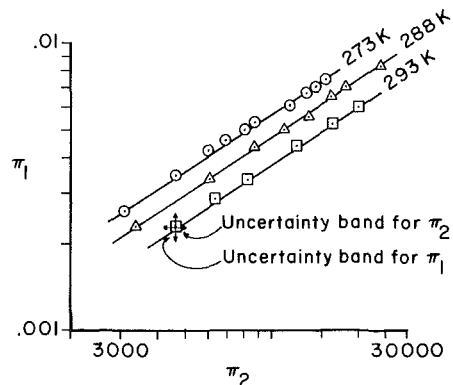


Fig. 3 Correlation of experimental data

wave speed a was calculated by scaling the time between several peaks, and knowing the distance L from the transducer Tx_2 to tank (B) and using time = $12L/a$ (for 3 cycles). For run 4-20 the initial wave speed $a_i = 457 \pm 5$ m/s. For the tests to be conducted without any initial free air if a_i was less than 457 ± 5 m/s the system was flushed again. The accuracy of measuring the wave speed was only dependent on the distance from the transducer to the reservoir and the scaled time from the oscillograph. The distance was known to a fraction of a meter and the time was scaled from the strip charts with a dial caliper to .5 mm. Normally three or four cycles of the reflected wave were scaled to improve the time determination.

Once the initial wave speed was measured and there wasn't any flow in the pipe, pressure in the reservoir was reduced to the vapor pressure by using a vacuum source, valve (G) was then quickly opened causing the water in the pipe to be subjected to vapor pressure for a specified period of time. For runs 2-4 the water in the pipe was held at vapor pressure for about 33 seconds. It is of interest to note that for tests without any initial free air when column separation was first initiated, the pressure dropped momentarily below P_v subjecting the water to a tensile stress of about $-.6$ kN/m². It is felt that this is a true measure of tension and not overshoot of the transducers or recorders. This finding agrees with the tensile stress measured by Parkin and Kermeen [14] for vaporous cavitation inception tests. For tests with some initial free air present in the system, the pressure did not drop below vapor pressure.

Table 1 Results of tests without initial free air

a_f m/s 1	$M_i \times 10^2$ kg/m ³ 2	$\Delta M \times 10^4$ (measured) kg/m ³ 3	Temp. K 4	P_v kN/m ² 5	t sec. 6	P_p kN/m ² 7	A Joules 8	$\pi_1 \times 10^{-3}$ 9	$\pi_2 \times 10^{-3}$ 10	$\Delta M \times 10^4$ (Eq. 13) kg/m ³ 11
409±5	2.45±.08	1.03±.08	283±1	1.25±.01	30.4±.3	163±3	1900±60	4.2±.4	6.0±.4	1.1 ±.08
402±5	"	1.23±.08	"	"	41.0±.3	163±3	1800±60	5.0±.4	8.1±.4	1.3 ±.06
392±5	"	1.50±.08	"	"	58.0±.3	163±3	1800±60	6.1±.4	11.6±.4	1.6 ±.08
385±5	"	1.71±.08	"	"	71.0±.3	164±3	1800±60	7.0±.4	14.3±.4	1.9 ±.08
417±5	"	.85±.08	"	"	24.0±.3	162±3	1900±60	3.5±.4	4.7±.4	.93±.08
476±5	"	.63±.08	"	"	16.1±.3	164±3	2000±60	2.6±.4	3.1±.4	.72±.08
382±5	"	1.81±.08	"	"	77.2±.3	164±3	1700±60	7.4±.4	15.6±.4	2.0 ±.08
405±5	"	1.13±.08	"	"	35.4±.3	163±3	1900±60	4.6±.4	7.0±.4	1.2 ±.08
399±5	"	1.30±.08	"	"	44.0±.3	163±3	1800±60	5.3±.4	8.8±.4	1.4 ±.08
386±5	"	1.66±.08	"	"	67.0±.3	163±3	1800±60	6.8±.4	13.5±.4	1.8 ±.08
420±5	2.19±.07	.75±.08	288±1	1.73±.01	23.0±.3	163±3	2000±60	3.4±.4	6.2±.4	.84±.08
411±5	"	.97±.08	"	"	33.0±.3	164±3	1900±60	4.4±.4	8.9±.4	1.1 ±.08
393±5	"	1.44±.08	"	"	61.0±.3	163±3	1800±60	6.6±.4	16.9±.4	1.6 ±.08
390±5	"	1.33±.08	"	"	65.6±.3	163±3	1800±60	7.0±.4	18.2±.4	1.6 ±.08
406±5	"	1.10±.08	"	"	41.2±.3	163±3	1900±60	5.0±.4	11.3±.4	1.2 ±.08
401±5	"	1.23±.08	"	"	49.5±.3	162±3	1800±60	5.6±.4	13.7±.4	1.4 ±.08
381±5	"	1.81±.08	"	"	86.0±.3	164±3	1700±60	8.3±.4	24.1±.4	2.0 ±.08
428±5	"	.57±.08	"	"	12.9±.3	162±3	2100±60	2.3±.4	3.4±.4	.58±.08
422±5	2.00±.06	.69±.08	293±1	2.38±.01	23.2±.3	164±3	2000±60	3.4±.4	8.4±.4	.77±.08
427±5	"	.58±.08	"	"	17.6±.3	163±3	2100±60	2.9±.4	6.4±.4	.65±.08
401±5	"	1.20±.08	"	"	53.7±.3	164±3	1900±60	6.0±.4	20.1±.4	1.3 ±.08
415±5	"	.87±.08	"	"	33.2±.3	163±3	2100±60	4.4±.4	12.3±.4	1.0 ±.08
433±5	"	.46±.08	"	"	13.0±.3	162±3	1900±60	2.3±.4	4.7±.4	.53±.08
407±5	"	1.05±.08	"	"	45.2±.3	163±3	1900±60	5.3±.4	16.9±.4	1.2 ±.08

$P_g = 153 \pm 2 \text{ kN/m}^2$
 $P = 85.6 \pm 2 \text{ kN/m}^2$
 $R = 287 \text{ Nm/kg K}$
 All pressures are absolute

Table 2 Results of tests with initial free air

a_f m/s 1	$M_i \times 10^4$ kg/m ³ 2	P_p kN/m ² 3	t sec. 4	a_f m/s 5	$\Delta M \times 10^4$ (measured) kg/m ³ 6	A Joules 7	$\pi_1 \times 10^{-3}$ 8	$\pi_2 \times 10^{-3}$ 9	$\Delta M \times 10^4$ (eq. 13) kg/m ³ 10
352±4	2.9±.3	117±3	60.6±.3	283±3	3.3±.2	440±30	3.8±.4	14.4±.4	3.4±.2
351±4	2.9±.3	157±3	32.1±.3	300±3	1.9±.2	590±30	2.2±.4	6.9±.4	2.2±.2
351±4	3.0±.3	125±3	28.0±.3	312±3	1.9±.2	470±30	2.2±.4	6.5±.4	2.1±.2
358±4	2.8±.3	100±3	36.9±.3	301±3	2.2±.2	380±30	2.6±.4	9.2±.4	2.6±.2
351±4	2.9±.3	135±3	23.8±.3	312±3	1.6±.2	510±30	1.9±.4	5.4±.4	1.9±.2
336±4	3.5±.3	177±3	18.3±.3	334±3	1.3±.2	640±30	1.5±.4	3.8±.4	1.5±.2
290±4	6.1±.3	134±3	52.9±.3	288±3	3.1±.2	430±30	3.6±.4	12.7±.4	3.1±.2
359±4	2.6±.3	117±3	51.9±.3	292±3	3.1±.2	450±30	3.6±.4	12.0±.4	3.1±.2

$P_v = 1.25 \pm .01 \text{ kN/m}^2$
 $T = 283 \pm 1 \text{ K}$
 $P = 85.6 \pm 2 \text{ kN/m}^2$
 $R = 287 \text{ Nm/kg K}$
 $M_c = 4.48 \pm .5 \times 10^{-2} \text{ kg/m}^3$
 All pressures are absolute

Pressure recovery was accomplished by first closing valve (G) and opening valve (J) (solenoid valve (E) and valve (D) closed), next raising the pressure in the reservoir (B) to a point slightly higher than the line pressure and then opening valve (G) suddenly to cause a quick recovery of pressure in the pipe. In order to control the agitation, the solenoid valve (E) at the downstream end was supplied with power during the time when the high pressure wave was traveling in the pipe causing the valve to open to change the dead end boundary condition to a reservoir boundary condition. This made it possible to obtain one large pressure rise simulating the collapse of column separation.

Figure 2 shows that for transducers T_{x2} , a single high pressure peak $P_p = 163 \pm \text{kN/m}^2$ was generated when the vapor cavities collapsed. When the pressure recovery was accomplished without using the solenoid valve, numerous pressure spikes were recorded.

While the water was flowing into tank (F), valve (J) was suddenly closed causing a small transient which allows the determination of the wave speed (see Fig. 2). This transient caused the periodic shaped traces to the right of the peak pressure P_p (Fig. 2 labeled final transient). Measuring the time between peaks provided a measure of the final wave speed. For run 4-20 $a_f = 414 \pm 5 \text{ mps}$. The mass of air released $\Delta M = 8.7 \pm .7 \times 10^{-5} \text{ kg/m}^3$ from equation (4).

Estimating the Quantity M_1 . One of the fundamental variables needed to predict the agitation is M_1 . By definition, M_1 is the mass of free air that exists before the occurrence of the agitation and cavity collapse. This means that M_1 is equal to the sum of the initial mass of free air M_i (if any) and the mass of evolving air during the time at low pressure (before agitation).

One of the reasons for having two transducers was to determine the wave speed while the water is at low pressure so that the wave speed can be calculated. By knowing the wave speed and using equation (4), the mass of released air could be estimated.

Early results of this research project [10], identified that for column separation tests made without any free air present in the water, almost all air comes out of solution when the pressure is raised from P_v to some positive level. (Refer to Fig. 2). When the pressure in the pipe was dropped to P_v and held there for about 33 seconds very little air was released. This was determined by measuring the wave speed as the pressure was increased in the pipe. This wave speed was determined from the time required for the wave to travel between the two transducers. The agitation, which could also be seen and heard because of its violent shaking of the pipe caused air to be released almost instantly. This follows the results of Schweitzer and Szebehely [2] regarding the important role of agitation on air release.

From the records of the tests run for water with no initial free air at a temperature of 10°C and saturated at atmospheric pressure (84.1 kN/m²), it was found that the amount of air released in a given time, while the water is at vapor pressure (without agitation), can be expressed by the equation:

$$M_1 = 2.47 \times 10^{-7} t^{.5} + M_i \quad (\text{kg/m}^3) \quad (11)$$

in which t is the time in seconds at vapor pressure and M_i is the initial free air.

The amount of air released while the water is at P_v and not being agitated is only a fraction of the amount of air released by the agitation at cavity collapse. However, even though the amount of air released at P_v is small, it has a significant influence on the amount released by the cavity collapse.

For column separation in a flowing system it is anticipated that the amount of air released during column separation would increase due to agitation caused by the turbulence of the moving water. For such a case the rate of air release would likely be dependent also on the Reynolds number.

Experimental Results

Tests were first made using water with no initial free air ($M_i = 0$) and maximum wave speed value (457 ± 5 m/s). These results were used to develop an empirical equation for predicting air release. A second group of tests was performed with initial free air ($M_i \neq 0$) and consequently an initial wave speed below 457 ± 5 m/s. The measured air release was compared with that calculated to see if the equation was valid for cases where there is initially free air.

For a test with no initial free air it was observed that no air was released unless the pressure was reduced to vapor pressure at the lab. For example, the water was subjected to a pressure about .7 kN/m² above vapor pressure for over 6 minutes and no air came out of solution. Nuclei created by agitation and low pressures are needed for convective diffusion to occur. Tests with water containing some free air produced deaeration anytime the pressure was below saturation pressure.

Tests With $M_i = 0$. The results of the first set of tests for $M_i = 0$ are summarized in Table 1. The water for these tests was air saturated at atmospheric pressure. The wave speed was checked before each test to be sure it was 457 ± 5 m/s which verified that there was no free air in the pipe. The wave speed after the test, measured again at atmospheric pressure, is listed in column 1 of Table 1. Values of M_i and M ($M = \Delta M$ for $M_i = 0$) in columns 2 and 3 were obtained from equations (3) and (4). The peak pressure P_p and the time t at vapor pressure were scaled from the output of the pressure transducers (see Fig. 2) and used to calculate the agitation term, equation (10).

The air release term, π_1 is plotted as a function of π_2 in Fig. 3 for the data in Table 1. For each line in Fig. 3, P_v , A , M_i , and M_i , are essentially constant. Therefore, the figure basically shows the fractional air release (π_1) as a function of time (π_2). The log-log plot produces straight lines suggesting a simple functional relationship between π_1 , π_2 , and T . One form of this relationship is:

$$\pi_1 = (1.9 \times 10^4 - 6.0 \times 10^{-7} T) \pi_2^{.62} \quad (12)$$

Replacing the P_i terms with their corresponding physical variables results, after simplifying and solving for ΔM , in the following expression:

$$\Delta M = (1.9 \times 10^{-4} - 6.0 \times 10^{-7} T) P_v^{.52} t^{.62} (M_i - M_i)^{.69} A^{-.21} \quad (13)$$

in which the masses are in mass per unit volume of air-water mixture (SI system). M_i is obtained from equation (3) and A from equation (10). Equation (13) may be used to approximate the amount of air released by a single column

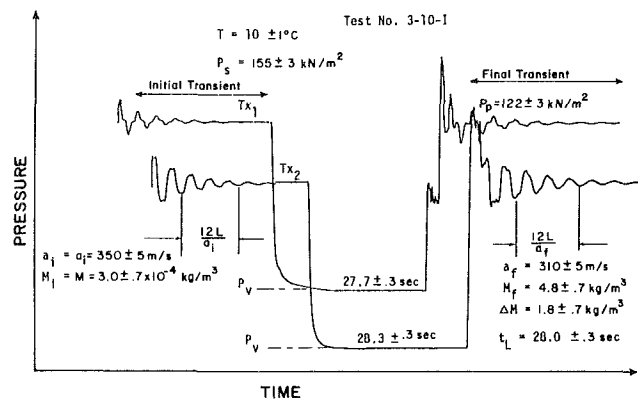


Fig. 4 Pressure traces from typical column separation tests ($M_i \neq 0$)

separation event. Columns 3 and 11 of Table 1 compare the measured ΔM and ΔM calculated by equation (13).

Tests With Initial Free Air. In order to cause the release of some free air before each one of these tests, one column separation was generated for a short time. Following this, the wave speed was determined and the initial mass of free air (M_i) calculated with equation (4). Then a second transient was generated following the procedure previously discussed.

A typical experimental record for a column separation test with $M_i \neq 0$ is shown in Fig. 4. There are two noticeable differences between Figs. 2 and 4. First, when the pipeline is instantly exposed to vapor pressure from tank (B) it takes several seconds for the pressure to reach P_v . This is due to the time required to expand the small air bubbles present in the system. The other difference is in the significantly lower peak pressure at column collapse. This is because there is more free air in the water before pressure recovery. The air acts as a shock absorber to cushion the transient and makes the agitation term much smaller (compare the values of A in Tables 1 and 2). This is in accordance with Weyler's [12, 13] finding. He described the distributed air bubbles in water as acting like small dampers which reduce the pressure change caused by the traveling wave. Although the increased amount of free air decreases the physical agitation of the system and lowers the resulting peak pressure a significant amount of air is released during subsequent transients.

For these tests the water was saturated at 153 ± 2 kN/m² so more air would be dissolved. The initial mass of free air listed in column 2 varied from about 0.5 to 1.4% of the total dissolved air. The amount released during the second transient (ΔM) is listed in column 6 Table 2. The calculated ΔM from equation (13) is in column 10. Equation (13) is capable of estimating air release for both cases of interest: the case of the first column separation when free air is initially absent, and the case of the subsequent column separations of the same transient when initial free air exists. The reliability of equation (13) when applied to other piping systems must be verified by experiments.

The uncertainty estimation utilized the method suggested by Kline and McClintock [15] with 20:1 odds. However, for parameters π_2 equations (1) and (2), A equation (10), and M equation (13) a modification of their method was necessary due to the complexity of the equations.

Conclusions

The amount of air released by column separation is a function of: 1) the amount of air dissolved in the water, 2) the amount of free air present before the transient, 3) vapor pressure, 4) temperature, 5) the length of time the water is at vapor pressure and, 6) the agitation caused when the cavities collapse. The rate of air release during column separation is

expressed by equation (11) for the case where there is no agitation (as was the case during this experiment). This amount of air is small compared to that released almost instantly by the agitation caused by cavity collapse. Empirical equations presented provide estimates of the amount of air released for the first cycle of a transient causing column separation and any subsequent column separation. The equations are valid for cases where there is no free air initially present and for initial free air. When there is no free air in the system, no air will be released until the pressure is reduced to vapor pressure. For this case the pressure momentarily drops about -0.6 kN/m^2 below vapor pressure before vaporization occurs. The amount of tension is dependent on the cleanliness of the water and the existence of any trapped air on the boundary of the pipe.

References

- 1 Wylie, E. B., and Streeter, V. L., "Solution by Characteristic Method," *Fluids Transients*, McGraw-Hill, 1978, p. 58.
- 2 Schweitzer, P. H., and Szebehely, V. G., "Gas Evolution in Liquids and Cavitation," *Journal of Applied Physics*, Vol. 21, 1950, pp. 1218-1224.
- 3 Wiggert, D. C., and Sundquist, J. J., "The Effect of Gaseous Cavitation on Fluid Transients," *ASME JOURNAL OF FLUIDS ENGINEERING*, Vol. 101, Mar. 1979, pp. 79-86.
- 4 Swaffield, J. A., "Column Separation in an Aircraft Fuel System," *Proceedings of the First International Conference on Pressure Surges*, Canterbury, England, Paper C2, BHRA Fluids Engineering, Sept. 1972, pp. 13-28.
- 5 Driels, M. K., "An Investigation of Pressure Transients in a System Containing a Liquid Capable of Air Absorption," *ASME JOURNAL OF FLUIDS ENGINEERING*, Paper No. 73-FE-28, 1973.
- 6 Enever, K. J., "Surge Pressures in a Gas-Liquid Mixture with a Low Gas Content," *Proceedings of the First International Conference on Pressure Surges*, Canterbury, England, Paper C1, BHRA Fluid Engineering, Sept. 6-8, 1972, pp. 1-11.
- 7 Kranenburg, C., "Gas Release During Transient Cavitation in Pipes," *Journal of the Hydraulics Division*, Vol. 100, No. HY10, Oct. 1974, pp. 1383-1398.
- 8 Baasiri, M., "A Quantitative Study of Free Air Release During Transient Flow," PhD dissertation, Utah State University, 1980.
- 9 Tullis, J. P., et al., "Waterhammer Analysis with Air Release," *Proceedings Second International Conference on Pressure Surges*, BHRA Fluid Engineering, Cranfield, Bedford, England, 1976.
- 10 Hsia, C., "Waterhammer and Air Release," M. S. thesis, Utah State University, Logan, Utah, 1979.
- 11 Keller, A., "The Influence of the Cavitation Nucleus Spectrum on Cavitation Inception, Investigated With a Scattered Light Counting Method," *ASME Journal of Basic Engineering*, Vol. 94, Dec. 1972.
- 12 Weyler, M. E., "An Investigation of the Effect of Cavitation Bubbles on Momentum Loss in Transient Pipe Flow," Ph.D. dissertation, University of Michigan, 1969.
- 13 Weyler, M. E., "An Investigation of the Effect of Cavitation Bubbles on Momentum Loss in Transient Pipe Flow," *ASME Journal of Basic Engineering*, Vol. 93, Mar. 1971, pp. 1-10.
- 14 Parkin, B. R., and Kermeen, R. W., "The Role of Convective Air Diffusion and Liquid Tensile Stresses During Cavitation Inception," *Proceedings IAHR Symposium on Cavitation and Hydraulic Machinery*, Sendai, Japan, 1962.
- 15 Kline, S. J., and McClintock, F. A., "Describing Uncertainties in Single-Sample Experiments," *Mechanical Engineers*, Jan. 1953, pp. 3-8.

Effects Of Surface Solidification on the Stability Of Multi-Layered Liquid Films

S. P. Lin¹

The linear stability problem of a n-layered liquid film with a solidified liquid-air interface is reviewed. The general formulation is applied to the special case of a two-layered film flow down an inclined plane. A stability condition is given explicitly in terms of the density, viscosity and thickness ratios. Based on this condition it is found that solidification of the free surface may have the effects of stabilizing the interfacial shear waves and destabilizing the gravity-capillary waves associated with top-heavy density stratification.

Introduction

The stability of rectilinear flows of several superposed liquid layers is of great importance in modern coating technology.

The linear stability analyses of two superposed liquid layers flowing steadily down an incline have been made by Kao [1, 2, 3] with Yih's [4] perturbation technique. Kao's analyses were extended to the case of an n-layered liquid film by Akhtaruzzaman et al. [5] and Wang et al. [6]. In their analysis, all of the interfaces are allowed to deform. However, in practice the air-liquid interface is solidified much more rapidly than the rest of the fluid. It behaves more like a floating rigid surface than a flexible free surface. The purpose of this study is to investigate the effects of a solidified free surface on the stability of a liquid film of more than one layer.

Stability Analysis and Results

Consider a film which consists of n -layers of Newtonian

liquid flowing parallel to each other down an inclined plane. Under favorable conditions, the flow is steady, two-dimensional and laminar. The velocity field \bar{v}_j in the j th layer is given by (7) of Akhtaruzzaman et al. [5]. The linear stability analysis of this basic flow without free surface solidification was formulated by Akhtaruzzaman [5] and solved by Wang et al. [6]. The same formulation can be applied with a minor modification to the analysis of the stability of the same basic flow but with free surface solidification. The only necessary modification is that the velocity perturbation at the solidified free surface must vanish. While solutions for the cases of more than ten layers are of practical interest, for example, in the manufacturing of color photographic films, the striking effects of free surface solidification tends to be buried in the numerical results. For this reason, it was decided to obtain a closed form solution to the simplest case of two-layered film. This explicit solution enables one to elucidate the effects sought.

It is well known that the linear stability analysis of a flow results in an eigenvalue problem. The instability of multilayered liquid films manifests itself as long waves with small wave number $\alpha = 2\pi d_1/\lambda$, where d_1 is the thickness of the top layer and λ is the disturbance wavelength. We therefore adopt the method used by Yih (1963) and expand the eigenfunctions and the eigenvalue in power series of the small wave number α . The method of analysis and solutions are standard, see for example (reference [6]). Therefore, they will be omitted here. Only the results are presented. It should be pointed out that stability criteria are not obtained until the second order solution in the usual small wave number expansion. However, for the case of weakly stratified multilayered films encountered in practice, the densities, viscosities, and the derivatives of the velocity profiles in the two liquid layers differ insignificantly at the interface. By use of this fact, one can obtain the stability criteria in the first order perturbation solution² [7, 8].

The solubility condition of the problem demands that the eigenspeed c_0 of the disturbance satisfies the following dispersion relation,

$$c_0 - \bar{u}_2 = \alpha \frac{\bar{u}'' [6HM - 2\epsilon_2 \delta_2 G - 12(\bar{u}' / \bar{u}'')(G - H)] + 4i[MH + 2\delta_2 G]I}{12M + 24\delta_2 - 24G + 24H + 4\delta_2 G - 12HM/\epsilon_2} \quad (1)$$

where \bar{u}_2 is the interfacial velocity divided by the free surface velocity, ϵ_2 , δ_2 are, respectively, the ratios of the viscosity and

¹Professor, Department of Mechanical and Industrial Engineering, Clarkson College of Technology, Potsdam, N.Y. 13676.

Contributed by the Fluids Engineering Division of THE AMERICAN SOCIETY OF MECHANICAL ENGINEERS. Manuscript received by the Fluids Engineering Division, March, 27, 1981.

²This was pointed out to the writer by Dr. E. Pitts of Eastman Kodak Company, U.K..

the film thickness of the second layer to those of the top layer, and

$$G = 1 - 3l^2 + 2l^3, H = 1 - 2l + l^2, M = 3 - 3l^2, l = 1 + \delta_2$$

$$I = \alpha^2 L_2 / \gamma_2 + (\cot \beta / \epsilon_2 K) (\gamma_2 - 1),$$

$$L_2 = T_2 \gamma_2 / (\epsilon_2 \rho_1 d_1^2 g K \sin \beta) \quad (2)$$

$$K = \frac{1}{2} - [(\gamma_2 - 1) / \epsilon_2] \delta_2 - (\gamma_2 / 2 \epsilon_2) (1 - l^2),$$

$$\alpha \bar{u}' = \bar{u}_2' - \bar{u}_1', \alpha \bar{u}'' = \bar{u}_1'' / \epsilon_2 - \bar{u}_2'',$$

γ_2 being the ratio of the density of the top layer to that of the bottom layer, β the angle of inclination of the substrate with respect to the horizontal, T_2 the interfacial tension, ρ_1 the density of the top layer, 1 and 2 denote, respectively, the top and bottom layers, and primes denote differentiation with respect to the dimensionless distance measured perpendicularly from the flat free surface into the liquid film, the nondimensionalization of the distance being accomplished by use of d_1 .

Consider first the case of two liquid layers of the same viscosity and thickness but of different density. Then, $\delta_2 = 1$, $\epsilon_2 = 1$, and we have from (1) and (2)

$$c_{0i} = -(\alpha/13)[\alpha^2 L_2 / \gamma_2 + \{(\gamma_2 - 1)/K\} \cot \beta], \quad (3)$$

$$c_{0r} - \bar{u}_2 = 64[(\gamma_2 - 1)/52K], \quad (4)$$

where c_{0i} and c_{0r} are, respectively, the imaginary and real part of c_0 , and K is found from (2) to be

$$K = \frac{1}{2} (3 + \gamma_2) > 0.$$

(3) and (4) characterize the gravity-capillary waves caused by solely by gravity potential and the interfacial tension. (3) indicates that both the interfacial tension and the slight bottom heavy configuration i.e., $\gamma_2 > 1$ are stabilizing factors. However, for the case of top heavy density stratification $\gamma_2 < 1$, and $c_i > 0$ if

$$\alpha^2 (L_2 \gamma_2) < [(1 - \gamma_2)/K] \cot \beta. \quad (6)$$

Thus, there exists a cutoff wave length above which the stabilizing capacity of interface tension gives way to the destabilizing configuration of top heaviness, in particular the film is unstable when $\alpha \rightarrow 0$. On the other hand, it is found numerically from previous results [6] that $c_i < 0$ as $\alpha \rightarrow 0$ for the same top heavy film with a free surface. Hence, we conclude that the free surface solidification has a destabilizing effect on long interfacial gravity waves. This is quite to be expected as the solidified flat free surface tends to accentuate the hydrostatic pressure variation along the interface. Note also from (4) that the relative speed of the gravity-capillary wave is greater or smaller than zero depending on if $\gamma_2 > 0$ or $\gamma_2 < 0$. The same is true for the case of unsolidified free surface [5].

Consider next the case of two-layered liquid film of the same thickness and density but of different viscosity. For this case $\delta_2 = 1$, $\gamma_2 = 1$, and we have from (1), (2), and (2) of [5]

$$c_{0r} - \bar{u}_2 = \frac{12(1 - \epsilon_2)}{27 - 40\epsilon_2} \quad (7)$$

$$c_{0i} = \frac{\alpha^2 L_2 \epsilon_2}{27 - 40\epsilon_2} \quad (8)$$

(7) and (8) characterize the interfacial shear waves. The relative speed of shear waves depends solely on viscosity stratification but the amplification rate depends on ϵ_2 as well as the interfacial tension and gravity through L_2 . It follows from (8) that $c_{0i} < 0$ if $\epsilon_2 > 27/40 = \epsilon_c$. A weakly stratified film where $\epsilon_2 \sim 1$ and $\epsilon_2 > \epsilon_c$ is stable with respect to long shear waves. On the other hand, viscosity stratified films with a deformable free surface have never been found stable in

previous studies [1, 2, 3, 6]. Moreover, it follows from (7) that the damped long interfacial shear waves propagate ahead of the interfacial fluid velocity if $\epsilon_2 \lesssim 1$ but behind it if $\epsilon_2 \gtrsim 1$.

Conclusions

The free surface solidification destabilizes the long interfacial gravity waves in a double-layered film with top heavy density stratification. However, free surface solidification stabilizes the long interfacial shear waves in a viscosity stratified double-layered film. The former effect is apparently due to the more pronounced uneven hydrostatic pressure distribution along the interface, and the later effect is probably due to the more efficient viscous dissipation resulting from the solidified free surface. However, it should be emphasized that the above conclusion cannot be regarded as generally valid for all possible combinations of δ_2 , γ_2 , and ϵ_2 . The correct conclusion concerning the stability can be made only after the sign of the imaginary part of the wave speed is found from (1) for each particular.

Acknowledgments

This work was supported in part by Eastman Kodak Company, and was performed while the author was on a sabbatical leave at the University of Rochester. Thanks are due them for providing a congenial and hospitable atmosphere.

References

- 1 Kao, T. W., "Stability of Two-Layer Viscous Stratified Flow Down An Inclined Plane," *Physics of Fluids*, Vol. 8, 1965, pp. 812-820.
- 2 Kao, T. W., "Role of the Interface in the Stability of Stratified Flow Down an Inclined Plane," *Physics of Fluids*, Vol. 8, 1965, pp. 2190-2194.
- 3 Kao, T. W., "Role of Viscosity Stratification in the Stability of Two-Layer Flow Down an Incline," *Journal of Fluid Mechanics*, Vol. 33, 1968, pp. 561-572.
- 4 Yih, C. S., "Stability of Liquid Flow Down an Inclined Plane," *Physics of Fluids*, Vol. 6, 1963, pp. 321-334.
- 5 Akhtaruzzaman, A. F. M., Wang, C. K., and Lin, S. P., "Wave Motion in Multilayered Liquid Films," *ASME Journal of Applied Mechanics*, Vol. 45, 1978, pp. 26-30.
- 6 Wang, C. K., Seaborg, J. J. and Lin, S. P., "Instability of Multilayered Liquid Films," *Physics of Fluids*, Vol. 21, 1978, pp. 1669-1673.
- 7 Li, C. H., "Instability of Three-Layered Viscous Stratified Flow," *Physics of Fluids*, Vol. 12, 1969, pp. 2473-2481.
- 8 Lin, S. P., "Effects of Surface Solidification on the Stability of Multilayered Liquid Films," Clarkson College of Technology MIE Report No. 80, 1982.

the film thickness of the second layer to those of the top layer, and

$$G = 1 - 3l^2 + 2l^3, H = 1 - 2l + l^2, M = 3 - 3l^2, l = 1 + \delta_2$$

$$I = \alpha^2 L_2 / \gamma_2 + (\cot \beta / \epsilon_2 K) (\gamma_2 - 1),$$

$$L_2 = T_2 \gamma_2 / (\epsilon_2 \rho_1 d_1^2 g K \sin \beta) \quad (2)$$

$$K = \frac{1}{2} - [(\gamma_2 - 1) / \epsilon_2] \delta_2 - (\gamma_2 / 2 \epsilon_2) (1 - l^2),$$

$$\alpha \bar{u}' = \bar{u}_2' - \bar{u}_1', \alpha \bar{u}'' = \bar{u}_1'' / \epsilon_2 - \bar{u}_2'',$$

γ_2 being the ratio of the density of the top layer to that of the bottom layer, β the angle of inclination of the substrate with respect to the horizontal, T_2 the interfacial tension, ρ_1 the density of the top layer, 1 and 2 denote, respectively, the top and bottom layers, and primes denote differentiation with respect to the dimensionless distance measured perpendicularly from the flat free surface into the liquid film, the nondimensionalization of the distance being accomplished by use of d_1 .

Consider first the case of two liquid layers of the same viscosity and thickness but of different density. Then, $\delta_2 = 1$, $\epsilon_2 = 1$, and we have from (1) and (2)

$$c_{0i} = -(\alpha/13)[\alpha^2 L_2 / \gamma_2 + \{(\gamma_2 - 1)/K\} \cot \beta], \quad (3)$$

$$c_{0r} - \bar{u}_2 = 64[(\gamma_2 - 1)/52K], \quad (4)$$

where c_{0i} and c_{0r} are, respectively, the imaginary and real part of c_0 , and K is found from (2) to be

$$K = \frac{1}{2} (3 + \gamma_2) > 0.$$

(3) and (4) characterize the gravity-capillary waves caused by solely by gravity potential and the interfacial tension. (3) indicates that both the interfacial tension and the slight bottom heavy configuration i.e., $\gamma_2 > 1$ are stabilizing factors. However, for the case of top heavy density stratification $\gamma_2 < 1$, and $c_i > 0$ if

$$\alpha^2 (L_2 \gamma_2) < [(1 - \gamma_2)/K] \cot \beta. \quad (6)$$

Thus, there exists a cutoff wave length above which the stabilizing capacity of interface tension gives way to the destabilizing configuration of top heaviness, in particular the film is unstable when $\alpha \rightarrow 0$. On the other hand, it is found numerically from previous results [6] that $c_i < 0$ as $\alpha \rightarrow 0$ for the same top heavy film with a free surface. Hence, we conclude that the free surface solidification has a destabilizing effect on long interfacial gravity waves. This is quite to be expected as the solidified flat free surface tends to accentuate the hydrostatic pressure variation along the interface. Note also from (4) that the relative speed of the gravity-capillary wave is greater or smaller than zero depending on if $\gamma_2 > 0$ or $\gamma_2 < 0$. The same is true for the case of unsolidified free surface [5].

Consider next the case of two-layered liquid film of the same thickness and density but of different viscosity. For this case $\delta_2 = 1$, $\gamma_2 = 1$, and we have from (1), (2), and (2) of [5]

$$c_{0r} - \bar{u}_2 = \frac{12(1 - \epsilon_2)}{27 - 40\epsilon_2} \quad (7)$$

$$c_{0i} = \frac{\alpha^2 L_2 \epsilon_2}{27 - 40\epsilon_2} \quad (8)$$

(7) and (8) characterize the interfacial shear waves. The relative speed of shear waves depends solely on viscosity stratification but the amplification rate depends on ϵ_2 as well as the interfacial tension and gravity through L_2 . It follows from (8) that $c_{0i} < 0$ if $\epsilon_2 > 27/40 = \epsilon_c$. A weakly stratified film where $\epsilon_2 \sim 1$ and $\epsilon_2 > \epsilon_c$ is stable with respect to long shear waves. On the other hand, viscosity stratified films with a deformable free surface have never been found stable in

previous studies [1, 2, 3, 6]. Moreover, it follows from (7) that the damped long interfacial shear waves propagate ahead of the interfacial fluid velocity if $\epsilon_2 \lesssim 1$ but behind it if $\epsilon_2 \gtrsim 1$.

Conclusions

The free surface solidification destabilizes the long interfacial gravity waves in a double-layered film with top heavy density stratification. However, free surface solidification stabilizes the long interfacial shear waves in a viscosity stratified double-layered film. The former effect is apparently due to the more pronounced uneven hydrostatic pressure distribution along the interface, and the later effect is probably due to the more efficient viscous dissipation resulting from the solidified free surface. However, it should be emphasized that the above conclusion cannot be regarded as generally valid for all possible combinations of δ_2 , γ_2 , and ϵ_2 . The correct conclusion concerning the stability can be made only after the sign of the imaginary part of the wave speed is found from (1) for each particular.

Acknowledgments

This work was supported in part by Eastman Kodak Company, and was performed while the author was on a sabbatical leave at the University of Rochester. Thanks are due them for providing a congenial and hospitable atmosphere.

References

- 1 Kao, T. W., "Stability of Two-Layer Viscous Stratified Flow Down An Inclined Plane," *Physics of Fluids*, Vol. 8, 1965, pp. 812-820.
- 2 Kao, T. W., "Role of the Interface in the Stability of Stratified Flow Down an Inclined Plane," *Physics of Fluids*, Vol. 8, 1965, pp. 2190-2194.
- 3 Kao, T. W., "Role of Viscosity Stratification in the Stability of Two-Layer Flow Down an Incline," *Journal of Fluid Mechanics*, Vol. 33, 1968, pp. 561-572.
- 4 Yih, C. S., "Stability of Liquid Flow Down an Inclined Plane," *Physics of Fluids*, Vol. 6, 1963, pp. 321-334.
- 5 Akhtaruzzaman, A. F. M., Wang, C. K., and Lin, S. P., "Wave Motion in Multilayered Liquid Films," *ASME Journal of Applied Mechanics*, Vol. 45, 1978, pp. 26-30.
- 6 Wang, C. K., Seaborg, J. J. and Lin, S. P., "Instability of Multilayered Liquid Films," *Physics of Fluids*, Vol. 21, 1978, pp. 1669-1673.
- 7 Li, C. H., "Instability of Three-Layered Viscous Stratified Flow," *Physics of Fluids*, Vol. 12, 1969, pp. 2473-2481.
- 8 Lin, S. P., "Effects of Surface Solidification on the Stability of Multilayered Liquid Films," Clarkson College of Technology MIE Report No. 80, 1982.

DISCUSSION

A. T. Kirkpatrick²

In this paper, Professor Lin presents two interesting analytical results concerning the effects of surface solidification on the stability of two layer liquid film. The author is able to derive a dispersion relation for the complex eigenvalue, c , using only a zeroth order expansion in wave number α by assuming that the densities, viscosities, and velocity gradients were equal at the interface between the two liquid layers. The solidification is modeled by assuming u' and v' are equal to zero at $y = 0$, the free surface. It should

²Assistant Professor, Mechanical Engineering Dept., Colorado State University, Fort Collins, Colo. 80523.

be noted that this surface solidification can also be characterized as plane Couette flow down an inclined surface.

The first result concerns density stratification. For top heavy density stratification, $\gamma_2 < 1$, the stability criterion of equation (6) implies that as the angle of tilt increases, the film interface becomes more stable. This result is somewhat surprising. For single layer [1] and top heavy double layer [2] inclined film flow, it has been established that increasing the angle of tilt causes the film to be more unstable, since less potential energy is required to distort the free surface and the interface of the film. The transverse component of gravity, $g \cos\beta$, is thus the destabilizing mechanism for the film with a flat free surface, but is the stabilizing mechanism for a film with a distortable free surface. The physical explanation of this behavior can be cast in terms of a Taylor instability, similar to Professor Lin's explanation of hydrostatic pressure variation along the interface.

It would be interesting to compare the cutoff wave number predicted by equation (6) with the neutral stability curve for an equivalent free surface two layer film. This would facilitate determination of the Reynolds numbers, R_j , above which free surface solidification would have a stabilizing effect on the shorter wavelength ($\alpha > 0$) interfacial wave.

The second result concerns viscosity stratification. The stability criterion of equation (8) indicates that only flat films with the top layer more than about 1.5 times as viscous as the bottom layer are unstable. The explanation given is that more efficient viscous dissipation takes place with a flat free surface. However viscous dissipation is proportional to $(\partial u / \partial y)^2$, which is zero at the surface for films with no surface shear. Thus it does not appear that enhanced viscous dissipation is

the entire explanation. It is possible that Professor Lin's assumption of continuous velocity gradients at the interface directly implies greater stability? One notes that for two layer plane Couette flow, instability is made possible only by the presence of different velocity gradients at the interface of the two layers [3]. Conversely, assumption of continuous velocity gradients could cause a two layer film to be more stable.

Additional References

- 1 Yih, C. S., "Stability of Liquid Flow Down an Inclined Plane," *Physics of Fluids*, Vol. 6, 1963, pp. 321-334.
- 2 Kao, T. W., "Stability of Two-Layer Viscous Stratified Flow Down an Inclined Plane," *Physics of Fluids*, Vol. 8, 1965, pp. 812-820.
- 3 Yih, C. S., "Instability Due to Viscosity Stratification," *Journal of Fluid Mechanics*, Vol. 27, 1967, pp. 337-352.

Author's Closure

The author appreciates Professor Kirkpatrick's fine interpretation of the results for density stratified films. The derivation of the results for the case of viscosity stratified films was apparently not sufficiently detailed. The derivatives of the velocity profiles in the two liquid layers were assumed to be small but not zero. This can be seen from the last two equations in (2). For a quantitative estimate of the effect of viscous dissipation, one must evaluate the integral of the viscous dissipation term. It is not sufficient to just look at the dissipation term at the interface.

New Skin Friction and Entrainment Correlation for Turbulent Boundary Layers¹

H. E. Weber.² The authors of this paper present an interesting and apparently effective method of calculating turbulent boundary layer behavior in both positive and negative pressure gradients. The simple lag theory with equations relating H , Λ , E , and β should be further pursued. The authors claim that the AFOSR-IFP-Stanford Conference [1] data correlates as well or better with their method as with any other previously available. Since the correlation or references to them are not presented one cannot confirm this claim.

There is a basic inconsistency however in equations (9), (10), and (12) (equation (11) is not included in the paper). Since equation (12) is valid for adverse pressure gradients as exist in diffusers it must also be good near separation. At separation $\Lambda = 0.5$, and equation (9) reduces to

$$E_{\text{sep}} = 4.24K e_{\text{sep}}$$

This equation may be combined with equation (10) and (12) of the paper resulting in

$$0.0038e^{-\beta/15} = -0.12$$

This result is impossible since the exponential can be no less than zero.

In Reneau et al. [2] is given a correlating equation for the boundary layer thickness as

$$\delta/\theta = 6.1 + 120e^{-2.5H}$$

For separation

$$\Lambda = \delta^*/\delta = 0.5$$

When these equations are combined we obtain $H = 12.2$. Although it is true that H is changing very rapidly near separation, this result states that separation occurs at a given value of H . Separation occurring at a given value of Λ or H is a different criteria than that given by Weber [3]

$$KRe_{\theta}^{1.163} = -0.0319$$

or Spalding [4]

$$KRe_{\theta} = -0.00668$$

where

$$K = (\nu/U^2) \frac{dU}{dx}$$

¹By J. H. Ferziger, A. A. Lyris, and J. G. Bardina, published in the December, 1982 issue of the JOURNAL OF FLUIDS ENGINEERING, Vol. 104, No. 4, pp. 537-540.

²Director, Graduate Center, Pennsylvania State University, Radnor, Pa. 19078.

and is related to β of the paper by

$$K = -\frac{\beta c_f}{2Re^*}$$

Of course the separation of Weber or Spalding is nearly an equilibrium value where $\beta \cong \text{constant}$ [5]. The Spalding and Weber criteria yield the same results at a momentum thickness Reynolds number of 15,000. Of course if the separation criteria is defined by $c_f = 0$, Ludwig-Tillman gives an infinite value of H . Even in this paper a separation value of $H = 12.2$ yields a negligible value of c_f . Weber [3] gives an equilibrium correlation of c_f [3] as

$$c_f = c_f(Re_{\theta}, \bar{K})$$

where \bar{K} is some upstream average of $K(x)$ to account for boundary layer history. Perhaps this equation could use the local value of K if modified with the entrainment rate and equation (7) of the paper.

The authors are to be commended for making progress in presenting a simplified calculation scheme for two-dimensional turbulent boundary layers.

References

- 1 Kline, S. J., M. V., Morkovin, G., Sovran, and D., Cockrell, "Computation of Turbulent Boundary Layers," 1968 AFOSR-IFP-Stanford Conference, Dept. of Mech. Engr., Stanford Univ., Calif., 1968.
- 2 Reneau, L. R., Johnston, J. P., and Kline, S. J., Rpt. RD-8, Thermosciences Div., Mech. Engr. Dept., Stanford Univ., Calif., 1966
- 3 Weber, H. E., "Boundary Layer Calculation for Analysis and Design," ASME JOURNAL OF FLUIDS ENGINEERING, Vol. 100, June 1978, pp. 232-236.
- 4 Kutateladze, S. S., and Leontev, A. I., *Turbulent Boundary Layers in Compressible Gases*, Translated by Spalding D. B., Academic Press, New York, N.Y., 1964, p. 96.
- 5 Clauser, F. H., ed. Dryden, H. L., and Von Karman, T., *Advances in Applied Mechanics, IV*, "The Turbulent Boundary Layer," Academic Press, New York, 1956, pp. 1-51.

Authors' Closure

Dr. Weber points out that the two entrainment correlations (one represented by equations (9) and (10) and the other by equation (12)) may not be consistent. We presented two correlations because the first is more robust, while the second is easier to apply in those cases for which it is intended. These correlations do not agree in all cases, but the scatter in the data leaves room for considerable variation. Also, the computed results do not appear to be very sensitive to the differences, at least in the region of separation.

With respect to Dr. Weber's point on the separation criterion, we would like to say that this paper is not directed toward that issue. We merely borrowed from the work of

Kline et al. (authors' reference [2]), and their paper should be consulted on this issue. Suffice to say here that their results are in substantial agreement with all of the data and with other correlations where they are applicable, and this is the reason why we have adopted it.

Modification of Vortex Shedding in the Synchronization Range¹

Owen M. Griffin.² Dr. Zdravkovich has provided some interesting interpretations of both recent and early studies of the oscillations of circular cylinders due to vortex shedding in air and in water. The experiments discussed by him give ample evidence once again of the complexity of the phenomenon of wake capture, or synchronization, between the vibrations and the vortex shedding. It is clear from the experiments discussed in this paper and several of its references that wake phenomena such as hysteresis in the fluctuating pressures and forces on the cylinder, and discontinuous variations in such quantities as the base pressure or drag, the lift force, and the wake width are dependent on both the displacement amplitude and the frequency of the oscillations.

For instance in Fig. 3 it is shown at the reduced velocities $W = 5.4$ and 5.9 that the paths of the vortices apparently twice cross the wake centerline when the displacement amplitude $A = \pm 0.7D$ and $\pm 0.55D$. These experiments were conducted in

¹By M. M. Zdravkovich, published in the December, 1982 issue of the JOURNAL OF FLUIDS ENGINEERS, Vol. 104, No. 4, pp. 513-517.

²Naval Research Laboratory, Washington, D.C. 20375.

water. However, the detailed flow visualization photographs of Griffin and Ramberg [15], taken in air, show at $W = 6.3$ and at $A = \pm 0.25$ that the vortex formation follows the more usual process that is indicated in the $W = 6.0$ photograph of Fig. 4. The vortices are shed and move away downstream with increasing lateral spacing on the same side of the wake. For these experiments of Griffin and Ramberg in the upper synchronization range, it was clear that the vortices were being shed at about $T/12$ (T is the period of the shedding) before the cylinder reached its equilibrium position at the wake centerline.

It would appear that some additional experiments are necessary in order to further clarify the interesting ideas put forward in this paper.

Authors' Closure

Dr. Griffin's discussion points out the important differences between laminar and turbulent synchronized wakes. These differences might have been expected because the Strouhal number dependence on the Reynolds number is different for the two states of flow in the wake of the stationary cylinder. Hence it is likely that these intrinsic differences will show up also in the synchronized wakes.

I fully agree that additional experiments are necessary. The main aim of my paper was to try to raise the fog of incomprehension which covered the synchronization phenomenon. Dr. Griffin's discussion clearly showed that I have left some fog for subsequent researchers.

Kline et al. (authors' reference [2]), and their paper should be consulted on this issue. Suffice to say here that their results are in substantial agreement with all of the data and with other correlations where they are applicable, and this is the reason why we have adopted it.

Modification of Vortex Shedding in the Synchronization Range¹

Owen M. Griffin.² Dr. Zdravkovich has provided some interesting interpretations of both recent and early studies of the oscillations of circular cylinders due to vortex shedding in air and in water. The experiments discussed by him give ample evidence once again of the complexity of the phenomenon of wake capture, or synchronization, between the vibrations and the vortex shedding. It is clear from the experiments discussed in this paper and several of its references that wake phenomena such as hysteresis in the fluctuating pressures and forces on the cylinder, and discontinuous variations in such quantities as the base pressure or drag, the lift force, and the wake width are dependent on both the displacement amplitude and the frequency of the oscillations.

For instance in Fig. 3 it is shown at the reduced velocities $W = 5.4$ and 5.9 that the paths of the vortices apparently twice cross the wake centerline when the displacement amplitude $A = \pm 0.7D$ and $\pm 0.55D$. These experiments were conducted in

¹By M. M. Zdravkovich, published in the December, 1982 issue of the JOURNAL OF FLUIDS ENGINEERS, Vol. 104, No. 4, pp. 513-517.

²Naval Research Laboratory, Washington, D.C. 20375.

water. However, the detailed flow visualization photographs of Griffin and Ramberg [15], taken in air, show at $W = 6.3$ and at $A = \pm 0.25$ that the vortex formation follows the more usual process that is indicated in the $W = 6.0$ photograph of Fig. 4. The vortices are shed and move away downstream with increasing lateral spacing on the same side of the wake. For these experiments of Griffin and Ramberg in the upper synchronization range, it was clear that the vortices were being shed at about $T/12$ (T is the period of the shedding) before the cylinder reached its equilibrium position at the wake centerline.

It would appear that some additional experiments are necessary in order to further clarify the interesting ideas put forward in this paper.

Authors' Closure

Dr. Griffin's discussion points out the important differences between laminar and turbulent synchronized wakes. These differences might have been expected because the Strouhal number dependence on the Reynolds number is different for the two states of flow in the wake of the stationary cylinder. Hence it is likely that these intrinsic differences will show up also in the synchronized wakes.

I fully agree that additional experiments are necessary. The main aim of my paper was to try to raise the fog of incomprehension which covered the synchronization phenomenon. Dr. Griffin's discussion clearly showed that I have left some fog for subsequent researchers.